

Newcastle University

Chemical and physical transformation of aerosol droplets in Raman tweezers

Anatolij Miloserdov

A thesis submitted for the degree of Doctor of Philosophy

School of Natural and Environmental Sciences

November 2021

To those who helped me in my darkest hours

Acknowledgements

First, I would like to thank my primary supervisor Dr Antonia Carruthers for her invaluable guidance, advice and discussions throughout my PhD studies, as well as discussing my ideas about the research and broadening my view on science. I feel honoured to be the first PhD student in her research group.

I would like to thank my second supervisor Dr Benjamin Horrocks, for his invaluable advice and helpful discussions.

I would like to thank a good friend of mine and colleague Calum Day, and a project student Emma Pearson with whom I worked on some of the things described in this thesis.

Last but not least, I would like to thank my friends Drs Julien Eng, Tomas Pope, Christopher Medcraft and Matthäa Holland-Cunz, along with Eva Gouguola, and my friends from aikido Amjad Natour, Danwen Huang, Joanna Brebner and Luc Racaut, as well as my other friends and family, who all know what they did.

Vilnius, November 2021

Anatolij Miloserdov

Abstract

Calcium carbonate (CaCO_3) particles are one of the most abundant mineral aerosol totalling to approximately 8% of the total mass of mineral aerosols in the atmosphere, amounting to a loading of $\sim 1.3 \text{ Tg}$.

It is possible to produce CaCO_3 via a “simple” ion exchange reaction between calcium chloride (CaCl_2) and sodium carbonate (Na_2CO_3). This reaction seems simple, however as a mineral CaCO_3 can also have multiple polymorphs, such as calcite, vaterite and a hydrated crystal ikaite (calcium carbonate hexahydrate, $\text{CaCO}_3 \cdot 6\text{H}_2\text{O}$). This reaction and its mechanism is important in both inorganic and biological chemistry, as CaCO_3 is major component of bones and shells of living organisms, and the exact mechanism of formation and transformation of the different polymorphs is not known. In the atmosphere it can react with various reactive gases, such as NO_x and SO_x gases.

This thesis can be split in to two major parts: a comparison of the hygroscopic responses of CaCl_2 , sodium chloride and a hydrocarbon (2-Hydroxypropyl)- β -cyclodextrin using aerosol optical tweezing and dynamic vapour sorption, and the other focusing on the investigation of the formation and transformation of CaCO_3 polymorphs in an optically tweezed aerosol droplet using Raman spectroscopy. In this thesis the formation and transformations CaCO_3 is looked at from different perspectives: a theoretical model of the changes in the equilibrium size of the particle at a set relative humidity as a function of depletion of CaCl_2 available for the reaction, and a spectroscopic point of view focusing on the evolution of the Raman spectrum of the droplet as the CaCO_3 forms and transitions between polymorphs.

The thesis also looks at potential ways of overcoming the issues encountered in the previously mentioned parts of the thesis, such as the use of Brownian motion of the droplet in a video recording for sizing.

Table of contents

Abstract.....	vii
Chapter 1 A very brief introduction	1
1.1. Overview	1
1.2. Atmospheric impact.....	1
1.2.1. <i>Particle travel</i>	1
1.2.2. <i>Clouds and Albedo</i>	2
1.2.3. <i>Chemical transformations</i>	3
1.3. <i>Human health</i>	4
1.3.1. <i>History</i>	4
1.3.2. <i>Airborne pathogens and allergens</i>	6
1.3.3. <i>Drug delivery</i>	6
1.3.4. <i>Impacts of pollution</i>	7
1.4. Calcium carbonate	7
1.4.1. <i>Physical properties</i>	7
1.4.2. <i>Formation of CaCO₃</i>	8
1.4.3. <i>Other instances</i>	8
1.4.4. <i>Effects of pollution on calcium carbonate</i>	9
1.5. Aims and Motivation	9
1.6. Structure	9
Chapter 2 Basics of optical trapping and Raman spectroscopy	11
2.1. Optical trapping regimes.....	11
2.2. <i>Optical forces in the geometric regime</i>	13
2.3. <i>Optical traps</i>	17
2.4. Raman Spectroscopy	20
2.5. <i>General principles</i>	20
2.6. <i>Comparison of Raman spectroscopy with other types of spectroscopy</i>	21
2.7. <i>Stimulated Raman Scattering</i>	22
2.8. <i>Raman instrumentation</i>	24
2.9. Summary.....	27
Chapter 3 Computer aided techniques.....	29
3.1. Some terminology.....	29
3.2. Brief introduction to “hard” optimization and the logic behind it	30
3.2.1. <i>Least squares problems</i>	32

3.2.2.	<i>Types of optimization algorithms</i>	34
3.2.3.	<i>Drawbacks</i>	35
3.3.	Conclusions	36
Chapter 4	Responding to humidity	38
4.1.1	<i>Definitions</i>	38
4.1.2	<i>Kelvin equation and its significance</i>	39
4.1.3	<i>Hygroscopic growth</i>	41
4.2	Defining arrested states	42
4.3	Single particle measurements vs multi particle measurements	44
4.4	Summary	45
Chapter 5	Experimental procedures	46
5.1.	Trapping cell preparation	46
5.2.	Aerosol injection	46
5.3.	Hygroscopic growth curves procedures	46
5.3.1.	<i>AOT:</i>	46
5.3.2.	<i>DVS:</i>	47
5.4.	The chemical reaction procedure:	47
5.5.	Experimental notes and suggestions	47
5.6.	Experimental setup	48
5.6.1.	Optical system	48
5.6.1.	<i>Relative humidity control and trapping cell equipment</i>	50
5.6.2.	Dynamic Vapour Sorption	53
5.6.3.	<i>DVS instrument</i>	53
5.7.	Decomposition software	54
5.8.	The growth factor fitting	56
5.9.	Summary	60
Chapter 6	Aerosol Hygroscopic Growth	61
6.1	Describing the hygroscopic response: Kreidenweis equation model, κ-Kohler model, and multicomponent aerosols (Zdanovskii–Stokes–Robinson theory)	61
6.1.1	<i>Kreidenweis equation model</i>	62
6.1.2	<i>κ-Kohler theory model</i>	62
6.1.3	<i>Comparing the Kreidenweis and κ-Kohler theory models</i>	63
6.1.4	<i>Zdanovskii–Stokes–Robinson Theory</i>	64
6.1.5	<i>Mass and molar fraction-based growth factor calculations</i>	65
6.2	Sodium chloride	67

6.2.1	<i>General description</i>	67
6.2.2	<i>AIOMFAC curve</i>	67
6.2.3	<i>Aerosol Optical Tweezers data</i>	71
6.2.4	<i>Dynamic Vapour Sorption data</i>	73
6.2.5	<i>Hygroscopic growth curves</i>	74
6.3	Calcium chloride	78
6.3.1	<i>General description</i>	78
6.3.2	<i>AIOMFAC curve</i>	79
6.3.3	<i>Aerosol Optical Tweezers data</i>	82
6.3.4	<i>Dynamic Vapour Sorption data</i>	83
6.3.5	<i>Growth curves</i>	84
6.4	Chemical reaction completion models based on the ZSR theory	86
6.5	2-hydroxypropyl-β-cyclodextrin	90
6.5.1	<i>General description</i>	90
6.5.2	<i>Dynamic Vapour Sorption data</i>	90
6.5.3	<i>Growth curves</i>	91
6.6	Conclusions	93
Chapter 7 “Anatomy” of a Raman peak		94
7.1.	What broadens a peak in the Raman Spectrum?	94
7.1.1.	<i>Frequency distribution of a laser</i>	94
7.1.2.	<i>Homogeneous and Inhomogeneous broadening</i>	98
7.2.	<i>Sodium Carbonate: dissolved, anhydrous and hydrated</i>	99
7.3.	<i>Water in a hydrated crystal</i>	101
7.4.	<i>Differentiating between polymorphs of calcium carbonate</i>	103
7.5.	Line profiles: A mathematical description	108
7.5.1.	<i>Gaussian profile</i>	108
7.5.2.	<i>Lorentzian profile</i>	108
7.5.3.	<i>Voigt profile and the Pseudo-Voigt approximation</i>	108
7.5.4.	<i>Asymmetry</i>	110
7.6.	Peak profile modelling	113
7.6.1.	<i>Calcite model</i>	114
7.6.2.	<i>Vaterite model</i>	118
7.6.3.	<i>Carbonate ion model</i>	129
7.7.	<i>Total model</i>	131
7.8.	Conclusions	131

Chapter 8	Forming calcium carbonate. Data and a conjecture.	132
8.1.	Literature.....	132
8.1.1.	<i>Temperature</i>	133
8.1.2.	<i>pH, ions and drying</i>	133
8.1.3.	<i>Computational studies</i>	134
8.1.4.	<i>Solubility</i>	134
8.1.5.	<i>Biological and inorganic amorphous calcium carbonate</i>	135
8.2.	Experimental results	135
8.2.1.	<i>Overview</i>	135
8.2.2.	<i>Data</i>	136
8.2.2.1.	<i>Direct formation of calcite</i>	136
8.2.2.2.	<i>Formation of calcite via vaterite</i>	139
8.2.2.3.	<i>Stability of vaterite</i>	142
8.2.2.4.	<i>Addition of excess Na₂CO₃ solution and formation of ikaite</i>	145
8.2.3.	<i>pH of solutions</i>	149
8.3.	<i>Discussion</i>	151
8.3.1.	<i>Direct formation of calcite</i>	151
8.3.2.	<i>Direct formation of calcite from the ACC</i>	152
8.3.3.	<i>The classic route formation of calcite via vaterite</i>	153
8.3.4.	<i>Stable vaterite</i>	154
8.3.5.	<i>Forming ikaite</i>	155
8.3.6.	<i>pH of solutions</i>	156
8.4.	The conjecture on the electromagnetic approach to ions in solution 163	
8.4.1.	<i>Electromagnetic model of nucleation</i>	163
8.4.2.	<i>Presence of H⁺ and OH⁻ ions within the ion hydration cluster</i> ... 169	
8.4.3.	<i>Solubility and phase separation of non-polar compounds</i>	172
8.4.4.	<i>Opposite polarities of ions in solution, proximity interactions and the dissolution-precipitation equilibrium</i>	175
8.4.5.	<i>Comparison with the Debye–Hückel theory</i>	176
8.4.6.	<i>Influence of additional ions on the localised distribution of H⁺ and OH⁻ ions, and by proxy the local electric field</i>	177
8.4.7.	<i>Literature and rationale</i>	179
8.4.8.	<i>Implications</i>	181
8.5.	Conclusions.....	187
Chapter 9	What we see ... we measure.....	190

9.1.	Aerosols from yet another perspective.....	190
9.1.1.	<i>Some physics</i>	<i>191</i>
9.1.2.	<i>Dampening.....</i>	<i>192</i>
9.1.3.	<i>Brownian motion</i>	<i>192</i>
9.1.4.	<i>General basics</i>	<i>193</i>
9.1.5.	<i>Spring stiffness</i>	<i>193</i>
9.2.	Image analysis basics	195
9.2.1.	<i>Optical transfer function.....</i>	<i>195</i>
9.3.	Motion tracking software.....	197
9.3.1.	<i>Comparison of principles of motion tracking with WGMs.....</i>	<i>198</i>
9.3.2.	<i>Image analysis.....</i>	<i>199</i>
9.3.3.	<i>Current issues</i>	<i>204</i>
9.4.	Conclusion	205
Chapter 10	Summary, Conclusions and Future Prospects.....	207
10.1.	Summary.....	207
10.2.	Conclusions	210
10.3.	Future prospects.....	213
10.3.1.	<i>Molecular fine structure determination using Raman spectroscopy</i>	<i>213</i>
10.3.2.	<i>Extending the conjecture on the electromagnetic approach to ions in solution</i>	<i>214</i>
10.3.3.	<i>Additional verification of the ZSR model</i>	<i>214</i>
10.3.4.	<i>Aerosol droplets as microreactors</i>	<i>214</i>
10.3.5.	<i>Aerosols as tunable optical cavities.....</i>	<i>215</i>
10.3.6.	<i>AOT automation</i>	<i>215</i>
10.4.	Final remarks.....	216
Chapter 11	Bibliography	217

Table of figures

Figure 1.1.....	2
Figure 1.2.....	3
<i>Figure 1.3.....</i>	5
Figure 2.1.....	12
Figure 2.2.....	14
Figure 2.3.....	15
Figure 2.4.....	16
Figure 2.5.....	16
Figure 2.6.....	18
Figure 2.7.....	19
Figure 2.8.....	19
Figure 2.9.....	20
Figure 2.10.....	22
Figure 2.11.....	24
Figure 2.12.....	24
Figure 2.13.....	25
Figure 2.14.....	26
Figure 2.15.....	27
Figure 3.1.....	33
Figure 3.2.....	36
Figure 4.1.....	40
<i>Figure 4.2.....</i>	41
<i>Figure 4.3.....</i>	42
Figure 4.4.....	43
Figure 4.5.....	44
Figure 5.1.....	49
<i>Figure 5.2.....</i>	51
<i>Figure 5.3.....</i>	52
Figure 5.4.....	53
<i>Figure 5.5.....</i>	54
Figure 5.6.....	57
<i>Figure 5.4.....</i>	60
Figure 6.1.....	68
Figure 6.2.....	70
Figure 6.3.....	72
Figure 6.4.....	73
Figure 6.5.....	74
Figure 6.6.....	75
Figure 6.7.....	76
Figure 6.8.....	77
Figure 6.9.....	78
Figure 6.10.....	79
Figure 6.11.....	81
Figure 6.12.....	82
Figure 6.13.....	83

Figure 6.14	84
Figure 6.15	85
Figure 6.16	86
Figure 6.17	88
Figure 6.18	89
Figure 6.19	91
Figure 6.20	92
Figure 6.21	92
Figure 7.1	96
Figure 7.2	97
Figure 7.3	100
Figure 7.4	102
Figure 7.5	104
Figure 7.6	105
Figure 7.7	110
Figure 7.8	111
Figure 7.9	111
Figure 7.10	113
Figure 7.11	116
Figure 7.12	118
Figure 7.13	120
Figure 7.14	122
Figure 7.15	125
Figure 7.16	128
Figure 7.17	130
Figure 8.1	134
Figure 8.2	137
Figure 8.3	138
Figure 8.4	140
Figure 8.5	141
Figure 8.6	143
Figure 8.7	144
Figure 8.8	146
Figure 8.9	147
Figure 8.10	148
Figure 8.11	149
Figure 8.12	151
Figure 8.13	152
Figure 8.14	154
Figure 8.15	155
Figure 8.16	155
Figure 8.17	156
Figure 8.18	165
Figure 8.19	166
Figure 8.20	167
Figure 8.21	169
Figure 8.22	170

Figure 8.23	171
Figure 8.24	173
Figure 8.25	176
Figure 8.26	182
Figure 8.27	183
Figure 9.1	191
Figure 9.2	193
Figure 9.3	196
Figure 9.4	197
Figure 9.5	201
Figure 9.6	202
Figure 9.7	202
Figure 9.8	203
Figure 9.9	203
Figure 9.10	204
Figure 9.11	205

Table of Tables

Table 5.1	59
Table 6.1	69
Table 6.2	85
Table 6.3	88
Table 6.4	93
Table 7.1	98
Table 7.2	101
Table 7.3	107
Table 7.4	115
Table 7.5	117
Table 7.6	119
Table 7.7	120
Table 7.8	121
Table 7.9	123
Table 7.10	123
Table 7.11	126
Table 7.12	126
Table 7.13	129
Table 7.14	131
Table 8.1	150
Table 8.2	150
Table 8.3	150

Chapter 1 A very brief introduction

1.1. Overview

Aerosols are an important part of the Earth's atmosphere affecting the planet we live on globally and locally and can be artificially created to affect human health. It is possible to see how the impact of natural and man-made aerosols can reach global and local effects, traveling vast distances. They are also responsible for many important chemical transformations in the atmosphere.^[1-14]

1.2. Atmospheric impact

1.2.1. *Particle travel*

Aerosol particles are known to linger in the atmosphere and can remain in the atmosphere for days and can be transported over long distances by atmospheric currents. For example dust storms originating in the Sahara desert raise sand particles in to the atmosphere, and are transferred across in to the Caribbean regions by atmospheric air currents, forming the islands. ^[3,12-14]Current meteorological tools allow tracking the flow of atmospheric particles all across the globe, and is an important tool in the understanding of weather, climate change and the

consequences of human activity, such as the tragic aftermath of Fukushima Daiichi nuclear power plant disaster.^[4,5]

During the Fukushima disaster large amounts of radioactive dust was ejected into the atmosphere. This dust was then picked up by the atmospheric air currents and transported across the Pacific Ocean to the United States, and in the opposite direction. For example, a large cloud of radioactive particular matter moved towards Tokyo between the 14 and 15 of March 2014.^[4] This cloud posed a significant potential threat to the population of Tokyo; with the possibility of evacuation.^[4,5]

1.2.2. Clouds and Albedo

Aerosol clouds can influence the changing climate of the planet through direct effects such as reflection of solar radiation and through indirect effects such as the evolution of aerosols through chemical transformation and the hygroscopic response of aerosols (aerosols acting as cloud condensation nuclei for droplets). This behaviour is particularly important as aerosols are thought to have a large contribution to decreasing the radiative forcing and through that influencing global warming.^[6]

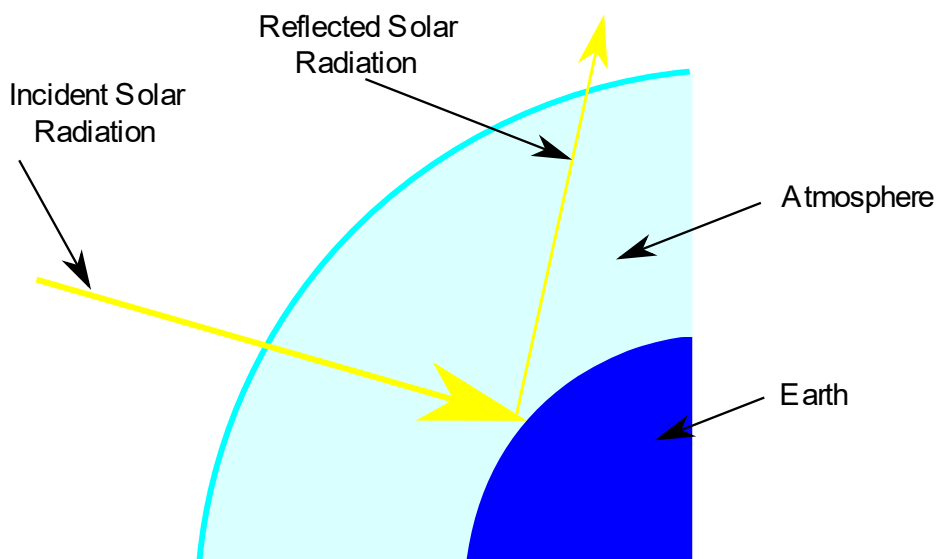


Figure 1.1 A schematic of the earth's albedo, which is the ratio of the reflected solar radiation incoming solar radiation. An albedo value of 1 signifies that 100% of the solar radiation was reflected. One of the ways it is possible to measure this effect is through measuring the albedo of the aerosol clouds. Albedo is defined as the ratio of the radiation scattered over the total intensity of radiation that it is irradiated with.^[15] (See Figure 1.1) This makes the albedo as general quantity applying both to clouds and different surfaces of the earth.^[16] A simple example of the influence of albedo on

the climate can be observed even on relatively small scales by for example observing the urban and rural microclimates.^[2,8,17–20]

As an example, sea spray aerosol droplets are known to have an albedo close to 1, almost completely reflecting the radiation it is irradiated with.^[21] On the other hand, soot particles, and black carbon particles must be mentioned, because unlike other aerosols black carbon particles contribute to a decrease in the overall albedo and can coat other, more reflective surfaces, thus preventing them from reflecting the incoming radiation.^[22–26] (See Figure 1.2)

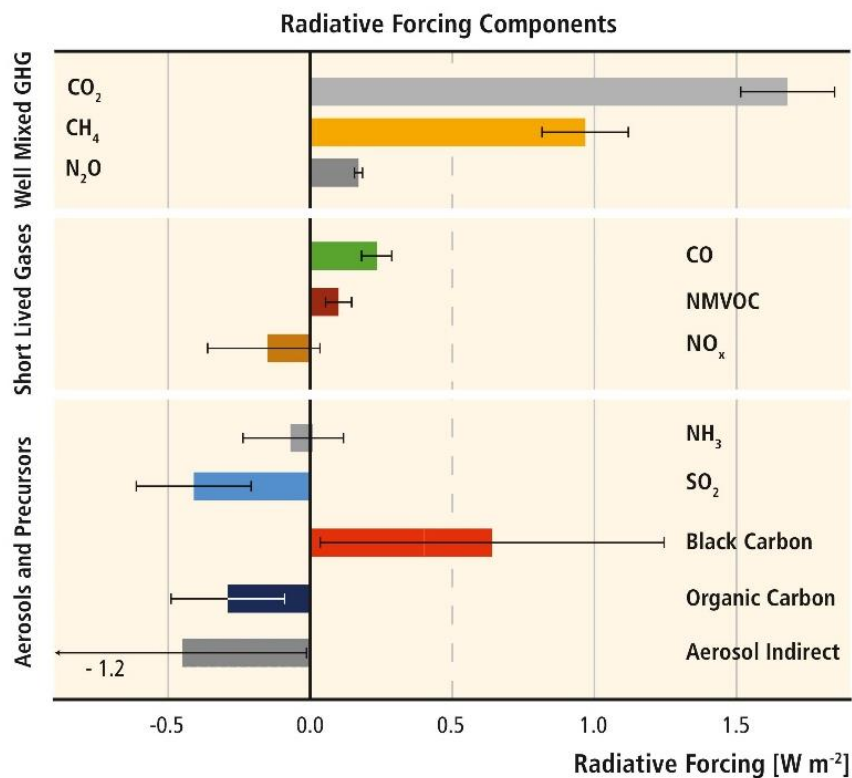


Figure 1.2 A table of the various components of the atmosphere and their impact on the radiative forcing.^[6] As mentioned previously, aerosol particles can act as cloud condensation nuclei. The process of equilibrating with the relative humidity (RH) of their surroundings, is known as the hygroscopic response. This process changes the size of the aerosol droplet and the concentration of the solute in the droplet as water evaporates or is absorbed to establish equilibrium. As the size of the droplet changes, a change in the albedo of the droplet can be observed, thus the knowledge of the composition of an aerosol and its hygroscopic response could be used for a better understanding of the physical processes happening in the atmosphere.^[27]

1.2.3. Chemical transformations

Since the atmosphere consists of many different gases and both liquid and solid aerosol particles; chemical reactions are bound to happen. Among the major groups of reactive chemicals are the NO_x (nitrous oxides) and SO_x (sulphuric oxide) species as well as gases CO₂, CO, NH₄, and various organic carbon species and volatile organic hydrocarbons.^[2,28] This allows for a wide variety of chemical transformations, which in turn will lead to changes in the hygroscopic response of the aerosol particle and produce a knock-on effect on the albedo of the particles and clouds. These factors make the study of chemical transformations in aerosols an important topic to study.^[28]

Another aspect of chemical transformations of aerosols is their sedimentation on Earth's surface. An example of this process is rain. The understanding of the chemical transformations can give insight in to the naturally occurring cycles of chemicals in nature and in more detail on the effects of human activity on the environment.^[6]

1.3. Human health

Mankind has had a long history of dealing with aerosols influencing human health. Research in to this specific field has produced many important discoveries that affect multiple aspects of our life. Currently aerosol research related to healthcare can be broadly divided in to 3 groups: airborne pathogens and allergens^[29–31], drug delivery^[32–36], and pollution^[8,25,37].

1.3.1. History

Since ancient times mankind has been interested in what we breathe and how it relates to our health. One of the earliest known uses of inhalable medicines can be traced back to ~1554 BC Egyptian papyrus Ebers (specific text). Other archaeological evidence shows that opium was smoked in ancient China as early as 1100 BC. Smoking and inhaling opium is also described by Avicenna as a treatment for severe coughs and noted that the patient needs to be monitored to prevent overdose. Other diseases such as asthma were also known in ancient times with texts dating circa 600 BC India, suggesting smoking a medicinal plant as a way of relieving symptoms of asthma. Asthma cigarettes were also used throughout history up until the 20th century.^[38,39]



Figure 1.3 A photograph of asthma cigarettes. Image courtesy of Mark Sanders. (Reproduction rights were purchased; Original image: <http://www.inhalatorium.com>)

All of this suggests that even in ancient times had some understanding of inhaled particles and their effect on human health. Another historical example of this are the masks used by plague doctors, commonly stuffed with a combination of various smelling objects ranging from lavender and spices to honey and vinegar. Their aim was to prevent the wearer from inhaling the illness when treating the patients and was in use after the plague has passed. Even though it is now known that the bubonic plague itself is not transmitted via inhalation, the use of the mask had a kernel of truth behind it as some diseases can spread this way.^[40] However not all of medical perspectives in history were reasonable, with treatments such as tobacco smoke enemas existing. This treatment was primarily used for resuscitating a person after drowning and required one to literally blow smoke up someone's rectum.^[41,42]

In the mid-19th century other methods of producing aerosols where introduced: atomisers and nebulisers, and dry powder inhalers. These are now commonly used in medical applications, as they both are portable, easier to control and do not require a source of heat unlike for example asthma cigarettes.^[39] Another important milestone of healthcare aerosols was the development of metered dose inhalers in the 1950s, which allowed the doses to be accurately measured out, improving the quality of life of people suffering from a variety of respiratory illnesses.^[39]

1.3.2. Airborne pathogens and allergens

Airborne pathogens are an extremely fast way of disease transmittance, as they merely require one only be in the same environment and breathe the same air in order to contract it. Even hundreds of years ago people suspected that some diseases could transmit via air, as evidenced by the creation of plague doctor's masks. Now we understand more about the transmission of airborne diseases, and research is being performed on the spreading of such diseases in closed environments, for example airplane cabins.^[43–45]

Airborne allergens can also have a significant impact on the patients suffering from the allergy. One of the most common allergies caused by airborne allergens is Allergic Rhinitis, commonly known as hay fever. Hay fever is an umbrella term for an allergy caused by airborne pollen. The allergic reaction causes increased secretion of mucus in the nose (rhinorrhoea), sneezing, etc. and can impact the quality of life of the person suffering from this allergy.^[30,31]

1.3.3. Drug delivery

Intuitively, aerosols are an effective way of delivering drugs to the respiratory system and in case of airway blockage can be a fast and reliable way of targeted delivery of drugs. One of the major benefits of delivering medication to the lungs via inhaled aerosol is that the local concentration of the drug in the lungs can be high, whilst the blood plasma concentration can be much lower. This allows mitigating some of the negative side effects of the medication. For example, in short term relief of asthma bronchodilators such as beta-2 adrenergic receptor (ADRB2) agonists (medications that produce a response when binding with a receptor, for example salbutamol sulphate) are used, to relax the smooth muscles in the bronchi. However, ADRB2 are located in all of the smooth muscles, not just the bronchi and a high concentration of such a drug could produce negative side-effects. Thus using aerosols to deliver the medication is beneficial.^[33–35,46–48]

It is important to note that aerosols can be used to administer a wide variety of medications, targeting a wide range of diseases. There is research into the use of aerosols to deliver insulin to diabetes patients, as well as medication for treatment of Alzheimer's disease. The use of aerosols could potentially allow people to inhale the

medication they need, instead of injecting it, which could significantly improve their quality of life.^[49,50]

Another important aspect of drug delivery are the overdose reversal nasal sprays, which are incredibly useful tools in reducing the lethality of drug overdoses. Most notably it is used in cases of opioid drug overdoses, such as heroin overdoses.^[51]

1.3.4. Impacts of pollution

Pollution has been strongly linked to human health. One of the most notable examples of this is the 1952 smog of London, when the pollution produced by the burning organic fuels caused an estimated 12000 deaths within a span of just a few months.^[37,52,53] Currently, even though measures are taken to control and reduce air pollution, it still causes global healthcare issues, with the WHO reporting a staggering 7 million deaths attributable to air pollution in 2016. Hence it is definitely an important issue to combat, and in my opinion should be one of the things that is tackled by all nations together, as aerosols demonstrate that they can quickly spread over vast areas.^[6]

1.4. Calcium carbonate

Formation and the chemistry of calcium carbonate (CaCO_3) is important in various areas of research. CaCO_3 is among the most abundant by mass mineral aerosols, constituting ~8% of mass of mineral dust aerosols, totalling to ~1.3 Tg or 1.3 million tonnes in the atmosphere. Some of the sources of mineral aerosols in general and CaCO_3 are deserts, arid and semiarid lands, where wind picks up the soil particles and raising them into the atmosphere. This allows mineral aerosols to travel extensive distances and react in the atmosphere with various gases, such as NO_x and SO_x gases as well as chloride containing and volatile organic compounds.^[28]

1.4.1. Physical properties

Calcium carbonate is an insoluble, typically white solid and is a major component of bio minerals such as bones and shells, as well as concrete and can also be commonly encountered with other compounds for example as chalk.^[54,55] Pure calcium carbonate can be most often found as several polymorphs, calcite and aragonite in particular. Another polymorph containing only CaCO_3 is vaterite, however it is not a stable polymorph and in the presence of water is converted in to

calcite, which is more thermodynamically stable.^[54,56–59] CaCO_3 can also exist as a hydrated crystal, particularly as monohydrocalcite and hexahydrocalcite also known as ikaite^[60–70]. All the polymorphs of CaCO_3 (calcite, aragonite and vaterite) as well as ikaite are birefringent, i.e. having multiple refractive indexes.^[54,71] CaCO_3 can also form an amorphous state^[57,59,72], which is suspected to have short range ordered structures corresponding to various polymorphs, often termed as proto-vaterite, proto-calcite and proto-aragonite, signifying their similarity to the different polymorphs.^[73,74]

1.4.2. Formation of CaCO_3

There are multiple chemical reactions that can be used to form CaCO_3 . In this thesis the reaction a seemingly simple ion exchange reaction between calcium chloride (CaCl_2) and sodium carbonate (Na_2CO_3) is performed in an optically tweezed aerosol droplet. This reaction yields a precipitate of CaCO_3 and sodium chloride (NaCl) as a by-product. However, this reaction mechanism does not specify the polymorphic composition of the CaCO_3 obtained. It is known that the addition of ions, for example magnesium ions^[75–78] and phosphate ions^[55,62,79], the pH^[62,79–82] and the temperature^[59,62,63,78,83] of the solution can alter the resulting polymorph. What is currently known is that calcite is the most stable polymorph and that vaterite can convert itself into calcite in an aqueous environment. It is also possible to produce CaCO_3 by reacting CaCl_2 with CO_2 in an aqueous environment^[54,80], which could be a potential way of reducing the amount of CO_2 in the atmosphere.

1.4.3. Other instances

As mentioned, CaCO_3 is also important in biomineralization, as it is one of the main components of bones, shells and corals.^[60,73,84–92] The ability of living organisms to utilise the properties of CaCO_3 extends to the point of some organisms producing composite materials with multiple types of CaCO_3 polymorphs.^[60,88,93,94]

1.4.4. Effects of pollution on calcium carbonate

Even though CaCO_3 is insoluble in water, with a solubility depending on the polymorph is in the order of $9\text{-}10 \text{ mmol kg}^{-1}$ at 25°C ^[55,70,81,95–99], it is soluble in dilute acids, which becomes an issue when the acidity of the environment increases. As one example the increase of the CO_2 in the atmosphere is known to be a factor contributing to an increase in the acidity of the earth's oceans. This affects the solubility of the CaCO_3 found in the shells, and has the potential to have disastrous consequences for marine life.^[85–87,100] A similar effect can be noticed in concrete structures, as CaCO_3 is one of its components.^[101–103]

1.5. Aims and Motivation

The aims of the research conducted in this thesis are:

- Investigate and compare single optically tweezed aerosol droplet and dynamic vapour sorption (DVS) methods of investigating the hygroscopic properties of chemical compounds.
- Produce and analyse a phase transition ion exchange chemical reaction between CaCl_2 and Na_2CO_3 forming CaCO_3 polymorphs in an optically tweezed aerosol droplet using Raman spectroscopy and video imaging.

1.6. Structure

Chapter 2 will describe the optical methods used in the research conducted in the duration of this thesis. The first part of the chapter will give a brief explanation of the principles of optical trapping and outline the differences between the different designs of optical traps. The second part of this chapter will be concerned with the principles of Raman spectroscopy, the distinctiveness of Raman spectroscopy in comparison with other spectroscopy techniques used in chemistry (IR absorption and Fluorescence). This will be continued with outlining the specific aspects of Raman spectroscopy in aerosol droplets, and the different instrumentation that could be used for Raman spectroscopy.

Chapter 3 will provide a brief introduction for the mathematical optimization algorithms used in this thesis, the least squares problem approach and some of the

philosophy behind mathematical optimization, as a way of solving problems such as fitting data to mathematical models.

Chapter 4 will be aimed at discussing the specific properties of aerosols, such as the difference between single aerosol droplets and bulk solutions, as well as briefly touching on the differences between the analysis of multiple aerosol droplets and single aerosol droplets.

Chapter 5 will describe the experimental procedure. The chapter will be concluded with a description of the optical tweezing and Raman spectroscopy setup used in the experiments discussed in this thesis. This chapter will also outline the theory and hardware used for dynamic vapour sorption, and the instrumentation used for control over the humidity in the aerosol trapping cell and the trapping cell itself. In this chapter an optimization software calculating the dry radius and the hygroscopic growth parameters is introduced and demonstrated to work on theoretical data.

In the following chapter (**Chapter 6**) will go into some detail regarding hygroscopic growth of aerosols, discussing and comparing the hygroscopic growth of a few examples of organic and inorganic compounds using aerosol optical tweezers and DVS. In this chapter several models will be suggested for tracking chemical reactions in aerosol droplets using the hygroscopic growth.

Chapter 7 the theory of the processes affecting the line profile of Raman spectra will be described. This will be continued with the theoretical models of the peak profiles used to decompose a spectrum into the different polymorphs CaCO_3 .

Chapter 8 will draw on the theory presented in chapter 7 and will explore the tracking of chemical reactions in aerosols using Raman spectroscopy.

Chapter 9 will take a different direction and look at imaging aerosols and how tracking the Brownian motion of an aerosol particle in the optical tweezers using video imaging and its potential application to tracking the size of an aerosol particle.

Chapter 10 will present the conclusions and potential future work.

Chapter 11 Bibliography

Chapter 2 **Basics of optical trapping and Raman spectroscopy**

Effects, which can easily be overlooked can sometimes become extremely important when looked at in detail. This is true for optical forces and Raman scattering, both of which were initially described as feeble^{1,2} and since their discoveries have become extremely useful tools in many scientific fields.³⁻⁵

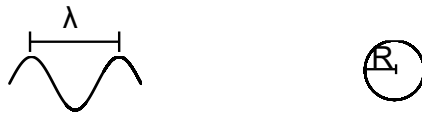
2.1. Optical trapping regimes

The principles of optical trapping and optical guiding were developed by A. Ashkin in 1970⁶ by optical guiding and in 1986⁷ by building the first single beam optical trap, which later became known as the optical tweezers⁸. This work has had a significant impact as it was a way of manipulating objects using focused laser beams and without any contact by an external object. This has found many uses in natural sciences in analysing the properties of light^{9,10}, the interactions of particles with one another¹¹, studying the properties of proteins and DNA⁵, and in studying single particles away from any surfaces^{12,13}.

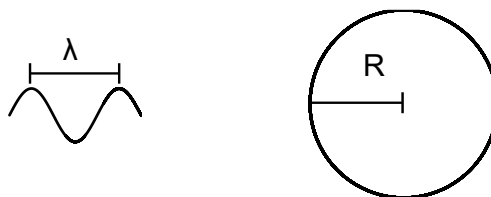
Optical trapping in general is divided in to 3 particle regimes: the Rayleigh regime, the geometric regime, and the intermediate regime. These regimes are based on the size of the particle relative to the wavelength of the light the particle is trapped with.¹⁴ (see Figure 2.1)

The distinction between these particle regimes can be summarised as when the particle is significantly smaller than the wavelength of the light it will act as a point dipole in an electromagnetic field, and the particle is classified as a particle in the Rayleigh regime. In a case when the particle radius is larger than the wavelength of the light it will be trapped due to the radiation pressure exerted on the particle as light is reflected, refracted and absorbed by the particle. The intermediate regime as the name suggests, is a regime where the particle will be trapped by the combination of the forces acting in the Rayleigh in geometric regimes (see Figure 2.1). In the research conducted for this thesis only particles in the geometric regime were looked at. For more details on the Rayleigh and intermediate particle regimes see J.H. Seinfeld and S.N. Pandis.^{14,15}

$R \ll \lambda$ for particles in the Rayleigh regime



$R \approx \lambda$ for particles in the intermediate regime



$R \gg \lambda$ for particles in the geometric regime

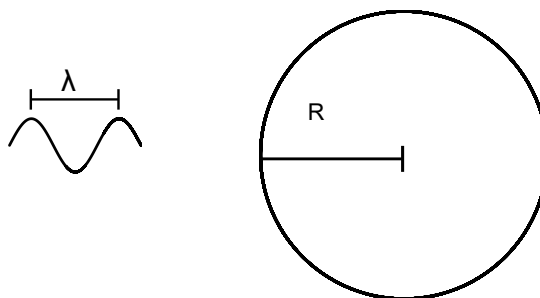


Figure 2.1 A Schematic representation and the comparisons of the characteristic parameters of the 3 particle trapping regimes. Here R is the radius of the particle and λ is the wavelength of light used to trap the particle.

2.2. Optical forces in the geometric regime

The principle optical trapping of particles in the geometric regime relies on the forces produced by the radiation pressure as consequence of Newtonian's 3rd law of motion which states:

“Actioni contrarem semper et aequalem esse reactionem: sive corporum duorum actiones in se mutuo semper esse aequales et in partes contrarias dirigi.” Sir Isaac Newton, *Philosophiae naturalis principia mathematica*¹⁶

Translation: " To every action there is always opposed an equal reaction; or, the mutual actions of two bodies upon each other are always equal and directed to contrary parts." ¹⁷

This results in two forces acting on an optically trapped particle: the scattering force and the gradient force. Whilst both of these forces are a consequence of radiation pressure they act on the particle in significantly different ways.

The scattering force is a force that pushes the particle along the path of the laser beam. Out of the two optical forces discussed in this chapter the scattering force is the most obvious consequence of radiation pressure as it will be directly due to light extinction properties of the particle (both scattering and absorption of light). The scattering force will exist with any ray of light and will always push a particle in the direction of propagation of light, regardless of the intensity profile of the beam of light.

In contrast to the scattering force, the gradient force relies on the difference in intensity profile of the laser beam as well as on the geometry of the beam itself. As a physical phenomenon the gradient force is also caused by the radiation pressure, but acts in a way that pulls the particle in to or away the region of the highest intensity of the light beam, depending on the refractive indexes of the particle itself and the surrounding medium.

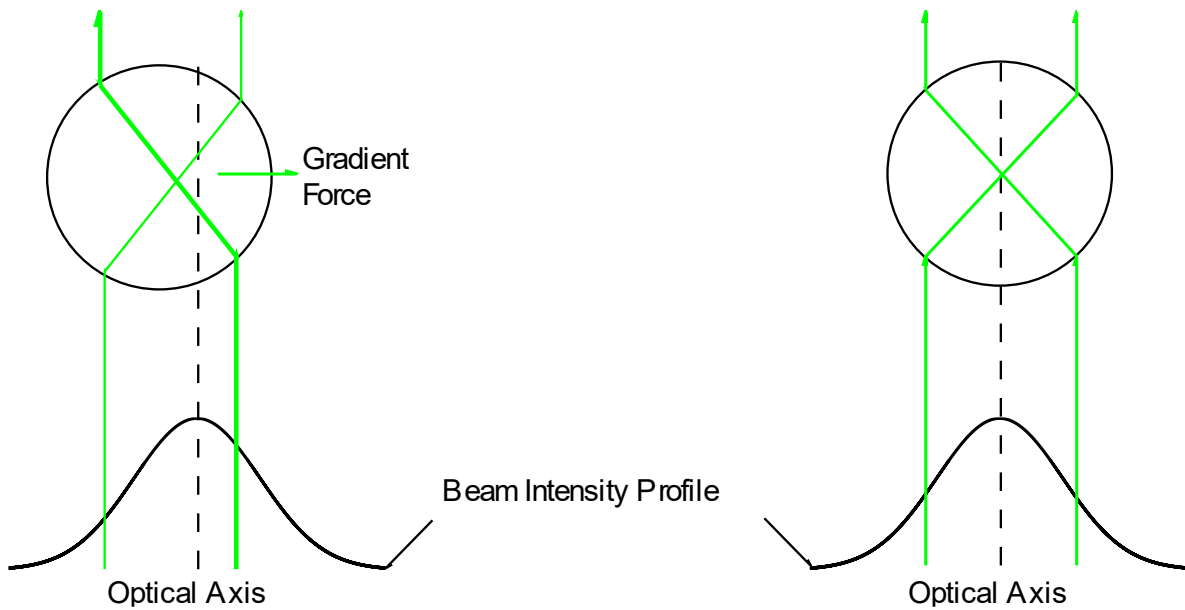


Figure 2.2 A schematic representation of the gradient force acting on an optically trapped particle. Here the particle has the higher refractive index than its surroundings.

In case of the particle having a refractive index higher than the surrounding medium, the particle will be pulled into the high intensity region of the laser beam. The inverse also applies: if the particle has a lower refractive index than the surrounding medium, the particle will be pushed out of the high intensity region of the laser beam. In these cases, the refractive index will affect the way that the light is refracted of the surface of the particle by the principle of the Snell's law¹⁸ (see Equation 2.1):

$$n_1 * \sin(\theta_1) = n_2 * \sin(\theta_2) \quad \text{Equation 2.1}$$

Here n_1 and n_2 are refractive indexes of materials 1 and 2 respectively, and θ_1 and θ_2 are the angles of the incident light and refracted light relative to the optical axis, which is always perpendicular to the interface between materials 1 and 2. As a consequence, the refractive index of the particle will dictate the direction of the gradient force acting on the particle. A special, case would be when the $\theta_1 = \theta_2 = 0$, i.e. the incident angle is completely perpendicular to the interface between the media and coincides with the optical axis. This results in the equation known as the Shell's law in the form of (see Equation 2.2 and Figure 2.3):

$$n_1 * \sin(\theta_1) = n_2 * \sin(\theta_2) = 0 \quad , \quad \text{due to } \sin(0) = 0 \quad \text{Equation 2.2}$$

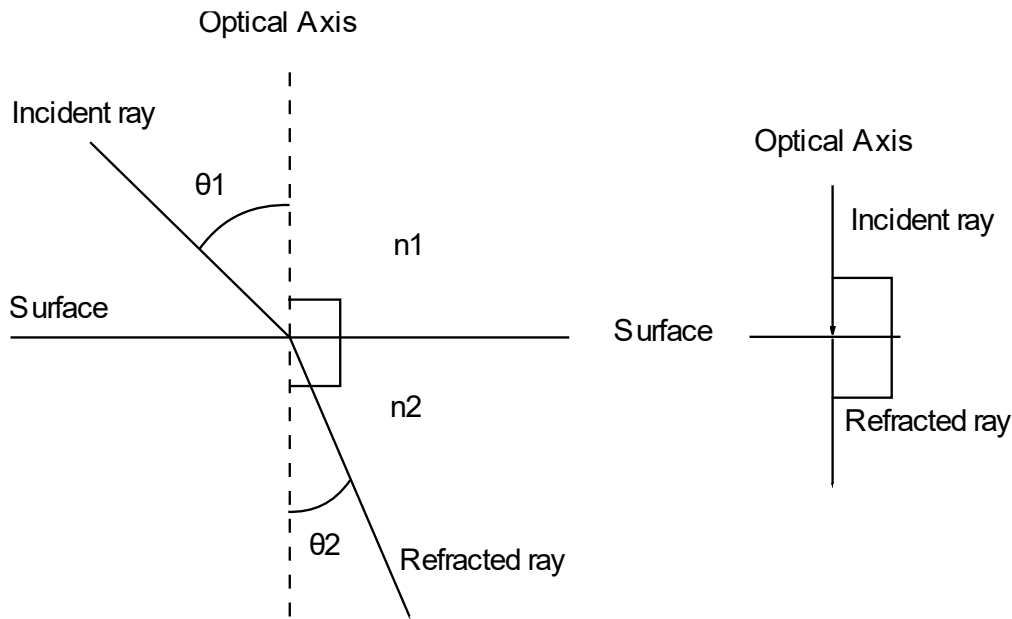


Figure 2.3 A schematic representation of the Snell's law. Left: the general representation of the Snell's law in equation 2.1. Right: the special case of $\theta_1 = \theta_2 = 0$. (see Equation 2.2)

In this case the refractive indexes of the particle and the surrounding medium will have no influence on the geometrical direction of the refracted light. Hence the radiation pressure acting on a particle as part of the gradient force will be minimal, making it the “preferred” position of the particle in an optical trap. When considering this case, it is important to keep in mind that even though a particle of a lower refractive index than the medium should be trapped, however it does not happen due to physical processes such as Brownian motion of the particle in the optical trap, which will slightly offset the particle from the ideal position, disrupting the $\theta_1 = 0$ condition and expelling the particle from the laser beam.

When considering a parallel beam with a Gaussian intensity profile a particle with a higher refractive index than the surrounding medium will be pulled into the beam by the gradient force and pushed along the direction of the propagation of light by the scattering force. This optical setup is known as an optical guide, as it will simply guide the particle trapping it in two dimensions perpendicular to the direction of propagation of light.

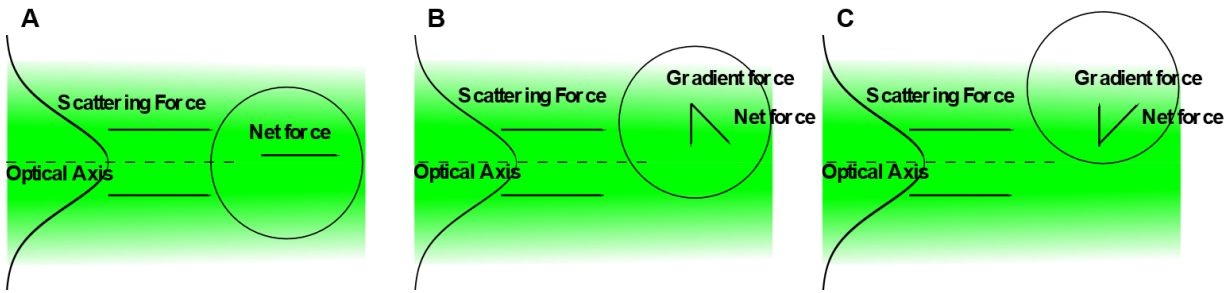


Figure 2.4 A schematic of scattering force and the action of an optical guide. A: the particle is pushed along by the scattering force, with the gradient force simply keeping the particle in the centre of the beam. B: the particle is pushed along by the scattering force and pulled into the beam by the gradient force, with the particle having a higher refractive index than its surroundings. C: the particle is pushed along by the scattering force and expelled by the scattering force, with the particle having a lower refractive index than its surroundings.

The gradient force can also be manipulated along the optical axis of the laser beam by focussing the laser beam. This results in optical trapping, as than the droplet is confined in all three dimensions. Optical trapping can be divided for distinction in to two groups: optical levitation and optical tweezing. (see Figure 2.5)

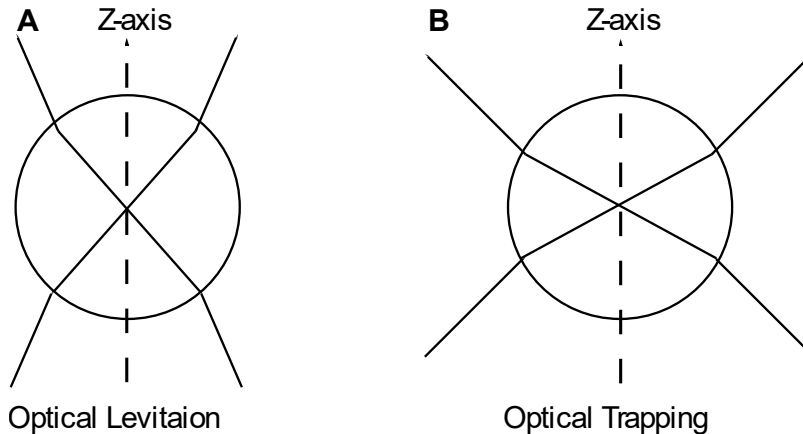


Figure 2.5 A schematic of the difference between optical levitation (A) and optical trapping (B). In case of optical levitation, the trapping laser is focused less tightly than in optical tweezing. This results in optical tweezing confining the particle along the z axis tighter, than in case of optical levitation.

The distinction between optical levitation and optical tweezing is mainly in the confinement along the optical axis of the trapping region of the optical setup. The rule of thumb is that in optical levitation the particle is confined more gently along the optical axis than in optical tweezing. This results in the possibility of describing all of

the mentioned optical manipulation tools being a family of optical manipulation tools with a gradient of confinement of the trapped particle along the optical axis.

As mentioned earlier only particles that have a refractive index higher than the surrounding medium will be pulled into the high intensity region, and the particles with a refractive index lower than the refractive index of the surrounding medium will be expelled from the laser beam. This could also be utilised to trap particles by forming a well in the shape of the laser beam, for trapping low refractive index particles.

When dealing with aerosol particles the case of the particles having a refractive index lower than the surrounding medium slightly less relevant than in other systems as aerosols are by definition colloidal dispersions of liquid or solid particles in a gas, and therefore the surrounding medium will have a refractive index close to 1, whereas most liquids and solids will have a refractive index higher than that, for example the refractive index of water is approx. 1.333.¹⁹ In the work described in this thesis all of the chemicals were in aqueous solutions and their response to changes in relative humidity, therefore all of the particles were liquid or had a liquid shell, and therefore had a refractive index close to or above that of water.

2.3. Optical traps

The simplest design of an optical trap was utilised by Ashkin in 1986 for trapping single dielectric particles in water, which was capable of trapping particles in ranges ranging from 10 μm down to ~ 25 nm with an argon laser at 514.5 nm wavelength.⁷ It utilises a single laser beam with a Gaussian intensity profile focused through a high numerical aperture microscope. This setup later became known as optical tweezers as it confined the trapped particle tightly in all three dimensions.⁷ (see Figure 2.6)

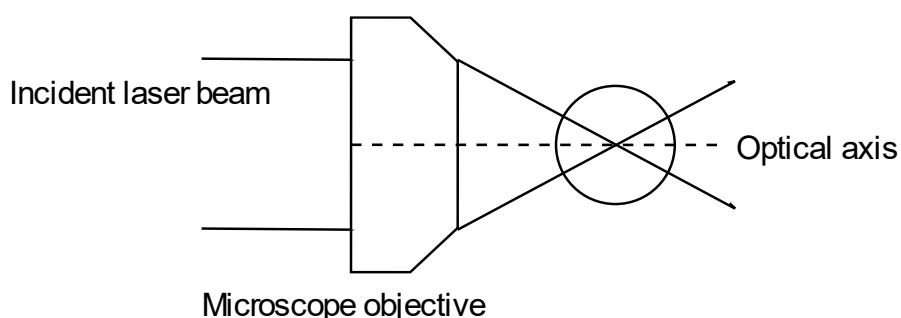


Figure 2.6 *The setup of a single beam optical tweezer. The microscope objective focuses the incident beam in order to trap the particle.*

A similar setup is used for the experiments described in this thesis. A single Gaussian beam was first expanded in order to fill the back of a high aperture microscope objective in order to maximise the gradient produced by the laser beam, maximising the gradient force of the optical trap. The trapping region was illuminated using a blue LED for imaging using a CMOS digital camera. The back scattered light was reflected through a beam splitter and analysed using Raman spectroscopy. (see this Chapter 2.3)

The benefits of using this setup are the simplicity of design of this trap the capability of the system to image the trapped particle and the use of the laser beam for both optical trapping and as a pump laser for Raman spectroscopy.

As a brief account of other systems that could be of beneficial to aerosol research are multi-particle traps and counter-propagating dual beam traps. Neither of these setups have been used in the research done for this thesis, however they will be considered as possible opportunities for future work.

In principle the multi-particle optical traps, as the name suggests have the capability of trapping and controlling multiple individual particles simultaneously. This is done through having multiple individual beams coming in through the microscope objective and as a consequence have multiple trapping regions. The simplest setup capable of this would have the trapping beam split using a beam splitter and then reflected so that both beams coincide almost completely. This generates two focal points, one for each beam and creates separate trapping regions for each of the beams. As both beams can be controlled independently, the setup could be used to perform experiments on controllably coalescing the droplets, exchange of volatile components between particles in close proximity, using one of the droplets as a relative humidity sensor or in biological applications such as DNA stretching.^{5,20} (see Figure 2.7)

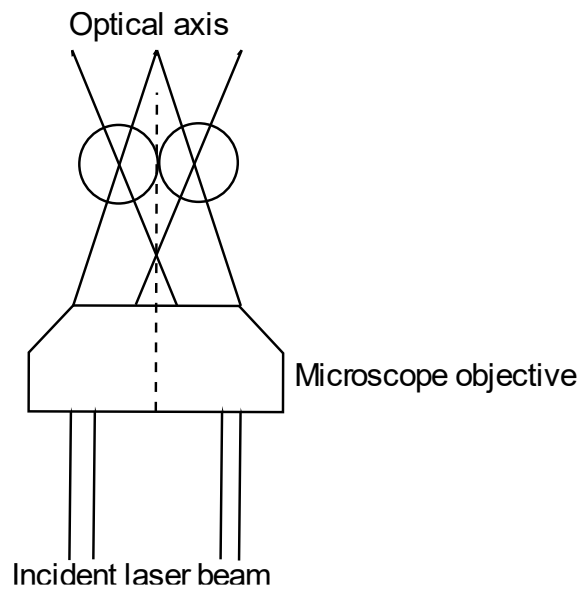


Figure 2.7 A schematic of a multiple particle trap. The beam is split into two before it is focussed by the microscope objective. This results in two focused trapping regions, each capable of trapping a particle.

The counter-propagating dual beam setup utilises two beams directed in opposite directions and focused at the same point in space. This allows using the scattering forces produced by the two beams to cancel each other out. In practice one must account for the inaccuracies in the system, such as the trapping regions of the beams not coinciding perfectly and the uneven split of the of the trapping laser beams. However, the principle still applies, and this type of an optical trap would still negate a part of the scattering force produced by any of the beams. One of the potential applications of this set up could be for studying particles with a rapidly changing refractive index, as in these traps the gradient force will be the dominant force acting on the particle.²¹ (see Figure 2.8)

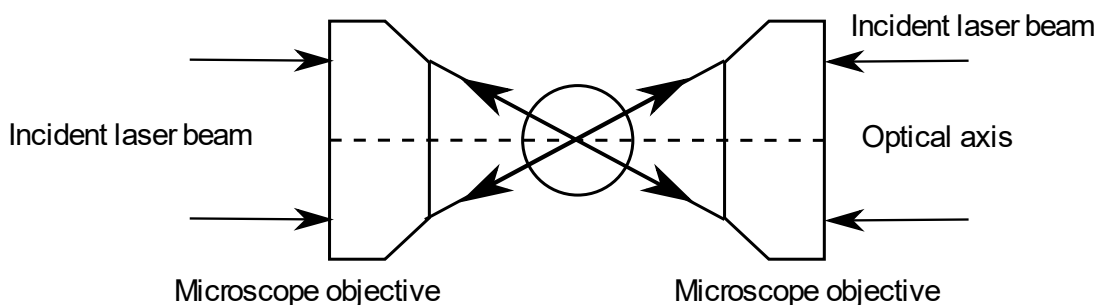


Figure 2.8 A Schematic of a counter propagating dual beam optical trap. Each of the incident laser beams is focused by its respective microscope objective, creating a trapping region. The trapping regions are spatially superimposed with each other

both trapping the same particle. This also utilises the counter propagation of the different beams in order to counteract the scattering force produced by the laser beams.

2.4. Raman Spectroscopy

Inelastically scattered light was first discovered by Sir C.V. Raman in 1928 in his paper “A new radiation”²² where he describes a new type of radiation as a scattering process, in contrast to it being referred to as a “feeble fluorescence”²². This is a crucial distinction which lead Raman to conduct an extensive investigation on the phenomenon, winning him a Nobel prize in Physics in 1930 and the effect being named after him, and is now often referred to as Raman Scattering.²² It is not unreasonable to describe Raman scattering as feeble, as spontaneous Raman signal, *i.e.* the signal produced without any enhancement is in the order of 10^{-12} photons when compared to Rayleigh scattered light (elastically scattered light).²³ There are techniques of enhancing the efficiency of the Raman scattering, such as Stimulated Raman Scattering (SRS).^{24–26}

2.5. General principles

Overall light can be scattered in two ways: as elastically scattered light also known as Rayleigh scattered light (named after its discoverer Lord Rayleigh) and as inelastically scattered light or Raman scattered light. The difference between the two is that in Rayleigh scattered light the scattered light has the same wavelength as the incident light, whereas in Raman scattered light the incident light will either impart (Stokes shift) or take (Anti-Stokes shift) a part of the energy when interacting with the bond.²⁷ (see Figure 2.9)

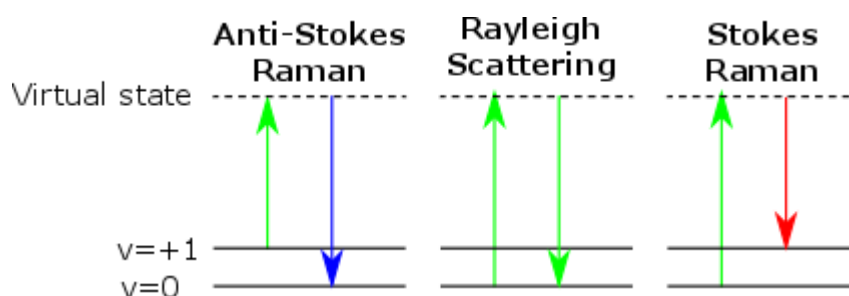


Figure 2.9 A diagram of spontaneous Raman Stokes and anti-Stokes, and the Rayleigh scattering. The green laser is the laser used for excitation of the sample.

Blue depicts the anti-Stokes signal, which has a higher energy than the excitation wavelength, i.e. blue shifted. Red signifies the Stokes signal, which has a lower energy than the excitation wavelength, i.e. red shifted. In none of the cases light is absorbed by the bond, hence no excited state. A virtual state is therefore used to schematically illustrate the scattering process and the changes in energy.

Raman spectroscopy relies on fluctuations in polarizability of a bond and is classified as part of vibrational spectroscopy. It is distinct from other forms of spectroscopy, as in Raman spectroscopy light is scattered when compared with IR spectroscopy (absorbance), and absorption and re-emission of light as in fluorescence. In Raman spectroscopy chemical information can be derived from the change in frequency between the irradiation frequency (the laser line) and the obtained signal frequency (Raman shift of a peak), which is always relative to the wavelength of the laser radiation.²⁷ This makes it possible to use Raman spectroscopy to study multiple effects such as rotation (ro-vibrational Raman spectroscopy and rotational Raman spectroscopy)^{28,29}, electron excitation (vibronic Raman spectroscopy)³⁰ and combining all of the three effects (ro-vibronic Raman spectroscopy)³¹. The principle of Raman scattering can also be extended in to the XRay region of the electromagnetic spectrum and used to analyse the electronic structure of compounds (X-ray Raman scattering)³².

2.6. Comparison of Raman spectroscopy with other types of spectroscopy

As mentioned, Raman spectroscopy is a distinct type of spectroscopy. However, Raman spectroscopy also has some similarities with other types of spectroscopy such as IR and fluorescence spectroscopies.²⁷

The distinction Between Raman spectroscopy and IR spectroscopy can be summarised in that IR spectroscopy is typically based on absorption/transmission of IR radiation, rather than scattering. Another key distinction is that IR spectroscopy relies on the change in the dipole moment of the vibrating bond, whereas Raman spectroscopy is sensitive to polarizability of the bond. This results in the well-known selection rules which dictate whether the vibration will be Raman or IR active.²⁷

Raman spectroscopy is also distinct from fluorescence spectroscopy, as in Raman scattering light is never truly absorbed, whereas in fluorescence it is absorbed and re emitted. Fluorescence in particular is an effect that needs to be considered when

recording a Raman spectrum, as fluorescence is significantly stronger than the intensity of Raman scattering. This can be counteracted by another distinction between Raman and fluorescence spectroscopies. As mentioned previously the signal produced by Raman scattering will always be relative to the excitation wavelength, whereas fluorescence will have a static excitation and emission wavelengths. Typically, fluorescence excitation wavelengths of most fluorescing compounds are in the violet and UV ranges of the electromagnetic spectrum, and Raman spectroscopy can be performed at longer wavelengths. This makes it possible to avoid an underlying fluorescence signal in Raman spectroscopy, which could lead to masking a part of the Raman spectrum of the compound by correctly choosing the excitation wavelength. Schematically it is somewhat similar to fluorescence, however it is actually very distinct as in light scattering the photon is never actually absorbed, thus having a virtual state (see Figure 2.9) in comparison to an excited state in fluorescence (see Figure 2.10).^{27,33}

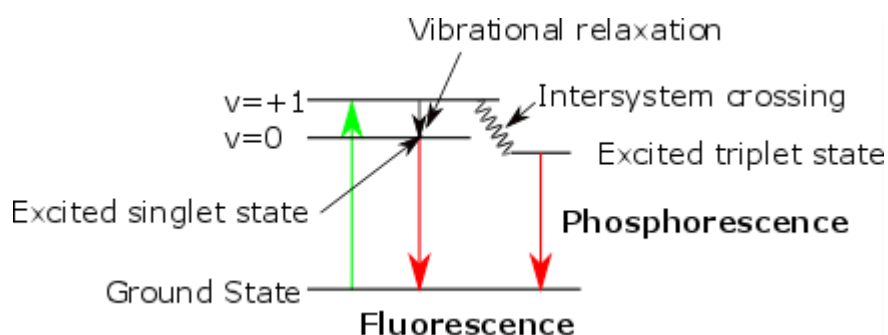


Figure 2.10 The Jablonski diagram, showing the principles of fluorescence and phosphorescence. *Fluorescence: the excitation is absorbed, part of the energy is released through the vibrational relaxation and reemitted as fluorescence. Phosphorescence: light is absorbed, some of the energy is used for an intersystem crossing (reversing the spin) of an electron, resulting in an excited triplet state, and then released through phosphorescence. Generally, fluorescence is a faster process than phosphorescence, as energy is stored for a longer period of time in the excited triplet state than in the excited singlet state.*³³

2.7. Stimulated Raman Scattering

Distinctly from the spontaneous Raman scattering, stimulated Raman scattering (SRS) is a 3rd order nonlinear process involving 2 photons interacting with the medium instead of only one in spontaneous Raman scattering.²⁴ In SRS the

stimulation of the Raman signal comes from the micro resonator properties of the aerosol droplets, thus can only appear when the necessary conditions for the droplet to act as a micro resonator are met. The micro resonator properties of the aerosol droplet appear due to the total internal reflections of the frequencies produced by spontaneous Raman scattering, coinciding with the optical cavity modes of the droplet. The optical cavity modes of the micro resonators span as a comb of frequencies across the visible spectrum that will be amplified by a droplet of a certain size and refractive. Therefore, the SRS could appear in any part of the spectrum, however the second condition of having an underlying simultaneous Raman scattering signal will prevent that from happening.³⁴

It is also important to note that due to the size of the optical cavity, micro resonators have an extremely high reflection quality factors, comparing to that of other optical cavities. This will influence the spread of the wavelengths amplified by the SRS, making it appear distinctively thinner than the chemical signals. The quality factor (Q) of the micro resonator is a property of the micro resonator which determines the width of the cavity mode and could be determined as a ratio of the frequency of the mode (ν) and its width (w).^{35,36}

$$Q=\nu/dw \qquad \text{Equation 2.3}$$

Comparing SRS to spontaneous Raman signal, SRS produces a more intense Raman signal, and therefore will be visible on top of the spontaneous Raman signal. This effect could be used to amplify some of the chemical signals, however in practice this is usually achieved only for broad spectral bands, such as the O-H vibrational modes with a Raman shift of approx. 3400 cm^{-1} .^{34,37} The resonance pattern appearing is known as Morphology Dependent Resonance (MDR), and often referred to as Whispering Gallery Modes (WGMs), which will be discussed in chapter 3. This signifies that the pattern produced by the SRS signals will be reflective of the morphology of the droplet and will only happen if the droplet has a morphology allowing it to act as a micro resonator and any processes that will affect the morphology of the droplet will be evident by the changes in the MDR pattern.³⁴

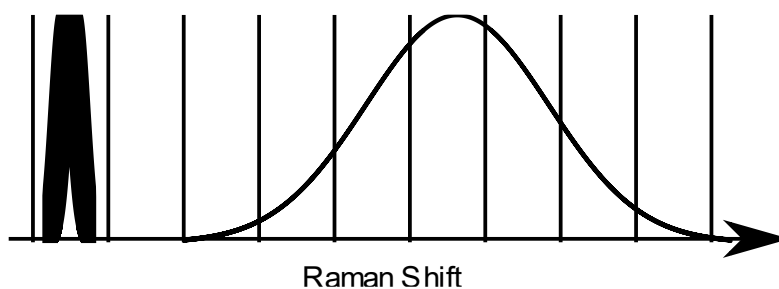


Figure 2.11 A schematic representation of the micro cavity modes overlapped over a schematic representation of a broad and a narrow peak in the spectrum. The broad peak has several micro cavity resonance modes, whereas the narrow peak could only have a maximum of 1 at any point in time.

When considering a Raman signal with a small width, it can be possible to either have the signal amplified by the cavity modes or not, hence the overall signal produced cannot be always regarded as SRS.^{34,38,39} This is a valuable distinction of the SRS occurring in an aerosol droplet³⁴ when compared to SRS spectroscopy²⁶, which uses two lasers one of which is constant and the other offset from it by a frequency equal to the Stokes shift. This changes the relative intensities if the two lasers increasing the intensity of the offset laser.^{24–26} (see Figure 2.12)

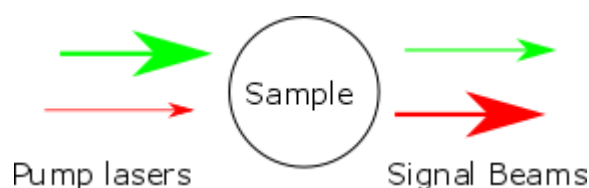


Figure 2.12 A schematic of the of the stimulated Raman scattering. The green beam is the pump laser and the red beam is the laser offset from the pump laser.

2.8. Raman instrumentation

Raman systems are comprised of an excitation laser, sample, a monochromator and a detector. In case of a Raman aerosol optical tweezers instrument the excitation laser is also the trapping laser and the trapped aerosol droplet is the sample, leaving only the monochromator and the detector to be characteristic of a Raman Optical tweezers instrument, compared to a general optical tweezers.⁴⁰

2.8.1. Types of monochromators

Monochromators in general can be divided in to two broad groups: dispersion monochromators and interferometers, both having their own advantages and

disadvantages. The simplest one that can be used is a Michelson interferometer, also known as the Fourier transform monochromator. (see Figure 2.13) While it doesn't truly monochromate the light it uses constructive and destructive interferences between the different wavelengths to produce an interferogram, which can be used to calculate a spectrum. This in itself allows to capture the entire spectrum and selectively amplify selected frequencies. Another not insignificant benefit is the internal calibration of the spectrum, as the excitation line will also be recorded in the interferogram providing an internal reference for the entirety of the spectrum. The same properties provide a major downside of this type of monochromator, as it will also record any light present which includes undesirable effects such as fluorescence and any additional light sources used for example for imaging.⁴¹

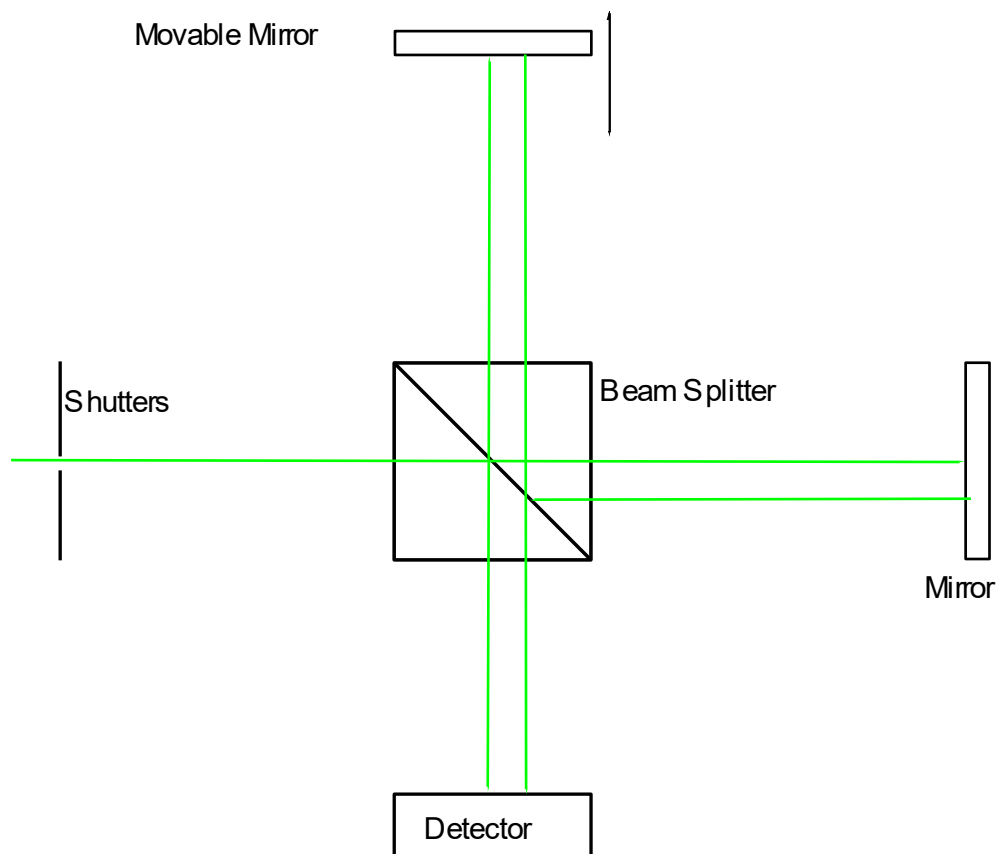


Figure 2.13 The schematic of a Michelson interferometer a movable mirror allows modifying the interference pattern detected by the detector. The modification of the interference pattern amplifies selected wavelengths and combined with the amount that the mirror has been moved allows calculating a spectrum.

Another type of monochromator is based on dispersion typically by dispersion gratings or prisms. When comparing this type of monochromator with the Michelson

interferometer this design does not record the entirety of the spectrum, rather focussing a specific “window” of frequencies on the different positions on a detector. This allows recording only a small and selective set of frequencies, allowing to filter out undesired frequencies, making it easier to continuously illuminate the sample whilst taking the spectrum. The most well-known type of a dispersion monochromator is the Czerny-Turner monochromator, which utilises a movable turret fitted with reflective gratings. The movement of the turret allows selecting the wavelengths that are focused on the detector.⁴¹ (see Figure 2.14)

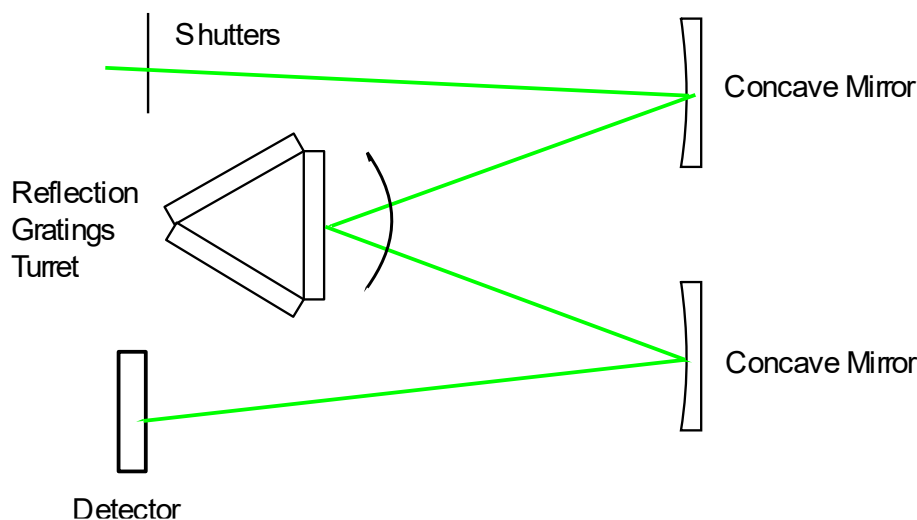


Figure 2.14 A schematic of a Czerny-Turner monochromator. The movement of the reflections grating turret allows changing the wavelengths detected, and changing the resolution by changing the gratings using turret rotation.

2.8.2. Detectors

The simplest and the first historically used was the photomultiplier tube (PMT). The photomultiplier tube uses a series of dynodes, which when hit with a photoelectron, will reflect the incident photoelectron and emit additional photoelectrons. The drawback of this setup is that all of the photons entering will contribute to the signal intensity, *i.e.* recording one wavelength at a time and a highly monochromated signal is necessary to obtain a good quality spectrum. The benefit of the PMT detector is the degree of amplification of the signal that can be achieved, simply by increasing the number of dynodes in the PMT.^{27,41} (see Figure 2.15)

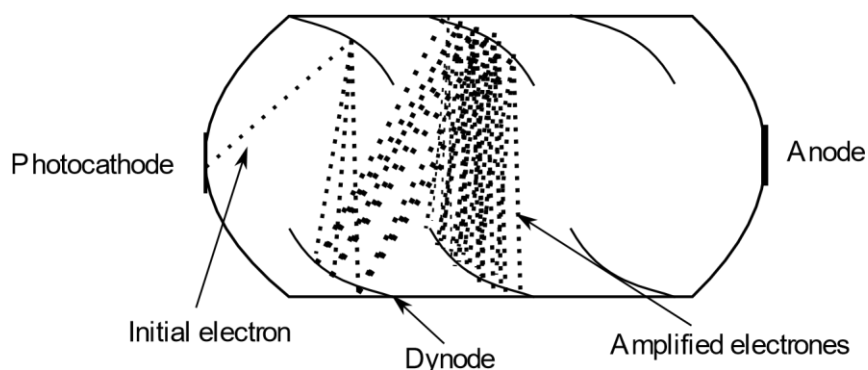


Figure 2.15 A schematic of a photomultiplier tube. The photocathode produces the initial electron, that by being reflected by the dynodes is amplified with each reflection. The total electron count is detected by being absorbed by the anode. The intensity of the resulting signal will be proportional to the number of initial electrons produced from the photocathode, which will be proportional to the intensity of the signal produced by the sample.

A successor of the PMT detector, (see Figure 2.15) and currently the most often used type of detector is the charge coupled device (CCD) detector. The CCD is extremely convenient for spectroscopic applications as it is a lot more compact than the PMT and can be manufactured in a way that allows detecting several wavelengths simultaneously. This is achieved by having an array of independent detectors (pixels) on a single surface next to one another. The intensity of the light falling on each of the pixels can then be recorded, compiling a spectrum. Another benefit is that due to the size of the individual pixels the separation of the of the different frequencies becomes a slightly lesser issue, when compared to a PMT. The downside of the CCD detectors is that the signal is not amplified, unlike in PMT detectors, however this is counteracted by the use of high quality (in terms of produced intensity and spectral linewidth) lasers.^{27,41} This type of detector was used in the experiments performed during this thesis.

A more recent technology that have emerged by combining the best qualities PMT and CCD detectors, resulting in the development of electron multiplied charge coupled devices (EMCCD) and intensified charge couple devices (ICCD). These devices are designed to increase the intensity of a signal whilst keeping the amount of noise as low as possible.⁴¹

2.9. Summary

This chapter has briefly outlined the basic principles of optical trapping and Raman spectroscopy, as well as the instrumentation used, highlighting contrasting features

with similar processes. The optics of the experimental setup was also described in this chapter. The aspects highlighted in this chapter lay the foundation, provide context and will be extensively drawn on in further chapters.

Chapter 3 Computer aided techniques

The use of computers and scientific software enable new methods of data analysis. This chapter will be focused on some of the software that was built as part of the research done for this thesis, as well as a brief introduction to the underlying algorithms, techniques and point of view used.

3.1. Some terminology

Defining the terminology used from here on in this thesis that refers only to anything computed or calculated, specifically optimization, models.

In this thesis model will refer only to an equation or a set of equations, including any constants, but excluding any values for variables (anything that is not a constant) and results. Thus, the results calculated using thermodynamic models (E-AIM and AIOMFAC web) will not be regarded as part of the model and referred to as computationally predicted data (or simply predicted data), regardless of the origins of the initial parameters or the method of derivation used for the model.^[104]

Optimization is the process of finding a best fitting parameter under a defined set of conditions.^[104] Fundamentally it can be considered as consisting of two sub-types: maximization and minimization, the goals of which are to find the maximum or minimum of a function respectively.

3.2. Brief introduction to “hard” optimization and the logic behind it

Mathematical optimization is a large and complex area of research that focuses on finding solutions to complex mathematical problems and is utilized in areas such as economics, engineering, geophysics and molecular modelling. The problem a mathematical optimization solves is finding the best plausible value of a variable, which can be represented by an equation:

$$f_{\text{experimental}} = f(x) , \quad \text{Equation 3.1}$$

Where $f_{\text{experimental}}$ is the experimental data, $f(x)$ is a mathematical function modelling the process or peak in a spectrum and x – the optimized parameter. Therefore, optimization algorithms are designed to find the value of x at which equation 3.1 holds true. In practice, due to effects such as noise, which introduces a random error into a spectrum, the problem could be reinterpreted as seen in **Equation 3.2** Equation 3.2:

$$fitting\ error = f_{\text{experimental}} - f(x) \rightarrow 0 \quad \text{Equation 3.2}$$

Conceptually, it is possible to interpret an optimization problem as finding a function consisting of irreducible variables and other functions that can also be eventually reduced to a set of irreducible variables, which models the experimental data. In this case it is possible to think of the irreducible variables as degrees of freedom and dimensions of an n -dimensional mathematical space, with the modelling function existing in that space.

$$G = I_g \exp\left(-\frac{(z-x)^2}{2W_g^2}\right) \quad \text{Equation 3.3}$$

The simplest example of this would be a simple graph, which for example follows the Gaussian profile function in equation 3.3 (repeated as equation 7.1), assuming that I_g - intensity, W_g -width and z - position are constants and for illustrative purposes $G=y$. In this case each point of the graph would follow the $y=f(x)$ formula and would exist only in 2 dimensions the independent x dimension and the dependent y dimension.

A step up from this model would be to consider 2 independent variables x (wavenumber) and z (wavenumber of the peak maximum). In this case the equation can be rewritten as $y=f(x,z)$ and would exist in 3 dimensions, each of which corresponding to x , y and z variables. By following the same principle using equation

3.3 it is possible to incorporate additional variables, and thus dimensions into this model. However, considering equation 3.3, which has a total of 5 variables (4 independent variables and 1 the function of those parameters), a 5-dimensional space is required to simultaneously demonstrate all possible values of the dependent variable y (or G in the original equation) and all combinations of independent variables. However, with each additional dimension it becomes increasingly difficult to illustrate, hence it is often impractical to simultaneously depict more than 3 dimensions.

This is also possible to link this concept to physics. A single point the 3-dimensional case could be considered as analogous to a description of position in a Euclidean space in terms of its x , y and z positions, with x and z being independent and $y=f(x,z)$. Hence a potential way to imagine any optimization problem is to imagine an n -dimensional space, as done in Hilbert spaces.^[105] Hilbert spaces are an abstract concept of n -dimensional spaces and the Euclidean space can be considered as part of Hilbert spaces with $n=3$ dimensions. Euclidean space-time (x , y , and z positions and a position in time) would correspond a Hilbert space with $n=4$, etc.

The function modelling the theoretical data could then be thought of as the mapping of all dimensions in a Hilbert space in to a lower dimensional Hilbert space, similarly to the principle of holography described by the Anti-de Sitter/Conformal Field Theory correspondence (AdS/CFT correspondence, also known the gauge-gravity correspondence conjecture).^[106,107] This analogy allows imagining dependant variables as functions of independent variables, and the functions as holograms, since the function itself will contain all information regarding all degrees of freedom, i.e. a specific value of a function $f(x,y,z)$ will correspond to a unique set of the independent variables x , y and z . In mathematics this concept is known as the function space, which is part of the functional analysis branch of mathematics. By utilising this approach to viewing experimental spectra it is likely possible to utilize the techniques of functional analysis in the analysis of experimental data.

When considering all values of the function these values will contain all possible values of its variables, with a unique set of variables corresponding to a specific value of the function. By using mathematical optimization, it is possible to find the set of variables that will produce the value of the function that the function was optimized for.

The mathematical optimization allows finding the solutions that would produce the best fit in a regression analysis of each individual spectrum. Applied in succession to a series of spectra it is plausible to obtain a series of values of the specific degrees of freedom that would reflect the chemical and physical processes recorded in the spectra. This produces a model of a chemical reaction that can be analysed in terms of individual chemical spectra and in terms of time dependent change of those spectra.

$$x = s(f(n), \lambda, t) , \quad \text{Equation 3.4}$$

where x is a specific point in a spectrum at a specific time, $f(n)$ is the function describing the combination of peak profiles that model the spectrum, λ – wavelength, and t – time.

Another point about the mathematical optimization algorithms is that they typically done in iterations, with each iteration being closer and closer to the optimum value of the function.^[105,108–110] This is one of the most classic examples of exploiting the power of computation, specifically computers. While it is possible to solve the problem by hand, due to the number of iterations necessary to solve the problem, making it efficient to utilize computers.

3.2.1. Least squares problems

The general principle of least squares is finding a minimum of the difference between a function and a data point or function. Thus, fitting experimental spectra with specific line profiles is a specific case by minimising the squared difference between the two spectra is a least squares problem. (see Figure 3.1)^[111–113]

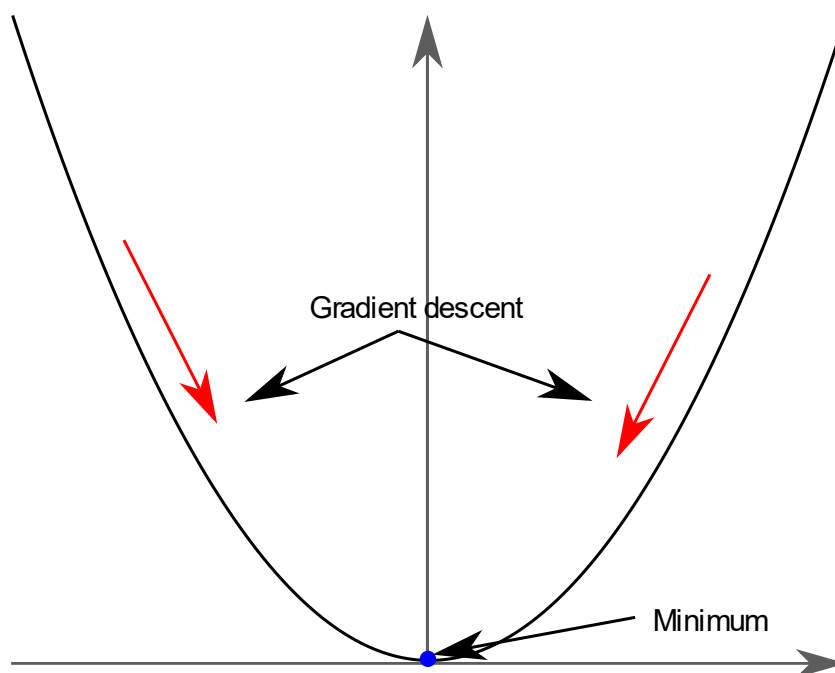


Figure 3.1 A schematic of the least squares type problem. In this type of problem, the optimization algorithms will descend the down (shown with red arrows) the curve (in black) to find the minimum position (blue dot). As the algorithm passes the minimum point the direction of the gradient changes, therefore converging on the minimum.

The overall analysis of the chemical reaction mapped out as a set of spectra can be viewed as two separate least squares problems, the wavelength dependent and time dependent analysis of the separate degrees of freedom. The algorithms used in the research done for this thesis are designed for dealing with least squares problems. Fundamentally, the least squares problem can also be considered as a way of viewing a mathematical problem, which focusses on finding an optimal solution. For example, finding the parameters of a model that would produce the best fit of the predicted data to the experimental data, determining the parameters of the model. It can also be used to find the most probable answers to any problem that can be mathematically put in a least squares problem form that will have a minimum, or a maximum if a maximization algorithm is used instead of a minimization algorithm.

The utilisation of the concept of least squares problems is not limited to by variables and thus dimensions that it exists in as all of the variables will be represented in the functional space of total function space. In the case of a decomposition of a map of spectra of a chemical reaction into its components, the dimensions of the final function space are: wavelength, amplitude and time.

The fact that least squares problems and optimization algorithms can and are utilised using computers allows analysing large sets of data in a short amount of time, which allows processing data efficiently. The analysis of data using the least squares method is not limited to simply fitting the parameters of a mathematical model to the experimental data, and along with other compute algorithms can be used to make decisions on the quality of the data and filter out outliers in the data. This fundamentally leads to the use of computational methods as decision support systems, which as the name suggests assist in decision making, making it easier to make decisions on individual data points or any subsets of data in a large data sets.

3.2.2. Types of optimization algorithms

The GRG algorithm is a generalised algorithm which can be used for both ascent and descent optimizations, and utilises the gradient based optimisation taking steps proportional to the negative gradient, i.e. a first derivative, of the function at a specific value reached during the previous iteration of the optimisation algorithm. The algorithm is stopped when the gradient of the function reaches 0, which corresponds to a local minimum or maximum. The difference between the ascent and descent is expressed by the sign of the gradient taken: the negative gradient for minimizing and positive gradient for maximising. (see Figure 3.1)^[114]

Quasi-Newtonian method is another method that is often used in mathematical optimization and is based on the general principle of Newton's method. The Newton's method relies on approximating the analysed function around the position achieved during the previous iteration of the algorithm with a second order polynomial function. Hence, the Newton's methods can only be applied to twice or more differentiable function. The difference between Newton's and Quasi-Newton methods is that the Newton's methods require the computation of a Hessian matrix, whereas in Quasi-Newtonian methods the Hessian matrix is approximated, making it computationally faster than the Newton's methods.^[109]

An optimisation method based of the Newton's method, which is designed to solve non-linear least squares problems is the Gauss-Newtonian algorithm. In contrast to Newton's method the Gauss-Newtonian algorithm does not require the computation of a Hessian matrix (a square matrix of second order partial derivatives), relying on the use of a Jacobian matrix (a typically square matrix consisting of first order partial

derivatives). This makes the Gauss-Newtonian algorithm less computationally taxing than the Newton's and Quasi-Newton methods.^[109]

The Levenberg–Marquardt algorithm (also known as Lev-Mar algorithm, LM algorithm or LMA) is a method of least squares of curve fitting, which can be used to find a local minimum of a function. It combines the least squares regression analysis and optimisation, interpolating between the Gauss-Newtonian and gradient descent methods. This allows the method to be used with the initial conditions that are further away than the ones required for the individual Gauss-Newtonian and gradient methods, whilst retaining the relative speed of optimisation, making it a very versatile and widely used non-linear function optimization algorithm.^[108,112,115,116]

3.2.3. Drawbacks

One of the drawbacks of the GRG and LM algorithms is that the number of variables will increase the number of potential combinations of variables corresponding to local minima in the regression analysis, and neither of the algorithms are designed to optimise for the global minimum. (see Figure 3.2) This produces an issue of the reliability of the optimization, which can be partially counteracted by looking at the time dependent change in the variables and determining if they follow a trend, effectively simulating a heuristic algorithm.^[117] A heuristic algorithm is a “soft” optimization algorithm, often used in artificial intelligence research, that can be utilized for example to automatically sacrifice the goodness of fit of individual data points in order to improve the fit of overall data to a trend. This is especially beneficial in continuous monitoring and analysis of chemical reactions using spectroscopy, as the evolution of the spectra with the passage of time will be determined by the kinetics of the reaction.

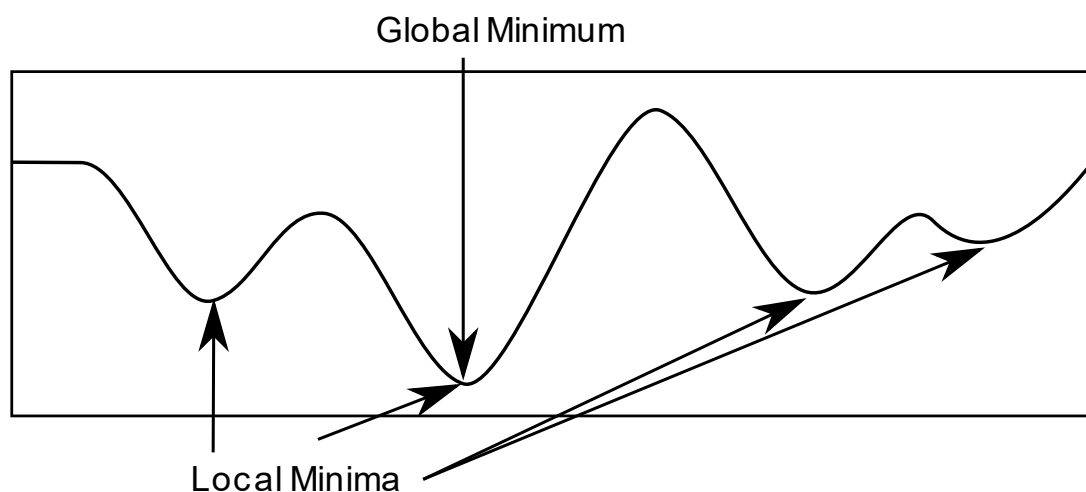


Figure 3.2 A schematic illustrating the concepts of local minima and the global minimum. The local minima illustrate that it is a minimal value within a small local set of values. In contrast, the global minimum is the minimal value among a large set of values, which can include several other local minima. Considered on a local scale the global minimum is also a local minimum. In this illustration

Overfitting and underfitting are two of the key issues of numerical optimization modelling. The problem of underfitting is whether the model is complex enough to model the significant parameters contained in the data. The opposite side of the problem is overfitting, i.e. what is the significance of the modelled parameter and how complex should the mathematical equation fitted to the experimental data be. Philosophically, this problem is solved by the application of the philosophical concept of the Ockham's razor in STEM sciences, which states that nothing should be more complex than necessary.^[118] Both of these problems are considered in the approximation theory, which is a field of mathematics concerned with finding "simpler" models that approximate more complex models, with a desired level of accuracy.^[119,120]

Another crucial point is that the user of these tool needs to be aware of the working principles of algorithms used and their limitations to avoid misuse.

3.3. Conclusions

In this chapter the basic principles of mathematical optimization have been covered. This includes one of the ways of viewing equations as multi-dimensional objects, which nicely leads to converting any equation-based problem in o a least squares type problem. The viewing of the equation as a multi-dimensional object is also

similar to some of the concepts used in physics such as Hilbert spaces and AdS/CFT correspondence conjecture, both of which were used as analogical examples to explain the equation as a multi-dimensional object idea. The same idea (of equations representing a multi-subnational object) was noted to fall into a mathematical field of functional analysis, highlighting the potential for the use of functional analysis techniques in chemistry in general and analysis of chemical data in particular.

The next part of the chapter gave a brief overview of the least squares problem concept as well as a brief overview of some of the types of optimization algorithms that can be used to solve least squares type problems. In this work two algorithms were used: the GRG and the LM algorithms, which were used as pre-programmed pieces of software without any alterations in the software created in Microsoft Excel and NI LabView respectively. The drawbacks of these methods have also been mentioned, such as overfitting and underfitting, both of which demonstrate that accurate model selection is vital for the analysis. Another drawback mentioned is that both of the used algorithms are designed to find the local minimum rather than the global minimum, which could lead to errors. Therefore, it is important for trends in the data to be logically consistent, and double checked manually. One of the ways to avoid this problem would be to develop heuristic algorithms which would be capable of sacrificing some of the accuracy of the fit in order to produce a clear trend. This solution would however also fall into artificial intelligence research, which highlights the possibility of designing AI based software useful in chemistry research.

In conclusion the arguments presented in this chapter demonstrate the usefulness of computer-based technologies in chemistry research and demonstrated the potential use of mathematical tools (such as functional analysis) and artificial intelligence tools for the analysis of chemical data.

Chapter 4 Responding to humidity

Responding to changes in humidity, known as hygroscopicity is an important property of many materials. It is particularly important to aerosols, as it regulates the size of the aerosol relatively to the humidity of its environment and the amount of solute present. There are multiple factors that influence the hygroscopicity such as the chemical composition of the aerosol and the size of the aerosol particles.

This chapter is aimed at discussing the specific properties of aerosols, such as the difference between single aerosol droplets and bulk solutions, as well as briefly touching on the differences between the analysis of multiple aerosol droplets and single aerosol droplets. This chapter will also outline the theory of hygroscopic growth, the schematics of the humidity control system in the aerosol trapping cell and hardware used for dynamic vapour sorption.

4.1 Aerosols vs Bulk

4.1.1 *Definitions*

When considering aerosols is important to distinguish a droplet's properties and behaviour in contrast to the bulk solution. To clarify, in this work bulk solution will always refer to a solution that will behave as a large volume of solution (>1 mL, this value is chosen arbitrarily and is used to clarify the meaning), in contrast with a volume of solution in an aerosol droplet.^[15]

An aerosol is a colloidal dispersion of solid and/or liquid in a gas or a mixture of gases; defined by IUPAC as: “Sol in which the dispersed phase is a solid, a liquid or a mixture of both and the continuous phase is a gas (usually air).” International Union of Pure and Applied Chemistry, Compendium of Chemical Terminology Gold Book, Version 2.3.3^[15].

In contrast with the definition of typical colloids, where colloid particles refer to a size range between 1 nm and 1 µm, aerosol particles can reach a particle size up to 100 µm (same lower limit) whilst remaining as colloid particles. This is an important distinction as the aerosol particles trapped during the experiments need to be >1 µm in radius in order to successfully size them using the Whispering Gallery Modes (WGMs).^[27]

An important definition in aerosol science is the definition of relative humidity (RH) and activity of water (a_w) above the surface of pure water:^[122]

$$\frac{RH}{100\%} = \frac{p}{p'} = a_w \quad \text{Equation 4.1}$$

By utilising changes in relative humidity, it is possible to assess the hygroscopic properties of a material by recreating a range of conditions from a complete absence of water vapour to a vapour pressure immediately above the surface of water. At 100% RH, i.e. in an environment fully saturated with water vapour: $p=p'=a_w \approx 1$, due to $p \approx p'$ at droplet radius $< 1 \mu\text{m}$, as seen in **Figure 4.2**, thus by rearranging equation 4.1:

$$\frac{p}{p'} = e^{\left(\frac{2\gamma V_m}{rRT}\right)} = a_w = RH = 1 \quad \text{Equation 4.2}$$

By changing the relative humidity, it is possible to achieve a range of humidities $0\% \leq RH \leq 100\%$, thus the equation 4.2 should be modified to accommodate it, thus becoming:

$$S \cdot \frac{p}{p'} = S e^{\left(\frac{2\gamma V_m}{rRT}\right)} = S a_w = \frac{RH}{100\%}, \quad \text{Equation 4.3}$$

Where S is the saturation ratio reflecting the saturation of the gaseous medium with the water vapour. In this thesis typical measurements were made within the range $0.1 \leq S \leq 0.95$, due to the limitations of the RH sensor used in the setup.

4.1.2 Kelvin equation and its significance

One of the key differences between aerosol droplets and bulk solution is the difference in vapour pressure between a spherical surface versus and a flat surface. This relationship was explored by William Thomson more widely known as Lord Kelvin, as evident in the equation that relates the two vapour pressures known as the Kelvin equation:^[122–126]

$$p = p' e^{\left(\frac{2\gamma V_m}{rRT}\right)}, \quad \text{Equation 4.4}$$

where p is the vapour pressure, p' is the equilibrium vapour pressure above a flat surface, γ is the surface tension, V_m is the volume of the molecule, r is the radius of the droplet, R is the gas constant ($8.314 \text{ J K}^{-1} \text{ mol}^{-1}$), and T is temperature in Kelvin (also named after him). According to this equation at constant V_m , γ and T , i.e. with a constant chemical composition, concentration and temperature, the vapour pressure will be dependent on the radius of the droplet:^[122]

$$p \propto r \quad ; \text{ at } T, V_m, \gamma \text{ and } p' = \text{constant} \quad \text{Equation 4.5}$$

This can be represented graphically as a ratio between the p and p' for: $T=300 \text{ K}$, $V_m = 1.8 \cdot 10^{-5} \text{ m}^3 \text{ mol}^{-1}$, and $\gamma = 0.072 \text{ J m}^{-2}$ by a curve, seen in Figure 4.2. It is possible to note that the droplet sizes studied in the experiments described in this thesis were typically $>3 \mu\text{m}$, that the increase in the vapour pressure due to the curvature will not be significant.^[122]

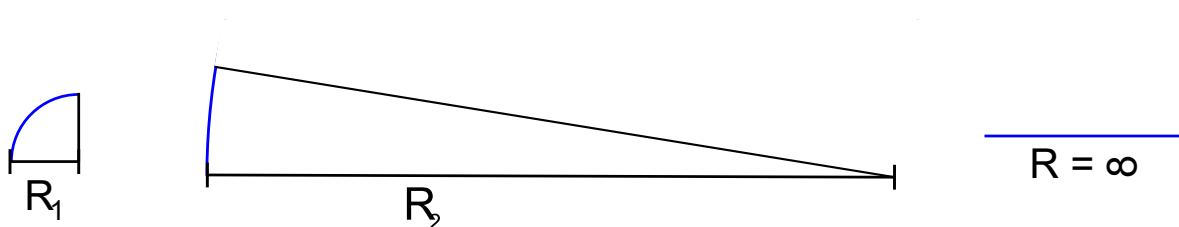


Figure 4.1 A schematic representation of the same distance (blue line) as part of a small droplet (left), large droplet (middle), and infinite curvature droplet (right). This demonstrates that the surfaces of droplets with a large radius will behave almost identically to flat surfaces, which is expressed in the Kelvin equation.

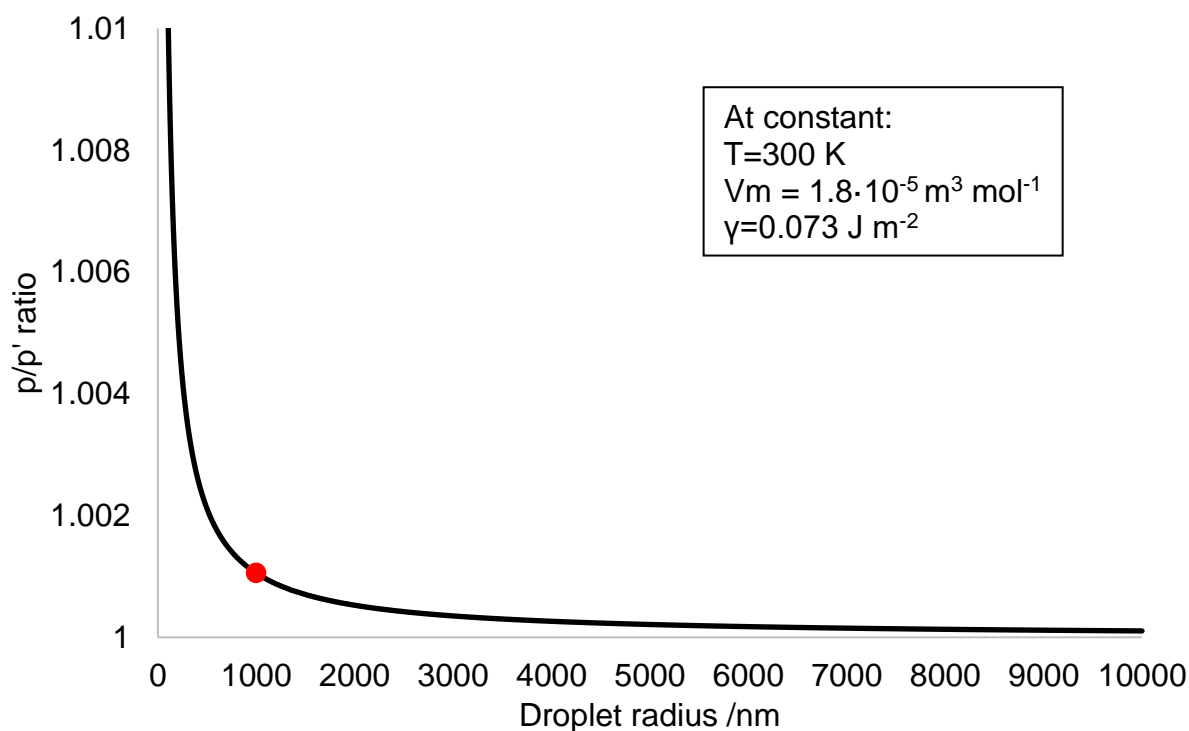


Figure 4.2 A graph of the ratio of the equilibrium vapour pressure of a curved convex surface vs the equilibrium vapour pressure over a flat surface as a function of the curvature radius (black line). The red dot is a selected data point corresponding to a droplet with a radius of $1\ \mu\text{m}$, which has the p/p' ratio of ~ 1.001 . This signifies that the contribution of the surface curvature to the vapour pressure above the surface of the droplet will be $\sim 0.1\%$ with a droplet with a $1\ \mu\text{m}$ radius, and even smaller for larger droplets.

4.1.3 Hygroscopic growth

An important parameter of a compound in an aerosol form is its hygroscopic response, often measured in terms of the Growth Factor (GF). The GF is a ratio of one of the parameters of the aerosol droplet related to the same parameter of a spherical anhydrous solvent particle, for example the radius of the droplet (R_{wet}) to the radius of the solute particle (R_{dry}):

$$GF = \frac{R_{wet}}{R_{dry}} \quad \text{Equation 4.6}$$

It is also possible to express the GF based on the mass of the dry particle and its wet mass, which is often denoted as mass-based GF.

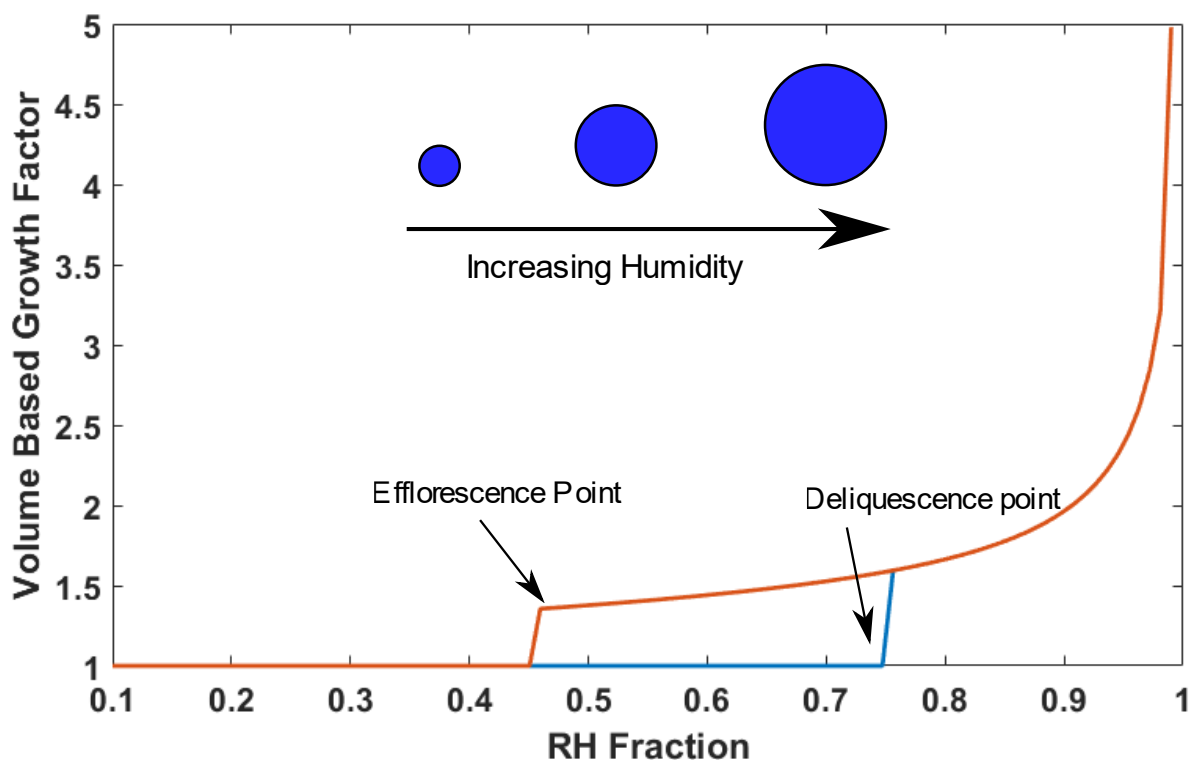


Figure 4.3 A theoretical plot of the hygroscopic response of a NaCl droplet produced using E-AIM, demonstrating: the efflorescence and deliquescence points, their hysteresis, and the hygroscopic growth curve (ascending- blue, descending - orange).^[27]

The hygroscopic growth curve demonstrates the point of equilibrium between the vapour pressure and the amount of water retained or taken up by the aerosol droplet at a specific humidity. The efflorescence and deliquescence points are the relative humidities at which water is rapidly taken up by a particle of solute (deliquescence) or lost by an aerosol droplet and the solute crystallizing (efflorescence). One of the characteristics of aerosols is the hysteresis between the deliquescence and efflorescence point, at which the solution droplet goes through a stable supersaturated state. This is mainly due to the absence of any solid surfaces in contact with the aerosol droplet, or any other nucleation seeds, which increases the energy barrier for crystallization.^[27]

4.2 Defining arrested states

As part of the hygroscopic response of an aerosol droplet is another important characteristic the retention of water by the solute. This can be accessed through the kinetics of water transport and release from the aerosol droplet, and can generally be

termed as arrested states. The arrested states fit on a spectrum of phases which retain water between liquids and solids, such as hydrated crystals. The arrested states also have can be divided into gels and glasses, each with their distinct properties. All of these physical states retain water molecules, however the difference among these arrested states lies in their structure.^[60,127–130]

Gels can be distinguished from other arrested states by the presence of a colloidal network with pockets of water within the network. Another characteristic of a gel is that it is a semi-solid, meaning that it will not behave as a true solid in that it will deform elastically under rapid pressure regaining its original shape, but under prolonged pressure a gel will deform plastically, i.e. will retain the deformed shape. This is due to the gel's colloid network readjusting to its new physical shape, equally redistributing stress along its surface. This property can also manifest as gels becoming liquid-like with vibration, thus behaving as a non-Newtonian fluid. Another way of looking at the structure as an interlaced network of molecules or particles, which exists as a network (see Figure 4.4 B) rather than an amorphous solid or crystal (see Figure 4.4).^[131–143]

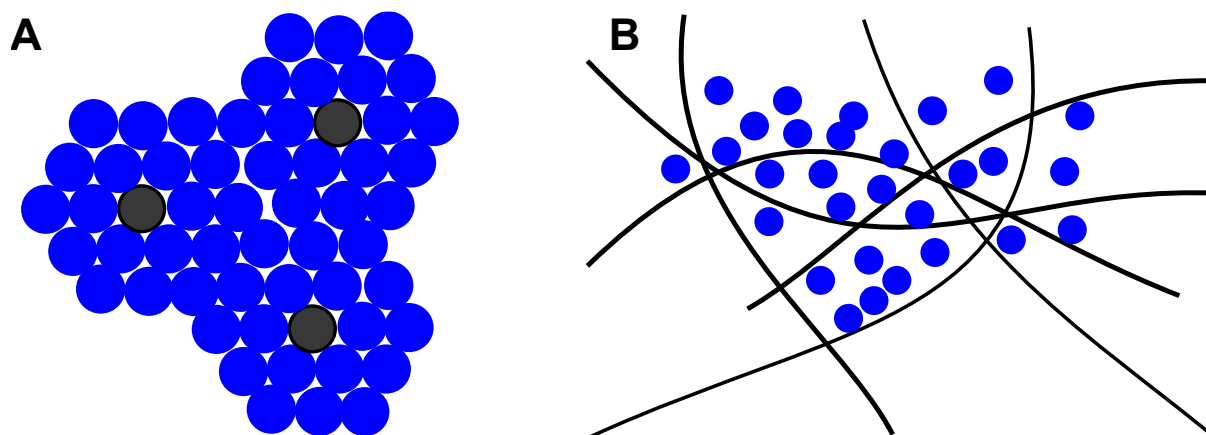


Figure 4.4 Schematic representations of a sol (A) and a gel (B), with grey dots representing particles, black lines representing long molecular strands and blue dots representing water. In A the dispersed particles are in solution having minimal interaction with one another. B exemplifies long molecular strands which create a flexible structure trapping water within the supramolecular structure.

Glassy states and materials are typically characterised by their high viscosity (above 10^{12} Pa, with a viscosity of $10^{12.3}$ Pa sometimes being used to define the glass transition)^[144], which is typically higher than that of gels. Another mechanical property

of glassy materials is that glasses deform only plastically at high temperatures, without elastic deformation. This leads to glassy materials typically being brittle. On a more structural level glassy materials can be differentiated from crystals, by the lack of a clear long-range order and lattice structure as in crystals, also known as being amorphous. Thus, glassy materials can be fully described as an amorphous solids, rather than a semi solid, such as gels(see Figure 4.5 A).^[15,130,144–151]

Hydrated crystals and crystals overall can be defined by the presence of a well-defined periodic structure as evident by a crystalline lattice (see Figure 4.5 B). Similarly to a glassy solid it can retain water within its structure, but in hydrated crystals the molecules of water become a part of the crystalline structure rather than contained as pockets within the amorphous structure of a glass.^[65,152–154]

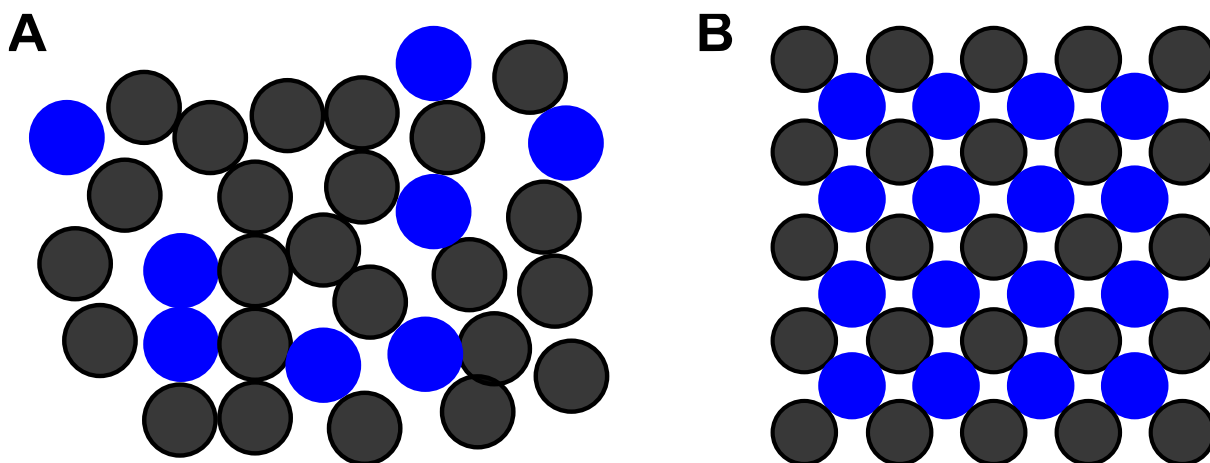


Figure 4.5 Schematic examples of glass phase (A) and hydrated crystal (B) structures, with grey dots representing particles and blue dots representing water. A demonstrates the disordered structure of a glass phase incorporating water in its structure, whereas B illustrates an ordered crystalline structure with water incorporated as part of the structure.

4.3 Single particle measurements vs multi particle measurements

It is important to compare the single particle methods such as aerosol optical tweezers (AOT)^[128,165] and electrodynamic balance (EDB)^[128] from many-particle aerosol measurements such as differential mobility analysers^[28,121,122,166], and surface measurements such as the DVS^[101,155], as each of them have their own advantages and disadvantages

One of the practical considerations that must be taken into account is that the single particle measurements, as the name suggests measure the response of a single aerosol droplet to changes in humidity, whereas many-particle measurements measure the average response of many aerosol particles. The benefit of single particle measurements, as there is no averaging of the droplets analysed, making the measurements more reliable. It is also important to note that no instrument is capable of producing a perfectly monodisperse aerosol, adding additional errors into the measurements of for example differential mobility analysers.^[165]

The drawback of the AOT is that it can be difficult to retain the droplets, especially during chemical reactions. Another drawback is the necessity of using of mathematical models describing the hygroscopic response of the droplet in order to compare droplets obtained in a set of experiments, as well as a higher number of experiments in order to obtain a representative sample.^[165]

4.4 Summary

This chapter has outlined the definitions of aerosols and the various states in which an aerosol particle can retain moisture, and discussed the basics of the hygroscopic response and how it is different from the response of the same solution in a beaker.

These definitions will be drawn upon in Chapter 6 in the descriptions of hygroscopic growth models and some of the experimental results.

Chapter 5 Experimental procedures

In this chapter the experimental procedures will be stated. While none of these experiments are significantly complex, it is difficult to maintain the aerosol droplet in the optical trap as CaCO_3 precipitates, therefore some notes and suggestions on how to achieve that are also included in this chapter.

5.1. Trapping cell preparation

The trapping cell was prepared by coating the insertable (bottom) cover slip by coating it with a hydrophilic coating by soaking them in a 50% solution of Decon90. The purpose of the hydrophilic coating is to prevent the formation of droplets on the coverslip in the optical path of the trapping beam.

5.2. Aerosol injection

The injection of aerosols was done by aiming the stream of aerosol produced by a medical nebuliser (micro air nebuliser) down the injection port of the aerosol trapping cell (see Figure 3.3).

5.3. Hygroscopic growth curves procedures

5.3.1. AOT:

1. Trap and coalesce the droplets for a droplet of sufficient size.

2. Set the RH of the nitrogen and engage the nitrogen flow.
3. Start recording the Raman spectra.
4. After the droplet has reached equilibrium with its environment adjust the RH to the next step of the hygroscopic growth curve.
5. Adjust the laser power as necessary to maintain the droplet in the trap.

5.3.2. DVS:

1. Put a clean, empty T0 pan on to the sample side of the balance.
2. Seal the humidity chamber.
3. Set the RH of the instrument to 0 (0% humidity), and turn on the N₂ (inert carrier gas) flow and wait until the system reaches equilibrium.
4. After the system reaches equilibrium tare the balance.
5. Take the sample T0 pan of the scale.
6. Add the dry powder on to the T0 sample pan, place it back on to the balance, seal the system.
7. Equilibrate the system to RH = 0 with the sample on the balance.
8. Once the equilibrium is reached record the dry weight of the sample, start the recording and initiate the automatic growth curve or adjust the RH manually.

5.4. The chemical reaction procedure:

1. Trap and coalesce the droplets of the first solution.
2. Start the Raman spectroscopy recording a map of spectra (spectra recorded in sequence).
3. Nebulise in the second reagent (Na₂CO₃ or CaCl₂ depending on the first reagent solution).
4. Adjust the laser power to maintain the droplet within the trap.

5.5. Experimental notes and suggestions

The injection of aerosols was done by aiming the stream of aerosol produced by a medical nebuliser (micro air nebuliser) down the injection port of the aerosol trapping cell (see *Figure 5.3*).

Trapping droplets with a highly disproportionate amounts of reagents produce a more stable droplet as the reagent that is in excess also acts as a buffer during the precipitation producing less extreme changes in the overall optical properties of the droplet.

After adding coalescing, the initial droplet with the droplets of the second reagent pre-emptively adjust the laser power to a lower value as typically the droplet will lose mass after the reaction. The pre-emptive adjustments allow a larger time frame for the critical initial adjustments.

Note that the following modification of procedure was not used in the experiments, and is purely a suggestion on how it may be easier to retain the droplet in the AOT during the precipitation of CaCO_3 . A potential way of making it easier to retain the droplet in the optical trap during the reaction is to make it a composite droplet of 3 solutions: CaCl_2 , NaCl and Na_2CO_3 , with the NaCl acting as a non-reactive buffer, allowing the droplet to retain more of its mass. This approach would make it easier to retain droplets with comparable amounts of CaCl_2 and Na_2CO_3 .

5.6. Experimental setup

5.6.1. Optical system

The optical tweezers used in the experiments described in this thesis has used a 532 nm continuous wave laser with a maximum output of ~3W (Laser Quantum, Opus) used for both trapping the particle and as an excitation source for Raman Spectroscopy. The laser was propagated through a beam expansion optical relay in order to maximise the gradient force produced by the system, as well as a conjugate plane lens relay. The beam was then directed through a beam splitter (Comar optics, 25 BQ 00) and focused through a Nikon (NA=1.25, Oil immersion, x100 magnification, CFI Achrom 100X Oil) microscope objective into a custom-built aerosol trapping cell. (see Chapter 3) The details of the aerosol trapping cell and the humidity control system will be discussed in a later in this chapter. (see Figure 5.1)

The backscattered light from the trapped aerosol droplet, is reflected from the beam splitter into a periscope and focused into a Czerny-Turner type monochromator (Horiba, iHR 550) and a CCD detector (Horiba, Sincerity, cooled to -60°C).

Additionally, the optical tweezers setup was fitted with a bright field imaging system consisting of a 447.5 nm light emitting diode (Luxeon, 1W) focused on to a CMOS camera (ThorLabs, DCC1645C). A continuum filter was positioned immediately in front of the CMOS camera to filter the laser wavelengths, and prevent overexposure of the image and damage to the camera.

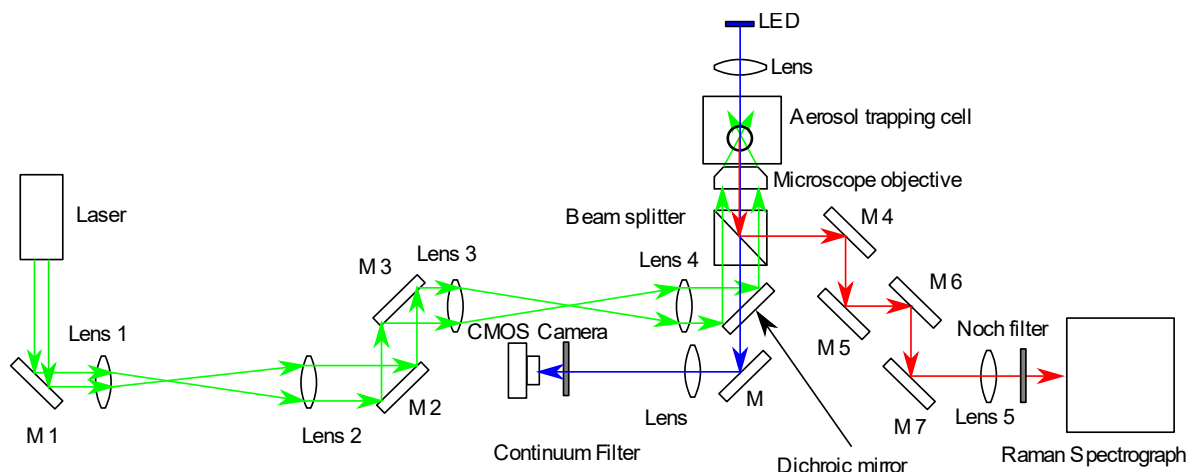


Figure 5.1 A Schematic of the experimental setup used for the experiments described in this thesis. The M on the schematic stands for mirror. The dichroic mirror is used to reflect the trapping laser but allow the light to form the LED to pass through and be used for imaging.

The focus of the work done in this thesis was on the study of the chemical reaction of formation of CaCO_3 and Raman spectroscopy, thus details such as the properties of the lenses and the distances between them were not recorded. However, a brief description of their purpose and functionality is provided below:

Mirror 1 redirecting the laser beam, effecting the surface footprint of the system, so that it would fit on the optical bench.

Lenses 1 and 2 are plano-convex lenses, comprise a beam expansion assembly, used to expand the laser beam to a size that would fill the back of the microscope objective, in order to fully leverage the properties of the microscope objective, maximizing the gradient force produced.

Mirrors 2 and 3 used for redirecting the expanded laser.

Lens 3 and 4 identical plano-convex convex lenses, positioned at $\times 2$ focal length of each, providing no magnification, preventing additional beam divergence, and allowing a larger error tolerance in the alignment between mirror 3 and the dichroic mirror.

The combination of mirror 2 and 3 and lenses 3 and 4 allow for finer control of the position of the laser beam reflecting off the dichroic mirror, making the alignment of optical components easier.

Dichroic mirror is used to reflect the trapping laser into the microscope objective, but allow the light from the LED to pass through for brightfield imaging using the CMOS camera.

The beam splitter is used to split the beam reflected and scattered from the sample that contains the Raman scattered signal and redirect it into the monochromator and Raman camera for analysis. As in this setup Raman backscattering (as opposed to 90-degree scattering) is used a lack of this beam splitter would make it impossible to measure Raman data.

Mirrors 4, 5, 6 and 7 (M 4, M 5, M 6, M 7; see Figure 5.1) provide vertical (mirrors 4 and 5) and horizontal (mirrors 5, 6 and 7) control of the Raman signal beam and direct it into the monochromator and Raman camera.

Lens 5 was a plano-convex lens positioned at its focal length away from the shutters of the monochromator, and was used to focus the Raman signal into the monochromator and magnify the image on to the mirrors in the monochromator.

The notch filter was used to filter out the excitation/trapping laser from the Raman signal in order to prevent damage to the highly sensitive Raman CCD detector.

5.6.1. Relative humidity control and trapping cell equipment

The control of the relative humidity in the immediate environment of the aerosol droplet consisted of 2 main parts: the humidity control system and the aerosol trapping chamber.

The humidity control system itself consists of a pressurised nitrogen cylinder containing oxygen free nitrogen gas, which was used as a carrier gas for the water vapour. The flow of the gas is split in to two each regulated by a mass flow controller (MKS INSTRUMENTS UK; GE50A013502SB1V020 Mass Flow Controller; Range: 500sccm N₂), allowing one to pass through a bubbler filled with deionised water, while the other remains dry. This allows the gas to pick up water vapor and by combining the two flows to control the ratio of the gas flow passing through the bubbler and remaining dry, thus controlling the RH. (see Figure 5.2 **Figure 5.2**) Prior

to the aerosol trapping cell the humidified nitrogen flow was passed through a capacitance humidity probe (Honeywell HIH-4602-A), in order to determine the actual water vapour saturation of the nitrogen flowing into the cell.

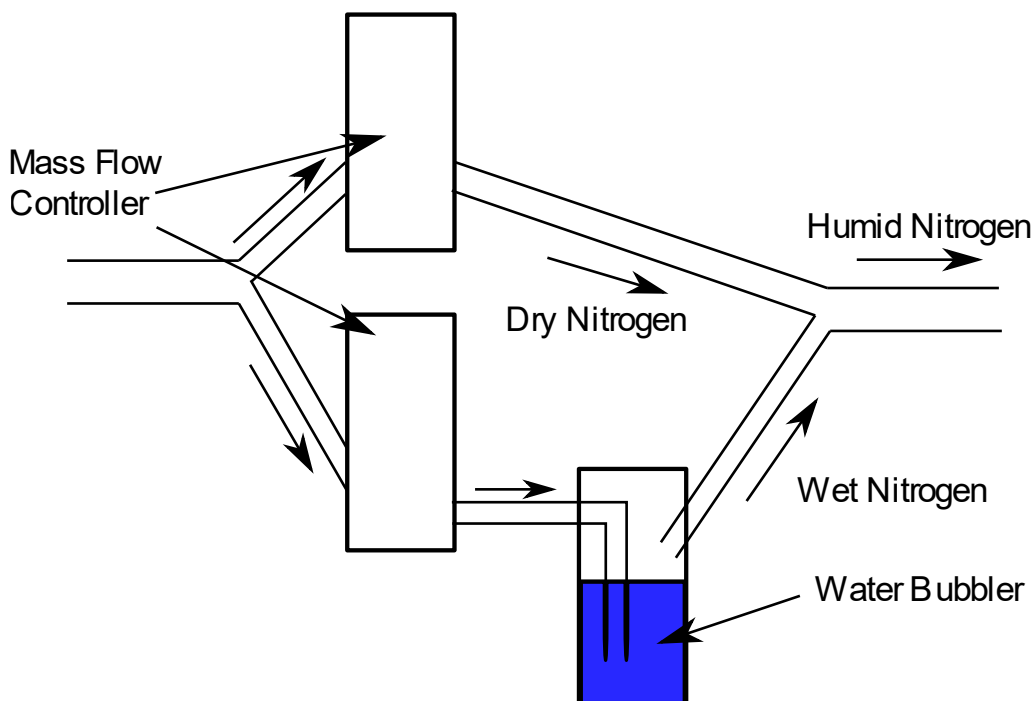


Figure 5.2 A schematic of the humidity control system both in the optical tweezers and integrated into the dynamic vapour sorption system.

The aerosol trapping cell consists of a stainless-steel casing with an aluminium insert, for 25 mm diameter glass coverslips of no. 1 thickness. The aluminium insert also had a rubber ring fitted in to it, so that it would provide a better seal between insert and the glass cover slip. The cover slip was pressed down by a Teflon insert with a “showerhead” ring, which disrupted the flow of the water vapour carrying nitrogen, thus producing a more homogeneous vapour saturation in the trapping cell. The cell was then covered and sealed by bolting down a stainless top cover lid with a glass coverslip. (see Figure 5.3)

The aerosol droplets produced by using a medical nebuliser (Omron, Portable MicroAir Nebulizer, NE-U22V). The droplets are trapped and grown in the trapping chamber, by directing the stream produced by the nebuliser through the aerosol injection tube seen in Figure 5.3.

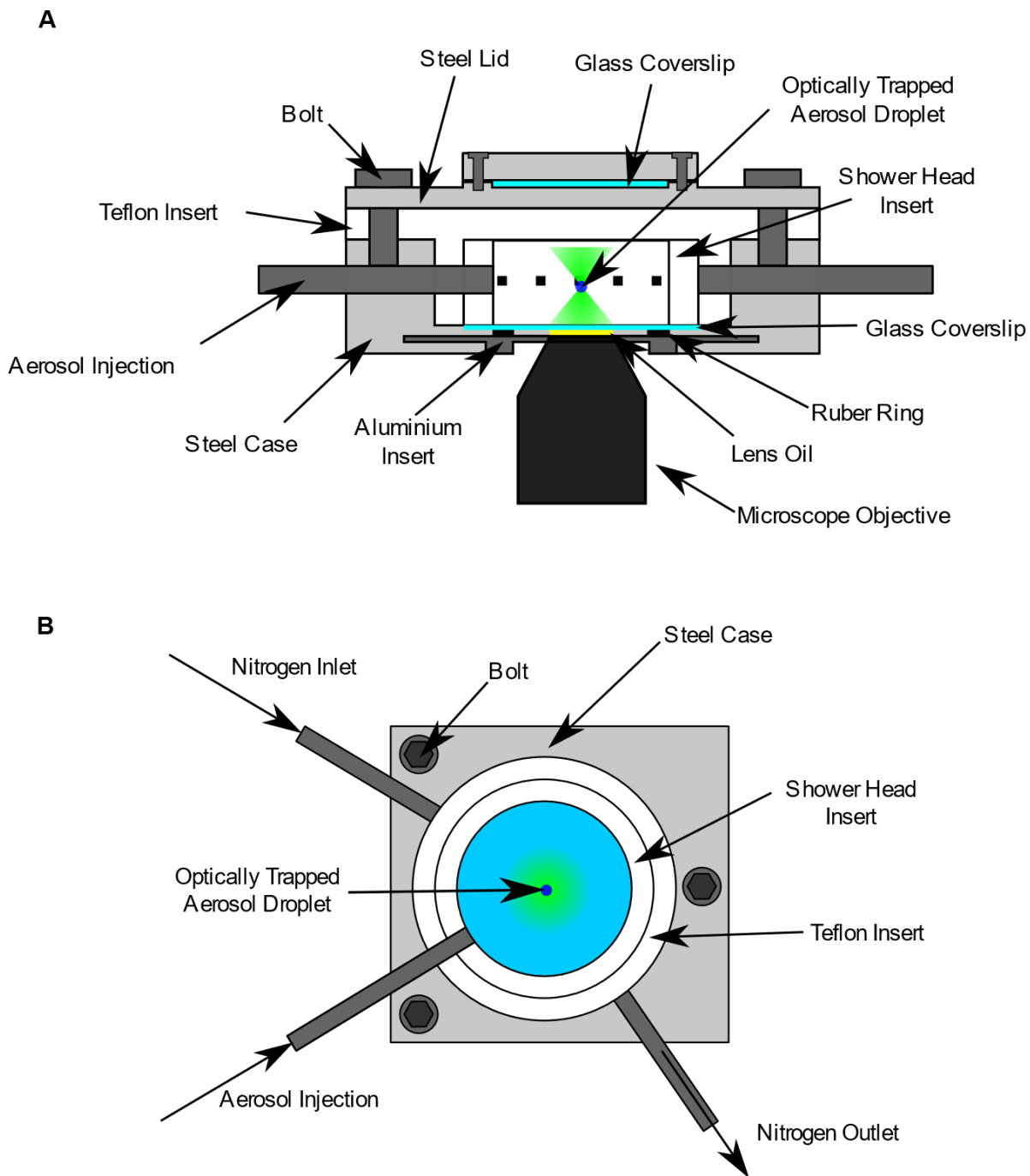


Figure 5.3 A schematic of the aerosol trapping cell side view (A) and top view (B).

5.6.2. Dynamic Vapour Sorption

Dynamic Vapour Sorption (DVS) is a gravimetric technique for analysing the amount of adsorbed moisture by analysing the change in mass of the sample at different relative humidities. (see Figure 5.5) This can be used in multiple ways as the amount of moisture adsorbed by an insoluble solid can be related to the surface area, which could be related to the porosity of a material using the Langmuir adsorption isotherm and Brunauer–Emmett–Teller (BET) theories.^[101,155–163] One of the approximations made in this theory is that the adsorbed molecules form a monolayer on the surface. (See **Figure 5.4**) When considering soluble compounds, DVS is used to analyse the hygroscopic properties of a material when in contact with a surface. This method is often used in the pharmaceutical industry in order to assess the hygroscopic properties of the pharmaceuticals.^[164]

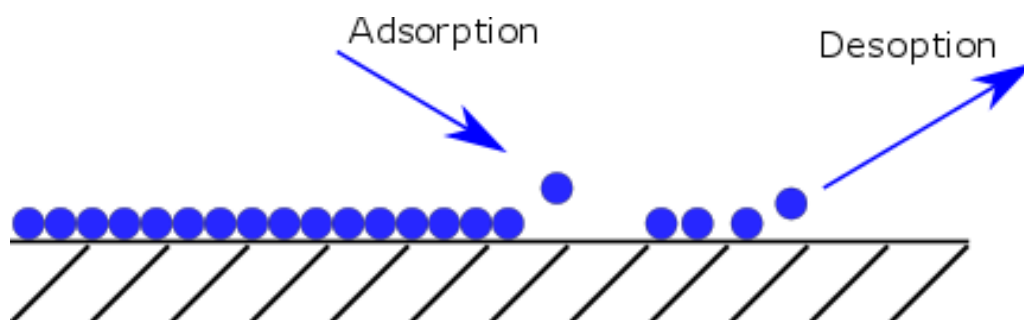


Figure 5.4 A schematic of adsorption and desorption of water (blue circles) on a solid surface, illustrating the BET adsorption theory.

5.6.3. DVS instrument

The instrument used for the experiments in this thesis is a Surface Measurement Systems DVS-2000 instrument, a schematic of which can be seen in Figure 5.5. the software used to control the DVS is the DVS WINDOWS - VERSION 2.06. The DVS produces a graph of mass vs time with changing humidity. The instrument itself can be set to 2 regimes which determine the point of the change in humidity a time dependent mode and a change in mass dependent (dm/dt) mode. It must be noted that the steps in the dm/dt mode are also restricted by time, hence in this mode the humidity is changed when the dm/dt value is below a certain threshold or if the time maximum for the step has been reached. The maximum time step that the system can be set is 600 min = 10 hours, which limits the usefulness of the automated RH change, as some compounds require longer equilibration times.

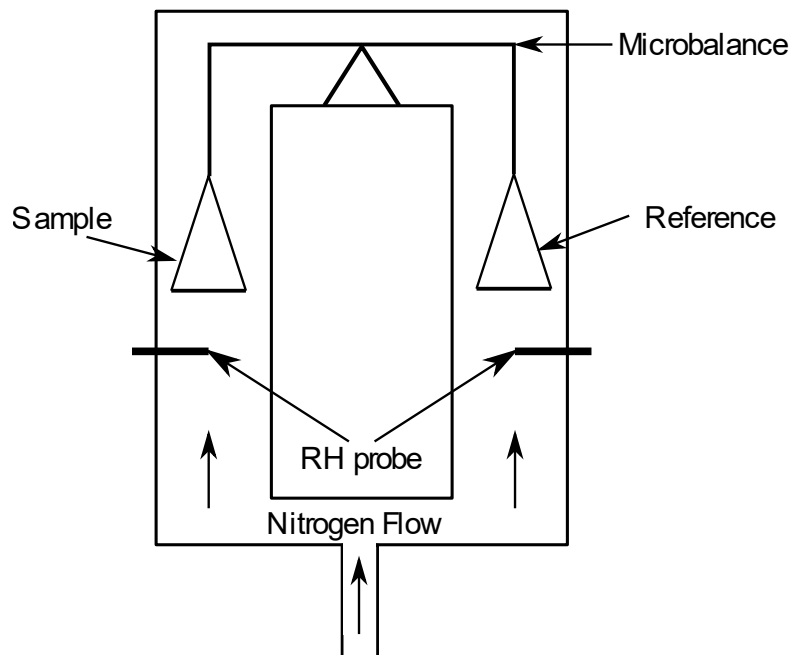


Figure 5.5 A schematic of the dynamic vapour sorption system used in the experiments. The nitrogen flow is pre-conditioned with a humidity control system similar to the one in Figure 5.2.

5.7. Decomposition software

In order to fit the experimental spectra with the theoretical models two different pieces of software were created: a MS Excel spreadsheet and a NI LabView based data analysis software. The spreadsheet in Microsoft Excel, taking advantage of the Solver add-in, specifically for the built in generalized reduced gradient (GRG) optimization algorithm. NI LabView software also utilizes separate pre-built algorithms for determining the slope and the offset of the spectra, and the line profile of the signal peaks.

For fitting the mathematical models two approaches were used. In both MS Excel and NI LabView, the optimized parameters were the parameters defining the peaks: position, width, intensity, profile asymmetry (see Chapter 7) and the background (background intensity and slope). As the optimization algorithms require optimizing all parameters simultaneously, the minimal necessary models for the peak profiles were determined separately. This was done to the optimization less computationally demanding on the hardware. (For model details see chapter 7)

The first approach was to utilise the GRG optimized sum of least squares approach to fit the spectra to the mathematical peak profiles. In this case it is possible to manipulate individual variables and their restrictions in using the MS Solver interface, makes this approach a good method to analyse the significance of the parameters in the model. This is also a relatively easy way to analyse a small number of spectra, as it does not require significant coding and the interface of Excel allows working almost intuitively. The downside of this algorithm is that it needs to be individually run for each spectrum, when large numbers of spectra need to be analysed.

Another approach taken in the duration of the research done for this thesis was to automate the fitting of the Raman spectra to the mathematical model using custom made software coded in NI LabView. This approach is be divided into two steps: the slope and offset correction and the mathematical modelling.

The first stage is to correct the background, accounting for the slope an offset. This is done by fitting a straight line through the analysed area of the spectrum, with the line being heavily weighted (by a factor of 1000, with a typical intensity of the Raman background ~150 relative intensity units.) at the extremes of the analysed area in order to avoid any influence of the spectral peak on the background correction. The slope and the offset are then subtracted from the spectrum, which can sometimes result in a small part of the spectrum at the extreme of the analysed area to have a negative value. Therefore, the absolute value of the spectrum after the slope and offset subtraction is used in further analysis.

The second stage utilises the in-built nonlinear curve profile fitting vi, which uses the Levenberg-Marquardt algorithm (see Chapter 3) to fit a non-linear curve consisting of the individual peaks in the total model optimised for. The optimization then produces a set of peak parameters, which when combined will model the spectrum, and separated into the respective peaks will demonstrate the composition of the C-O bond environments, corresponding to the polymorphic composition of the CaCO₃ precipitate.

A downside of the pre-programmed vi used for curve profile fitting is that it does not accurately fit all of the spectra. To counteract this drawback a digital filter was constructed that will calculate the error percentage of the fit for every data point in a spectrum, and filter off any spectra where the maximum error percentage is above a set threshold. While this method does reduce the number of data points produced, it

ensures the quality of the output data. In this particular case this reduction in the outputted number of spectra would not cause an issue, due to the overall quantity of initial data.

This approach allows a large throughput of data enabling accurate modelling of processes. In this particular case the processes monitored are: the precipitation of CaCO_3 , the polymorphic composition of the initial CaCO_3 precipitate, the stability of the polymorphs and their transformations, as well as changes to the crystalline structure of a stable polymorph, observed in the narrowing of the calcite peak over time when only calcite is present. This thinning down could be interpreted as the equilibration of the ions within the crystalline structure, thus the removal of structural defects. This serves to illustrate the variety of potential applications of such an analysis of the Raman spectrum.

5.8. The growth factor fitting

The least squares regression is a powerful tool which along with optimization algorithms (in this particular case the GRG nonlinear algorithm) can be used to find a solution to many different problems. Another one of such problems can be solving a system of equations consisting of a large number of equations. Such an approach could be leveraged find a solution for example finding the hygroscopic characteristics and dry size of several individual droplets of the same qualitative composition. This requires setting two types of variables: a global variables, corresponding to the hygroscopic characteristics of the solute, and local variables, corresponding to the dry sizes of the different droplets. This also requires three assumptions:

The first assumption: the dry size remains the same regardless of the relative humidity and time at which the measurement was taken, meaning that this approach applies without any other adjustments only for non-volatile, non-degrading solutes.

The second assumption: different droplets of the same composition and at the same concentration measured at the same relative humidity will only be different due to different dry sizes of the solute.

The third assumption: the selected mathematical model (Kreidenweis equation or κ -Kohler equation; see chapter 4 for details) is correct and accurate, and that the experimental data is at isopiestic equilibrium.

Using these assumptions, it is possible to use a model describing the hygroscopic parameters of a material for example using the κ -Kohler theory equation^[121] (discussed in more detail in chapter 4). It can be used to calculate the activity of water using the κ value and the dry and wet diameters of the droplet. The resulting system of equations will have a common hygroscopic parameter across all equations, smaller sub-sets, which will consist of the measurements of the same droplet at different relative humidity, with all droplets in these sub-sets having the same dry radius as well as the same hygroscopic parameter. In the case of the κ -Kohler equation this will result in a system of equations seen in **Figure 5.6**. This approach allows predicting a total wet radius of the droplet based on assumed dry radius and hygroscopicity parameter. Therefore, by minimising the absolute difference between the predicted value and the experimental value, which is a least squares type problem. This allows finding the parameters that would produce a curve that would pass through the experimental data points and has the unique shape dictated by the dry radius of the droplet and the hygroscopicity parameter.

System of equations

$$\begin{aligned}
 D1_{m1} &= f(RH_1, R_{dry_1}, k) \\
 D1_{m2} &= f(RH_2, R_{dry_1}, k) \\
 D1_{m3} &= f(RH_3, R_{dry_1}, k) \\
 D1_{m4} &= f(RH_4, R_{dry_1}, k) \\
 D2_{m1} &= f(RH_5, R_{dry_2}, k) \\
 D2_{m2} &= f(RH_6, R_{dry_2}, k) \\
 D2_{m3} &= f(RH_7, R_{dry_2}, k) \\
 D2_{m4} &= f(RH_8, R_{dry_2}, k) \\
 &\dots \\
 Dn_{ml} &= f(RH_l, R_{dry_n}, k)
 \end{aligned}$$

Figure 5.6 A system of equations calculating all of the experimental data points, to be solved simultaneously. In the equations Dn_{ml} – is the experimentally measured wet radius, where Dn – indicates droplet number n and ml – measurement number l , RH_l – is the RH of the measurement l , R_{dry_n} – is the dry radius of the droplet, and κ – is the hygroscopicity κ -Kohler parameter. As part of the experimental measurement the Dn_{ml} and RH_l are recorded, therefore the only values that need to be determined are the R_{dry_n} and k parameters. The red highlights the different sections where the

dry radius is the same. The blue highlights that all of the κ parameters are the same regardless of the RH of the measurement or the dry radius of the droplet.

One of the benefits of this method is that it is a data analysis tool which allows determining the hygroscopic parameters purely from experimental aerosol measurements. Combined with an analysis using a thermodynamic aerosol model predictions (such as E-AIM), this allows for additional robustness of the analysis. Another benefit of this approach is that it does not rely on the accuracy any individual measurement, therefore any random errors would be counteracted simply by increasing the total number of measurements used, which could come from different droplets.

The only drawback of this technique is in the optimization algorithms, as they are designed to stop after the gradient of change is less than a specified value, meaning that there is going to be some margin of error within the optimized parameters. This is counteracted by multiplying the absolute error (between the predicted value and experimental value) values by a constant value. Another drawback of this system is that any value that is less than 1 when squared will be smaller than the original value (the one being squared). This issue can be counteracted by using the absolute error, rather than the error squared value, with the only drawback being that for values above 1 the gradient of the absolute error will be smaller than that of the error squared. Because the absolute value is used rather than the squared value, the term of least squares may not strictly apply, however only the gradient of change is altered, maintain the minimal value as the minimal value, thus the same optimization tools can be used without any alterations.

A case example: a set of 5 data sub-sets of NaCl Droplets were produced using the E-AIM thermodynamic model based on the κ -Kohler theory (model 3, Kohler curves, data input set as "*Particle radius, volume fractions of solids, and κ (kappa)*"), with a $k=1.22$ ^[121] (growth factor derived, for details on the growth factor see Chapter 4), a volume fraction of NaCl set to 1, the formation of solids suppressed (i.e. solids cannot form, which models the behaviour of an aerosol with decreasing RH; see chapter 4 for details) and unique dry radii for each of the 5 data sub-sets. In order to approximate an experimental scenario, several random points between RH 0.97 and 0.6 taken from each data set were taken to approximate experimental data.

As the data used in this example was produced using E-AIM (this example has nothing to do with any laboratory experiments done by the author of this thesis), it is assumed to be free from experimental errors and treated as 100% accurate. This is not the case for any experimental data, as which will have errors in both size measurements and RH measurements.

By solving a system of equations for the data obtained using E-A using the GRG nonlinear algorithm in MS Excel, the optimized parameters were within ~0.05% of the parameters originally set in E-AIM (i.e. 99.95% accurate compared to the set parameters). (See Table 5.1 and Figure 5.4)

	R _{dry} set	R _{dry} optimised	Error
Drop 1	1.00E-06	1.00E-06	0.0023%
Drop 2	2.44E-06	2.44E-06	0.0146%
Drop 3	3.14E-06	3.14E-06	0.0097%
Drop 4	2.96E-06	2.97E-06	0.0404%
Drop 5	2.89E-06	2.89E-06	0.0175%
	κ	κ optimised	Error
	1.22	1.22	0.0461%

Table 5.1 A comparison of the dry radii and κ -Kohler parameters set in E-AIM and values determined by optimization. The error percentages are calculated as the absolute difference between the set and optimised values as a fraction of the optimised value.

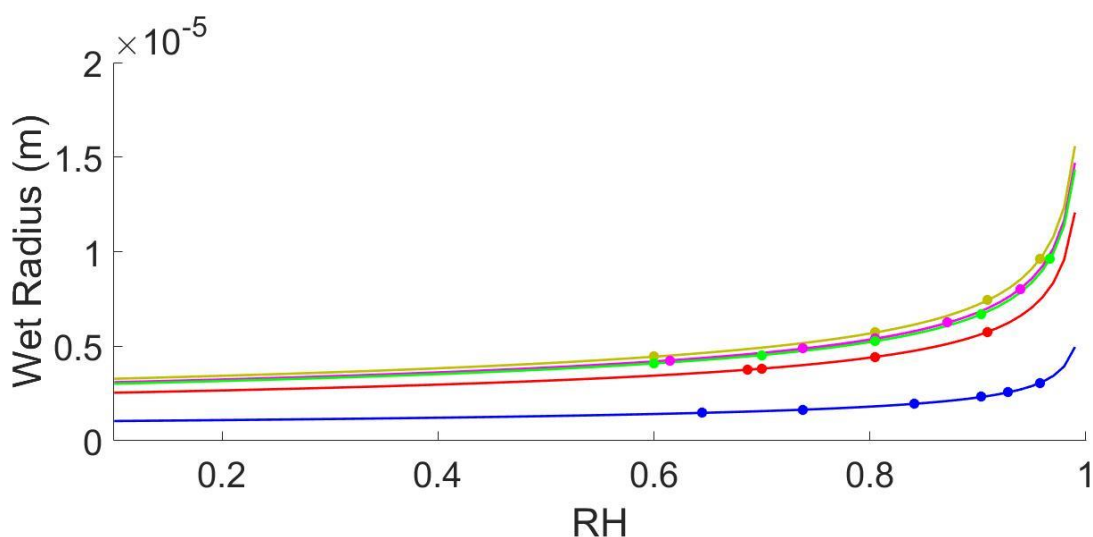


Figure 5.7 A graph of the E-AIM produced data points (dots) and the corresponding optimised curves produced using the optimised parameters produced by the software. The colours of the curves correspond to the colours of the E-AIM predicted data points. On this plot the error bars are not shown as they are visually indistinguishable from the plotted curve (the thickness of the plotted line overlaps the error bars).

5.9. Summary

In this chapter the experimental procedures and experimental apparatus were described.

The final two parts of this chapter are describing the software used for the decomposition of chemical spectra and a case example of a data analysis tool for finding the hygroscopic parameters and the dry size of the solute based on the sizes and relative humidity values of multiple droplets (with multiple measurements of each droplet at different relative humidities). Using the k-Kohler theory (explained in a further chapter) equation as a basis for this tool and 5 data sets generated using E-AIM thermodynamic model (using the same k-Kohler theory with a $k=1.22$) yielded a 99.95% accuracy, of finding the initially set parameters (k and dry sizes) which were used to generate the data sets (see Table 5.1 and Figure 5.5).

Chapter 6 Aerosol Hygroscopic Growth

This chapter will go into some detail regarding hygroscopic growth of aerosols, discussing and comparing the hygroscopic growth of a few examples of organic and inorganic compounds using aerosol optical tweezers and DVS. In this chapter several models will be suggested for tracking chemical reactions in aerosol droplets using the hygroscopic growth.

6.1 Describing the hygroscopic response: Kreidenweis equation model, κ -Kohler model, and multicomponent aerosols (Zdanovskii–Stokes–Robinson theory).

From a practical point of view it is necessary to describe the hygroscopic response of an aerosol droplet mathematically, as that allows interpolating a model that incorporates all points along the hygroscopic response, thus determining the size of the droplet at any relative humidity. This also allows comparing aerosol droplets with different chemical compositions and relating the hygroscopic responses of different droplets to one another.

As described in chapter 4, this is especially important for single particle measurements, as each droplet trapped will not be exactly the same as the other droplet within a set of experiments. This can be a source of error in multi particle

measurements, making single droplet measurement techniques and experiments that much more important.

6.1.1 Kreidenweis equation model

One of the first ways of describing was proposed by Kreidenweis et al in 2005.^[122] This model will be referred to as the Kreidenweis equation, to name it, making it easier to refer to, and to distinguish it from the κ -Kohler theory^[121].

The Kreidenweis equation is a model describing the hygroscopic growth of a solute through a second order polynomial equation. The Kreidenweis equation is^[122]:

$$GF = \left(1 + (a + b * a_w + c * a_w^2) \frac{a_w}{1-a_w}\right)^{1/3},$$

Equation 6.1

Where a, b and c are the coefficients describing the hygroscopic growth of a solute, and a_w – is the activity of water. This equation can be combined with equation 5.6, to calculate the wet diameter of the droplet:

$$r_{total} = r_s \left(1 + (a + b * a_w + c * a_w^2) \frac{a_w}{1-a_w}\right)^{1/3}, \quad \text{Equation 6.2}$$

Where r_{total} and r_s are the total (wet) and dry radii of the droplet respectively.

6.1.2 κ -Kohler theory model

In 2007 Petters and Kreidenweis proposed a second model replacing the second order polynomial equation, used in the Kreidenweis equation with a single parameter, making it easier to compare the different compounds. The equation stated as the defining equation of the κ -Kohler theory by M.D. Petters and S.M. Kreidenweis^[121](see Equation 6.3):

$$S(D) = \frac{D_{wet}^3 - D_{dry}^3}{D_{wet}^3 - D_{dry}^3 (1-\kappa)} \exp\left(\frac{4\sigma_s/a M_w}{RT \rho_w D}\right), \quad \text{Equation 6.3}$$

Where D_{wet} and D_{dry} are the wet and dry diameters of the droplet as labelled, κ is the κ -Kohler, R – the gas constant, T - absolute temperature, $\sigma_{(s/a)}$ is the droplet surface – air surface tension, M_w -molecular weight of water, ρ_w – density of water, D is the total droplet diameter, and $S(D)$ is the diameter-based saturation ratio. The saturation ratio is related to the activity of water as (see Equation 6.4):

$$S = a_w \exp\left(\frac{4\sigma_s/a_w M_w}{RT\rho_w D}\right) \quad \text{Equation 6.4}$$

By looking at equation 6.4 it is possible to notice that the exponential term is simply a factor converting the activity of water into the saturation ratio, and that it is present in both equations 6.3 and 6.4. Thus, by combining equation 6.3 and equation 6.4 solved for a_w , as well as taking in to account the assumption that $a_w=RH$ made by S.M. Kreidenweis et. al.^[121] (discussed in detail in chapter 5) results in a simplified version of the equation 6.3 solved directly for RH (see Equation 6.5):

$$RH = a_w = \frac{D_{wet}^3 - D_{dry}^3}{D_{wet}^3 - D_{dry}^3(1-\kappa)} \quad \text{Equation 6.5}$$

The same publication also contains another equation that relates the k-Kohler value to the a_w via volume:

$$\frac{1}{a_w} = 1 + k\left(\frac{V_s}{V_w}\right), \quad \text{Equation 6.6}$$

Where V_s and V_w are dry volume (volume of solute) and volume of water respectively. The volume of water is also related to the total wet volume (V_{total}) of the droplet as (see Equation 6.7):

$$V_{total} = V_s + V_w \quad \text{Equation 6.7}$$

The equation 6.6 can be combined with equation 6.7 and volume of a sphere ($V=4/3\pi r^3$), and rearranged to solve for the total wet radius of aspherical droplet using the dry radius (radius of a spherical solute article) (see Equation 6.8):

$$r_{total} = \left(r_s^3 + \frac{a_w k r_s^3}{1-a_w}\right)^{1/3} \quad \text{Equation 6.8}$$

The equation 6.8 can be modified to directly calculate the growth factor (see Equation 6.9 and 6.10):

$$GF_{volume\ based} = \frac{V_{total}}{V_s} = 1 + k \frac{a_w}{1-a_w} \quad \text{Equation 6.9}$$

$$GF_{radius\ based} = \frac{r_{total}}{r_s} = \left(1 + k \frac{a_w}{1-a_w}\right)^{1/3} \quad \text{Equation 6.10}$$

6.1.3 Comparing the Kreidenweis and κ -Kohler theory models

Comparing the two hygroscopic growth models one thing stands out is when comparing equation 6.1 and equation 6.10 it is possible to notice that the term k in

equation 6.10 replaces the second order polynomial in equation 6.1. This difference influences the accuracy of the predictive capability of the model, with the Kreidenweis equation being the more accurate of the two. (See this chapter 6.2.2 and 6.3.2)

Another point that can be noticed that from the same equations (equation 6.1 and equation 6.10) is that both equations are bound to having no water at $RH \rightarrow 0$, i.e. the growth factor will be fixed to be at 1, which is reflected by the constant 1 in both equation 6.2 and equation 6.10. This presents a problem as some materials are capable of forming hydrated crystals, which contain water in their structure. (See this chapter 6.3.2)

A significant advantage of the κ -Kohler theory model over the Kreidenweis equation model is the convenience of comparing the hygroscopicity values of different chemical compounds using only one parameter.

6.1.4 Zdanovskii–Stokes–Robinson Theory

The Zdanovskii-Stokes-Robinson (ZSR) is a theory of the dependency of the activity of water above a solution of two or more solutes on the properties of the individual solutions and their molar ratio at isopiestic equilibrium (at equilibrium with the surrounding humidity). This theory was proposed independently by Zdanovskii in 1936 (empirical)^[167] and by Stokes and Robinson in 1965^[168] (derived and proven experimentally). The general equation that summarises the ZSR theory is (see Equation 6.11):

$$\sum_j \frac{m_j}{M_j} = 1, \quad \text{Equation 6.11}$$

Where M – molality of a pure solution, and m – molar fraction of solute j in the mixture. This implies that a multi-solute solution will behave as a linear combination of pure solutions in accordance with their molar fraction in the multi-solute solution.

In their paper Stokes and Robinson demonstrate this principle using aqueous mixtures of sucrose and a second solute. The presented data demonstrates that there are some deviations from the prediction especially in the sucrose-urea solution, which this likely caused by solute-solute interactions, such as dimerization. This suggests that so long as the mixed solutes do not affect one-another the principle holds true, therefore making the equation 6.11 is valid. This assumption is also used in the κ -Kohler theory paper was reformulated as (see Equation 6.12):

$$\kappa = \sum_i \varepsilon_i \kappa_i, \quad \text{Equation 6.12}$$

Where κ is the κ value of the multi-solute solution, ε_i is the dry component volume fraction of component i , and κ_i is the κ value of component i . This equation allows applying the ZSR theory directly the κ -Kohler theory equation and easily calculating the hygroscopic response of a multi-solute solution.

Later in this chapter, equation 6.12 is used to determine the relative amounts of individual components after a chemical reaction has happened.

6.1.5 Mass and molar fraction-based growth factor calculations

As previously mentioned, the DVS method of measuring the hygroscopic response of a chemical substance relies on the measurement of a change in mass of the sample according to the RH of it's environment. Thus, a method of calculating the growth factor using mass-based calculations is necessary. Additionally, the second theoretical model of aerosol hygroscopic response AIOMFAC (Aerosol Inorganic-Organic Mixtures Functional groups Activity Coefficients) outputs the molar fractions of the components of the aerosol at a given RH, thus the GF needs to be calculated.

Starting on the basis of the equation for the volume based GF, assuming that the solute equilibrates with relative humidity, attracting H₂O from it's environment, and assuming that the solute is non-volatile (see equation 6.13):

$$GF_{volume\ based} = \frac{V_{wet}}{V_{dry}} = \frac{V_{H_2O} + V_{dry}}{V_{dry}} = \frac{V_{H_2O}}{V_{dry}} + \frac{V_{dry}}{V_{dry}} = \frac{V_{H_2O}}{V_{dry}} + 1, \quad \text{Equation 6.13}$$

Where V_{wet} , V_{dry} and V_{H_2O} are wet and dry volumes, and volume of water respectively. The dry volume is the volume of only solute (or any other individual component) and can be calculated using some basic calculation:

$$V = \frac{m}{\rho}, \quad \text{Equation 6.14}$$

Where m is the mass of the solute, and ρ is the density of the same solute. The mass can be calculated as:

$$m = n M, \quad \text{Equation 6.15}$$

Where n is the number of moles of the compound, and M is the molar mass of the compound. A related equation is the equation of the molar fraction (x) for a solute and H₂O mixture is:

$$x_{solute} = \frac{n_{solute}}{n_{H_2O} + n_{solute}}, \quad \text{Equation 6.16}$$

Equation 6.16 can be rearranged to calculate the number of moles of water based on the molar fractions of the solute and water, and number of moles of the solute:

$$n_{H_2O} = \frac{\frac{n_{H_2O}}{n_{H_2O} + n_{solute}}}{\frac{n_{solute}}{n_{H_2O} + n_{solute}}} \times n_{solute} = \frac{x_{H_2O}}{x_{solute}} \times n_{solute} \quad \text{Equation 6.17}$$

Combining equations 6.13 – 6.17:

$$\begin{aligned} GF_{volume\ based} &= 1 + \frac{\frac{n_{H_2O} M_{H_2O}}{\rho_{H_2O}}}{\frac{n_{solute} M_{solute}}{\rho_{solute}}} = 1 + \frac{\left(\frac{x_{H_2O}}{x_{solute}}\right) n_{solute} M_{H_2O} \rho_{solute}}{n_{solute} M_{solute} \rho_{H_2O}} \\ &= 1 + \frac{\left(\frac{x_{H_2O}}{x_{solute}}\right) M_{H_2O} \rho_{solute}}{M_{solute} \rho_{H_2O}} \quad \text{Equation 6.18} \end{aligned}$$

This allows an easy calculation of the volume based growth factor from the output of AIOMFAC-web calculations. This can be easily converted into a radius based GF calculation, as the relationship between the two can be easily seen by combining equations 6.9 and 6.10:

$$GF_{radius\ based} = GF_{volume\ based}^{1/3} \quad \text{Equation 6.19}$$

Rearranging N GF can be calculated on a mass basis as:

$$GF_{volume\ based} = 1 + \frac{m_{H_2O} \rho_{solute}}{m_{solute} \rho_{H_2O}} \quad \text{Equation 6.20}$$

With the mass of water calculated as:

$$m_{H_2O} = m_{RH} - m_{solute} \quad \text{Equation 6.21}$$

Therefore, combining equation 6.20 and equation 6.21:

$$GF_{volume\ based} = 1 + \frac{(m_{RH} - m_{solute}) \rho_{solute}}{m_{solute} \rho_{H_2O}} \quad \text{Equation 6.22}$$

Equations N are used for the DVS and AIOMFAC-web output calculations in their radius based equivalents, with the relationship demonstrated in equation 6.20

6.2 Sodium chloride

6.2.1 General description

Sodium chloride (NaCl) aerosols are one of the most well studied aerosols due to the relative ease of work. For this reason, it is often used as a standard for testing theories such the Kreidenweis equation and κ -Kohler theory. Thus, it makes sense to use NaCl aerosols for calibration. In nature NaCl aerosols appear most notably as part sea spray aerosols.^[169]

6.2.2 AIOMFAC curve

A model of a hypothetical (i.e. not an experimental droplet) droplet was produced using AIOMFAC-web model^[170-172], with the data used to convert the molar fractions in to GF using equation 6.18. In the case for NaCl, it will be represented by the ions it forms as it dissolves in water: Na⁺ and Cl⁻. This approach provides a way of comparing the accuracy of the Kreidenweis equation and κ -Kohler theory models in representing the hygroscopic response of NaCl produced using AIOMFAC-web.

As the use of AIOMFAC had not required the input of any experimental data in this case it is treated as fully accurate, i.e. it is treated as if it has no errors same as the example e-AIM data in Chapter 5.8 It is also optimized using the Least squares approach and the GRG nonlinear algorithm. The plotted errors demonstrate that not all of the data points will contribute equally to the accuracy of the model parameters derived from them, with the best results achieved at the lowest error values. (See Figure 6.1)

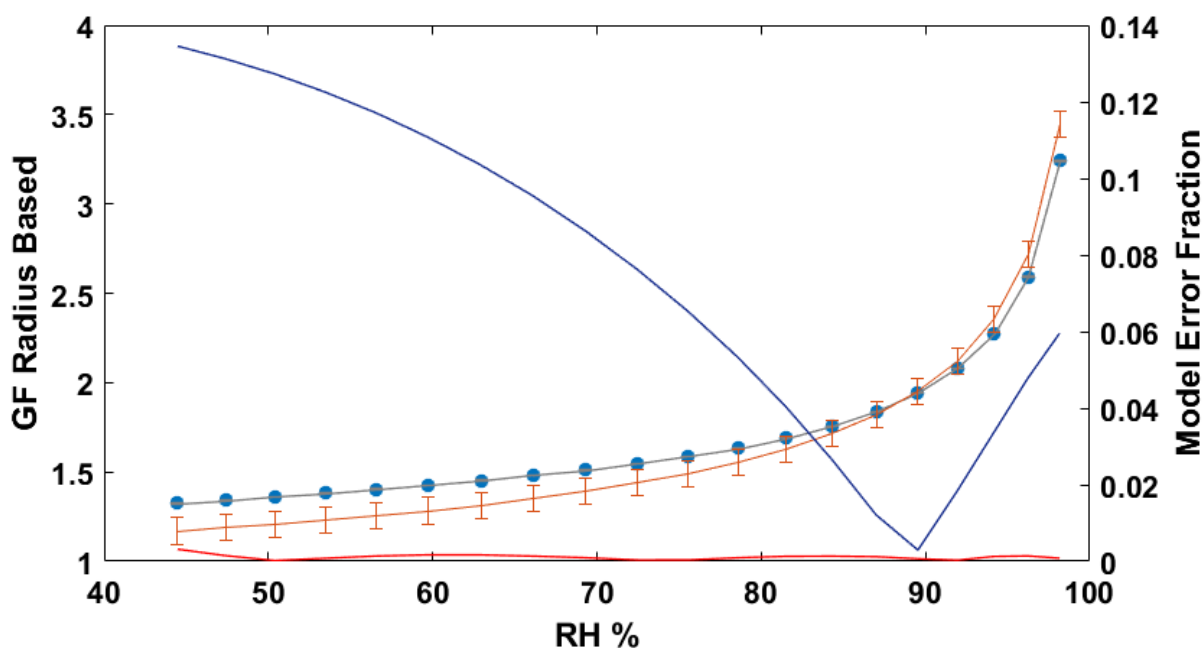


Figure 6.1 A plot of the hygroscopic growth of NaCl produced using AIOMFAC (light blue dots), calculated using equation 6.18. The data was fitted with both Kreidenweis equation model ($a=2.97028$; $b=-3.4776$; $c=1.1021$; average absolute error = 0.11%) and κ -Kohler theory model ($\kappa=0.75$; average absolute error = 7.36%), with plotted errors between AIOMFAC and the hygroscopic growth models between RH 97% to RH 44%, where aqueous NaCl aerosols have been proven to be stable. The model parameters were fitted for both models using the least error squared method using the GRG nonlinear algorithm (see chapter 4 for details). The error bars of the Kreidenweis equation model are smaller than the thickness of the line, therefore are not visible on the plot. The red and dark blue lines demonstrate the errors between the AIOMFAC produced data and the Kreidenweis equation model (in red) or κ -Kohler theory model (blue).

This demonstrates that the Kreidenweis equation model is more accurate at describing the hygroscopic growth of NaCl than the κ -Kohler model, however both models are reasonably accurate above RH \approx 0.80. This demonstrates that the κ -Kohler theory model is advantageous for the quick estimation, however this would suggest that the Kreidenweis equation model would be more advantageous for applications where accuracy is necessary.

A significant point that needs to be made is that the a, b and c parameters as well as the κ -Kohler parameter in figure 6.1 are different from that published by Kreidenweis et.al. ($a = 3.89243$; $b = -4.49667$; $c = 1.62110$; $\kappa = 0.91$) This could be due to the measurements taken are within a small range of RH values (between RH ~ 0.75 and ~0.85), as well as an unspecified method of fitting the coefficients and undisclosed goodness of fit (fitting error) in the literature.

The plotted errors (see Figure 6.1) demonstrate the adherence of the hygroscopic growth model to the hygroscopic response predicted using the AIOMFAC model. This approach is fundamentally not restricted to the examples demonstrated in this chapter. The benefit of plotting the error values between a model and the data it was optimized for is that it demonstrates which points produce the highest quality results, thus demonstrating the reliability of the derived model parameters. Which is to say that the hygroscopic parameters derived from experimental data gathered at different RH regions can have different values, i.e. the κ value derived from a data set measured at RH values between 0.7 to 0.8 will be different from that determined from data sampled at rh between 0.8 to 0.95. this principle is illustrated by a comparison of figure 6.1 and figure 6.2, with a summary of the parameters in table 6.1.

Model	RH range optimized for (%)	81.5 - 94.16	72.46 - 81.5	44.47 - 98.16
κ -Kohler theory	κ value	0.74	0.94	0.75
	average error	7.45%	6.35%	7.32%
Kreidenweis equation	a	3.018872	2.930065	2.970280
	b	-3.519679	-3.428932	-3.477585
	c	1.089495	1.109913	1.102141
	average error	0.21%	0.23%	0.11%

Table 6.1 A table of the optimized parameters used to plot the Kreidenweis equation and κ -Kohler theory models in figures 6.1 (full set) and 6.2. The optimized parameters demonstrate the importance of the range of RH values of the experimental data for finding the parameters of the models for a given compound or mixture. The average error of the model was calculated based on a full set of data ranging from 44.47% to 98.16% RH.

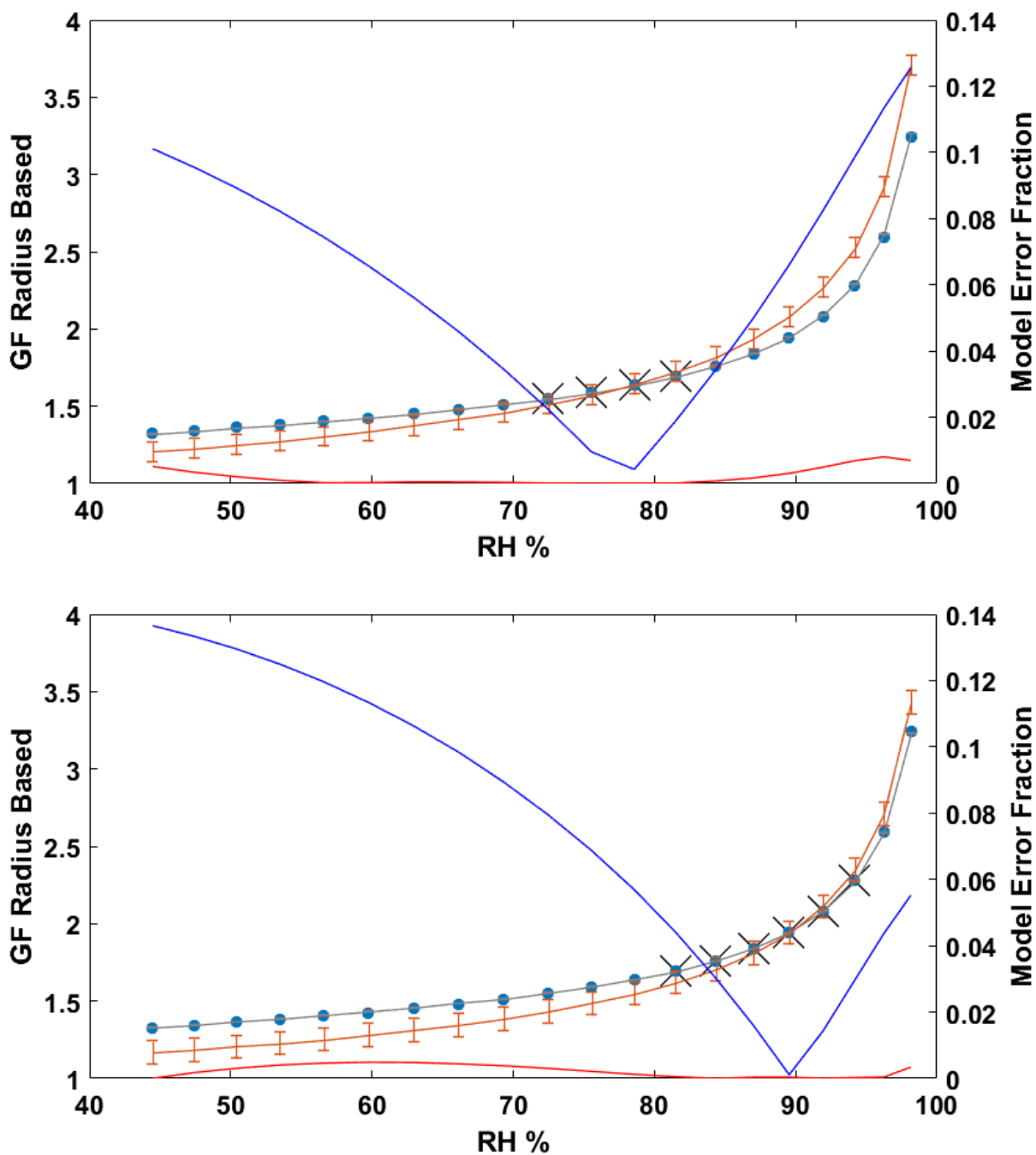


Figure 6.2 Plots of the hygroscopic growth of NaCl produced using AIOMFAC (light blue dots), with the Kreidenweis equation (grey) and κ -Kohler theory (orange) models plotted, with the plot of the error values associated with them in red (Kreidenweis equation) and blue (κ -Kohler theory). Optimized using the sum of least squares approach and using the GRG nonlinear algorithm. The colours on both graphs have the same meaning. On each plot the data subset that the parameters of the models were optimized for are highlighted with X symbols. The top graph was optimized for a range of RH from 72.46% to 81.5% and the bottom graph was optimised for RH 81.5 - 94.16%. The optimized parameters of both models and the associated average

error for both graphs, along with the parameters from figure 6.1 can be seen in table 6.1.

6.2.3 Aerosol Optical Tweezers data

The main method of investigation of the data produced using AOT is the use of the Live Aerosol Raman Analysis (LARA) software which used the WGMs pattern in the Raman spectrum produced by the droplet. For the purposes of this thesis all of the hygroscopic data presented in this chapter was collected at 10 s accumulation time and at 600 gr cm^{-1} grating, therefore each frame corresponds to 10 s in time.

The output of the LARA software can sometimes have inaccuracies in the calculation of the radius and refractive index, which is why it is important to have a sizable sample size, so that the majority of the points is easy to identify. This allows manually checking the data, which should follow a trend of a decrease in radius should correspond with an increase in RI. This allows identifying the trends in the data output of LARA, thus sizing the droplet.

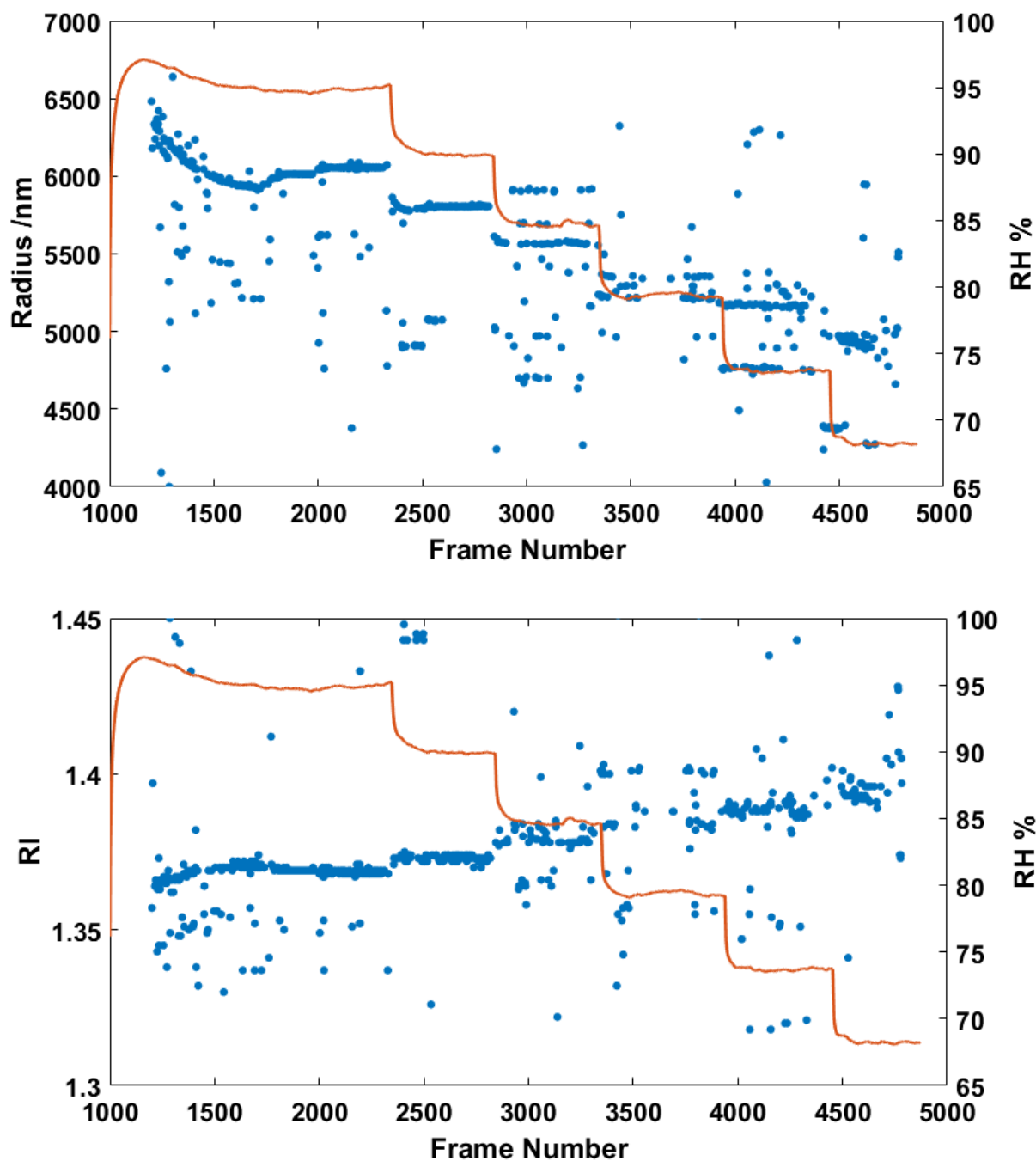


Figure 6.3 An example of the hygroscopic data of NaCl collected using Raman AOT and analysed using LARA. On both graphs the output of LARA is in blue (top graph – size; bottom graph – refractive index), and the RH is plotted in orange. The Raman AOT data was collected using the 600 grooves cm^{-1} grating with a 10 s accumulation time per frame. For the purpose of the LARA analysis starting frame was renumbered from frame number 0 (in the Raman AOT data) to frame number 1000, adjusting the later frames accordingly.

6.2.4 Dynamic Vapour Sorption data

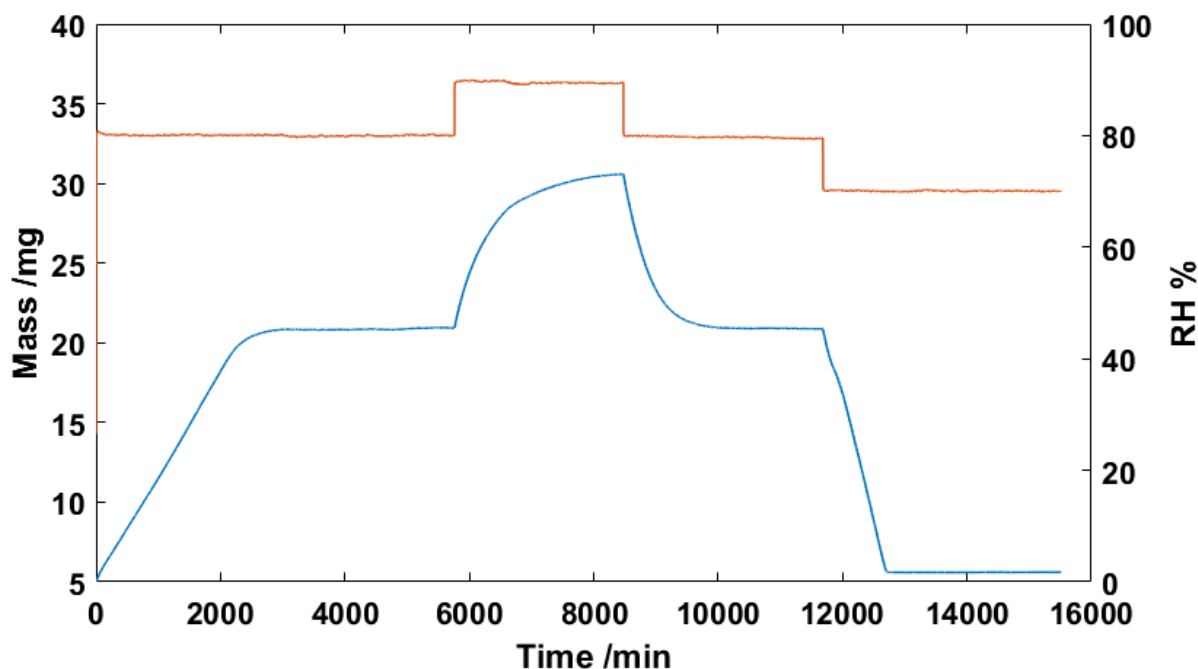


Figure 6.4 An example of the hygroscopic data of NaCl produced using DVS. The mass of the sample is in blue, whereas the RH is indicated in orange. The graph demonstrates that when in contact with a surface NaCl will crystallize at RH between 70 and 80%, which is consistent with the literature. This plot also demonstrates the long equilibration times of NaCl which are in the order of 2000 minutes. The data was obtained by manually monitoring the DVS instrument and manually changing the RH whilst continuously recording the data. The data was recorded as an average of 1 min of measurement at 1 measurement per second.

A demerits of the DVS technique as opposed to the AOT are that it is extremely time consuming and it is incapable of accessing the super-saturated states of the NaCl solution, as it had been demonstrated that the NaCl stays as a liquid droplet at RH > 45%. One of the benefits of the DVS is that it does not suffer from issues caused by crystallization, as it can happen with the AOT, when a crystalline layer is formed on a coverslip, distorting the optics, which causes droplet to fall out.

Another demerit of the DVS is the comparatively long time needed for the experiment as it can be seen in figure 6.4.

6.2.5 Hygroscopic growth curves

Hygroscopic growth of NaCl is well known, which makes it a good standard for assessing the reliability of the instrumentation and experimental procedure. It is also a way of identifying potential systematic errors. Thus as it can be seen in figures 6.5 - 6.9 the data obtained for NaCl using the AOT (see Figures 6.5 – 6.8) and DVS (see Figure 6.9) demonstrate adherence to the theoretical values calculated using AIOMFAC-web and E-AIM^[173,174], which in turn demonstrates that the data produced using either system is of good quality.

The DVS data (see Figure 6.9) demonstrates that dry NaCl dissolves itself at RH between 70 and 80 %, which is consistent with the literature. The DVS data also demonstrates that due to the nature of the instrument (i.e. a small amount of chemical in a pan) it cannot achieve supersaturation, thus in some cases DVS may not be suitable for determining hygroscopic behaviour of aerosols.

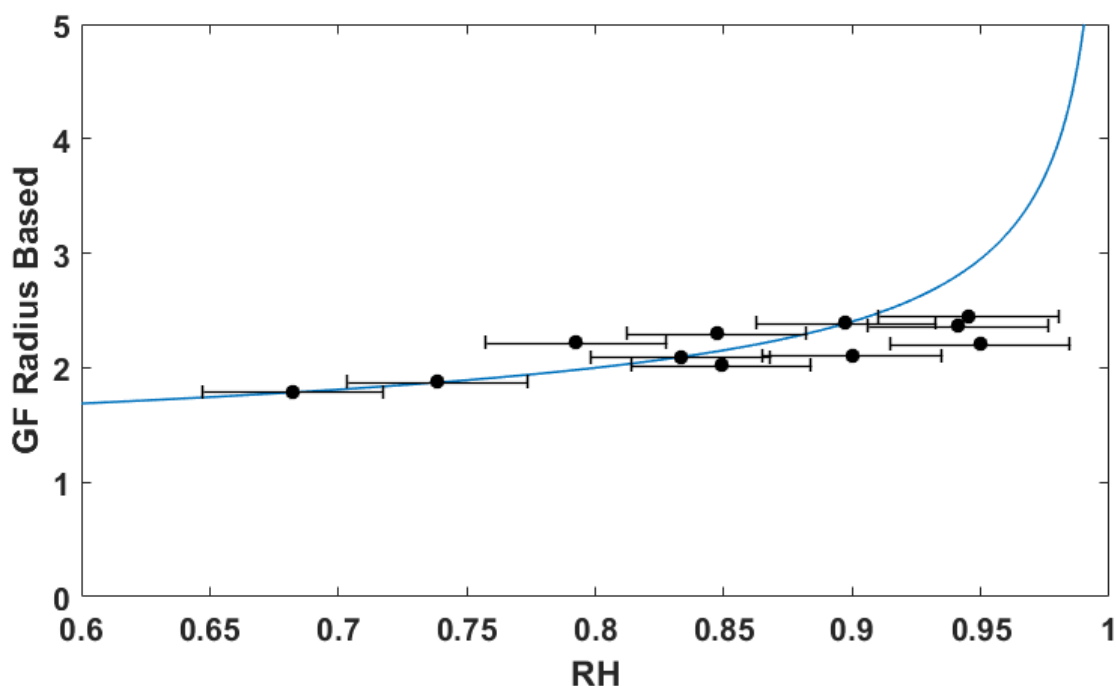


Figure 6.5 A Growth curve (a plot of the GF vs RH) of NaCl produced using the Raman AOT data analysed using LARA (in black), and the theoretical growth curve produced using E-AIM software^[173,174] (in blue). The dry sizes of the various droplets were calculated using the refractive index vs concentration calculation, which was used to calculate the GF. The error bar across the x-axis is caused by the RH probe, which has a stated error of $\pm 3.5\%$.

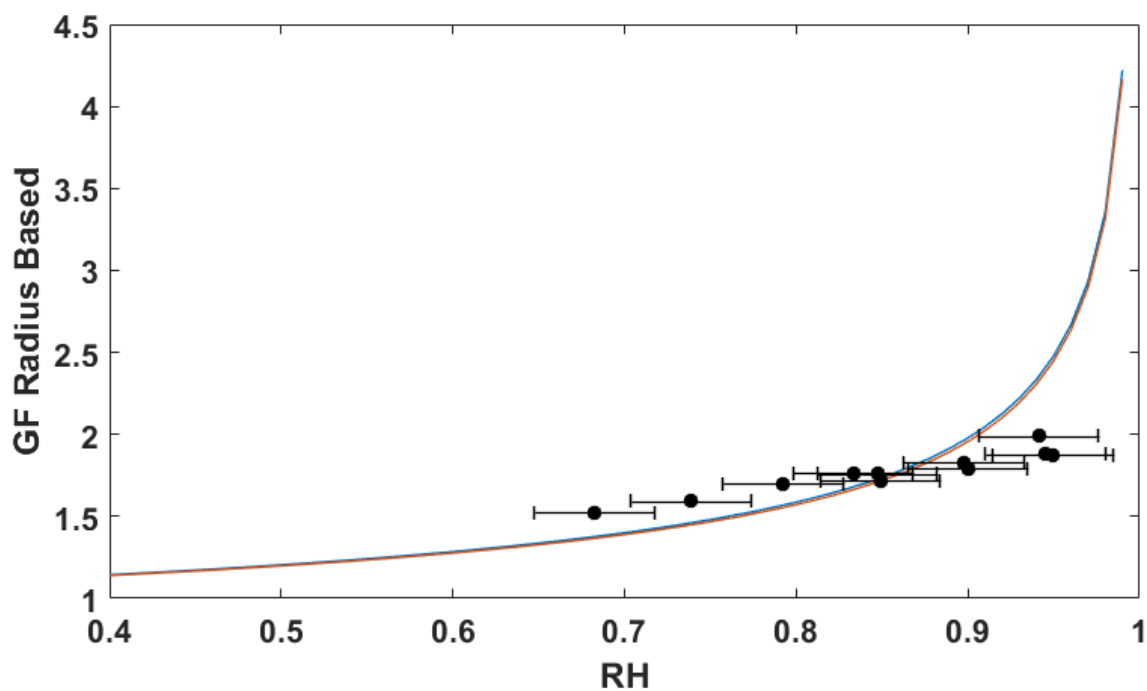


Figure 6.6 A Growth curve (a plot of the GF vs RH) of NaCl produced using the Raman AOT data analysed using LARA (in black), and the theoretical growth curves produced using the optimization software outlined in chapter 4.3 using the κ -Kohler theory model optimized for the data (in orange; $\kappa = 0.7205$) and the values optimized for the AIOMFAC data in figure 6.1 (in blue; $\kappa = 0.7493$). The error bar across the x-axis is caused by the RH probe, which has a stated error of $\pm 3.5\%$.

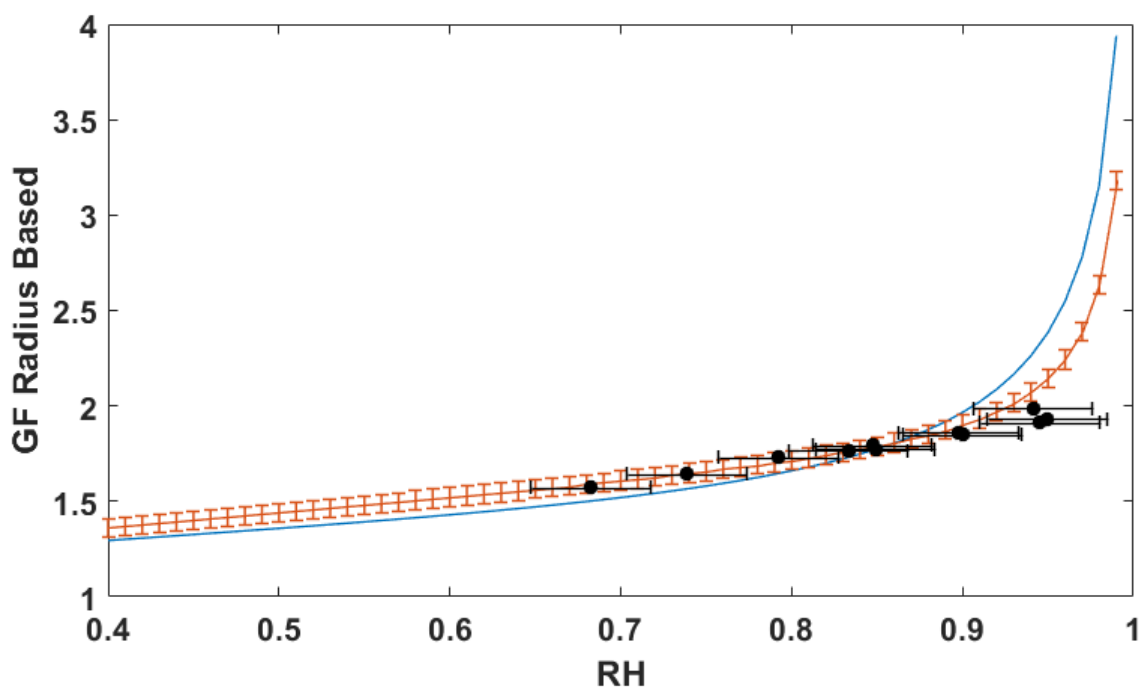


Figure 6.7 A Growth curve (a plot of the GF vs RH) of NaCl produced using the Raman AOT data analysed using LARA (in black), and the theoretical growth curves produced using the optimization software outlined in chapter 5.3 using the κ -Kohler theory model optimized for the data (in orange; $a = 3.2796$, $b = -2.1550$, $c = -0.8480$) and the values optimized for the AIOMFAC data in figure 6.1 (in blue; $a = 2.9703$, $b = -3.4776$, $c = 1.1021$). The error bar across the x-axis is caused by the RH probe, which has a stated error of $\pm 3.5\%$. The error bar of the optimised hygroscopic growth curve is the average difference between the AOT data optimized curve and the AIOMFAC optimized curve (5% error).

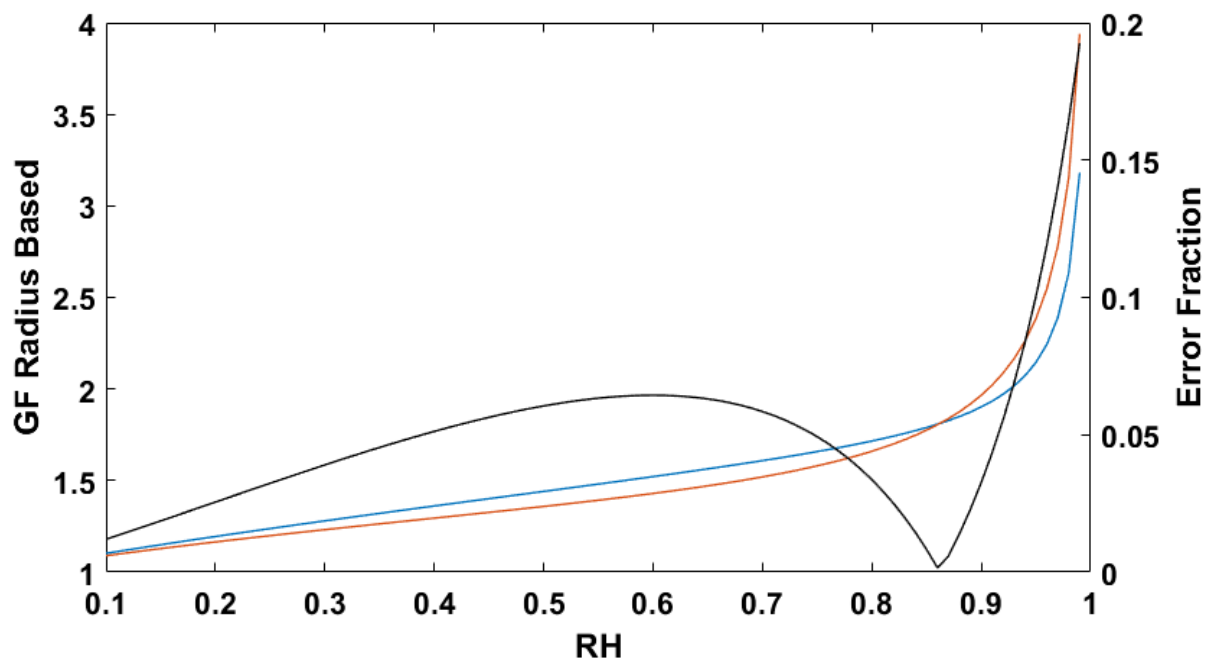


Figure 6.8 A plot of the optimised hygroscopic growth curves, data optimized curve (in orange), the AIOMFAC optimized curve (in light blue), both are the curves from figure 6.7 and the fit error between the two models (in grey) with an average error of ~5%. This demonstrates that both curves are relatively similar, thus the AOT data is of reasonable quality.

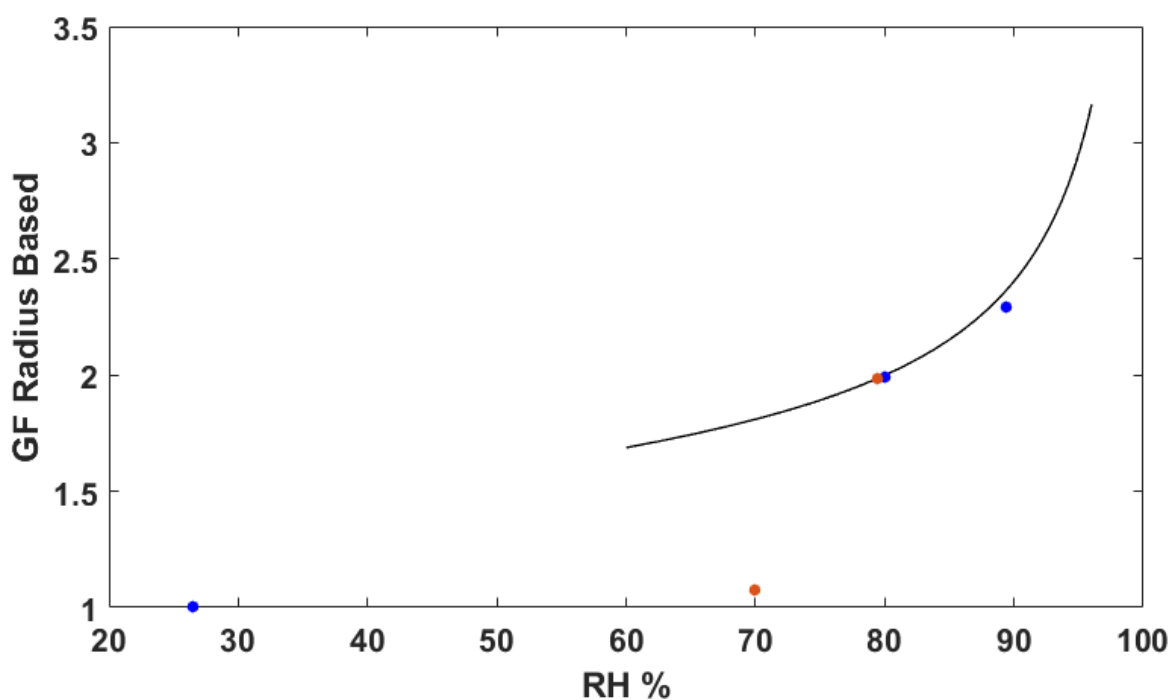


Figure 6.9 A plot of CaCl_2 data obtained using the DVS. The orange dots represent the ascending RH data, the blue points - descending RH, and the black line the E-AIM data.

6.3 Calcium chloride

6.3.1 General description

Calcium chloride (CaCl_2) is a Ca^{2+} salt, often used for its hygroscopic properties, and is commonly used as a desiccant. In aerosols CaCl_2 is one of the products of atmospheric ageing of CaCO_3 . In the work done for this thesis CaCl_2 aerosol droplets are reacted with Sodium Carbonate (Na_2CO_3) to produce optically trapped aerosol droplets containing CaCO_3 . This reaction is important, as it provides a route to studying aerosols containing CaCO_3 inclusions and other water insoluble inclusions.

6.3.2 AIOMFAC curve

Following the same procedure as was used for the AIOMFAC curves of NaCl earlier in this chapter (see Chapter 6.2.2).^[170–172]

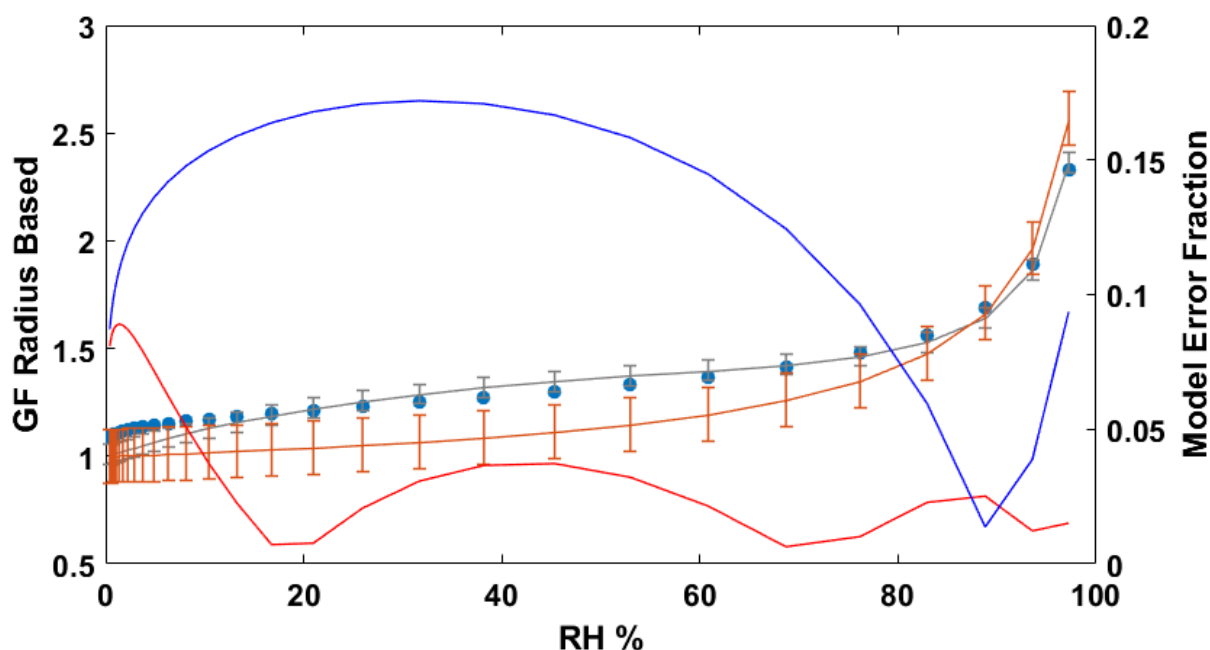


Figure 6.10 A plot of the hygroscopic growth of CaCl_2 produced using AIOMFAC (blue dots), calculated using equation 6.18. The data was fitted with both Kreidenweis equation model ($a= 4.6576$; $b= -8.1518$; $c= 3.82511$; average absolute error = 4.65%) and κ -Kohler theory model ($\kappa=0.45$; average absolute error = 12.38%), with plotted errors between AIOMFAC and the hygroscopic growth models between RH 97% to RH 44%, were aqueous NaCl aerosols have been proven to be stable. The model parameters were fitted for both models using the least error squared method using the GRG nonlinear algorithm (see chapter 3 for details). This demonstrates that the Kreidenweis equation model is more accurate at describing the hygroscopic growth of NaCl than the κ -Kohler model. The red and blue lines demonstrate the errors between the AIOMFAC produced data and the Kreidenweis equation model (in red) or κ -Kohler theory model (dark blue).

This demonstrates the same conclusion as for the NaCl (see this chapter section 6.2.2), in that the κ -Kohler theory model is more convenient for the initial estimation, however the Kreidenweis equation model fits the data better.

When considering the GF, one must consider not just the ratio of a solid particle to a liquid particle but a particle of solute that lacks any water in its structure. A point to

support this would be that after the solute attracts enough water molecules from its environment to dissolve, the resulting solution would be indistinguishable from the solution made from the anhydrous material, assuming the same amount of solute (in mols) are added. Therefore, while a hydrated crystal would be a solid particle it would not have a GF of 1, as it contains water within the solid structure. An important point to consider is that, as noted previously both models are fixed to have a $GF \rightarrow 1$ at $RH \rightarrow 0$, however this would not hold true for materials that tend to form hydrated crystals which contain water as part of the crystalline structure. This can also be seen on figure 6.2 as the data obtained from AIOMFAC-web does not trail off to a value of $GF=1$.

As both the Kreidenweis equation and the k-Kohler theory models are designed to provide an easy way of calculating the hygroscopic properties of various chemicals (i.e. represent real-life physical processes and properties), it would make sense to alter them when they fail to do so. In both equations 6.1 and 6.10, there is a term independent of the activity of water, set as a constant to have a value of 1. As such, it is dictating the value of the GF at $RH=0$ and therefore would be the one to alter in order of the equation to accommodate the presence of a hydrated crystal state. Thus, the resulting in modified Kreidenweis equation and k-Kohler models (see Equation 6.23 and Equation 6.24):

$$GF(\text{radius based}) = \frac{r_{total}}{r_s} = \left(x + k \frac{a_w}{1-a_w} \right)^{1/3} \quad \text{Equation 6.23}$$

$$GF = \left(x + (a + b * a_w + c * a_w^2) \frac{a_w}{1-a_w} \right)^{1/3}, \quad \text{Equation 6.24}$$

Where

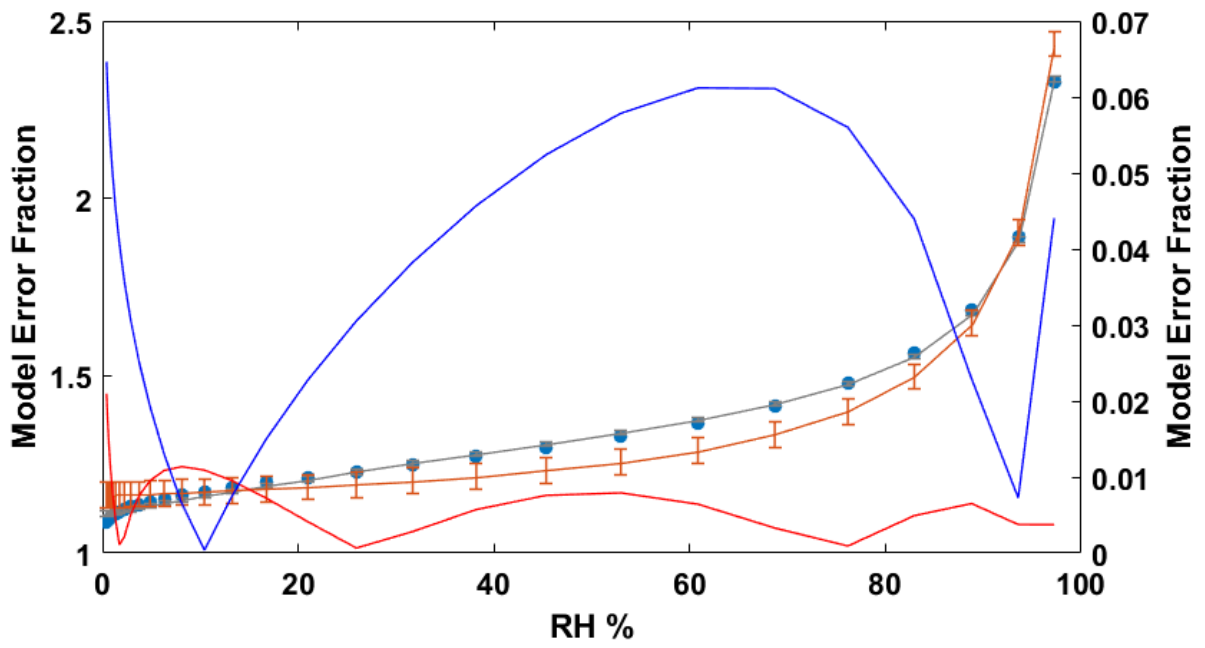
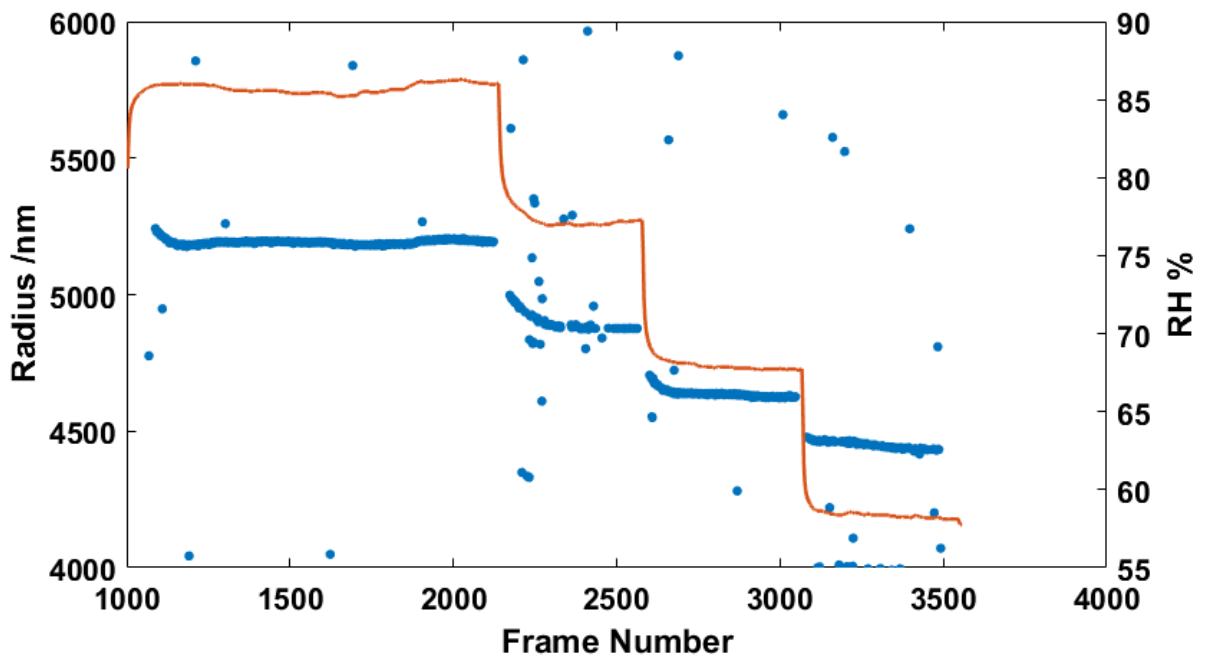
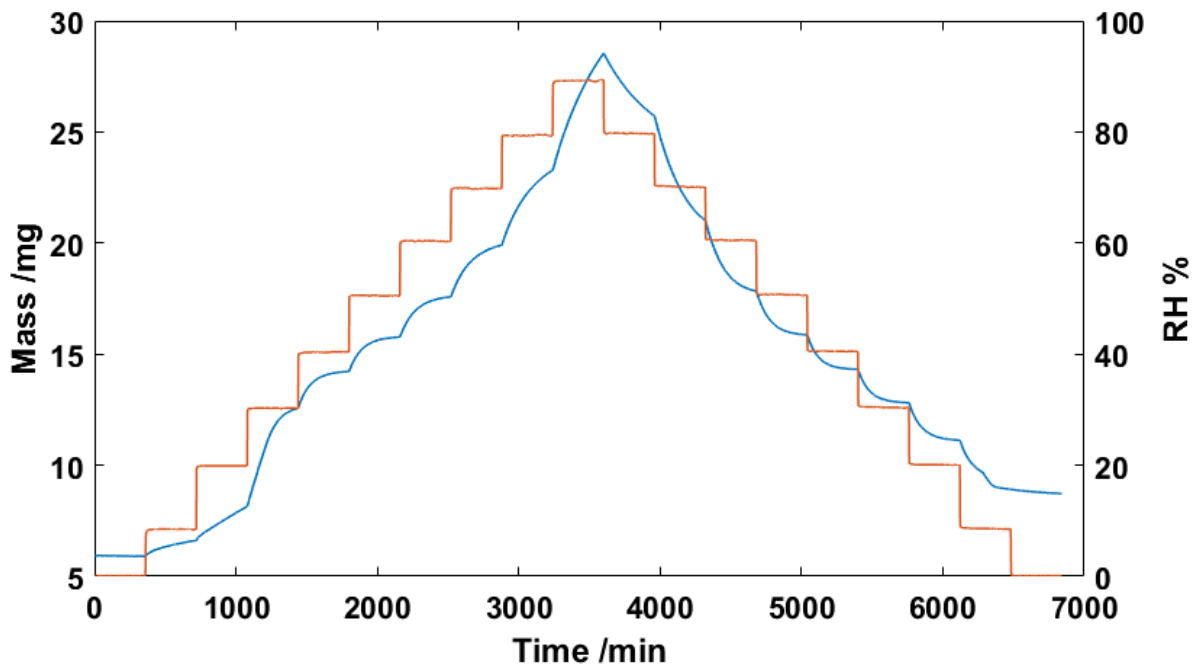


Figure
As

6.3.3 Aerosol Optical Tweezers data

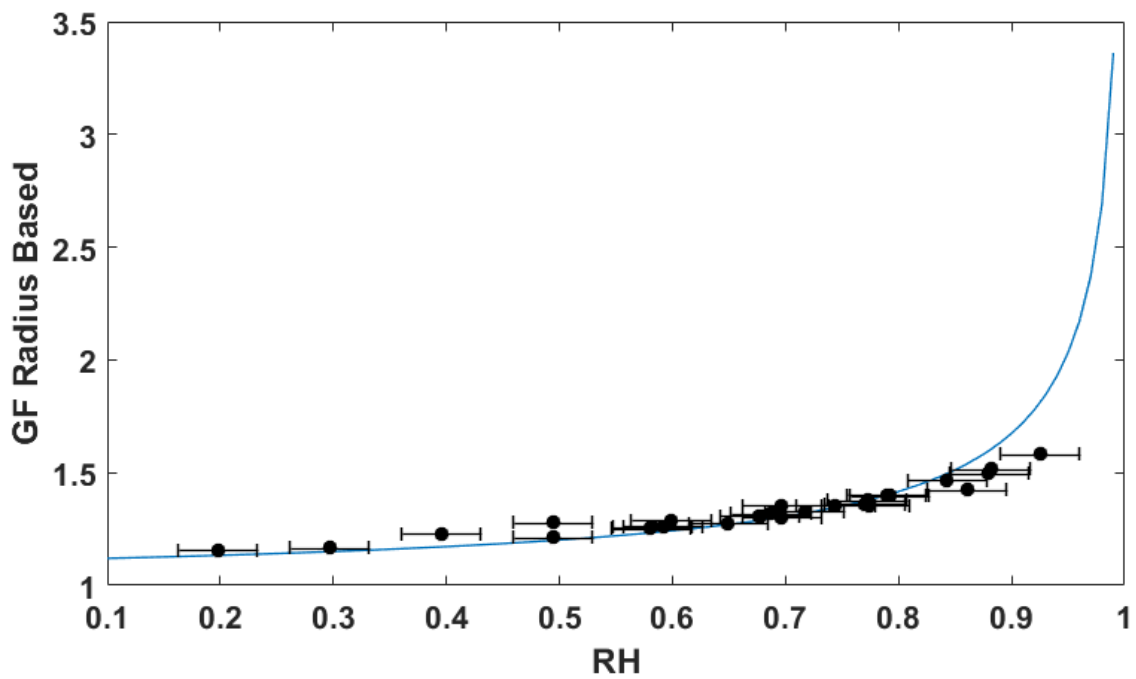


6.3.4 Dynamic Vapour Sorption data



The

6.3.5 Growth curves



Figure

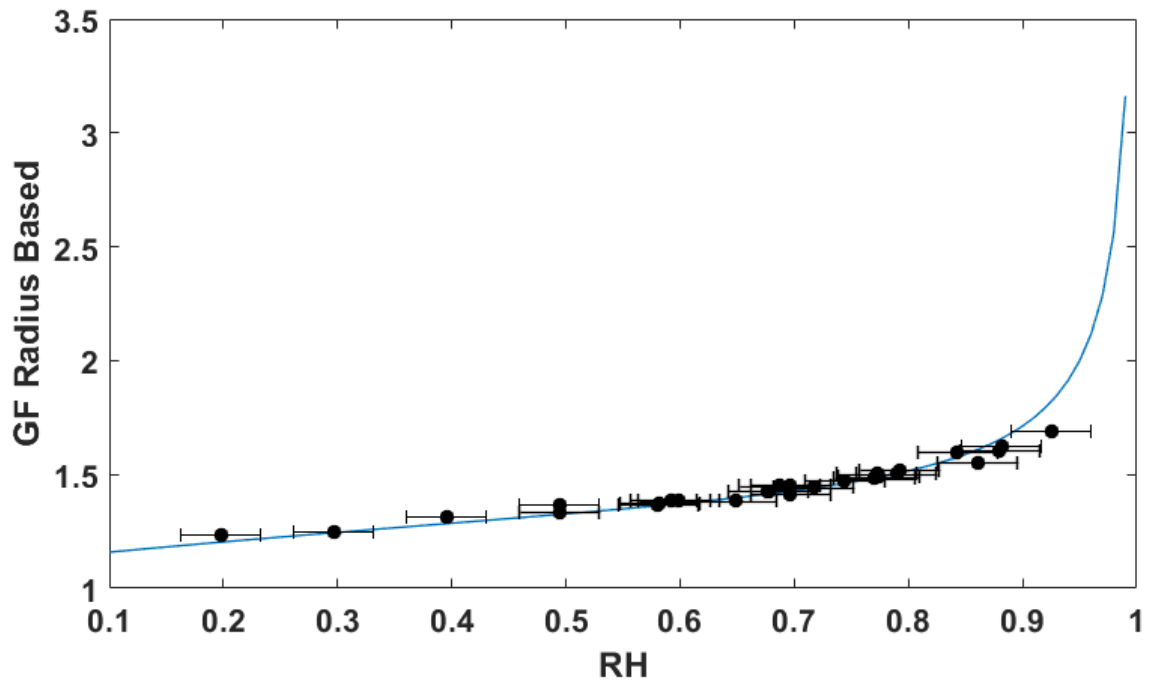


Figure 6.15 A plot of the AOT data analysed using LARA software (in black) with the dry sizes optimized for the modified Kreidenweis equation model (in light blue) (see

R
E
F

–
R
e
f
4
5
0
8
1
7
3

Common Parameters		
	κ -Kohler theory	Kreidenweis equation
x	1.3636	1.3636
K	0.37	-
a		1.9528
b		-2.2571
c	-	0.5991
Sample ID	Dry Radius /m	
131217	3.5341 E-06	3.2516 E-06
41217	3.4751 E-06	3.2382 E-06
231117	4.2361 E-06	3.8512 E-06
191117	4.1726 E-06	3.8209 E-06
291017	3.5429 E-06	3.2446 E-06
60118	3.6200 E-06	3.3835 E-06

Table 6.2 A table of model parameters and dry radii plotted in figures 6.14 and 6.15.

h

|

*

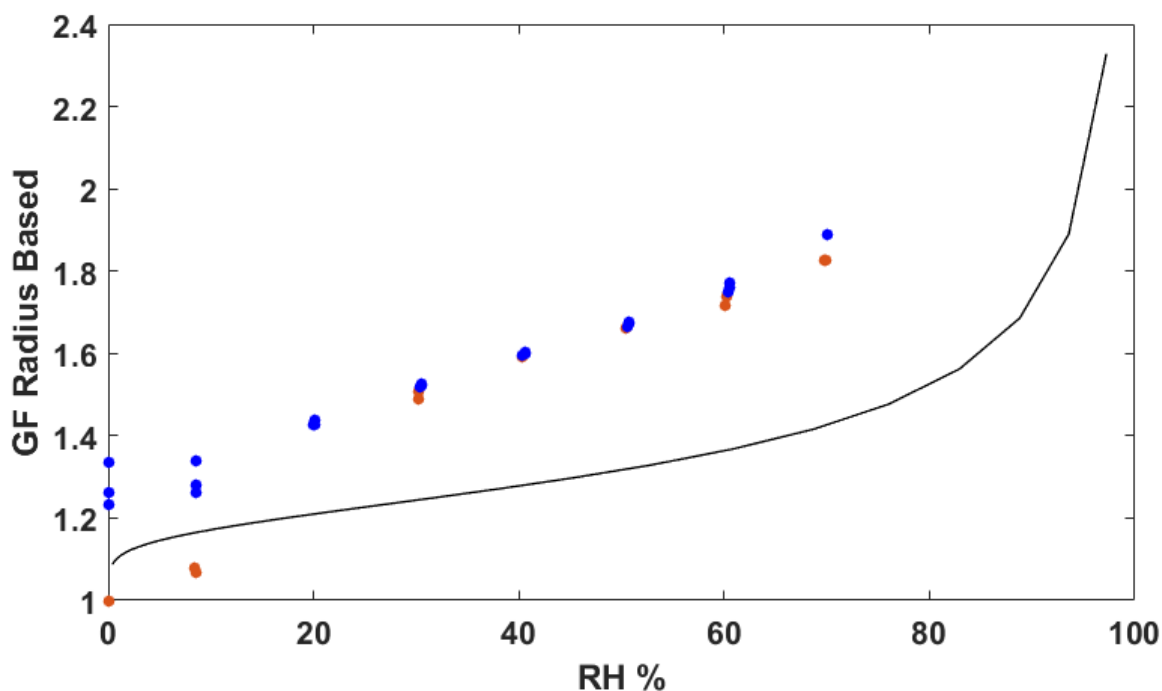


Figure 6.16 A plot of CaCl_2 data obtained using the DVS. The orange dots represent the ascending RH data, the blue points - descending RH, and the black line the AIOMFAC data.

The data in figure 6.16 demonstrates that CaCl_2 forms a hydrated crystal, which can be seen by comparing the ascending and descending RH masses at $\text{RH} \approx 0\%$. Another notable trend is that the DVS data does not adhere to the AIOMFAC model suggesting that CaCl_2 could have multiple hygroscopic growth curves, which depend on its environment, in this case contact with a solid surface. This is also supported by the AOT data, as it adheres closely to the AIOMFAC model (see Figures 6.14 and 6.15).

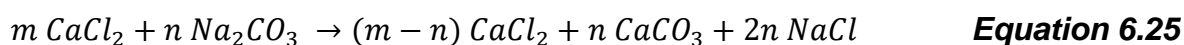
6.4 Chemical reaction completion models based on the ZSR theory

As stated previously in this chapter, the ZSR theory was designed non-interacting solutes. However, that is not true for all solutes as some of them can react in an aqueous medium producing, for example insoluble compounds. One of such reactions is the reaction between CaCl_2 and Na_2CO_3 (calcium chloride and sodium carbonate, respectively), which produces an insoluble precipitate CaCO_3 (calcium carbonate) and a soluble by-product NaCl (sodium chloride).

Assuming that during the reaction 100% of Na_2CO_3 is consumed, the mixed solution after the reaction is a mixture of $1-n \text{ CaCl}_2$, $n \text{ CaCO}_3$ and $2n \text{ NaCl}$, where n is the

fraction of CaCl_2 consumed during the reaction with Na_2CO_3 and corresponds to producing n amount of CaCO_3 and $2n$ amount of NaCl due to the stoichiometry of the reaction. Such an adjustment would enable to roughly account for the solute-solute interaction within the mixed solution, thus enabling the application of the ZSR theory for calculating the completeness of a chemical reaction.

When considering this chemical reaction with respect to the consumption of CaCl_2 , several logical conclusions can be made. The first conclusion is that at 0% consumption of CaCl_2 , no Na_2CO_3 was added, thus the solution will consist only of CaCl_2 and water. The second conclusion is that assuming no excess Na_2CO_3 was added and 100% of CaCl_2 were consumed during the reaction the resulting solution will consist of NaCl , CaCO_3 and water. Lastly the third conclusion is that any point in between the boundary conditions stated in conclusion one (0% consumption of CaCl_2 , a pure CaCl_2 solution) and conclusion two (100% consumption of CaCl_2 , a mixed aqueous solution of NaCl and CaCO_3) will be some mixture of the two, i.e. a mixed aqueous solution consisting of CaCl_2 , NaCl and CaCO_3 . This in turn leads to a conclusion that the maximum and minimum values of any calculations done on the mixture with respect to the fraction of CaCl_2 consumed will always be at 0% and 100% consumption of CaCl_2 . (see Equations 6.25 and 6.26)



$$\kappa_{total} = y \kappa_{\text{CaCl}_2} + x \kappa_{\text{CaCO}_3} + 2x \kappa_{\text{NaCl}} \quad \text{Equation 6.26}$$

Here m is the total amount of CaCl_2 in the initial droplet, n is the amount of Na_2CO_3 added, y is the mole fraction of CaCl_2 in the end droplet, and x is the mole fraction of CaCO_3 .

This is illustrated by the calculations of the volume using the κ -Kohler theory model (unmodified, based on equations 6.10 and 6.12 and, see Figure 6.17) and the total κ value of the mixed aqueous solution after the reaction (see Figure 6.18). The calculations were based on the unmodified κ -Kohler theory model (see Equation 6.10) and the ZSR theory (see Equation 6.12). The parameters used for these calculations were taken from the literature (see Table 6.3) set for a spherical CaCl_2 particle with a radius of $1\mu\text{m}$ (corresponding to 8.19×10^{-20} mol of CaCl_2) and set for $\text{RH} = 0.8$. (See Figure 6.17 and

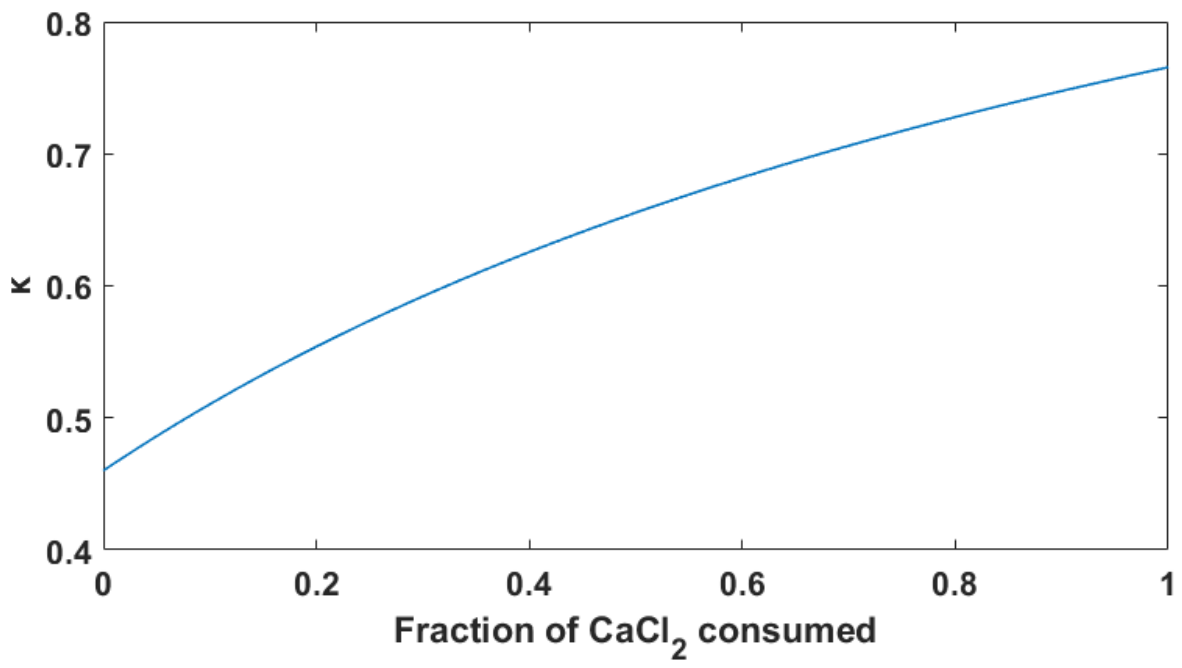


Figure 6.18)

	κ	Density g ml ⁻¹	Molar mass g mol ⁻¹
CaCl ₂	0.46 ^[28]	2.17 ^[166]	110.98 ^[166]
CaCO ₃	0.015 ^[28]	2.71 ^[175]	100.09 ^[175]
NaCl	1.28 ^[121]	2.17 ^[175]	58.44 ^[175]

Table 6.3 A table of the parameters used for the calculation for the graphs in figures 6.17 and 6.18.

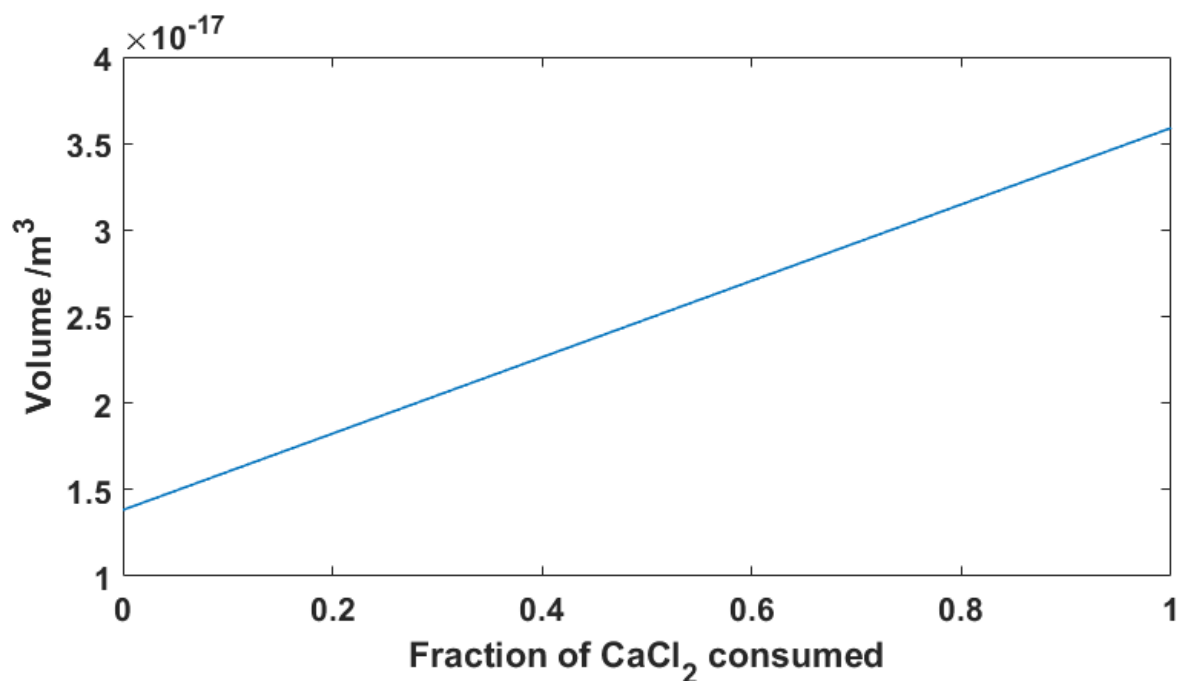


Figure 6.17 A graph demonstrating the change in the wet volume of a droplet with respect to the percentage of CaCl₂ consumed by a chemical reaction with Na₂CO₃, assuming 100% reaction efficiency. On this graph the 0% demonstrates a pure aqueous solution of CaCl₂ and 100% demonstrates that all of the CaCl₂ was consumed in the reaction however no excess of NaCO₃ was added, thus at 100% the only solutes present in the droplet are NaCl and CaCO₃. The theoretical parameters used in this calculation can be seen in Table 6.3, the RH was fixed to 80% and the dry radius of a spherical particle of CaCl₂ was 1 μm.

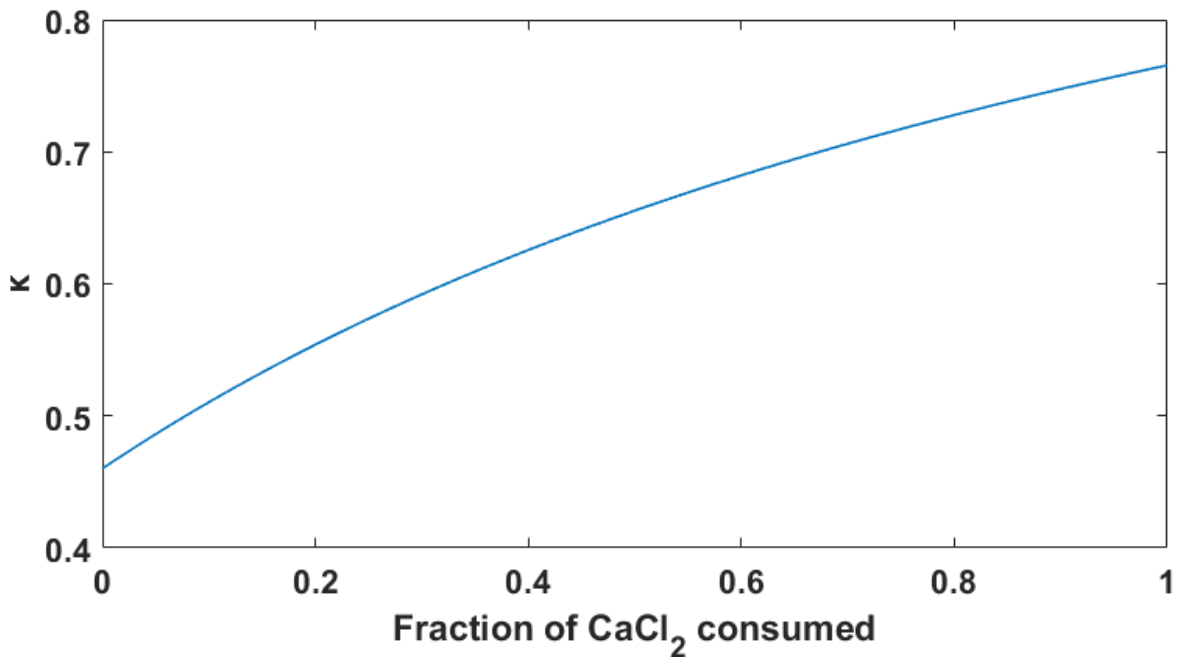
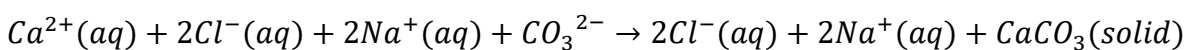


Figure 6.18 A graph demonstrating the change in the total κ value of the mixed solution calculated using equation 6.12 with respect to the percentage of CaCl_2 consumed by a chemical reaction with Na_2CO_3 , assuming 100% reaction efficiency. On this graph the 0% demonstrates a pure aqueous solution of CaCl_2 and 100% demonstrates that all of the CaCl_2 was consumed in the reaction however no excess of Na_2CO_3 was added, thus at 100% the only solutes present in the droplet are NaCl and CaCO_3 . The theoretical parameters used in this calculation can be seen in table 5.3, the RH was fixed to 80% and the dry radius of a spherical particle of CaCl_2 was $1\mu\text{m}$. Same as for figure 6.17.

Such an approach provides a clear way of estimating the amount of Na_2CO_3 that was added to a measured CaCl_2 droplet and the amounts of NaCl and CaCO_3 produced. If one would consider the states of the ions in an aqueous solution pre and post chemical reaction it is possible to write the chemical equation in a different form (see Equation 6.27):



Equation 6.27

This demonstrates that by considering the ions themselves as solutes it is possible to consider this chemical reaction as an example of a solute-solute interaction between the Ca^{2+} and CO_3^{2-} ions. Thus, the outlined approach used in the demonstrated case of a chemical reaction producing CaCO_3 could also be used to quantify other

chemical reactions or solute-solute effects by their effect on the total hygroscopicity of the resulting solution.

6.5 2-hydroxypropyl- β -cyclodextrin

The work on the 2-hydroxypropyl- β -cyclodextrin project was done in collaboration with C.P.F. Day, a PhD student from the research group led by Dr. A.E. Carruthers.

6.5.1 General description

2-hydroxypropyl- β -cyclodextrin (2-HP- β -CD) is an oligosaccharide a part of the cyclodextrin family and is specifically a β -cyclodextrin consisting of 7 glucopyranose units modified with hydroxypropyl groups. The cyclodextrins in general are extremely useful for pharmaceutical purposes, due to the fact that they form a hydrophobic cavity, which can be used to increase the solubility of hydrophobic drugs. Other benefits of cyclodextrins are their high solubility in water and high toxicity threshold, with the solubility of 2-HP- β -CD is $>600 \text{ mg mL}^{-1}$ and acute LD_{50} in rats at 10 g kg^{-1} intravenously and $>2 \text{ g kg}^{-1}$ orally. (LD_{50} is a measurement of toxic threshold corresponding to a lethal dosage to 50% of the population.) A combination of these properties makes cyclodextrins a valuable carrier substance for water insoluble drugs, thus has the potential to be an efficient drug carrier for inhalable administration.^[176,177]

6.5.2 Dynamic Vapour Sorption data

The DVS data of 2-HP- β -CD demonstrates that 2-HP- β -CD does not adsorb a lot of water, while adsorbing water quite rapidly as it can be seen in figure 6.19. An interesting thing that can be noticed in the data is a relatively large increase in mass at RH 10 and 20, suggesting that 2-HP- β -CD is undergoing some kind of transformation, which is likely to be either dissolution or the formation of a liquid crystal state. In figures 6.13 and 6.16, a similar trend can be noticed as CaCl_2 equilibrates to RH 20%, and CaCl_2 is known to form hydrated crystals^[178].

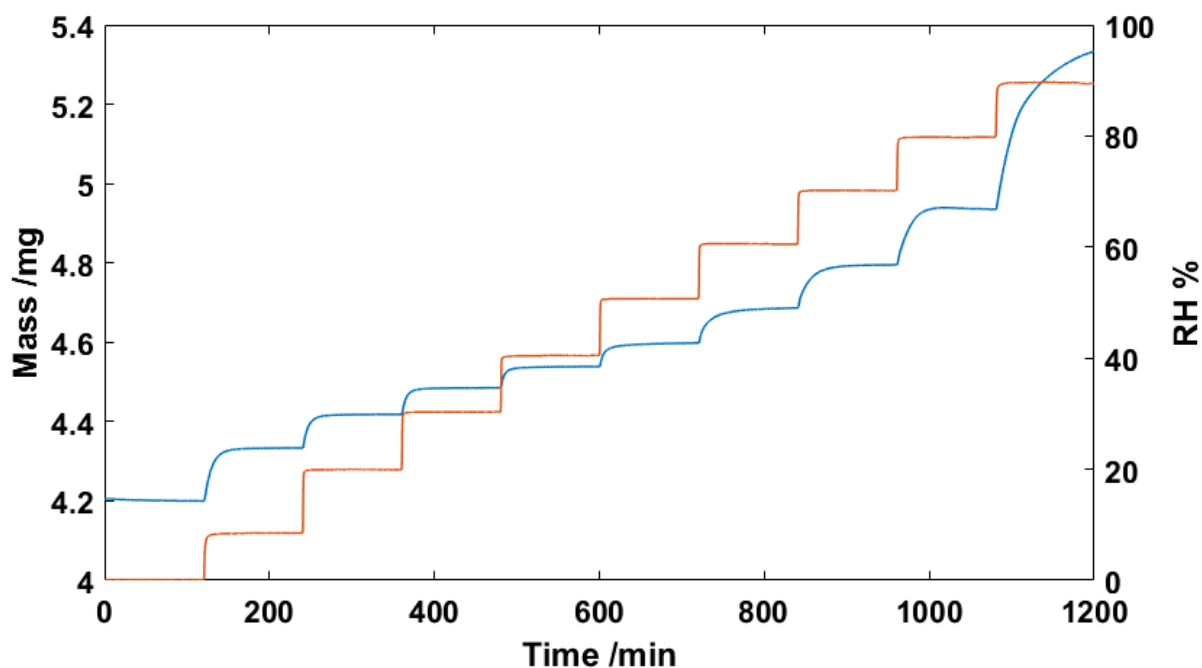


Figure 6.19 An example of the DVS data of the 2-HP-b-CD data with ascending RH only. See Table 6.4 for details.

6.5.3 Growth curves

One of the facts that need to be considered is that equation 6.22 relies on having a known density of solute, in this case 2-HP- β -CD, which does not have a known or predicted density, as it is not a crucial parameter for medicinal applications.

Therefore, for the purpose of these calculations the density of a closely related compound β -cyclodextrin was used, which has a predicted density $1.6 \pm 0.1 \text{ g cm}^{-3}$ was used instead^[179]. This allows at least estimating the GF of 2-HP- β -CD and should be updated as data becomes available. (See **Figure 6.20** and **Figure 6.21**)

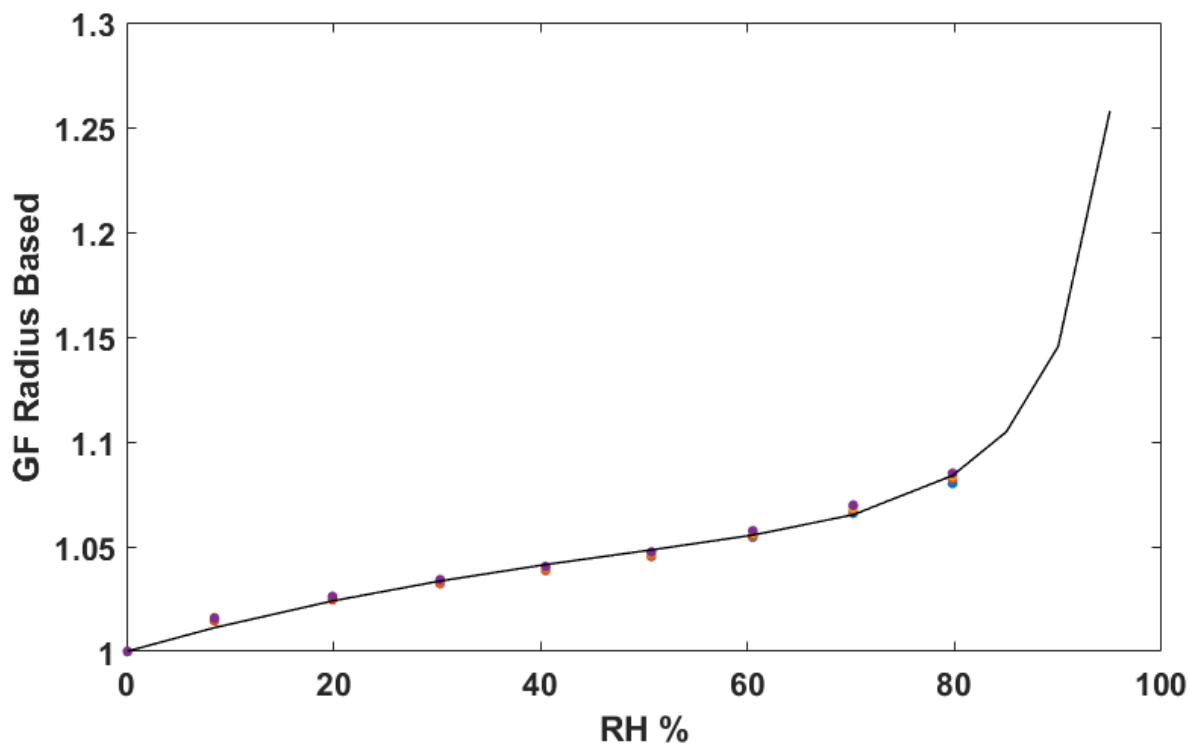


Figure 6.20 DVS data of the 2-HP-b-CD data (ascending RH only) fitted with the Kreidenweis equation model, extended to RH 95%. See Table 6.4 for details.

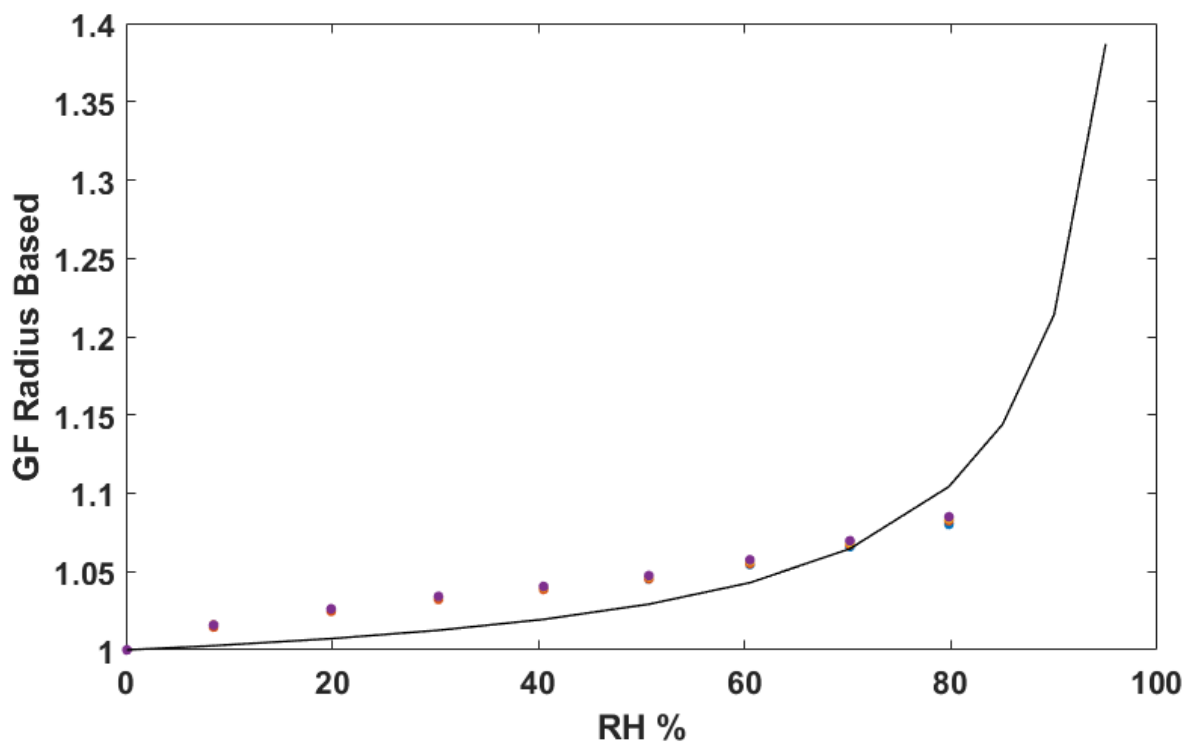


Figure 6.21 DVS data of the 2-HP-b-CD data (ascending RH only) fitted with the κ -Kohler theory model, extended to RH 95%. See Table 6.4 for details.

	Parameter		Average error
κ -Kohler theory	k	0.0877	12%
Kreidenweis equation	a	0.4312	2%
	b	-0.7401	
	c	0.3589	

Table 6.4 A table of the optimized parameters for the DVS data for the κ -Kohler theory and Kreidenweis equation models. The average error is the average error between the optimized model and the experimental data. The error is averaged across both RH and the data sets.

Continuing with the trend noticeable in both NaCl and CaCl₂, that the Kreidenweis equation models the experimental data better than the κ -Kohler theory model. It can also be noted that 2-HP- β -CD attracts only a small amount of water reaching a GF of <1.1 at 80% RH.

6.6 Conclusions

In this chapter some of the main theories regarding the hygroscopic growth of chemicals were presented. These include two mathematical models: κ -Kohler theory and Kreidenweis equation, which are outlined and described in chapters 6.1.2 and 6.1.3. Both of these theories are used to model the hygroscopic growth of NaCl, CaCl₂ and 2-HP- β -CD. In this data a trend of the Kreidenweis equation model is the more accurate of the two.

When examining the CaCl₂ data one of the most notable aspects is that the κ -Kohler theory and Kreidenweis equation need to be modified in order to accommodate for the formation of a hydrated crystal state, which retain moisture even at RH \approx 0%. This modification allows removing the limitation of both models of having a restricted GF = 1 at RH = 0% (see chapter 6.3.2).

Another theory discussed in this chapter is the ZSR mixing theory and a potential application of this theory for calculating the change in size of a droplet as a chemical reaction occurs. The calculation of the size of the droplet post reaction could also be viewed as an example of adjusting the ZSR theory to accommodate solute-solute interactions.

Chapter 7 “Anatomy” of a Raman peak

In this chapter the theory of the processes affecting the line profile of the chemical signature in Raman spectra. This will be continued with the theoretical models of the peak profiles used and principles of decomposing a spectrum into the different polymorphs present.

7.1. What broadens a peak in the Raman Spectrum?

In spectroscopy in general and Raman spectroscopy in particular the wavelength and the shape of the signal peak confers information about the properties of the chemical analysed. In Raman spectroscopy the signal peak contains information about the local environment of the vibrational mode that the signal peak corresponds to. However, as Raman scattering is a relative process it also invariably contains both the signal caused by the sample and the spectroscopic profile of the laser.

7.1.1. Frequency distribution of a laser

Real-world measurements always have an inherent amount of error that cannot be avoided, hence it is impossible to have absolute accuracy in every measurement or any instrument.^[180,181] This is exemplified by the width of the laser line. Even though, the laser used for the work in this thesis has a narrow laser line width it will still affect the produced Raman spectrum.^[182]

When considering the inherent error introduced by the laser it is plausible to consider an ideal Raman scattering material, i.e. a material that when irradiated with an ideally monochromatic light will produce an ideally monochromatic Raman signal. In case when the ideal scattering material has only one state, the laser line width in the spectrum will be the same as the distribution of frequencies of the incoming light. Similarly, if the scattering material has 2 ideal states closely together, the resulting spectrum will be a superposition of the frequency distributions produced by each of the states. The same logic follows for a non-ideal material, as it could be thought of as a distribution of N ideal states, thus the spectrum produced will be a convolution of the frequency distribution of the incoming laser and the distribution of the material.^[182] (See figure 7.1)

In light of this it is necessary to note that as the Raman signal will depend on the specific system used to produce a spectrum, it can also be thought of as unique to the system, having some influence on the spectrum, specifically with regards to the actual Raman shift. However, this influence is relatively small (a few cm^{-1}) and the patterns of the Raman peaks will remain the same.^[182]

Another important point to make is that the influence of the laser line width becomes significant with narrow peaks, which have a width similar to the width of the laser frequency distribution. In broad peaks, such as the O-H band at $\sim 3500 \text{ cm}^{-1}$ ^[183], the produced peak is extremely broad, and the laser line width does not have a major influence on its shape.

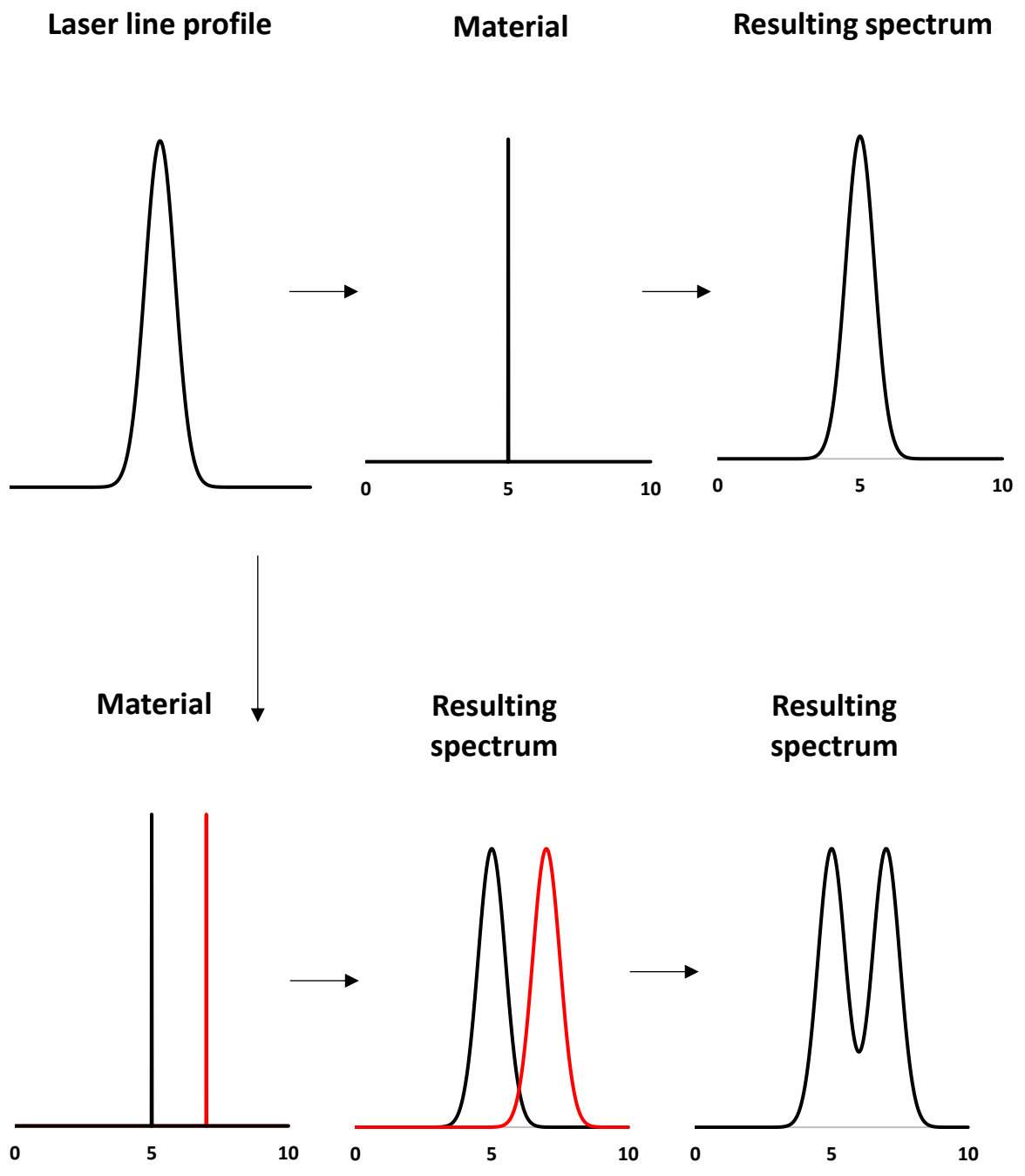


Figure 7.1 A schematic representation of the influence of the laser line width on the shape of the signal in a Raman spectrum.

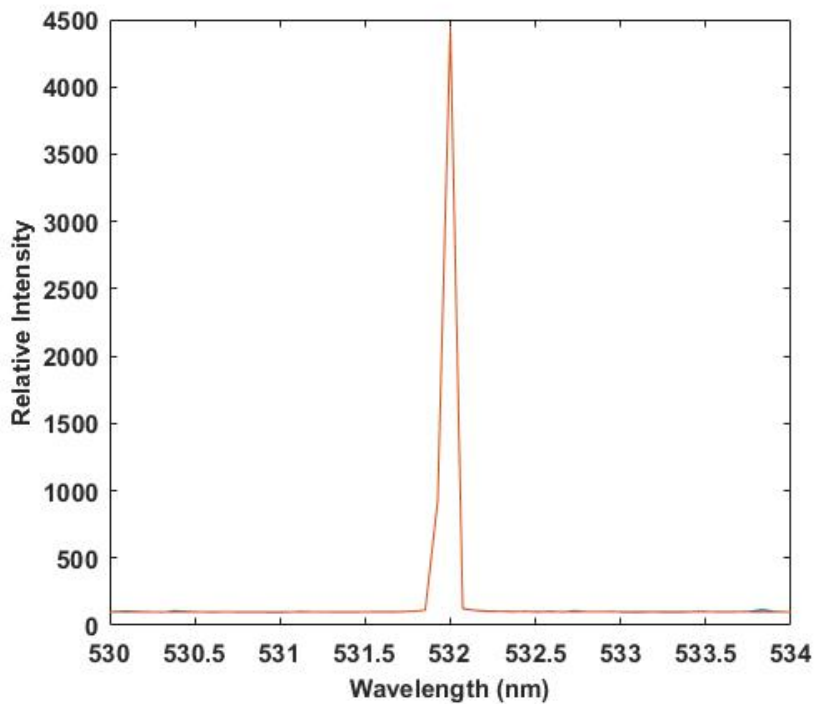
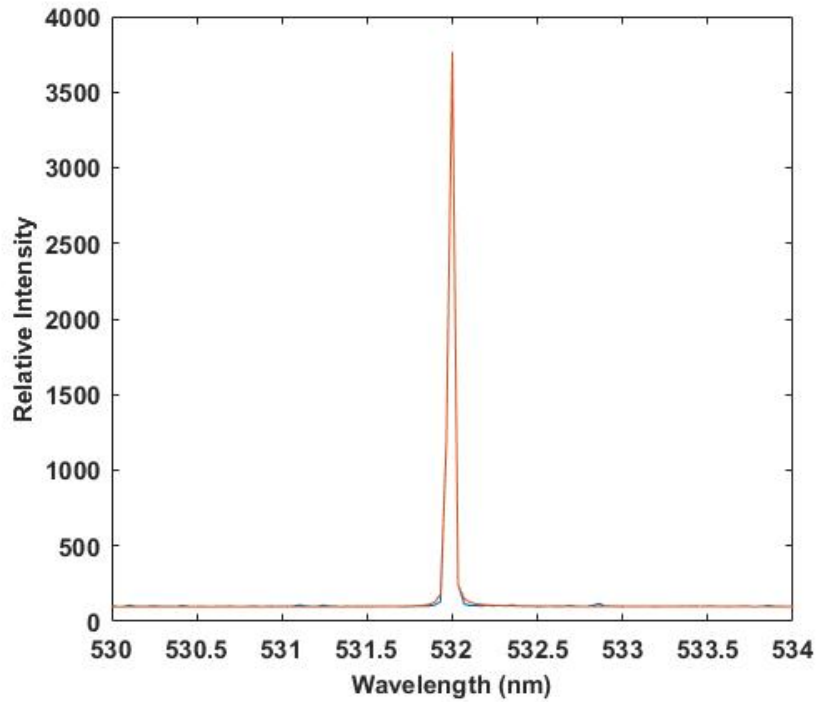


Figure 7.2 Spectra of the laser line at 1200 grooves cm^{-1} (top) and at 600 grooves cm^{-1} (bottom) resolution. The blue lines are the experimental data and the dashed orange line is the theoretical model fitted using the least squares regression optimised using the GRG nonlinear minimization algorithm.

Grating (grooves/mm)	1200	600
Position	531.98661	531.9676
Gaussian Intensity	7933.2924	23948.0019
Gaussian FWHM	0.01757	0.0279
Lorentzian Intensity	22108.37389	23971.1217
Lorentzian FWHM	0.02363	0.1381
Asymmetry	2.57491	2.6590
Lorentzian/Gaussian ratio	0.37948	0.0084

Table 7.1 The table of the theoretical parameters used to model the laser line spectrum in figure 7.2. The parameters are based on the Asymmetric Pseudo-Voigt model described in equation 7.7.

7.1.2. Homogeneous and Inhomogeneous broadening

When considering the factors that increase peak width it is important to note that there are two types of line broadening: the homogeneous and inhomogeneous line broadening.^[184]

Homogeneous broadening is a type of line broadening affecting all molecules equally. Homogeneous broadening includes processes such as natural broadening and pressure broadening, present in all phases of matter gas, liquid and solid.^[184] Natural broadening is intrinsic to any bond visible in a Raman spectrum as it is related to the lifetime of the excited/virtual state, hence will always be present even at temperatures approaching 3 K (~-270°C), where temperature effects are minimised, therefore determining the minimal possible width of the Raman peak.^[185]

In contrast, inhomogeneous broadening is a type of broadening that affects molecules differently based on their local environments. Inhomogeneous broadening is generally present in condensed states of matter such as liquids, glasses and crystals, as it relies on the difference in the local environment of the vibrating bond, such as interfaces and defects, such as the crystallinity of the material and hydration states of crystals.^[185] A notable example of this effect is its use in Raman spectroscopy of graphite and carbon nanotubes. Due to the layered structure of graphite, single monolayers of graphite have a characteristic peak (the G-band at ~1582 cm⁻¹) in the Raman spectrum, which is suppressed by additional layers, making it possible to use the Raman spectrum to identify a small number of graphite

layers.^[186] This property of graphite can also be used to identify the number of layers in carbon nanotubes. Similarly, Raman spectroscopy has been potential uses in protein analysis as a way of analysing secondary structures of proteins, such as α -helixes and β -sheets, etc.^[183] Another example of inhomogeneous broadening is the Doppler broadening is a consequence of the bond vibrating which is related to the temperature of the Raman scattering material, thus can be reduced and as mentioned become insignificant at extremely low temperatures.^[185]

In all cases of inhomogeneous broadening of a Raman peak, the essence remains the same: inhomogeneous broadening mechanisms reflect the different local environments the observed covalent bonds of the analysed material, conveying structural information about the material. Another aspect of this lies in considering multiple vibrational modes observed in a Raman spectrum. The different vibrational modes can be used to deduce the difference in energy in different vibrations, giving further insight into the structure of the material. This can be used to differentiate between different polymorphs of calcium carbonate (CaCO_3): Calcite, Vaterite, Aragonite, Ikaite and monohydrocalcite, as well as solvated anhydrous and hydrated sodium carbonate (Na_2CO_3) crystals, and provide information regarding the hydrated crystal state of a purely ionic solid, such as calcium chloride (CaCl_2).^[178,187–192]

7.2. Sodium Carbonate: dissolved, anhydrous and hydrated

As mentioned earlier in this chapter and in Chapter 2, Raman spectroscopy is very sensitive to changes in the local environment, which can be exemplified by Na_2CO_3 . The simplest spectrum of the local environments the CO_3^{2-} ion studied in this thesis is the spectrum of an aqueous solution of Na_2CO_3 . As expected fully aqueous Na_2CO_3 will exist as 2Na^+ and CO_3^{2-} ions, producing a single peak of the C-O v1 (Symmetric stretch) vibrational mode. This can be used as a reference point for a v1 vibration of a CO_3^{2-} ion surrounded by water.^[193,194] (See Figure 7.3)

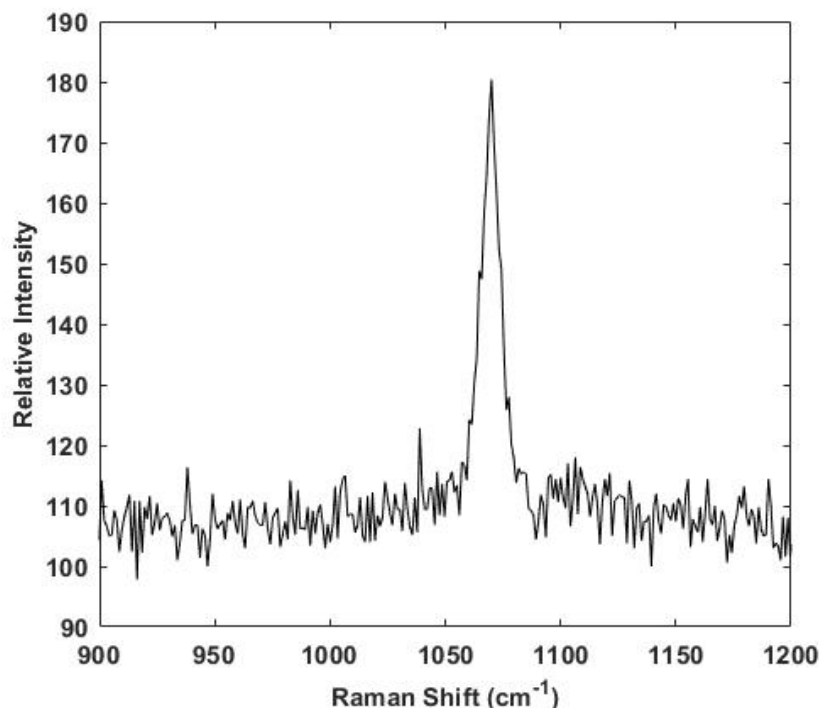


Figure 7.3 A spectrum of an aqueous Na₂CO₃ solution (droplet on a coverslip mounted in place of the aerosol trapping chamber) showing the ν_1 vibrational mode at 1070 cm⁻¹.

A Raman spectrum of fresh anhydrous Na₂CO₃ shows a ν_1 vibrational mode that contains a double peak, suggesting that the C-O bond is present in 2 major vibrational environments in the crystalline lattice. This can be corroborated by crystal structure of natrite (mineral Na₂CO₃, crystal structure very similar to γ -Na₂CO₃)^[195], and γ -Na₂CO₃ considered to have two distinct oxygen environments^[196], determined by computational analysis, X-ray diffraction and synchrotron experiments with average Na-O distances (see Table 7.2) .^[195,196] As it can be seen in Table 7.2 the Na1-O2 and Na2-O1 are extremely similar to one another, likely forming one peak, whereas the other peak is likely formed due to the Na2-O2 environment. This suggests that the two peaks produced by the two extreme environments result from an average Na-O difference of ~ 0.1 Å in, which can be identified in a Raman spectrum with resolution of ~ 1 cm⁻¹. It is likely that the Na1-O1 environment could not be resolved, because the difference between the peak positions in the Raman spectra is ~ 2 cm⁻¹.

Distance	Average distance (Å)
Na1-O1	2.377 (2)
Na1-O2	2.340 (2)
Na2-O1	2.326 (3)
Na2-O2	2.435 (2)

Table 7.2 A table of average Na-O distances in γ - Na_2CO_3 taken from Dusek et al. (2003)^[196].

The Raman spectrum of an “old” sample of Na_2CO_3 is somewhat similar to the spectrum of fresh anhydrous Na_2CO_3 , however it also contains an additional double peak. This could be due to the presence of hydrated Na_2CO_3 crystals ($\text{Na}_2\text{CO}_3 \cdot n\text{H}_2\text{O}$), as either a pure hydrated crystal or as a mixture of hydrated and anhydrous Na_2CO_3 .^[197] (See figure 7.4) At this moment Raman spectra of $\text{Na}_2\text{CO}_3 \cdot n\text{H}_2\text{O}$ are not available in the literature, the determination of the stoichiometry of the hydrated crystals implausible.

7.3. Water in a hydrated crystal

When considering hydrated crystals, it is important to consider the water within the crystal structure, specifically the O-H band at $\sim 3500 \text{ cm}^{-1}$. As mentioned in chapter 2 and earlier in this chapter, only covalent bonds can be observed in a Raman spectrum, which makes purely ionic compounds in solution “invisible” in a Raman spectrum. This remains true in hydrated crystals as well, the fingerprint of the ionic compound is not observed, however a change in the profile of the O-H band can be observed. This change is observed as the different states of hydration of the crystal alter the local environment of the water molecules, which in turn alters the vibrations of the O-H bonds in the molecules.^[178,197]

In case of CaCl_2 the overall shape of the peak can be used to differentiate between the different hydrated crystal phases of the $\text{CaCl}_2 \cdot n\text{H}_2\text{O}$, with $n=2, 4, 6$. A similar principle is also exploited in the determination of the distinct phases of ice crystals. In both cases the structure of the multiple overlapping vibrational modes comprising the $\sim 3500 \text{ cm}^{-1}$ O-H band are, initially determined under supercooled conditions, so that the contribution of the doppler broadening would be minimized, which resolves the different Raman active vibrational modes of the O-H bond.^[178]

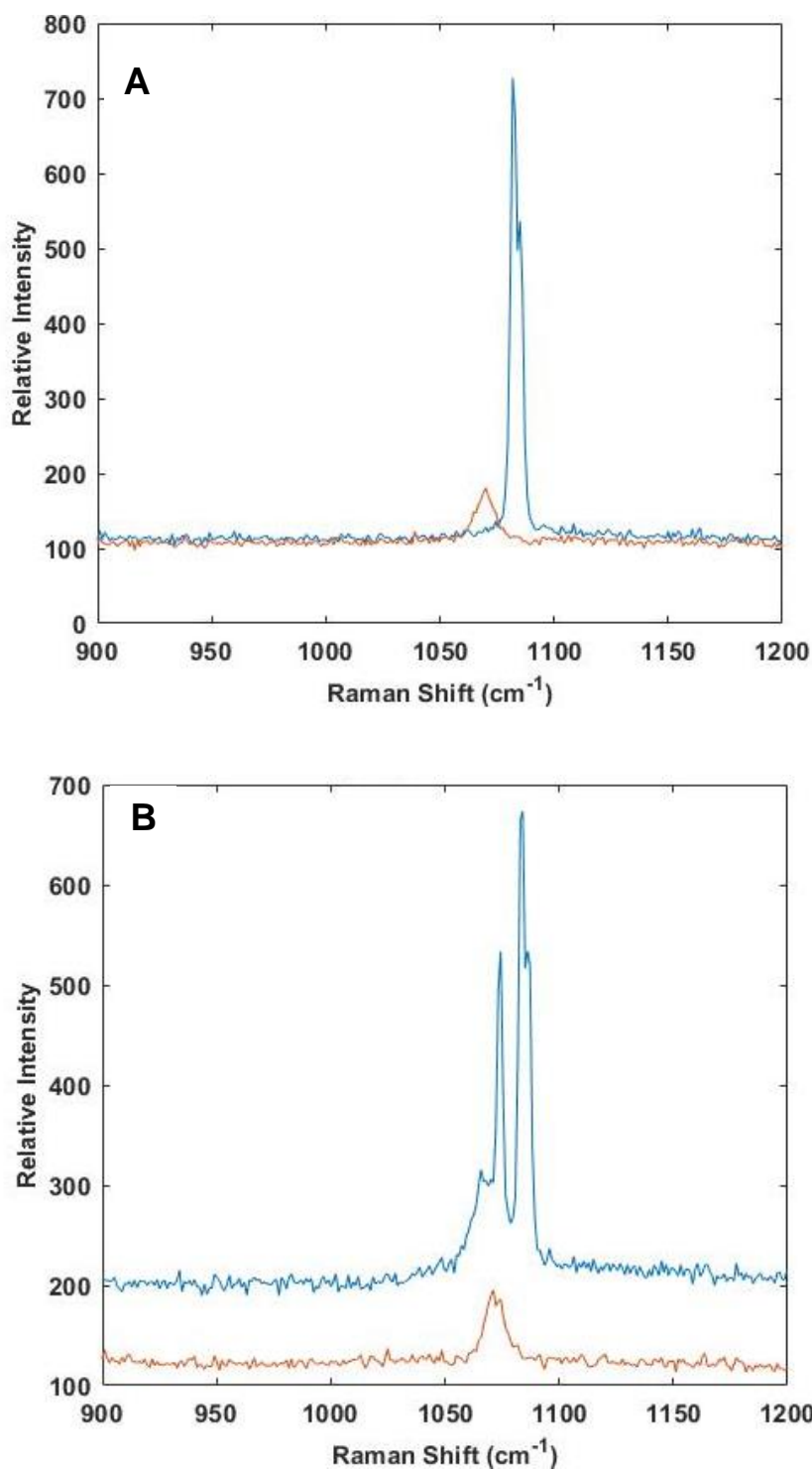


Figure 7.4 A) Spectra of dissolution of fresh dry Na_2CO_3 powder (blue line dry, orange line dissolved) on a microscope coverslip (top), demonstrating a characteristic double peak of the ν_1 vibrational mode of the C-O bond in the CO_3^{2-} ion. B) Spectra of dissolution of “old” Na_2CO_3 powder (blue line dry, orange line dissolved) on a microscope coverslip. It shows the same structure as the dry fresh Na_2CO_3 and a secondary structure more closer resembling the dissolved Na_2CO_3 (orange line), which is likely due to the presence of water within the crystalline structure.

7.4. Differentiating between polymorphs of calcium carbonate

As stated in chapter 1, calcium carbonate exists as several distinct polymorphs, with different physical and chemical properties. Thus, when dealing with CaCO_3 it is vital to distinguish between the polymorphs.

7.4.1. Amorphous Calcium Carbonate

Amorphous Calcium Carbonate (ACC) is typically the first occurring polymorph of CaCO_3 during formation and precipitation, serving as a precursor to formation of other polymorphs. The term amorphous refers to all solid materials that do not have a well-defined long-ranged order, present in crystals, with its crystalline lattice structural sub-units. From this definition the glassy phases as defined in chapter 5 of aerosols will also fall under the definition of amorphous, and to distinguish the two terms, in this thesis the term glassy will not refer to ACC.

The formation of ACC is an important process in the formation of skeletal and shell structures, the ACC lacking of a crystalline order, is stabilised by proteins, allows the overall structure to remain solid.^[73]

From the point of view of spectroscopy, the ACC is an interesting material, as it produces a very broad peak, when compared to other polymorphs of CaCO_3 and the CO_3^{2-} ion peaks in the ν_1 vibrational mode region at $\sim 1080 \text{ cm}^{-1}$. This signifies that there is a large distribution of different local environments observed in the Raman spectrum of ACC, and the position of the peak indicate the presence of short-range orders corresponding to various polymorphs of CaCO_3 , such as calcite, vaterite, etc. This is corroborated by FTIR and computational studies. ^[73,198,199]

These sub-morphologies of the ACC are named according to the crystalline polymorph they resemble, with a prefix proto- to signify that it is still not a crystal, but an amorphous solid. Examples of these sub-morphologies of ACC are proto-calcite and proto-vaterite. Nevertheless, this distinction between the various states of ACC is important, as these proto-states are the precursors to the formation of other polymorphs of CaCO_3 . Another significance of the proto-morphologies is the presence of short-range order within an amorphous solid, as it can be used for a better understanding of the overall process of crystallization in an amorphous material.^[73]

7.4.2. Calcite

Under ambient conditions calcite is the most thermodynamically stable anhydrous polymorph of CaCO_3 , and as such is the most abundant mineral form of CaCO_3 . Among other CaCO_3 polymorphs, calcite is also the least soluble, which is potentially one of the reasons why it is preferred as an exoskeleton by many organisms such as the Coccolithophores phytoplankton, Molluscs and crustaceans, as well as eggshells of eggs of birds.^[94,200,201]

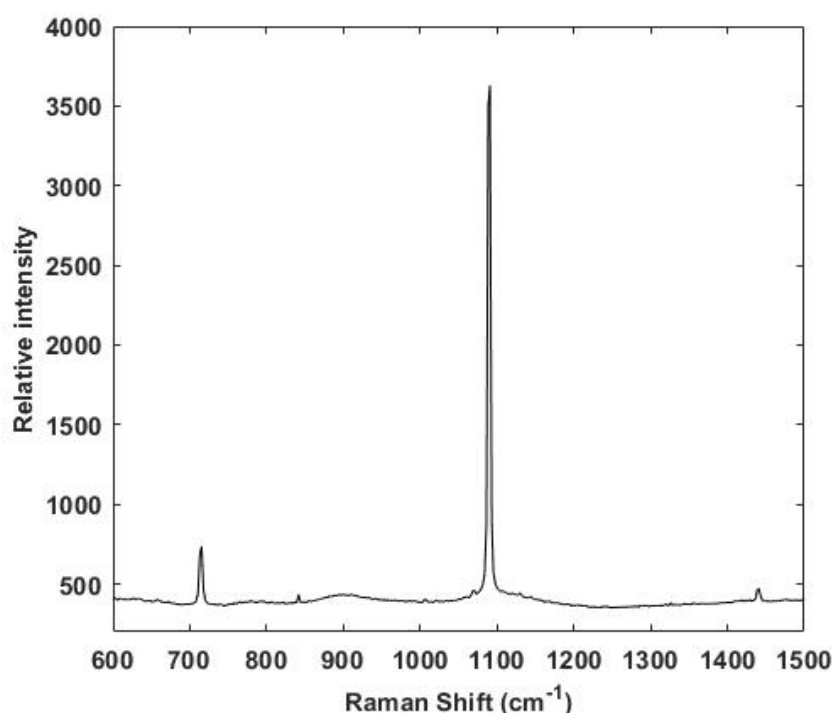


Figure 7.5 A spectrum of solid calcite on a microscope cover slide. The spectrum shows the v_1 vibrational mode at 1087 cm^{-1} and v_4 vibrational mode at 711 cm^{-1} .

In the Raman spectrum, calcite shows two highest intensity peaks for the v_1 at 1092 cm^{-1} and v_4 at 717 cm^{-1} vibrational modes each containing a single peak. (See Figures 7.5) This suggests high similarity of all vibrational environments, suggesting that there are no orientations at which there would be any strain in the average lattice inside the crystal, which can be related a uniform entropy distribution within a crystal.

[60,192,194,202–204]

7.4.3. Vaterite

Apart from ACC, vaterite is the least stable anhydrous polymorph of CaCO_3 forming at moderately high pH ($\sim\text{pH } 9$)^[205], at room temperature. Another way of obtaining

vaterite is by dehydrating ikaite by heating.^[60] One of the interesting aspects of vaterite is that it forms spherulitic aggregates as opposed to well defined crystals, which makes it an important material in optics research, both due to vaterite forming spherical particles and its birefringence (having multiple refractive indexes), which can be used to rotate the vaterite particle using a circularly polarized beam, which could be useful in microrheology.^[187–190,202,206,207]

The Raman spectrum of vaterite consists of a characteristic triple peak of the ν_1 vibrational mode, with the middle peak being close enough to be reported as a shoulder to the lower Raman shift peak. In the literature the ν_4 vibration is described as a wide band with a weak intensity, and in the spectra obtained in the duration of the research completed for this thesis is not observed.^[79,187,192,204,208] (see Figure 7.6)

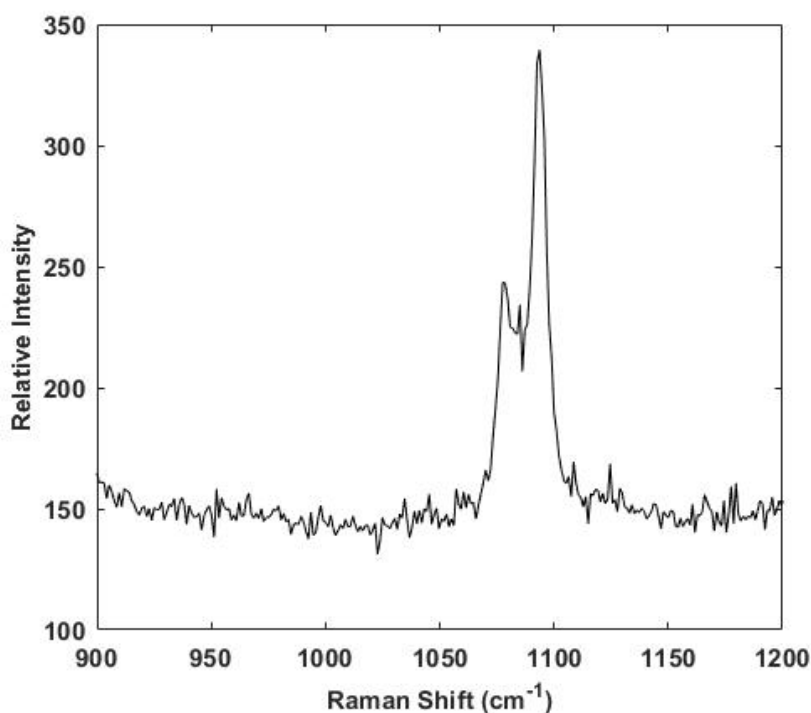


Figure 7.6 A spectrum of vaterite in an optically tweezed aerosol droplet after ~3 h 20 min after the reaction between CaCl_2 and Na_2CO_3 in an aerosol droplet, showing characteristic triple peak pattern of vaterite's ν_1 vibration mode.

7.4.4. Ikaite

Ikaite or hexahydrocalcite ($\text{CaCO}_3 \cdot 6\text{H}_2\text{O}$) is one of the naturally occurring hydrated crystal polymorphs. It is found naturally occurring in a Nordic fjord^[209] as a mineral

and in the shrimp shells.^[60] Synthetically, ikaite can be synthesized at pH values higher (pH 13.4) than that required for the synthesis of Vaterite (pH 9).^[205]

The Raman spectrum of ikaite has a single peak corresponding to the v1 vibrational mode at 1076 cm^{-1} only with a shift difference of only few wavenumbers from the v1 vibration of CO_3^{2-} ion, which is likely indicative of the amount of water present on the crystalline system.^[60,65,79,189]

7.4.5. Aragonite

Aragonite is the second most stable anhydrous polymorph, often found as the “skeleton” of coralline algae, as well as mollusc and cephalopod shells.^[100] Similarly to calcite, aragonite can also be found as a mineral. In the Raman spectrum the v1 vibration mode appears at the same position as calcite, and on its own it cannot be used to differentiate the two polymorphs. The v4 vibrational modes allow the distinction between calcite and aragonite, with aragonite having a weak triple peak at $\sim 705\text{ cm}^{-1}$.^[69,188,192,208]

7.4.6. Monohydrocalcite

Monohydrocalcite is another form of a hydrated CaCO_3 crystal, which stoichiometrically only one water molecule within the structure ($\text{CaCO}_3 \cdot \text{H}_2\text{O}$) compared to 6 in ikaite ($3 \cdot 6\text{H}_2\text{O}$). It is often found as a thin shell on other materials and as a milky suspension.^[65,190]

Polymorph	Literature		This study		Literature description
	v1 (cm ⁻¹)	v4 (cm ⁻¹)	v1 (cm ⁻¹)	v4 (cm ⁻¹)	
Calcite	1087 ^[194]	715 ^[194]	~1090 (strong)	~711 (weak)	Sharp single peaks at v1 and v4.
	1087 ^[203]	712 ^[203]			
	1085 ^[204]	711 ^[204]			
	1086 ^[192]	711.8 ^[192]			
	1086 ^[60]	712 ^[60]			
Vaterite	1074 ^[204]	665 ^[204] 683 ^[204] 728 ^[204]	1094 (strong) 1084 (weak) 1078 (medium)	-	Sharp double (or triple) peak at v1 and two broad v4 bands.
	1081 ^[204]	744 ^[204]			
	1094 ^[204]	751 ^[204]			
	1075.0 ^[192]	667.2 ^[192] 674.0 ^[192] 684.8 ^[192] 738.4 ^[192]			
	1081.4 ^[192]	743.5 ^[192]			
	1090.9 ^[192]	751.3 ^[192]			
	1090 ^[60]	750 ^[60]			
	1077 ^[60]	738 ^[60]			
CO ₃ ⁻² ion	1063 ^[194]	680 ^[194]	1070 (medium)	-	Sharp v1 peak and a v4 band.
	1063 ^[193]	680 ^[193]			
Amorphous	1080 ^[199]	714 ^[199]	1085 (weak)	-	Very broad peaks showing a lack of uniform structure.
	1086 ^[198]	-			
Aragonite	1085 ^[204]	716 ^[204]	Not observed		Sharp v1 peak at the same position as for calcite, v4 peak is split into a triple peak.
	1085 ^[192]	702 ^[192]			
	1087 ^[192]	703 ^[192]			
	1085 ^[208]	701 ^[208] 705 ^[208]			
Ikaite (Hexahydrocalcite)	1070 ^[60]	719 ^[60]	1076		Suspected in presence of a large excess of Na ₂ CO ₃ .
	1071 ^[79]	718 ^[79]			
	1072 ^[65]	722 ^[65]			
Monohydrocalcite	1069 ^[65]	723 ^[65] 699 ^[65]	Not observed		-

Table 7.3. A table of literature and experimental data on the Raman signals of the different calcium carbonate polymorphs, the peak position of the CO₃⁻² ion and a brief description of the peak shape.

7.5. Line profiles: A mathematical description

The different line broadening mechanisms affect the line total spectral profile in different ways, producing different statistical distributions. The phenomena comprising homogeneous broadening produce two types of statistical distributions: Gaussian (primarily inhomogeneous broadening) and Lorentzian (primarily homogeneous broadening), which translate in to the Gaussian and Lorentzian line profiles respectively, as well as their combination the Voigt profile.^[184]

7.5.1. Gaussian profile

The Gaussian line profile is produced as a consequence of the Doppler broadening and the pressure broadening mechanisms. The Gaussian distribution is also known as the normal distribution and is widely used outside of spectroscopy. It is characterised by being broad at half maximum and small wings.^[184,210] (see Equation 7.1)

$$G = I_G \exp\left(-\frac{(x-x_0)^2}{2w_G^2}\right) \quad \text{Equation 7.1}$$

Here G is the total Gaussian profile, I_G – the intensity of the gaussian profile, x – wavelength, x_0 – peak position, w_G – the Gaussian width parameter equal to $FWHM/1.665$.

7.5.2. Lorentzian profile

Unlike Doppler and pressure broadening, natural broadening produces a different line profile: the Lorentzian profile, also known as Cauchy distribution. Distinctly from the Gaussian profile the Lorentzian profile is narrower at half maximum intensity, however the wings of the Lorentzian distribution are larger than that of the Gaussian profile.^[184,210]

$$L = I_L \left(\frac{w_L^2}{w_L^2 + (x-x_0)^2} \right) \quad \text{Equation 7.2}$$

Here L is the total Lorentzian profile, I_L – the intensity of the Lorentzian profile, and w_L is the Lorentzian width parameter equal to $FWHM/2$.

7.5.3. Voigt profile and the Pseudo-Voigt approximation

The Gaussian and Lorentzian distributions are representative of the various physical processes such as natural broadening (Lorentzian profile) and Doppler broadening

(Gaussian profile). Both Gaussian and Lorentzian profile can be used on their own in the analysis of spectra at extreme temperatures, such as demonstrated in the case of identification of the hydration state using Raman spectroscopy^[185]. At extremely low temperatures, when contribution of the thermal doppler broadening to the total width of the peak is minimised, the total peak profile becomes similar to the Lorentzian profile. An example of the reverse is used when analysing plasmas, as the profile of the peak becomes virtually indistinguishable from a Gaussian profile, due to the overwhelming contribution of the temperature Doppler broadening.^[184]

At room temperatures both profiles need to be considered, as with the example of Doppler broadening the temperature is not high enough in order to approximate the profile to a purely Gaussian profile, however not low enough to approximate it to a Lorentzian profile. Hence the need for a different profile that incorporates contributions from both Gaussian and Lorentzian profiles, which is known as the Voigt profile. The Voigt profile is a mathematical convolution of Gaussian and Lorentzian profiles, combining the full width at half maximum of a Gaussian profile with the extended wings of a Lorentzian profile.^[184]

However, a convolution of two mathematical functions is not a trivial mathematical operation^[105], which makes the incorporation of the Voigt function difficult^[211], hence an approximation known as the Pseudo-Voigt profile is used in this thesis. The Pseudo-Voigt approximation relies on the sum of the percentage contributions contributed to the peak by the Gaussian and Lorentzian functions, with the ratio r . This approximation allows an uncomplicated way of accurately describing the peak in the spectrum and is used as the basis for a generic peak profile in this thesis (see Equation 7.3 and Figure 7.7).^[184]

$$V_{Pseudo} = I_G \text{EXP} \left(- \left(\frac{(x-x_0)^2}{2w_G^2} \right) \right) (1 - r) + I_L \left(\frac{w_L^2}{w_L^2 + (x-x_0)^2} \right) r \quad \text{Equation 7.3}$$

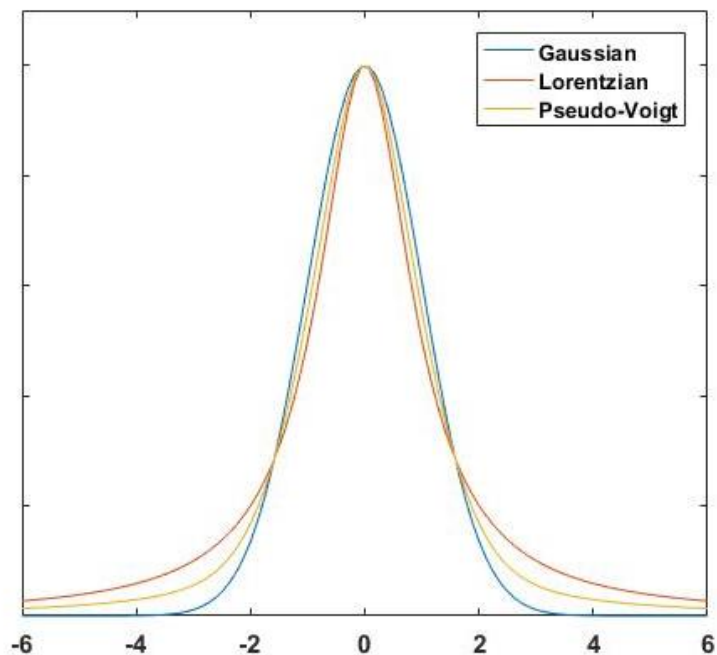


Figure 7.7 A graph of the Gaussian (blue line), Lorentzian (orange line) and Pseudo-Voigt (yellow line) line profiles described by equations 7.1, 7.2 and 7.3 respectively.

7.5.4. Asymmetry

As mentioned previously not all inhomogeneous broadening mechanisms such as different local environments will broaden the signal peak symmetrically. Therefore, the introduction of an asymmetry parameter into the line profile equations is necessary. This necessity can be noticed when fitting experimental spectra with symmetric functions, such as Gaussians. The experimental peak profile requires two Gaussian profiles to accurately model the peak, and as time passes the position of one of the peaks shifts closer and closer to the position of the second peak. Thus the two peak system should be replaced by a single asymmetric peak, as the second peak (the one that moves) is not a separate state, but an extension of the same peak, which can be due to the defects in the crystal lattice of a newly formed crystal.^[192,212] (see Figures 7.8 and 7.9)

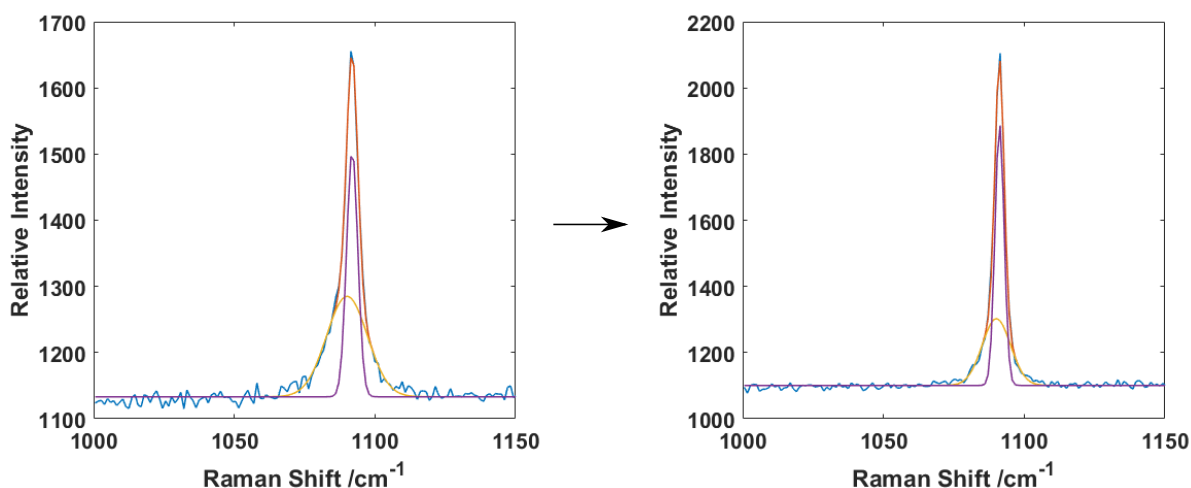


Figure 7.8 A comparison of spectra of calcite immediately after reaction (left) and ~1 h 40 min after the reaction (right). The blue line is the experimental spectra the orange line is the combined profile of two Gaussian profiles (in purple and yellow).

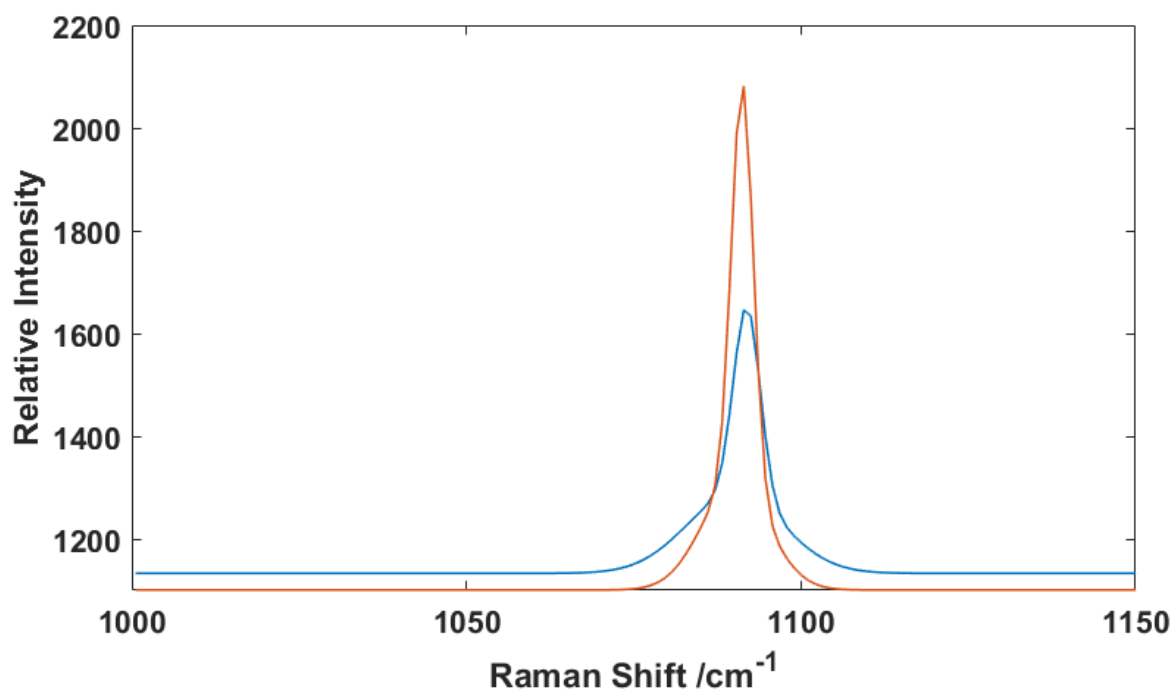


Figure 7.9 An overlay of the theoretical profiles seen in Figure 7.8. The blue line is the profile immediately after the reaction and the orange line is the profile after ~1 h 40 min after the reaction. As it can be seen on the plot, the peak in the blue spectrum is wider than in the orange spectrum which is likely caused by the crystalline structure defects caused by the formation of calcite which later equilibrate to a more perfect crystalline structure.

A simple way of introducing asymmetry, applicable to both Gaussian and Lorentzian profiles (and by extension the Voigt and Pseudo-Voigt profiles), is by modifying the width parameter of the modelled function by introducing a single asymmetry parameter, which will vary the asymmetry as a sigmoidal function, as introduced for IR spectra.^[213]

The sigmoidal function is a class of mathematical functions that produces an S-shaped curve. Some of the examples of this class of functions are the arctangent function, the hyperbolic tangent and the error function (also known as the Gauss error function). The sigmoidal function used for introducing asymmetry is:^[213]

$$w_{asym} = \frac{2w_0}{1+\exp(a(x-x_0))} \quad \text{Equation 7.4}$$

Where w_{asym} is the asymmetry adjusted width parameter, w_0 is the symmetric width parameter, and a is the asymmetry parameter. This allows producing a peak with varying degrees of asymmetry simply by changing the asymmetry parameter with the peak being symmetrical at $a=0$, skewed left at $a>0$ and right at $a<0$. Equations incorporating the asymmetry equation (see equation 7.4) into the Gaussian (see equation 7.5) and Lorentzian (see equation 7.6) line profiles are:

$$G_{asymmetric} = I_G \exp\left(-\frac{(x-x_0)^2}{2\left(\frac{2w_G}{1+\exp(a(x-x_0))}\right)^2}\right) \quad \text{Equation 7.5}$$

$$L_{asymmetric} = I_L \left(\frac{w_L^2}{w_L^2+(x-x_0)^2}\right) \quad \text{Equation 7.6}$$

$$V_{Pseudo} = I_G \exp\left(-\left(\frac{(x-x_0)^2}{2\left(\frac{2w_G}{1+\exp(a(x-x_0))}\right)^2}\right)\right) (1-r) + I_L \frac{\left(\frac{2w_L}{1+\exp(a(x-x_0))}\right)^2}{\left(\frac{2w_L}{1+\exp(a(x-x_0))}\right)^2+(x-x_0)^2} r \quad \text{Equation 7.7}$$

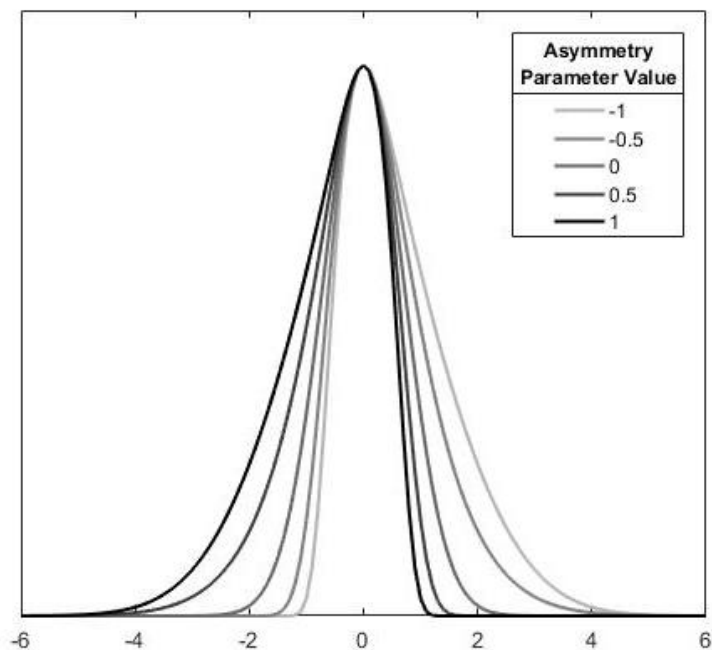


Figure 7.10 A plot of a Gaussian peak profile (see equation 7.5) with asymmetry parameters -1; -0.5; 0; 0.5; 1, with the colours dependent on the asymmetry value -1 the lightest grey and 1 darkest grey.

This produces a final profile of an asymmetric Pseudo-Voigt function that was used as a generic initial guess profile (see equation 7.7) and was simplified where the complexity of the asymmetric Pseudo-Voigt did not bring significant benefit, based on the fitting error between the experimental data and the model.

7.6. Peak profile modelling

In order to overcome the issues of overfitting and underfitting different models were fitted to the experimental data, using least squares regression, optimised using the GRG non-linear algorithm pre-programmed into MS Excel Solver. The quality of the fit of the optimised model to the data is judged as a ratio to the minimum, where fitting error squared parameter of the best fit model is taken as 1 and the rest are calculated as a ratio to it. The ratio to the minimum parameter allows easy identification of the best model suited for the peak. The complexity of the model was judged by the number of variables required to model one peak.

The models compared are:

Gaussian symmetric model following equation 7.1

Gaussian asymmetric (sigmoidal) model following equation 7.5

Lorentzian symmetric model following equation 7.2

Lorentzian asymmetric (sigmoidal) model following equation 7.6

Symmetric Pseudo-Voigt model following equation 7.3

Asymmetric Pseudo-Voigt (sigmoidal) model following equation 7.7

Asymmetric Lorentzian Gaussian linear sum ^[210]:

$$V_{(linear\ sum)} = I \left(b * \exp \left(-\frac{\ln 2}{s^2} \left(\ln \left(\frac{2s(|x-x_0|)}{w} + 1 \right) \right)^2 \right) + \frac{1-b}{1 + \frac{\left(\ln \left(\frac{2s(|x-x_0|)}{w} + 1 \right) \right)^2}{s^2}} \right)$$

Equation 7.8

L*G asymmetric model^[210]:

$$V_{(L \times G)} = I \frac{\exp \left(-\frac{1-b}{2} \left(\frac{(x-x_0)}{w(1+s(x-x_0))} \right)^2 \right)}{1 + b * \left(\frac{(x-x_0)}{w(1+s(x-x_0))} \right)^2}, \quad \text{Equation 7.9}$$

where b is a non-parameter variable, with constraints: $0 \geq b \geq 1$.

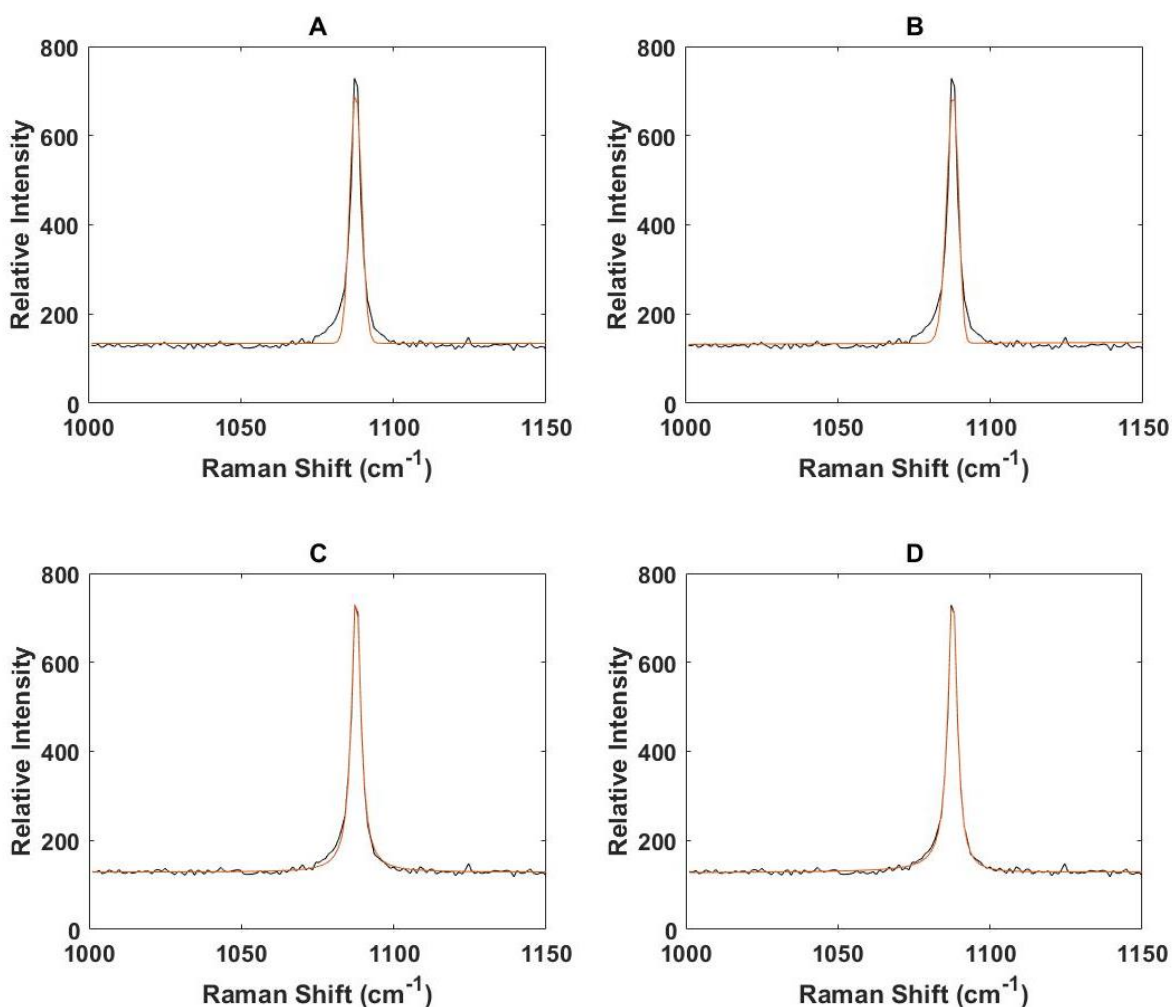
7.6.1. Calcite model

The calcite phase of calcium carbonate has two prominent peaks corresponding to the ν_1 vibrational mode at $\sim 1088 \text{ cm}^{-1}$ and ν_4 vibrational mode at $\sim 711 \text{ cm}^{-1}$. Both peaks can be used to identify the polymorph especially in distinguishing between calcite and aragonite.

7.6.1.1. ν_1 vibrational mode peak

Type	Fitting error squared	Ratio to the minimum
Symmetric Gaussian	3.71E+04	10.37
Asymmetric Gaussian	3.54E+04	9.90
Symmetric Lorentzian	5.16E+03	1.44
Asymmetric Lorentzian	3.60E+03	1.01
Symmetric Pseudo-Voigt	4.79E+03	1.34
Asymmetric Lorentzian Gaussian linear sum	5.23E+03	1.46
Asymmetric Lorentzian Gaussian product	4.86E+03	1.36
Asymmetric Pseudo-Voigt	3.58E+03	1.00

Table 7.4 A comparison of models of the ν_1 vibrational mode peak in a spectrum of dry calcite. The ratio to the minimum demonstrates the ratio between the value of the sum of least squares and the smallest value among the compared models.



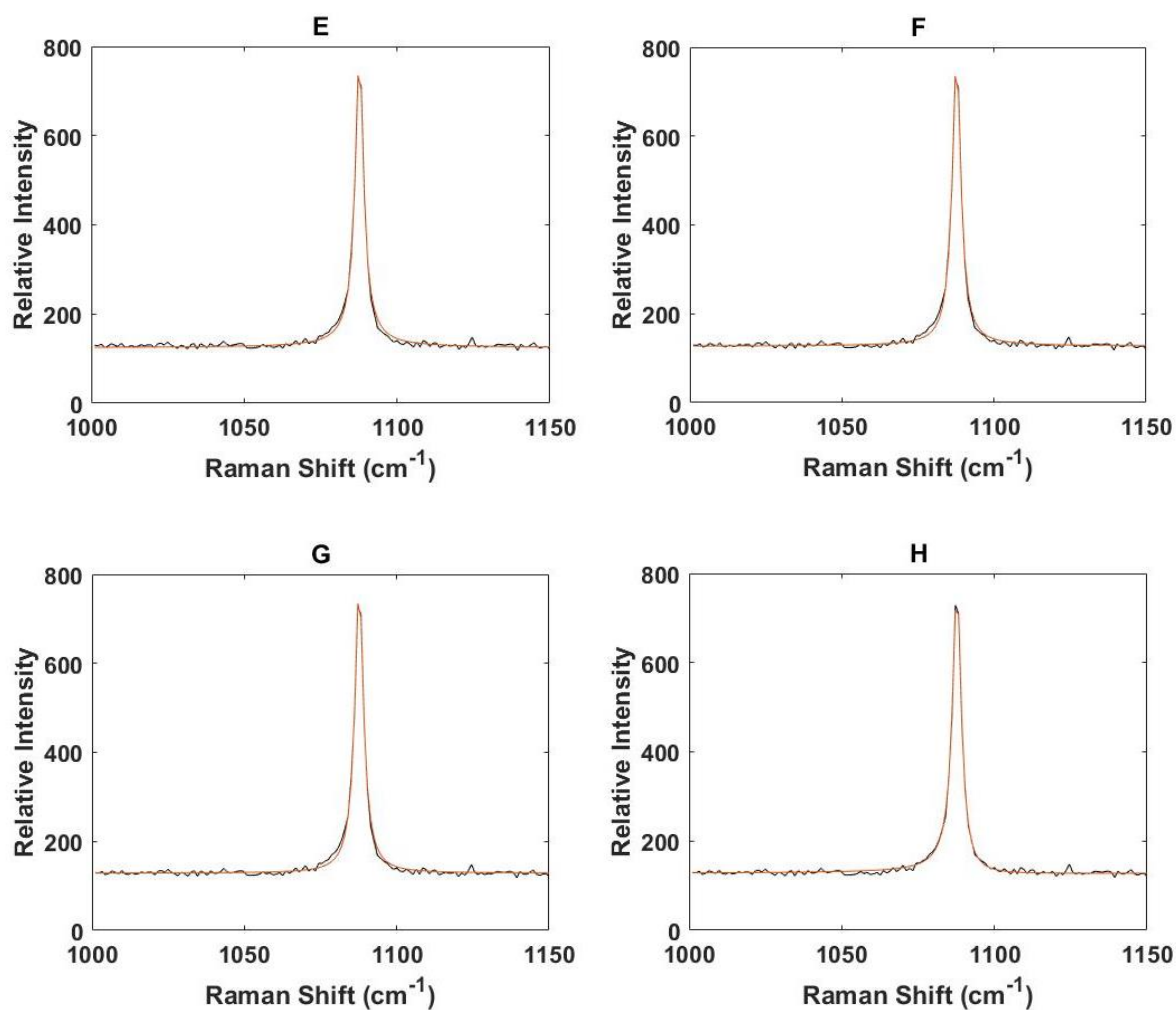
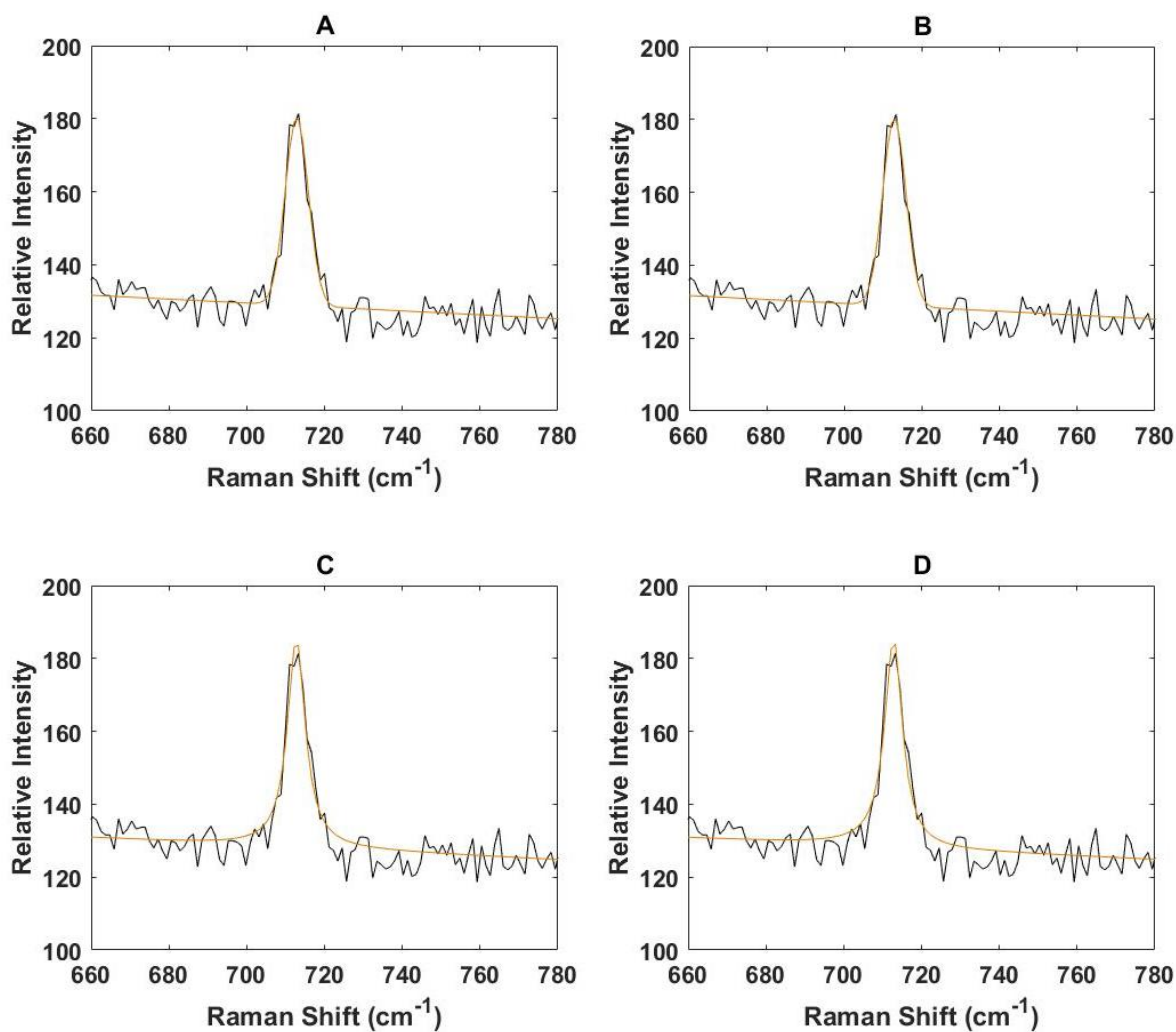


Figure 7.11 Graphs of the different of models of the ν_1 vibrational mode peak in a spectrum of dry calcite compared in the table 7.4. The black line is the experimental spectrum and the orange line is the theoretical model. A – is the Symmetric Gaussian model, B – Asymmetric Gaussian model, C – Symmetric Lorentzian model, D – Asymmetric Lorentzian model, E – Lorentzian-Gaussian sum model, F – Lorentzian-Gaussian sum model, G – Symmetric Pseudo-Voigt model, H – Asymmetric Pseudo-Voigt model.

7.6.1.2. ν_4 vibrational mode peak

Type	Fitting error squared	Ratio to the minimum
Symmetric Gaussian	2.09E+03	1.00
Asymmetric Gaussian	2.09E+03	1.00
Symmetric Lorentzian	2.41E+03	1.16
Asymmetric Lorentzian	2.41E+03	1.16
Symmetric Pseudo-Voigt	2.26E+03	1.08
Asymmetric Lorentzian Gaussian linear sum	2.25E+03	1.08
Asymmetric Lorentzian Gaussian product	2.09E+03	1.00
Asymmetric Pseudo-Voigt	2.89E+03	1.39

Table 7.5 A comparison of models of the ν_4 vibrational mode peak in a spectrum of dry calcite. The ratio to the minimum demonstrates the ratio between the value of the sum of least squares and the smallest value among the compared models.



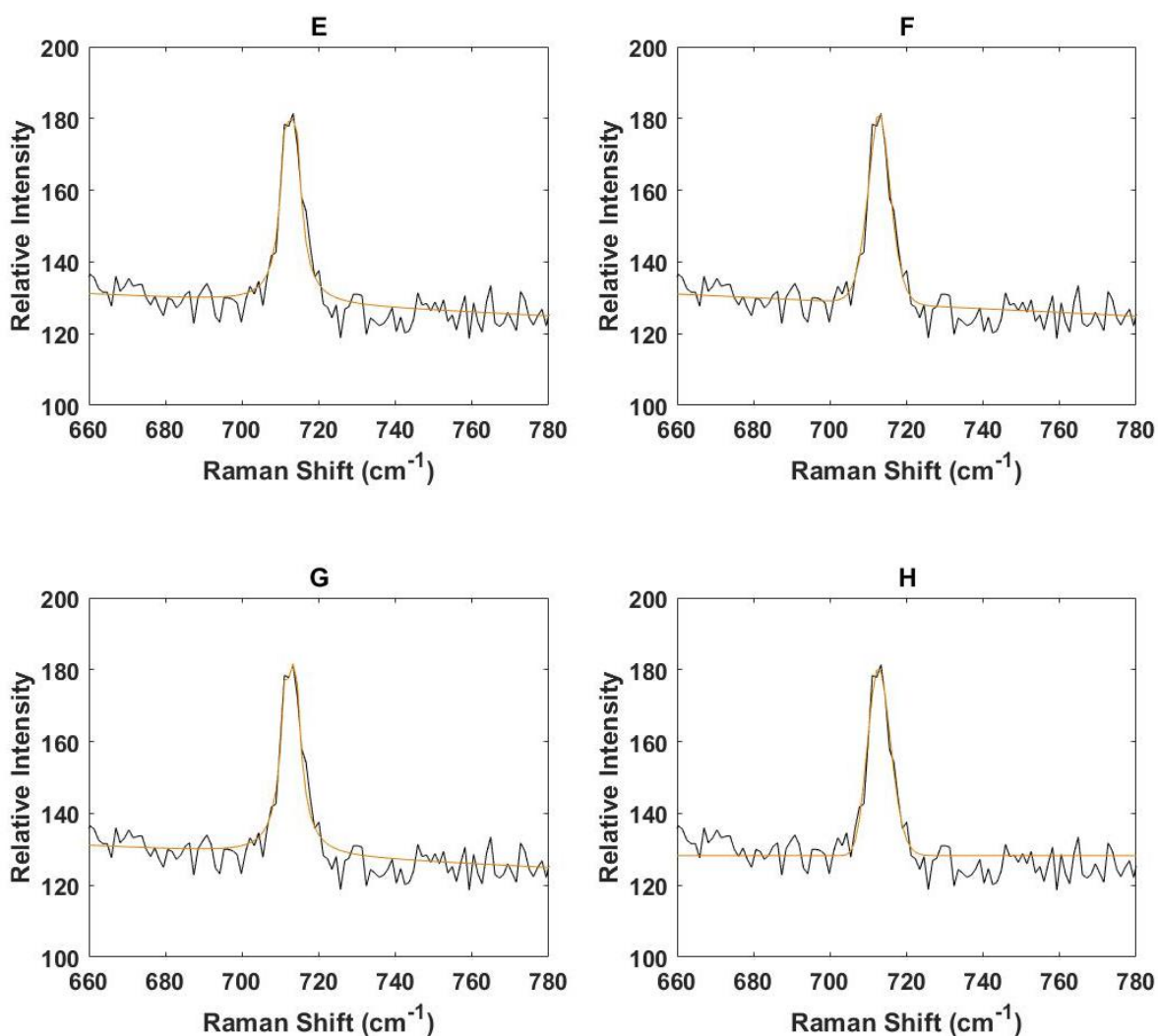


Figure 7.12 Graphs of the different of models of the v_4 vibrational mode peak in a spectrum of dry calcite compared in the table 7.5. The black line is the experimental spectrum and the yellow line is the theoretical model. A – is the Symmetric Gaussian model, B – Asymmetric Gaussian model, C – Symmetric Lorentzian model, D – Asymmetric Lorentzian model, E – Lorentzian-Gaussian sum model, F – Lorentzian-Gaussian sum model, G – Symmetric Pseudo-Voigt model, H – Asymmetric Pseudo-Voigt model.

7.6.2. Vaterite model

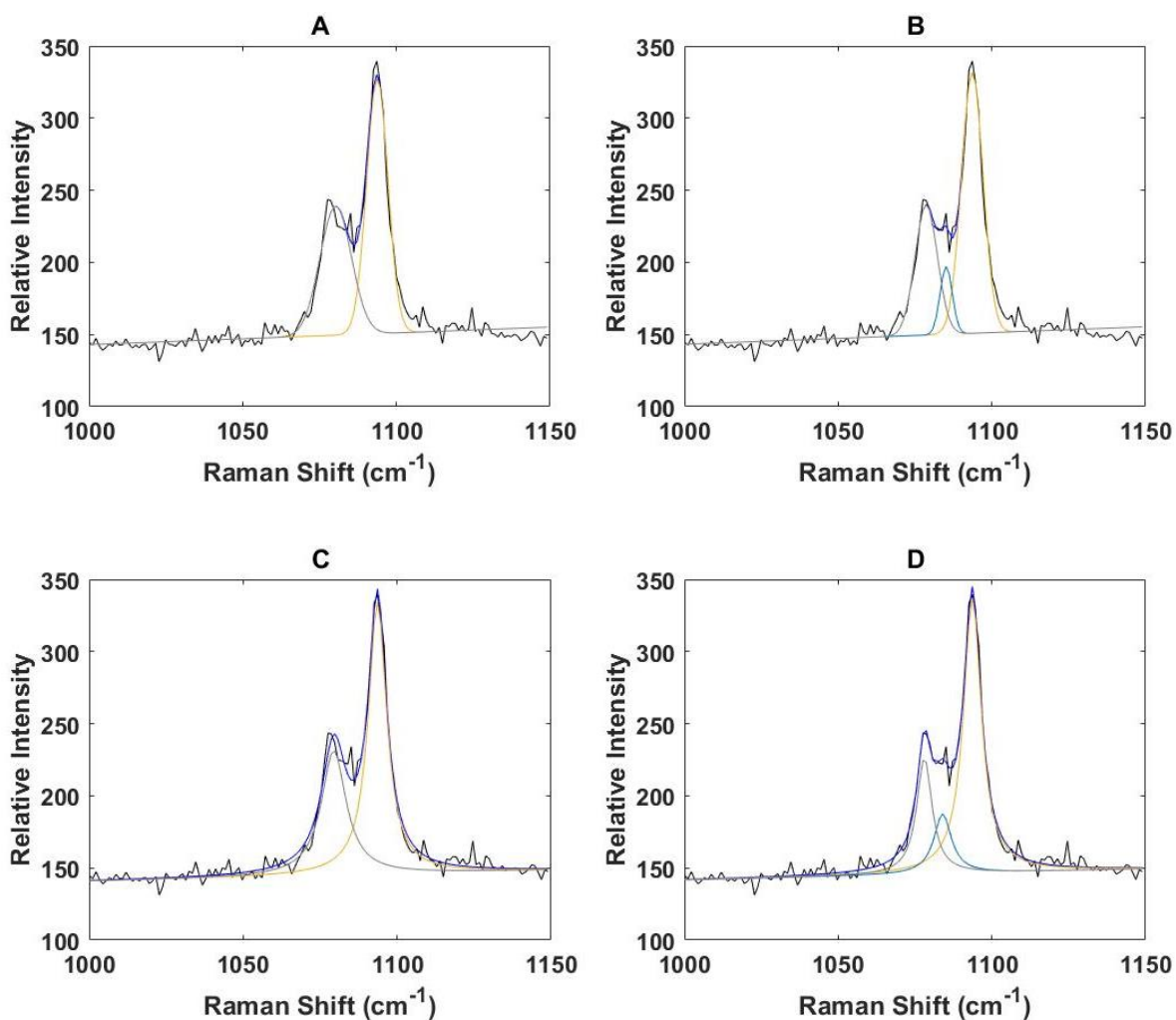
One of the complexities of modelling vaterite is the characteristic v_1 vibrational mode peak structure that is comprised of multiple peaks. Depending on the literature the peak is described as a double or triple peak, which may be due to the accuracy of the model used, quality of the experimental data and the crystallinity of the vaterite crystal. A similar discrepancy has been highlighted in theoretical calculations by de

Leeuw and Parker, when the idealised and the model that includes structural defects. Therefore, before determining the correct modes to describe the different peaks, an appropriate model needs to be selected.

7.6.2.1. Peak multiples: 2 vs 3

Type	Fitting error squared	Ratio to the minimum
2 Symmetric Gaussian	5.64E+03	2.06
3 Symmetric Gaussian	4.81E+03	1.75
2 Symmetric Lorentzian	4.04E+03	1.47
3 Symmetric Lorentzian	2.74E+03	1.00
2 Asymmetric Pseudo-Voigt	3.88E+03	1.41
3 Asymmetric Pseudo-Voigt	2.90E+03	1.06

Table 7.6 A table of 2 and 3 peak models of vaterite, compared using the sum of least squares value. The ratio to the minimum demonstrates the ratio between the value of the sum of least squares and the smallest value among the compared models.



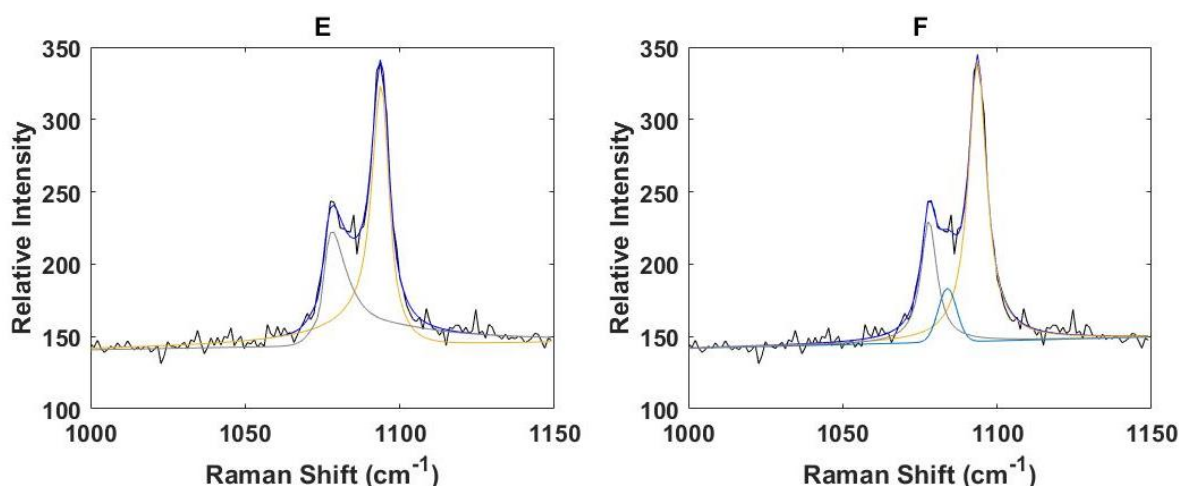


Figure 7.13 A graphs of 2 and 3 peak models fitted to the experimental data of a vaterite peak. The comparison is summarised in table 7.6. The black line is the experimental spectrum, the dark blue line is the total theoretical model, and the yellow, grey and light blue lines are the different peaks within the total theoretical model. A – is the Symmetric Gaussian model, B – Asymmetric Gaussian model, C – Symmetric Lorentzian model, D – Asymmetric Lorentzian model, E – Lorentzian-Gaussian sum model, F – Lorentzian-Gaussian sum model.

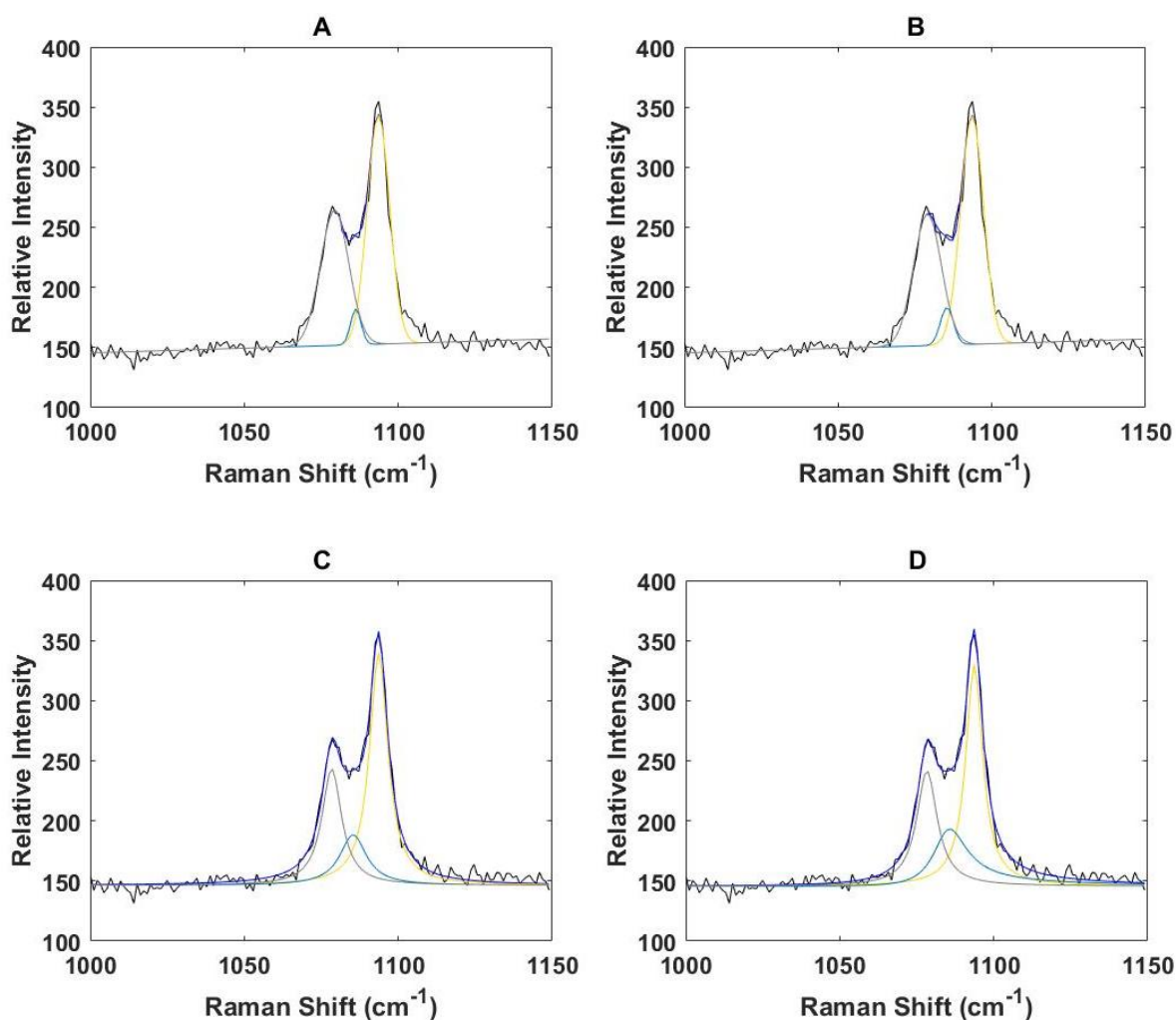
7.6.2.2. Frame 1400

Type	Fitting error squared	Ratio to the minimum
Symmetric Gaussian	5.45E+03	1.94
Asymmetric Gaussian	5.67E+03	2.01
Symmetric Lorentzian	3.54E+03	1.26
Asymmetric Lorentzian	3.15E+03	1.12
Symmetric Pseudo-Voigt	2.82E+03	1.00
Asymmetric Lorentzian Gaussian linear sum	3.32E+03	1.18
Asymmetric Lorentzian Gaussian product	3.24E+03	1.15
Asymmetric Pseudo-Voigt	2.82E+03	1.00

Table 7.7 A comparison of the different models used for modelling vaterite after ~20 min after the reaction between CaCl_2 and Na_2CO_3 in an aerosol droplet. The ratio to the minimum demonstrates the ratio between the value of the sum of least squares and the smallest value among the compared models.

Background	94.19	Slope	0.05
	Peak 1	Peak 2	Peak 3
Position	1093.73	1083.09	1078.14
Gaussian Intensity	0.00	50.52	0.00
Gaussian FWHM	1.69	10.74	2.30
Lorentzian Intensity	191.73	124.81	70.42
Lorentzian FWHM	14.40	0.00	14.88
Asymmetry	0	0	0
Ratio	1	0	1

Table 7.8 A table of the peak parameters of the asymmetric Pseudo-Voigt model in table 7.7. The asymmetry parameter demonstrates that the peak is symmetric, and the ratio of the peaks demonstrate a Lorentzian-Gaussian-Lorentzian profile pattern.



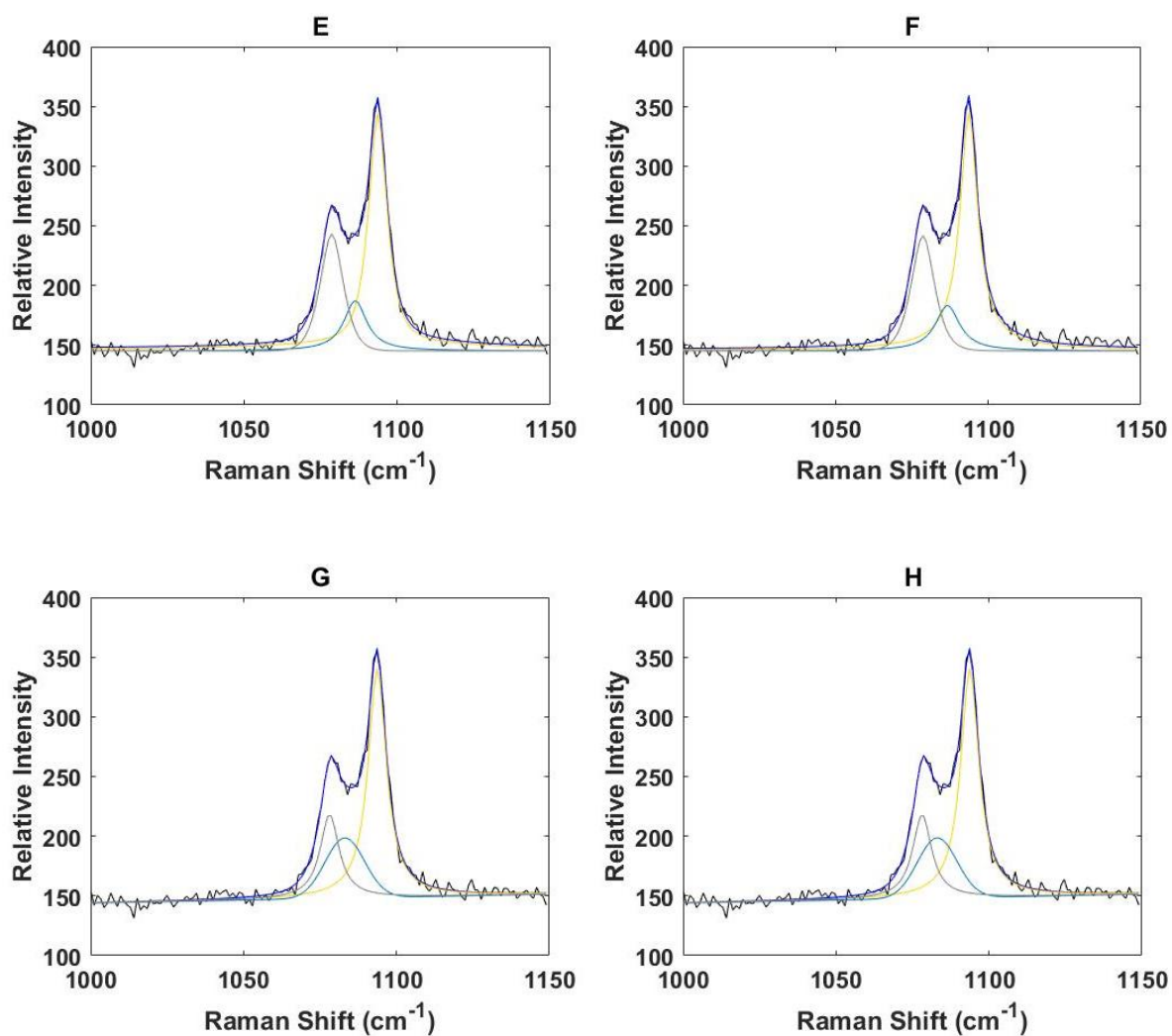


Figure 7.14 Graphs of the different models used for modelling vaterite after ~20 min after the reaction between CaCl_2 and Na_2CO_3 in an aerosol droplet. The data is summarised in table 7.7. The black line is the experimental spectrum, the dark blue line is the total theoretical model, and the yellow, grey and light blue lines are the different peaks within the total theoretical model. A – is the Symmetric Gaussian model, B – Asymmetric Gaussian model, C – Symmetric Lorentzian model, D – Asymmetric Lorentzian model, E – Lorentzian-Gaussian sum model, F – Lorentzian-Gaussian sum model, G – Symmetric Pseudo-Voigt model, H – Asymmetric Pseudo-Voigt model.

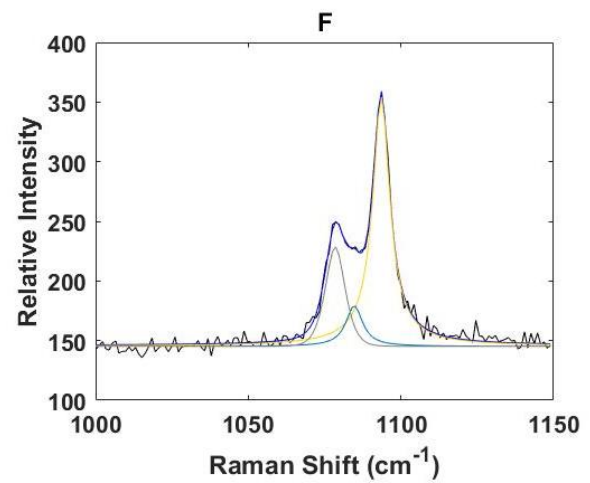
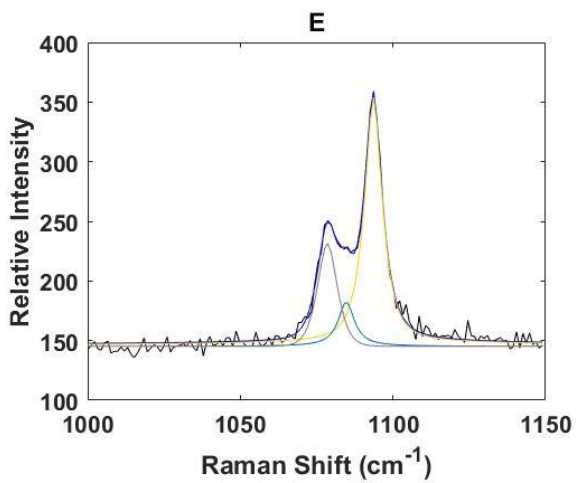
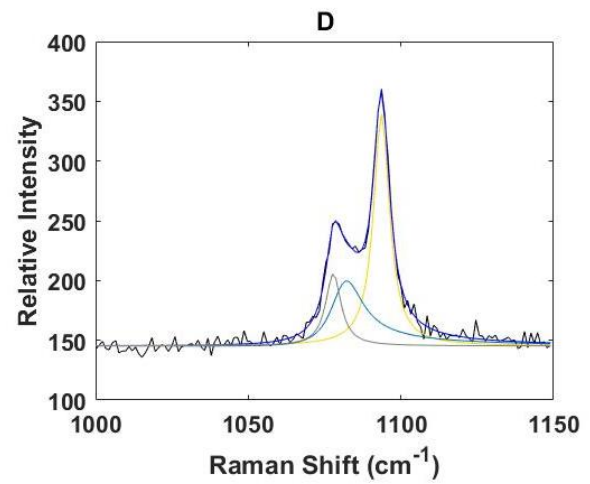
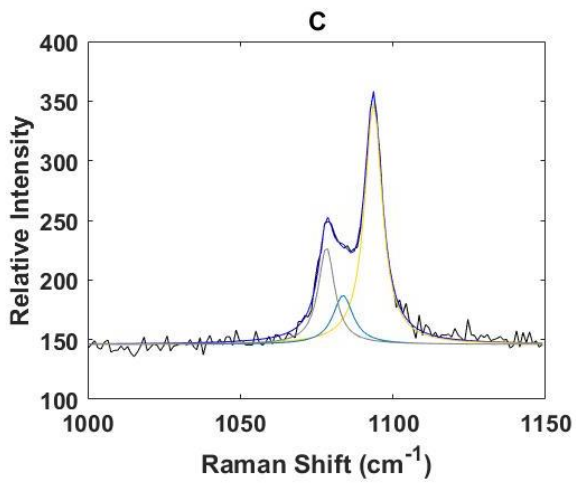
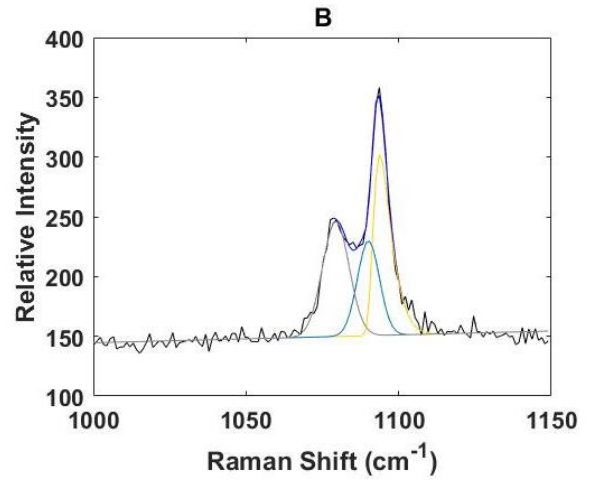
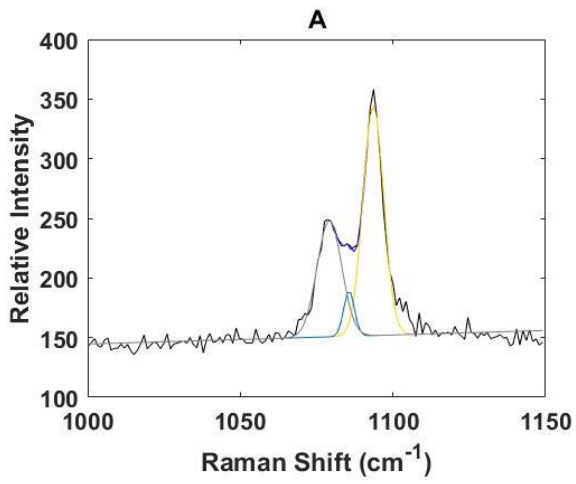
7.6.2.3. Frame 5000

Type	Fitting error squared	Ratio to the minimum
Symmetric Gaussian	5.81E+03	2.21
Gaussian asymmetric	4.09E+03	1.55
Symmetric Lorentzian	3.19E+03	1.21
Lorentzian asymmetric	2.78E+03	1.06
Symmetric Pseudo-Voigt	2.63E+03	1.00
Asymmetric Lorentzian Gaussian linear sum	3.27E+03	1.24
Asymmetric Lorentzian Gaussian product	2.99E+03	1.13
Asymmetric Pseudo-Voigt	2.63E+03	1.00

Table 7.9 A comparison of the different models used for modelling vaterite after ~1 h 20 min after the reaction between CaCl_2 and Na_2CO_3 in an aerosol droplet. The ratio to the minimum demonstrates the ratio between the value of the sum of least squares and the smallest value among the compared models.

Background	97.32	Slope	0.05
	Peak 1	Peak 2	Peak 3
Position	1093.73	1083.09	1078.14
Gaussian Intensity	0.00	0.00	0.00
Gaussian FWHM	10.53	2.30	4384.18
Lorentzian Intensity	0.00	76.53	0.00
Lorentzian FWHM	23.05	13.58	0.00
Asymmetry	0	0	0
Ratio	1	0	1

Table 7.10 A table of the peak parameters of the asymmetric Pseudo-Voigt model in table 7.9. The asymmetry parameter demonstrates that the peak is symmetric, and the ratio of the peaks demonstrate a Lorentzian-Gaussian-Lorentzian profile pattern.



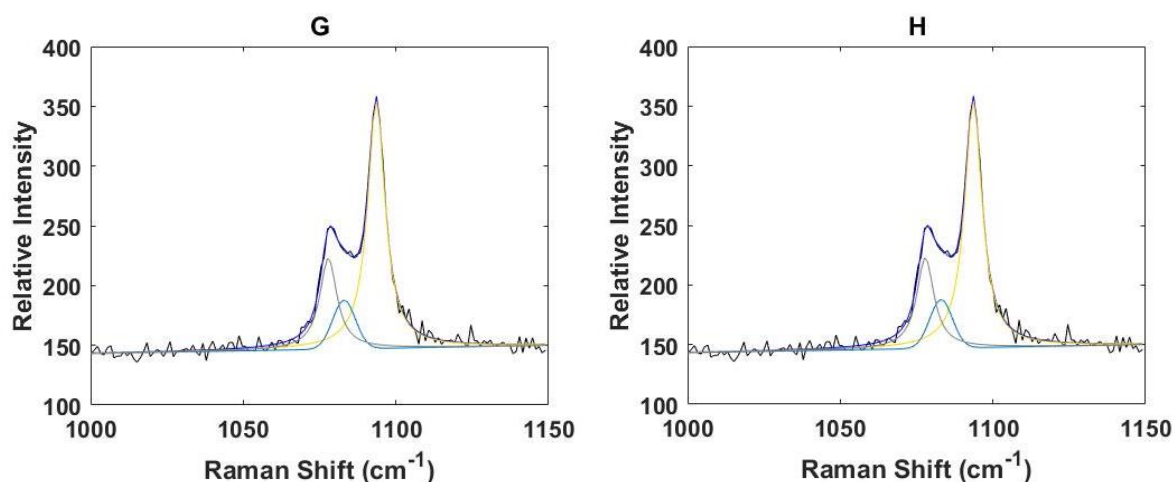


Figure 7.15 Graphs of the different models used for modelling vaterite after ~1 h 20 min after the reaction between CaCl_2 and Na_2CO_3 in an aerosol droplet. The data is summarised in table 7.9. The black line is the experimental spectrum, the dark blue line is the total theoretical model, and the yellow, grey and light blue lines are the different peaks within the total theoretical model. A – is the Symmetric Gaussian model, B – Asymmetric Gaussian model, C – Symmetric Lorentzian model, D – Asymmetric Lorentzian model, E – Lorentzian-Gaussian sum model, F – Lorentzian-Gaussian sum model, G – Symmetric Pseudo-Voigt model, H – Asymmetric Pseudo-Voigt model.

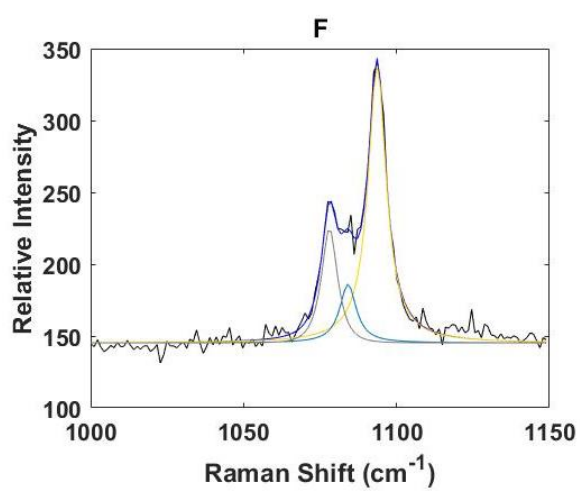
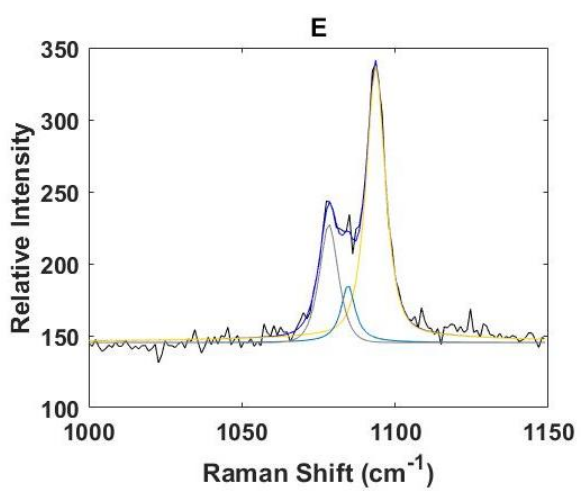
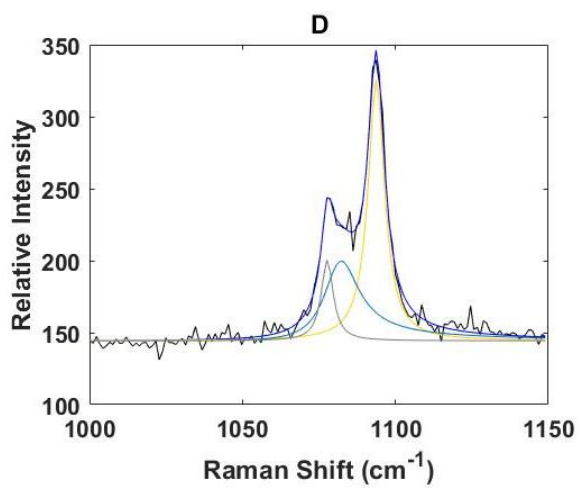
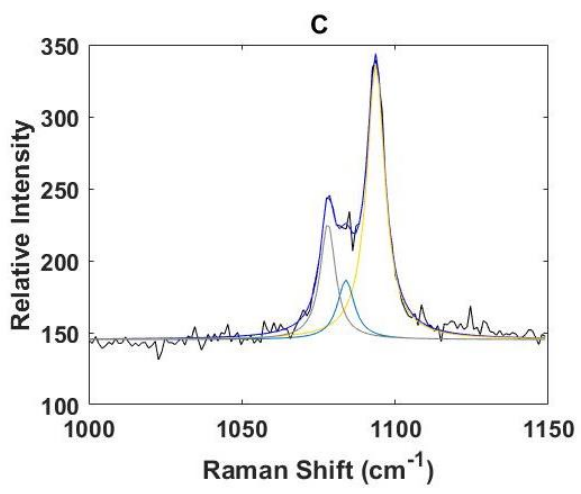
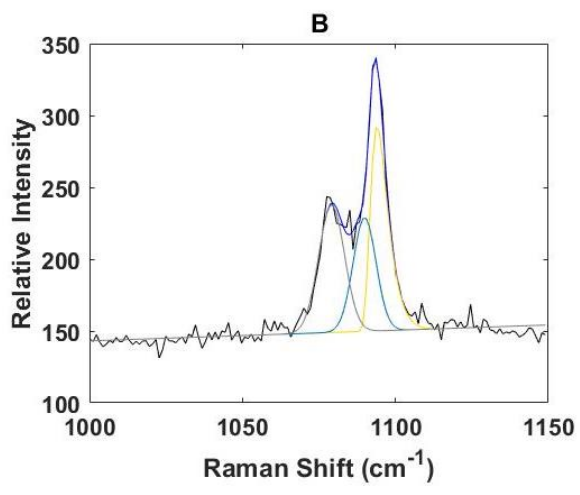
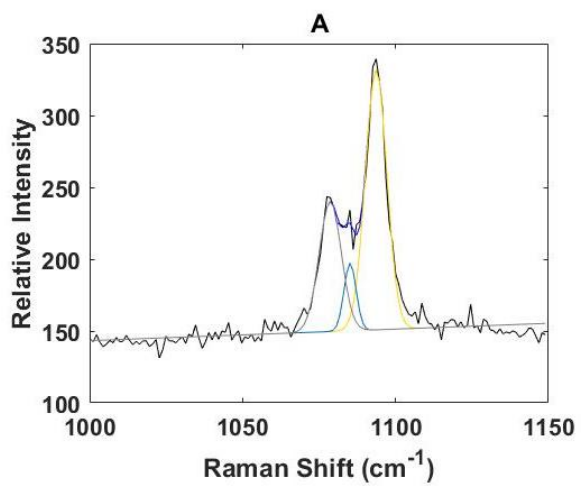
7.6.2.4. Frame 11570

Type	Fitting error squared	Ratio to the minimum
Symmetric Gaussian	4.81E+03	1.75
Gaussian asymmetric	3.99E+03	1.45
Symmetric Lorentzian	3.41E+03	1.24
Lorentzian asymmetric	3.12E+03	1.13
Symmetric Pseudo-Voigt	2.76E+03	1.00
Asymmetric Lorentzian Gaussian linear sum	3.54E+03	1.28
Asymmetric Lorentzian Gaussian product	3.49E+03	1.27
Asymmetric Pseudo-Voigt	2.76E+03	1.00

Table 7.11 A comparison of the different models used for modelling vaterite after ~3 h 20 min after the reaction between CaCl_2 and Na_2CO_3 in an aerosol droplet.

Background	89.37	Slope	0.05
	Peak 1	Peak 2	Peak 3
Position	1093.73	1083.09	1078.14
Gaussian Intensity	0.00	37.28	0.00
Gaussian FWHM	1.69	4.97	2.30
Lorentzian Intensity	194.96	124.81	84.57
Lorentzian FWHM	14.19	0.00	12.33
Asymmetry	0	0	0
Ratio	1	0	1

Table 7.12 A table of the peak parameters of the asymmetric Pseudo-Voigt model in table 7.11. The asymmetry parameter demonstrates that the peak is symmetric, and the ratio of the peaks demonstrate a Lorentzian-Gaussian-Lorentzian profile pattern.



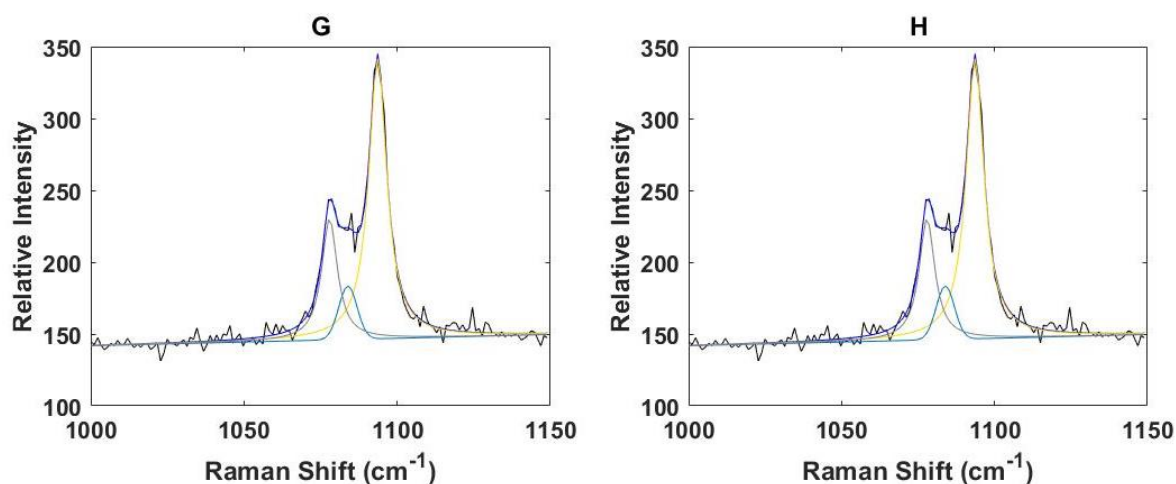


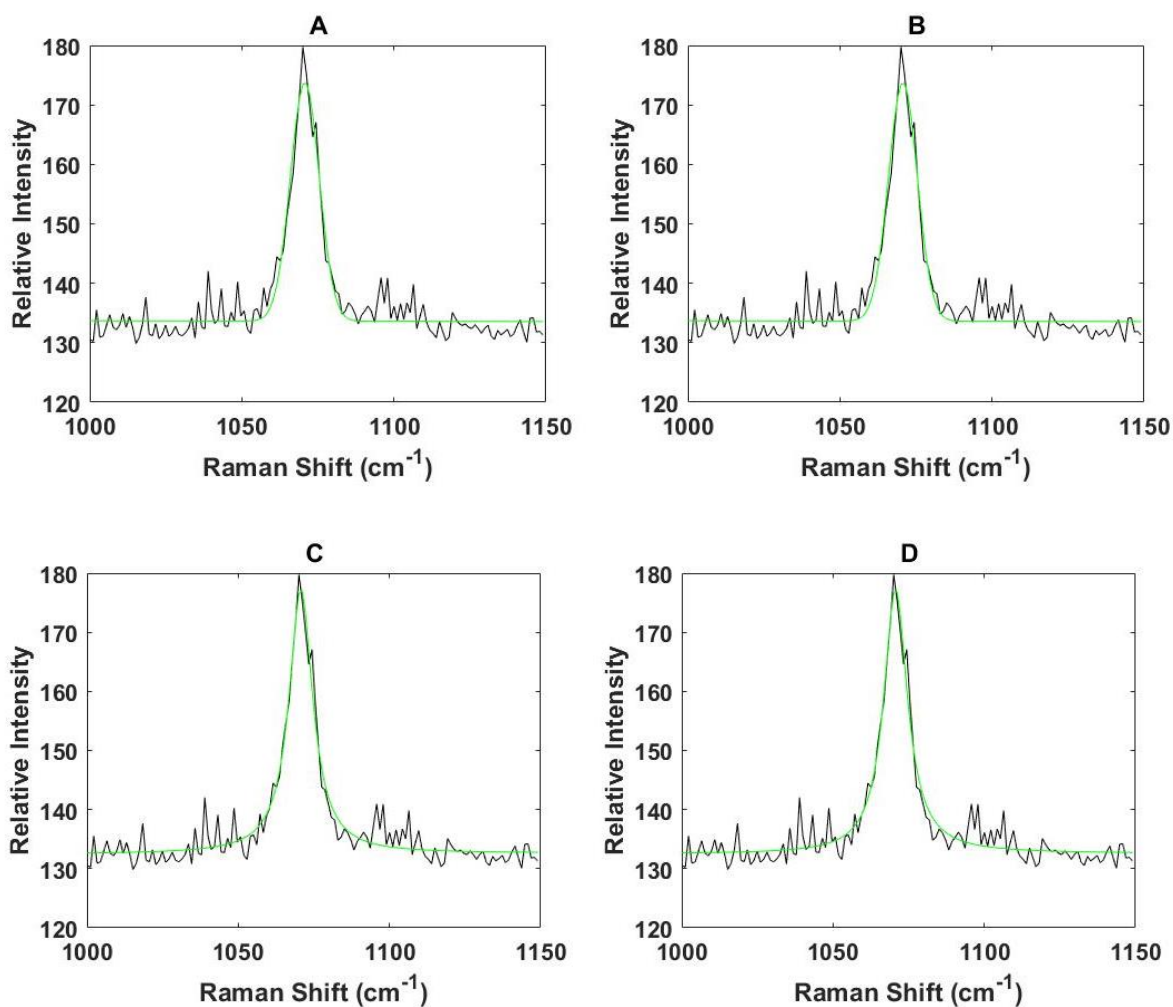
Figure 7.16 Graphs of the different models used for modelling vaterite after ~1 h 20 min after the reaction between aqueous CaCl_2 and aqueous Na_2CO_3 through coalescence of aerosol droplets. The data is summarised in table 7.11. The black line is the experimental spectrum, the dark blue line is the total theoretical model, and the yellow, grey and light blue lines are the different peaks within the total theoretical model. A – is the Symmetric Gaussian model, B – Asymmetric Gaussian model, C – Symmetric Lorentzian model, D – Asymmetric Lorentzian model, E – Lorentzian-Gaussian sum model, F – Lorentzian-Gaussian sum model, G – Symmetric Pseudo-Voigt model, H – Asymmetric Pseudo-Voigt model.

7.6.3. Carbonate ion model

The carbonate ion is another important component of the total theoretical model, as it is a product of dissolution of sodium carbonate.

Type	Fitting error squared	Ratio
Symmetric Gaussian	8.68E+02	1.30
Asymmetric Gaussian	8.68E+02	1.30
Symmetric Lorentzian	7.01E+02	1.05
Asymmetric Lorentzian	7.00E+02	1.05
Symmetric Pseudo-Voigt	6.67E+02	1.00
Asymmetric Lorentzian Gaussian linear sum	6.91E+02	1.04
Asymmetric Lorentzian Gaussian product	7.09E+02	1.06
Asymmetric Pseudo-Voigt	6.66E+02	1.00

Table 7.13 A comparison of models of the CO_3^{2-} ion an optically tweezed aerosol droplet of aqueous Na_2CO_3 v1 vibrational peak.



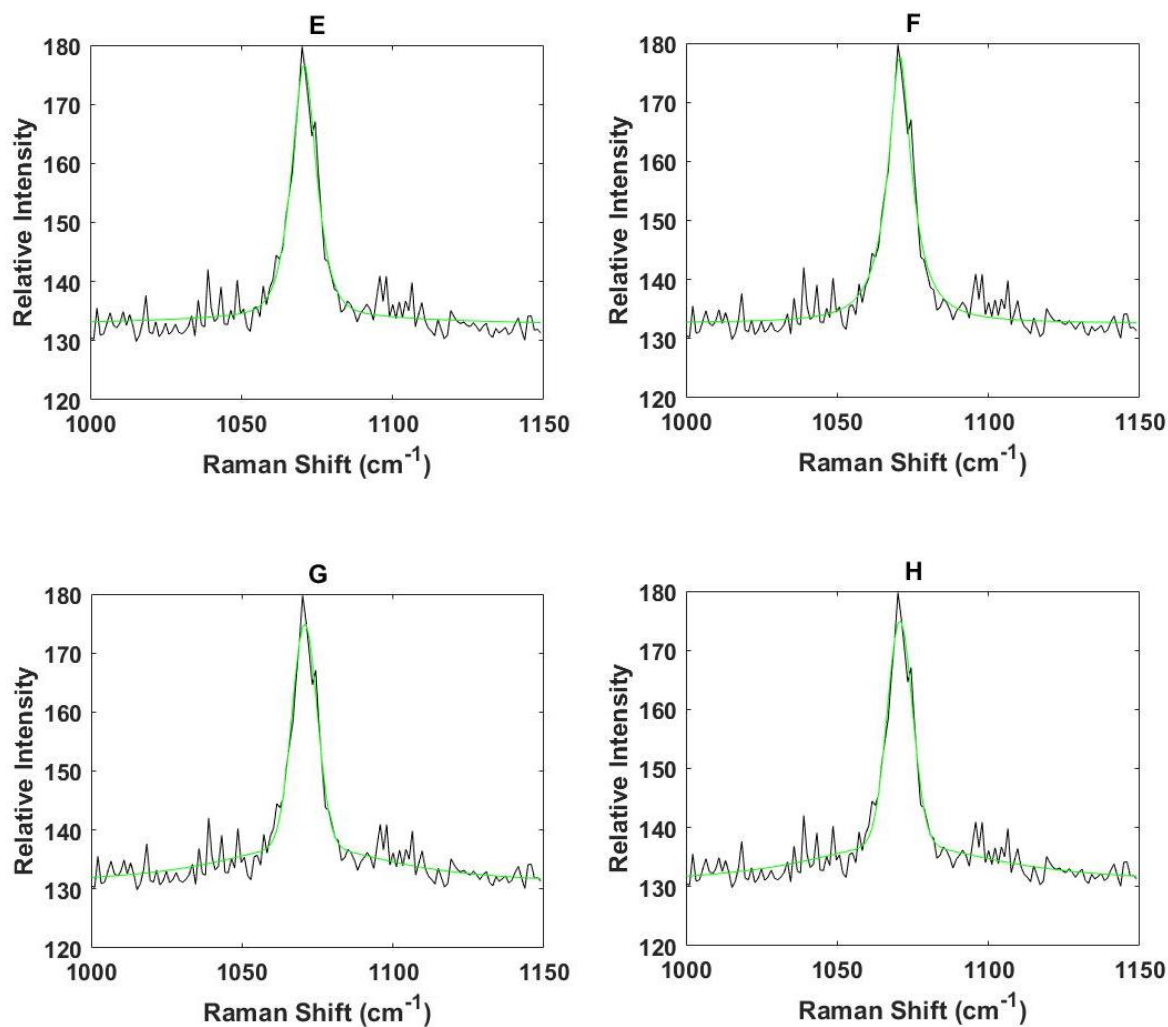


Figure 7.17 Graphs of the ν_4 vibrational mode of C-O bond in an optically tweezed aerosol droplet of aqueous Na_2CO_3 . The black line is the experimental spectrum and the green line is the theoretical model. A – is the Symmetric Gaussian model, B – Asymmetric Gaussian model, C – Symmetric Lorentzian model, D – Asymmetric Lorentzian model, E – Lorentzian-Gaussian sum model, F – Lorentzian-Gaussian sum model, G – Symmetric Pseudo-Voigt model, H – Asymmetric Pseudo-Voigt model.

7.7. Total model

Therefore, the total of theoretical model used to fit the spectra is:

Polymorph	Line profile
Calcite	Asymmetric Pseudo-Voigt
Vaterite	Symmetric Lorentzian
Vaterite	Symmetric Gaussian
Vaterite	Symmetric Lorentzian
CO ₃ ²⁻	Asymmetric Lorentzian
Amorphous calcium carbonate	Symmetric Gaussian

Table 7.14 A table summarising the theoretical model used to analyse the experimental spectra of the chemical reaction in chapter 8.

7.8. Conclusions

Raman spectroscopy is a powerful tool for analysing the chemical composition of materials and solutions, that could be linked to the structural properties of crystals, molecular ions and solutions. Raman spectroscopy is also extremely sensitive to changes in their local environment, which can be a useful tool in analysing the vibrational structure of water contained in hydrated crystals.

There are a number of different physical factors that can influence the appearance of a peak. These factors include but are not limited to temperature, natural broadening and pressure broadening. These effects have different contribution profiles with Gaussian and Lorentzian profiles, which combine to form the Voigt profile. These profiles can occur in two different types of broadening, the homogeneous and the inhomogeneous broadening which reflect the phase and the part of the material the is being analysed.

Statistical modelling and mathematical optimization are extremely powerful tools that can be used in combination with spectroscopic techniques. The application statistical models to spectroscopic data allows decomposing the data into its constituents, allowing to uncover the details of the composition of materials. Mathematical optimisation is a key tool aiding statistical modelling, allowing to accurately find solutions, fitting complex mathematical models and as it is a computational tool it can be run many times in succession, in practice allowing the analysis of large amounts of data. This makes statistical analysis invaluable in the analysis of chemical reactions, as the materials can be looked at in terms of their composition and their physical properties, such as the crystallinity of the formed material.

Chapter 8 Forming calcium carbonate. Data and a conjecture.

The end goal of any theoretical model is to describe the processes happening in practice and provide insight into the mechanisms governing these processes. Hence, the model discussed in chapter 6 that describes a way of modelling the different polymorphs of calcium carbonate and the CO_3^{2-} ion, along with the mathematical techniques provide a powerful toolkit, which is necessary for the analysis of complex chemical reactions. As previously mentioned, one of such reactions is the formation of calcium carbonate, with its different possible polymorphs. Other implications of the importance of this chemical reaction were mentioned in chapters 1 and 6, which talk about the importance of calcium carbonate in biological processes.

8.1. Literature

As mentioned earlier in this chapter there are multiple studies published looking at the formation and polymorphic transitions of calcium carbonate. Some of the key publications focus on the influence of temperature, pH and ions other than the ones present in aqueous solutions of CaCl_2 and Na_2CO_3 . Such changes can have significant effects on the polymorphic composition. It is also possible to use temperature to transform polymorphs in dry samples^[60] and identify the presence of proto-polymorphs in the amorphous calcium carbonate. ^[214–216]

8.1.1. Temperature

At present there have been many studies on the reaction mechanisms of formation of different polymorphs of CaCO_3 , studied using a vast array of techniques such as molecular simulations, x-ray techniques, infrared spectroscopy, Raman spectroscopy, NMR and cryo-electron microscopy. There was a debate regarding the mechanism of polymorph transformation, specifically whether it happens via a direct solid transition or via a dissolution - re-precipitation mechanism.^[59]

This debate was considered by T.Ogino et.al.^[59], where the conjecture was made that the transformation occurs via the dissolution - re-precipitation mechanism, although it was outlined that this may not be the actual case.^[59]

The same paper looks at the formation of calcite, vaterite and aragonite polymorphs at different temperatures. An interesting observation was made that aragonite does not form at room temperature, which leads to the conclusion that the production of aragonite during the chemical reaction between CaCl_2 and Na_2CO_3 in an optically tweezed aerosol droplet is unlikely, unless the droplet is heated up significantly by the trapping laser. Another observation made in the same paper is that both calcite and vaterite are converted in to calcite, which proves the stability of the calcite polymorph.^[59]

8.1.2. pH, ions and drying

The presence of ions during the chemical reaction particularly well studied are the Mg^{2+} ions and phosphate ions (PO_4^{2-}). A particularly interesting study was done by Hu et. al., which examined the influence of alkaline pH conditions and the presence of phosphate ion on the formation of vaterite and ikaite polymorphs. A conclusion reached in that publication:^[62]

“Both pH and phosphate contribute to the polymorph switch between vaterite and ikaite. At moderate alkaline conditions, formation of ikaite is favoured over vaterite in the presence of phosphate; at high alkaline conditions, no phosphate is needed to trigger ikaite formation. “

– Hu et.al., “Effect of pH and Phosphate on Calcium Carbonate Polymorphs Precipitated at near-Freezing Temperature”, *Crystal Growth & Design* (2015).^[62]

The pH values examined in that paper were pH 9 and pH 13.4, which indicates that the pH of the solution will have a significant impact on the formed polymorph. (see Figure 8.1) The influence of pH has also been noted in the presence of pre-nucleation clusters in ACC (Amorphous Calcium carbonate).^[62]

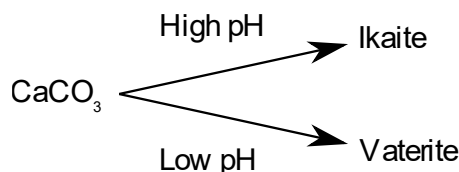


Figure 8.1 A mechanism of the reaction explored in by Hu et.al. 2015. In the paper it was demonstrated that the presence of PO_4^{2-} ions had allowed ikaite to form at a lower pH. Here high pH is pH 13.4 and low pH is pH 9.

It is also possible to force a dry polymorph ikaite (monohydrocalcite) in to vaterite by heating up the sample. This dries the sample out, forcing the ikaite to evaporate the water from within the crystalline structure, and forcing the now anhydrous calcium carbonate to transform in to vaterite.^[60]

Another ion that is often present in $CaCO_3$ environments is the Mg^{2+} ions.^[82,217] It can often be found in minute amounts in mineral calcium carbonate samples. Magnesium, similarly to calcium can also form insoluble carbonate compounds, such as dolomite ($CaMg(CO_3)_2$)^[200,218], lansfordite ($MgCO_3 \cdot 5H_2O$)^[65], nesquehonite ($Mg(HCO_3)(OH) \cdot 2H_2O$)^[65]. This again demonstrates the influence of the presence of ions in the formation of calcium carbonates and carbonate materials in general.^[82,217]

8.1.3. Computational studies

The formation of $CaCO_3$ is a complex reaction, making it interesting to study using computational studies. Among main aspects studied by computation were the surface solvation of the different polymorphs, the structural defects within the crystalline lattice and the potential mechanisms of reaction.^[212,217,219,220]

8.1.4. Solubility

There have been a few studies looking at the solubility of calcium carbonates in water in particular: calcite, vaterite, aragonite and ikaite. A general trend can be noticed that calcite ($pK_C = 8.48$)^[95] and aragonite ($pK_A = 8.34$)^[95] have a similar solubility, with vaterite ($\log K_V = -7.902$)^[221] having a slightly higher solubility than the calcite and aragonite, and ikaite ($\log K_V = -6.585$)^[70] being the most soluble

polymorph. It should be mentioned that all CaCO_3 polymorphs have extremely low solubility, and for most intents and purposes can be considered insoluble.^[70,200,222]

8.1.5. Biological and inorganic amorphous calcium carbonate

Multiple studies have presented data on the amorphous calcium carbonate polymorph of CaCO_3 . It is known that the ACC can have short range orders within the amorphous structure, which closely resemble the commonly known anhydrous polymorphs: calcite, aragonite and vaterite. Such proto-states have been experimentally found in biological systems.^[214] The proto polymorphs have also been found in inorganic systems. Prior to this work, the existence of proto-calcite has not been confirmed in the literature, as the reaction forming calcite directly from ACC.^[216] The presence of the proto-calcite is however predicted computationally.^[223]

8.2. Experimental results

8.2.1. Overview

In the experiments produced for this thesis the reaction followed one out of four pathways, namely formation of ikaite, forming stable vaterite, formation of calcite via vaterite, and direct formation of calcite. All of the reactions exemplified described in this part of the chapter were performed as described in chapter N. All of these reactions were continuously monitored in the AOT using Raman spectroscopy (at 1200 gr cm^{-1} grating resolution) from before the addition of the second reagent, CaCl_2 or Na_2CO_3 as appropriate. This was done to collect the maximum amount of data available with the instrumentation, ensuring that the reaction could be studied to the highest detail possible. The original data was collected at 1 s accumulation time and pre-processed to reduce the complexity of the analysis by averaging spectra in batches of 10, effectively reproducing a 10 second accumulation time.

8.2.2. Data

8.2.2.1. Direct formation of calcite

One of the main highlights of the data presented in this thesis is the data on the direct formation of vaterite which can be seen in Figure 8.2 (overall map of spectra of the chemical reaction) and Figure 8.3 (peak profile decomposition of select spectra from Figure 8.2). The combination of a highly pronounced ν_1 peak and visible ν_4 peak is used to identify the primary forming polymorph as calcite and demonstrate the formation of CaCO_3 from CO_3^{2-} ions. The jumps in the background intensity were caused by an increase in the laser power intensity, necessary to retain the aerosol droplet in the optical trap. The instability of the droplet was caused by the rearrangement of the CaCO_3 crystal aggregate. The decomposition of the individual spectra Figure 8.3 provides further insight into the reaction demonstrating that once calcite from Na_2CO_3 , confirming direct formation of calcite. Figure 8.3 A at 10 s recording demonstrates the a lack of a C-O stretch identifying the initial droplet composition as a CaCl_2 droplet. Figure 8.3 B spectrum was recorded after the addition of Na_2CO_3 solution to the initial droplet at ~310 s. Figure 8.3 C demonstrates that at 600 s (after 5 minutes) the chemical reaction has not yet started, as there is no major change in the position of the C-O peak. Figure 8.3 D recorded at 610 s demonstrates the chemical reaction occurring. Figure 8.3 E at 640 s shows that rapid chemical reaction had stopped, with calcite forming as the primary product, and suspectedly ACC forming as a byproduct of the reaction. Figure 8.3 F at 2500 s demonstrates the conversion of the ACC into calcite after the rapid formation of CaCO_3 had stopped. Figure 8.3 G at 12600 s demonstrates the stability of the formed calcite.

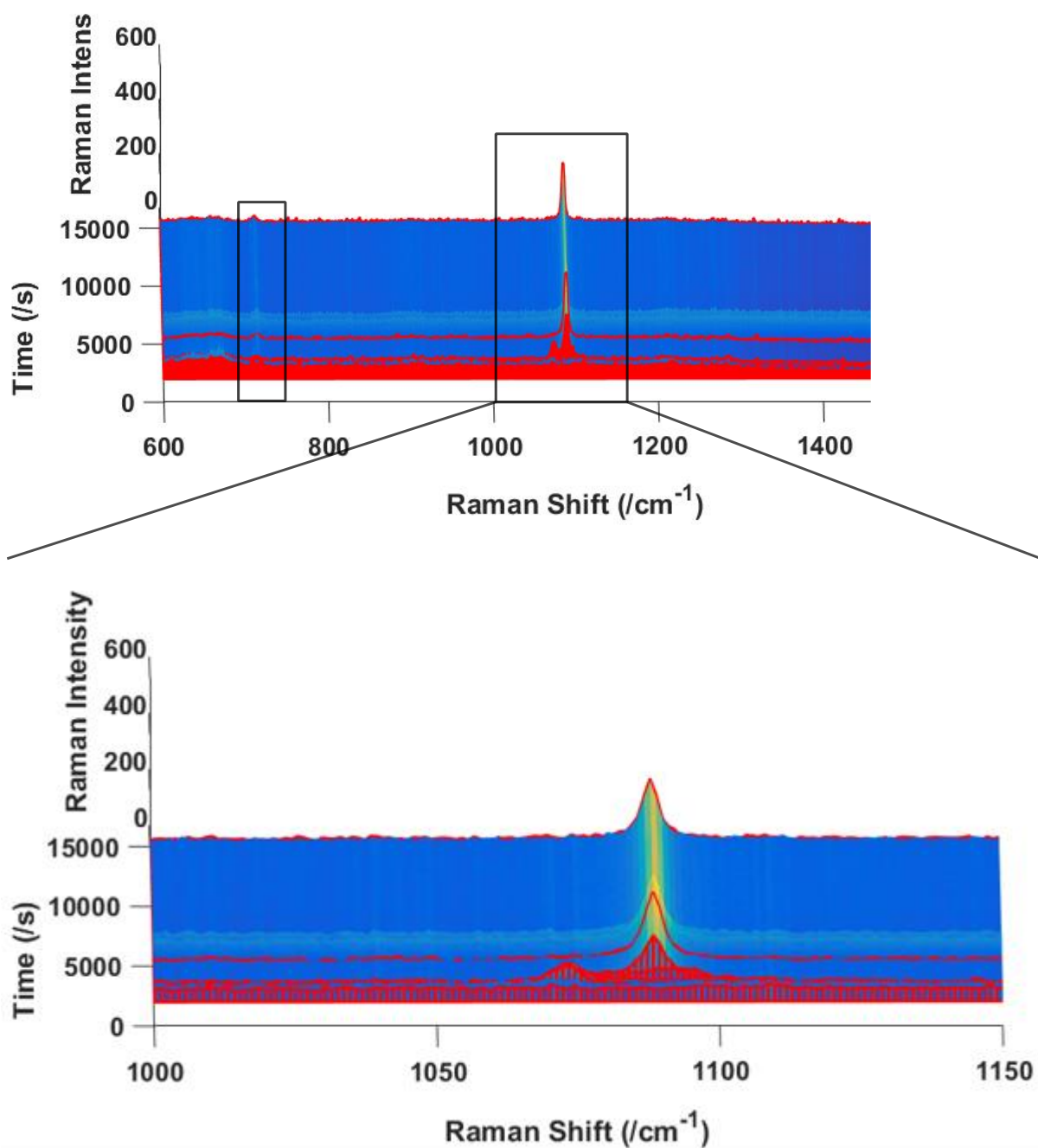


Figure 8.2 Maps of spectra of a reaction demonstrating the direct formation of calcite. The red highlights signify the representative spectra analysed in more detail in **Figure 8.3**. Top: a map of spectra with highlighted ν_1 and ν_4 peak locations of the C-O bond. The sharp peak at the Raman Shift corresponding to the ν_4 vibrational mode ($\sim 711 \text{ cm}^{-1}$) demonstrates the presence of calcite in the reaction. Bottom: the same map of spectra as the top image zoomed in on the ν_1 vibrational mode Raman shift.

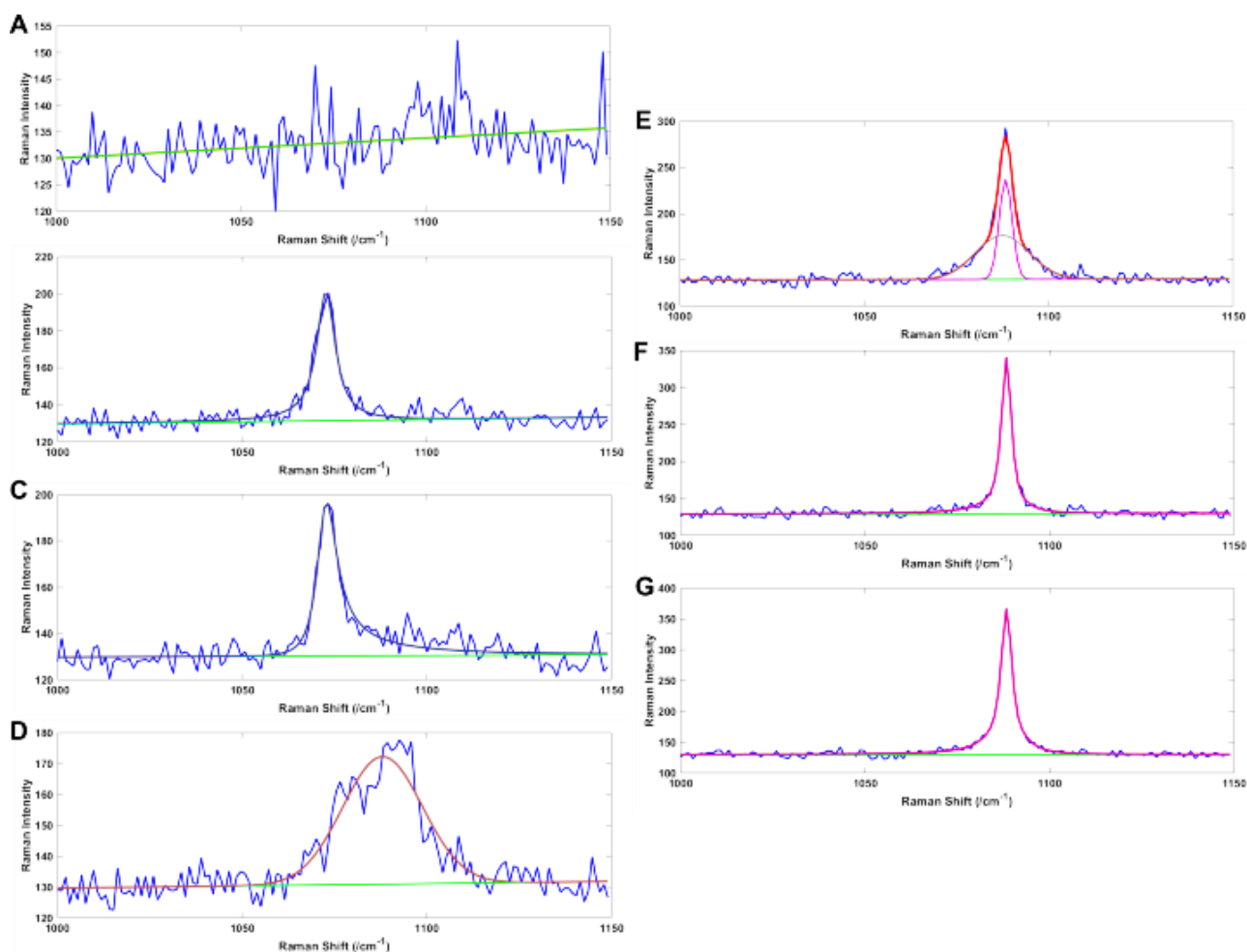


Figure 8.3 Spectroscopic decomposition of the highlighted individual spectra from **Figure 8.2**. The spectra A-G are arranged consecutively from the earliest to the the latest recorded in the experiment. In the decomposition blue is the experimental data, red is the total theoretical profile green is the background dark blue is the CO_3^{2-} peak; grey – ACC; purple – calcite. **A** at 10 s; **B** at 310 s. **C** at 600 s (after 5 minutes); **D** recorded at 610 s; **E** at 640 s; **F** at 2500 s; **G** at 12600 s.

8.2.2.2. Formation of calcite via vaterite

This was a common and well reported way of calcite formation, which serves to demonstrate that the observed direct formation of calcite in is not an anomaly, but a case of the same reaction happening near the boundary of possible reaction condition. In this specific case a large excess of CaCl_2 solution. Formation of calcite via vaterite can be seen in Figure 8.4 and

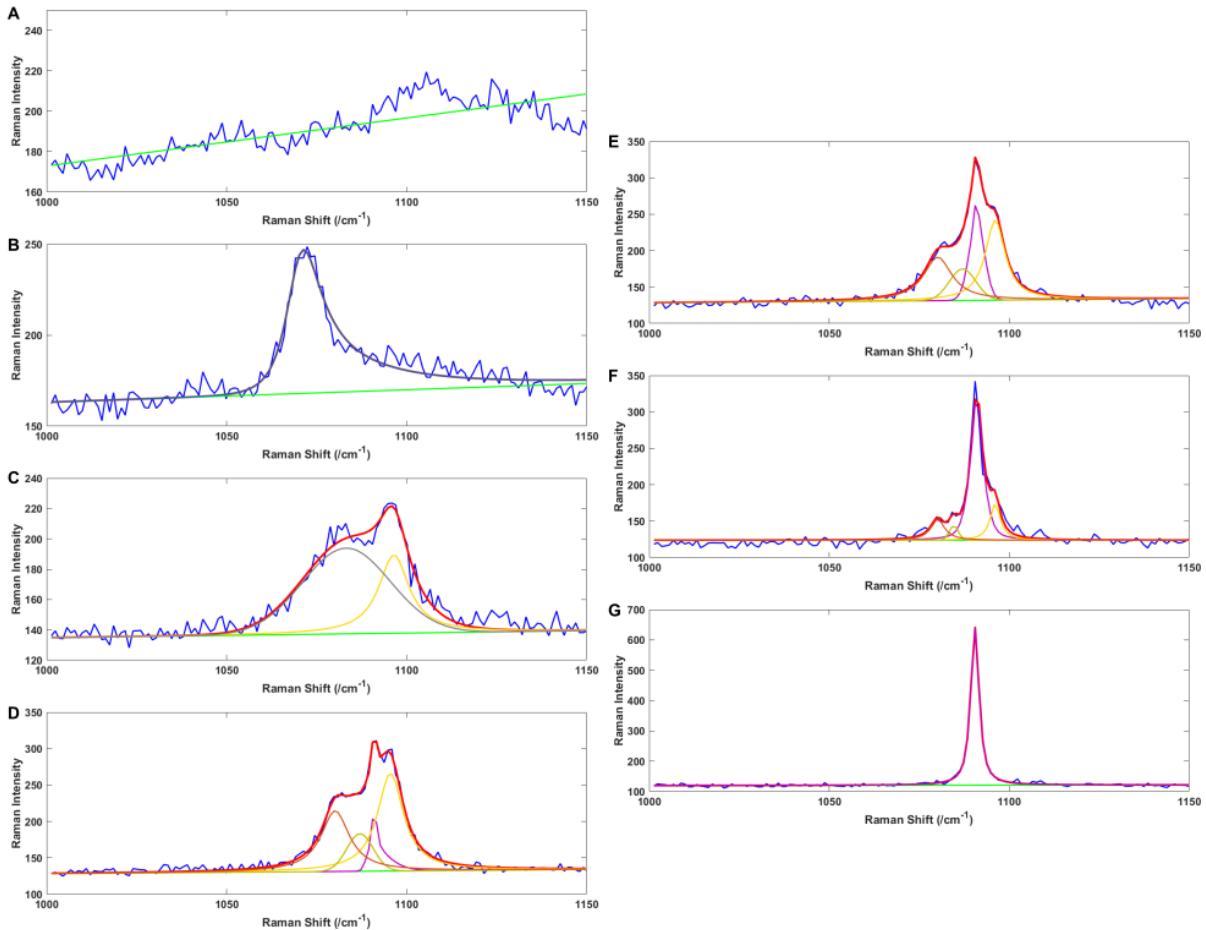


Figure 8.5. The appearance of the pronounced v4 peak and a single sharp v1 peak in Figure 8.4 confirm that the reaction's final product is calcite. The details that are easier to see in

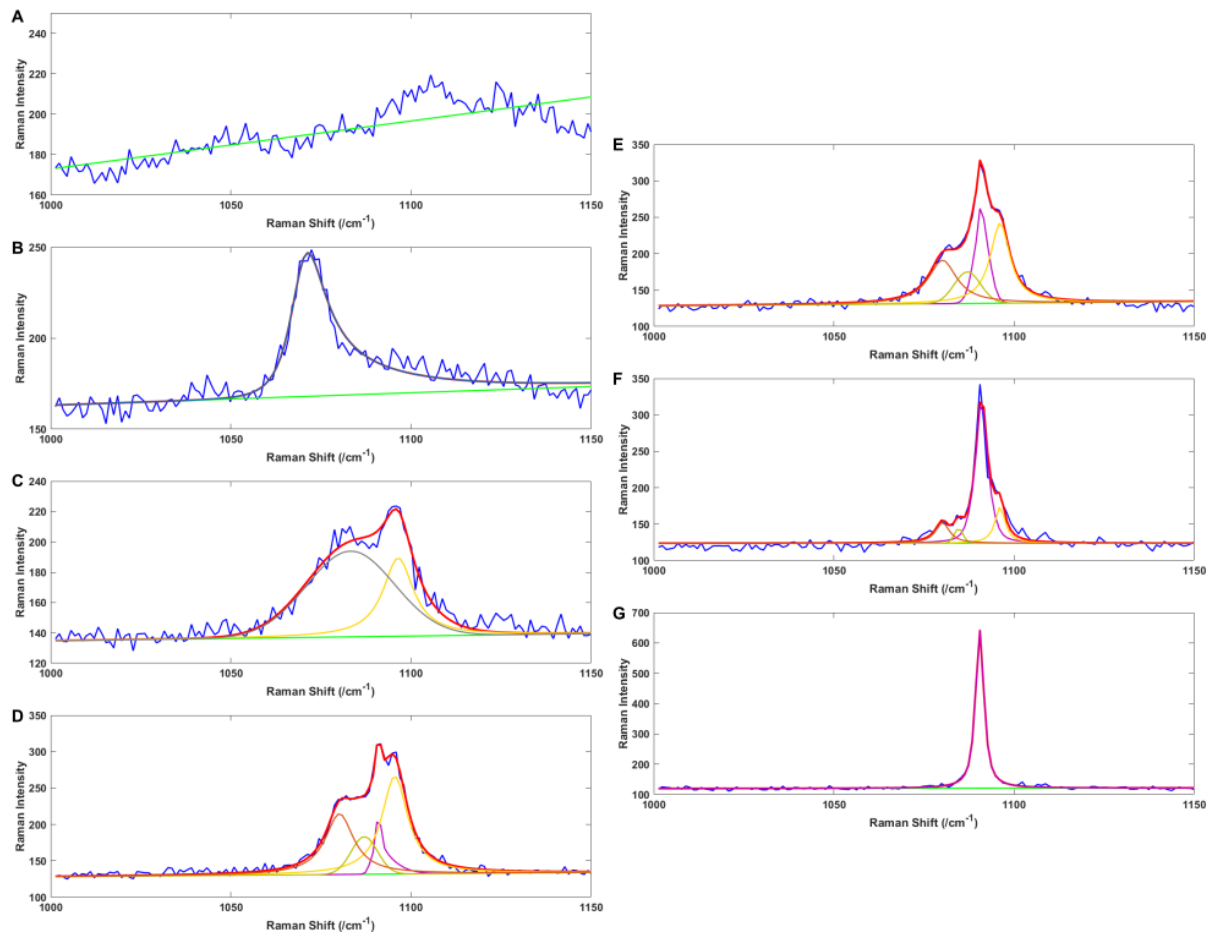


Figure 8.5 make it easier to identify that the primary polymorph is vaterite, which slowly transforms into calcite.

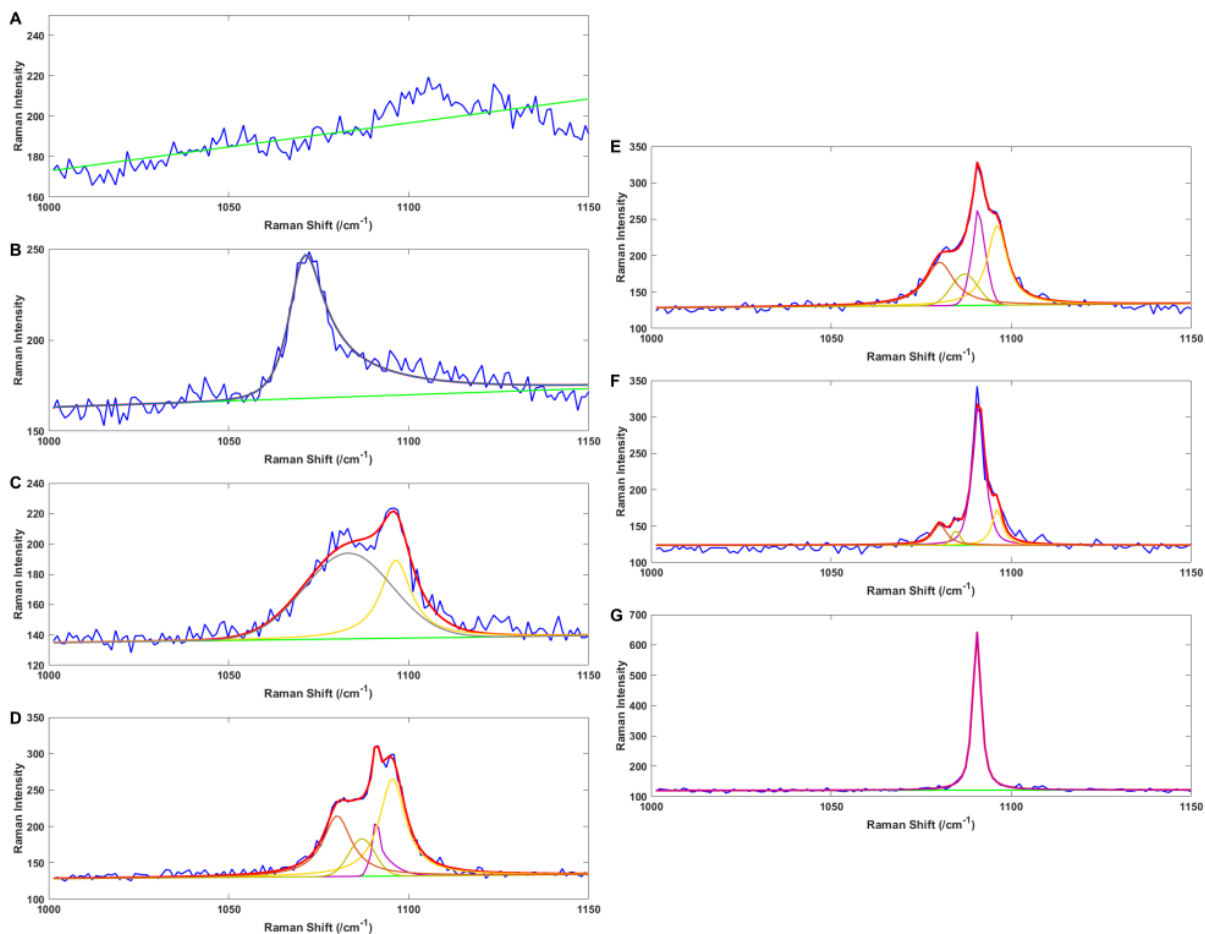


Figure 8.5 A at 10 s recording demonstrates the lack of a C-O stretch identifying the initial droplet composition as a CaCl_2 droplet.

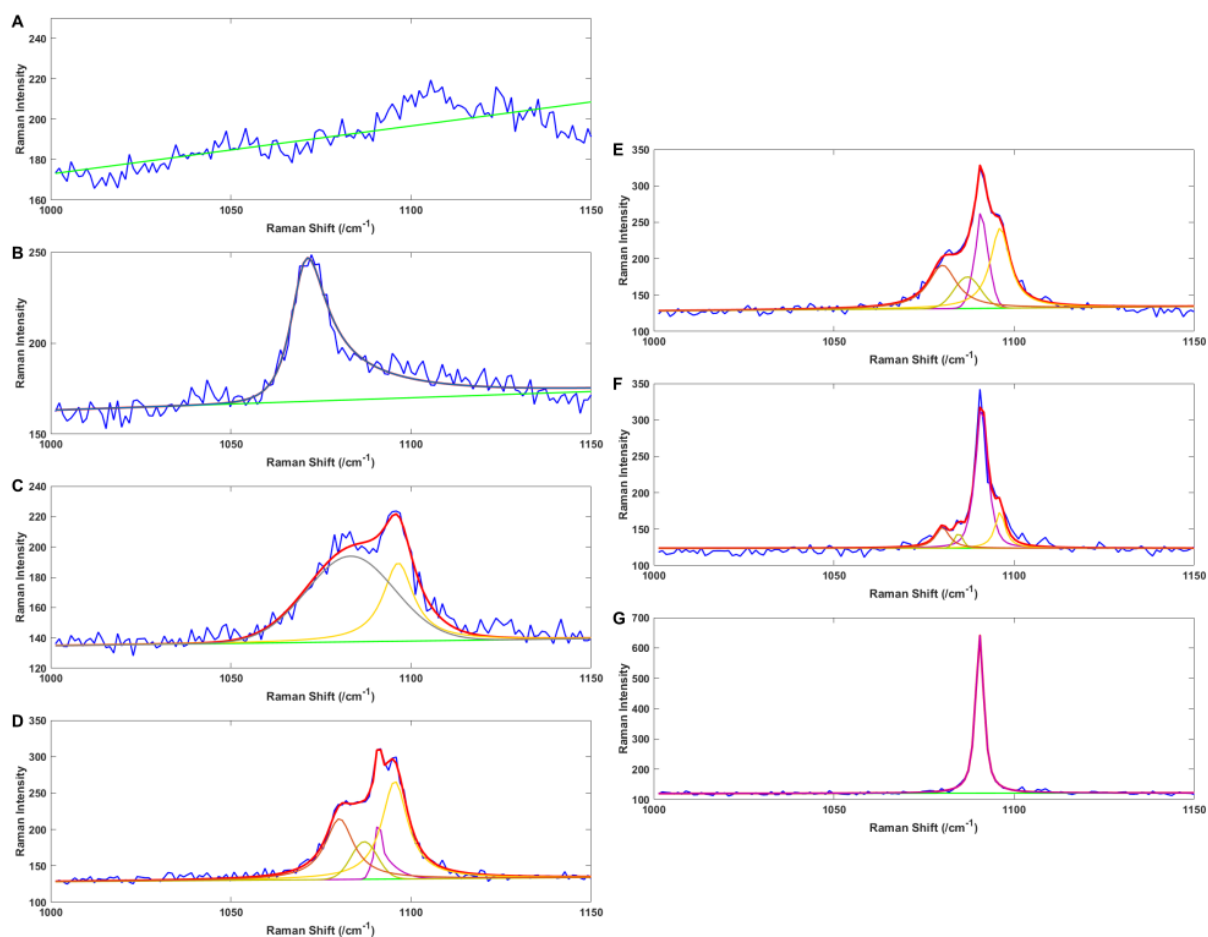


Figure 8.5 B spectrum was recorded after the addition of Na_2CO_3 solution to the initial droplet at 90 s.

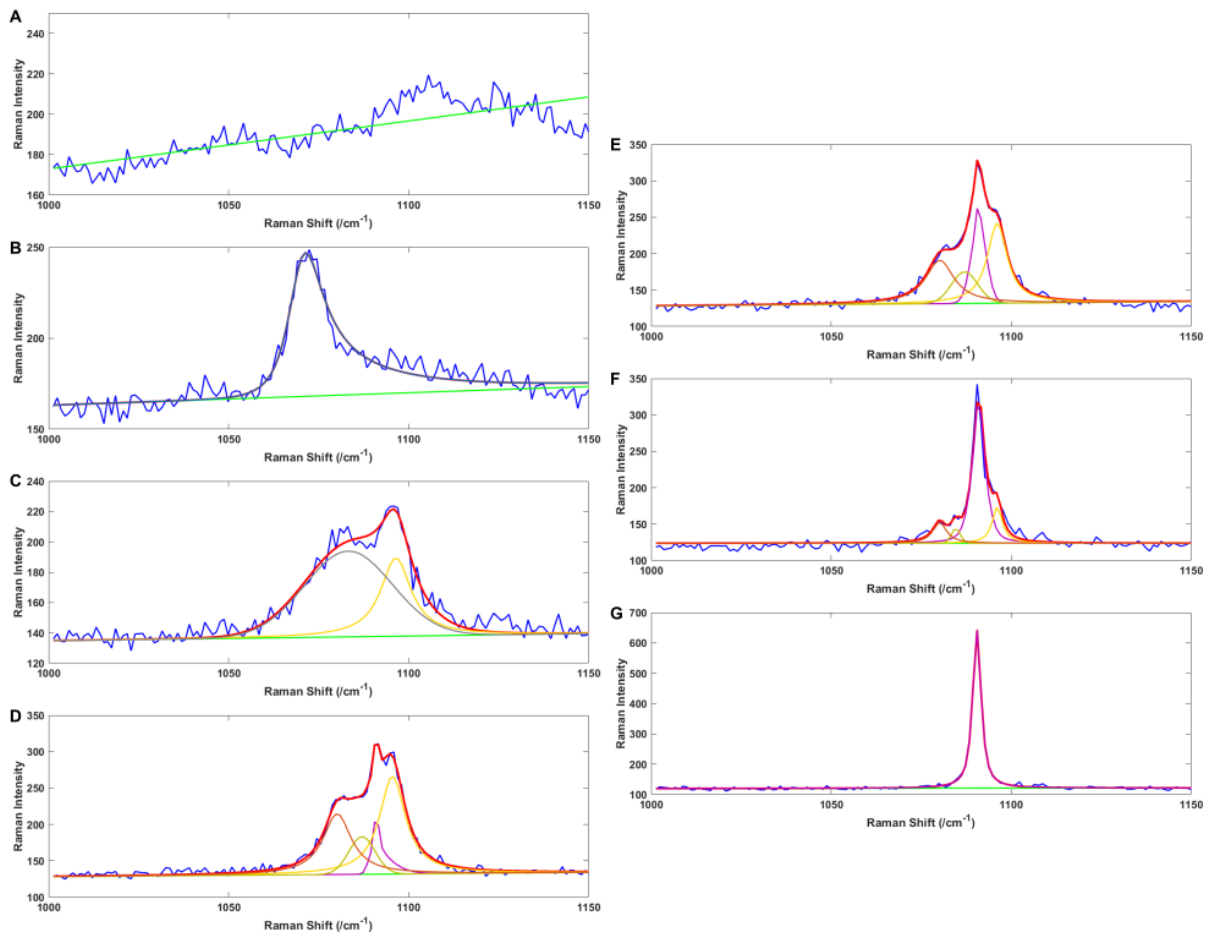


Figure 8.5 C demonstrates that at 280 s the formation of CaCO₃ polymorphs had started, with a fairly pronounced peak for vaterite.

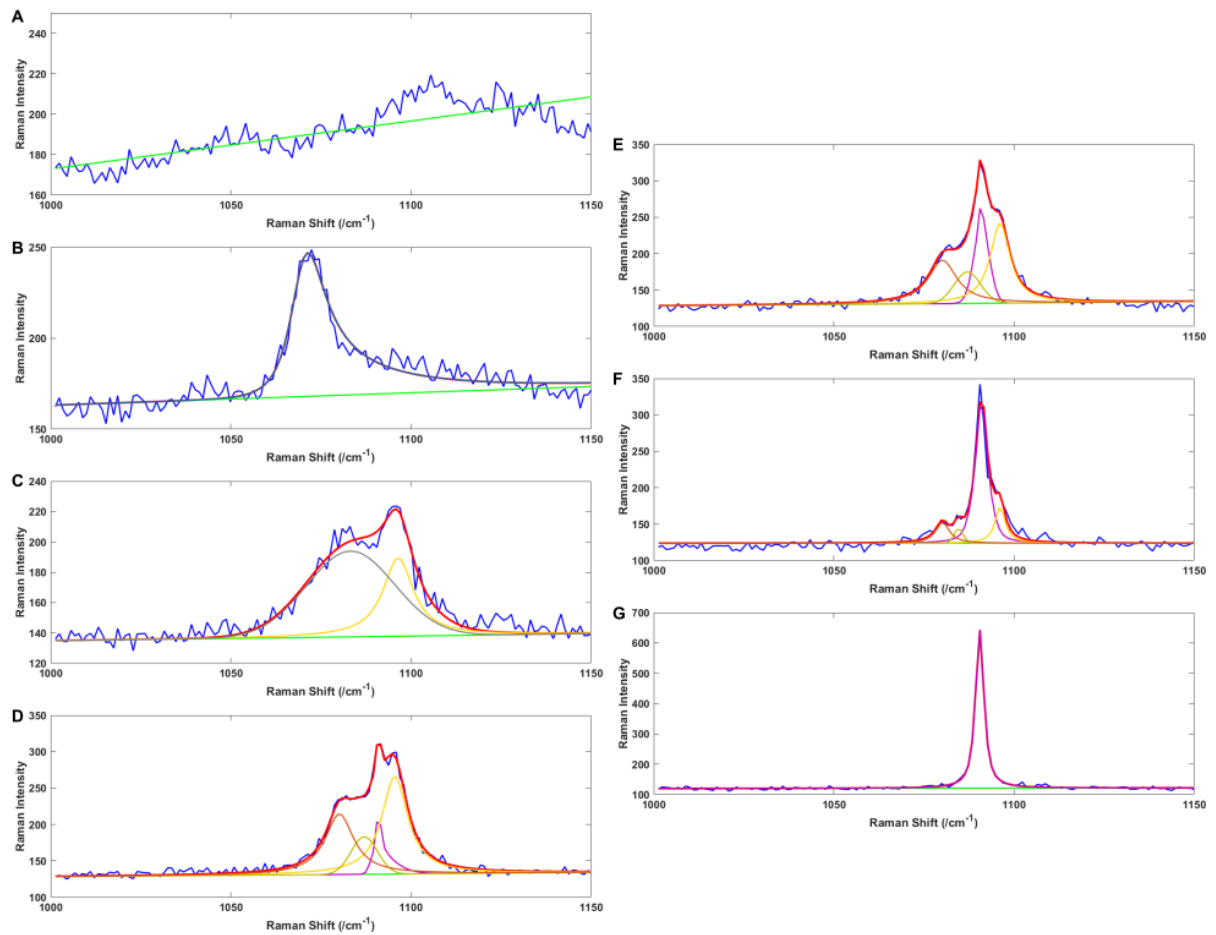


Figure 8.5 D recorded at 300 s demonstrates the end of the rapid chemical reaction producing primarily vaterite with some amount of calcite present.

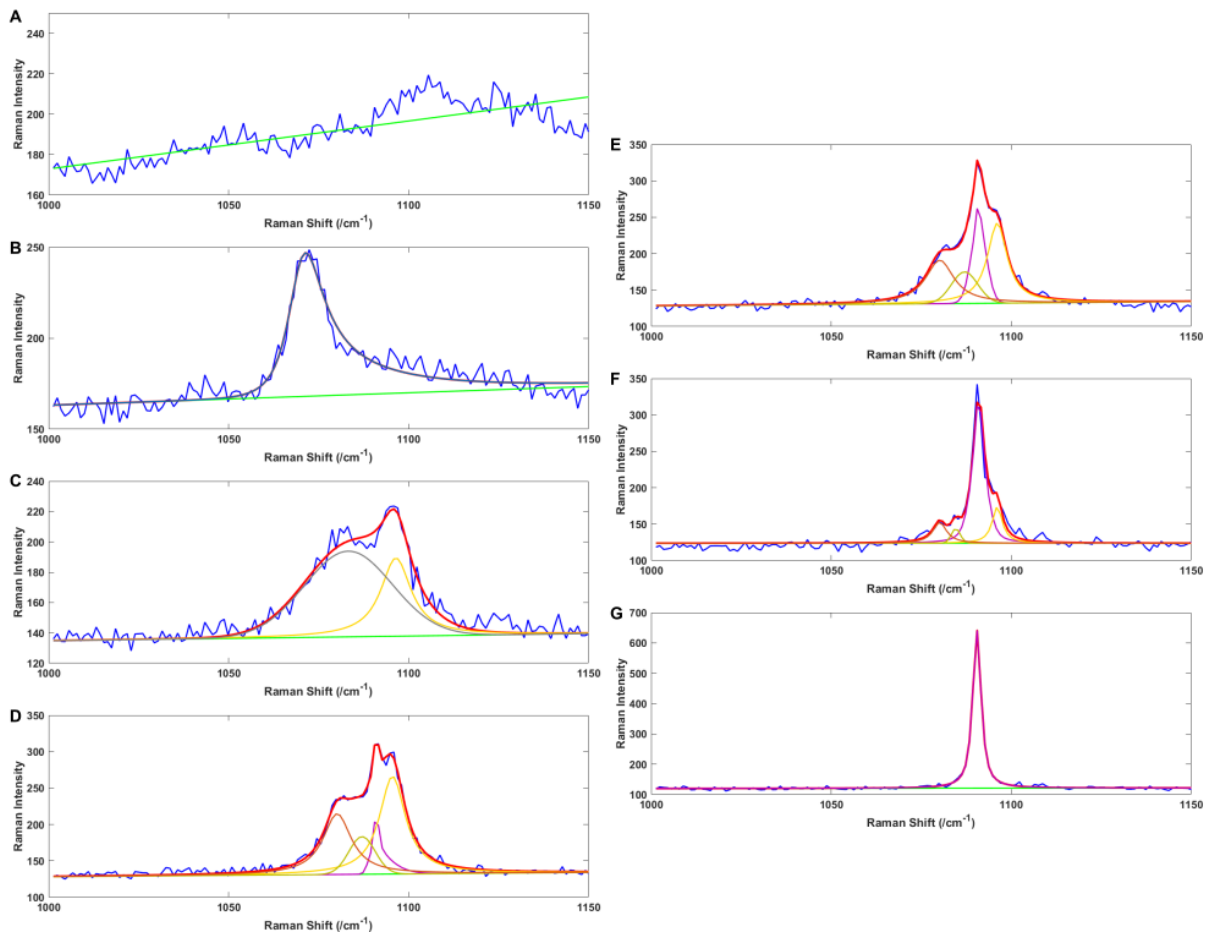


Figure 8.5 E and F at 310 s and 2000 s respectively demonstrate the conversion of vaterite in to calcite after the rapid formation of CaCO₃ had stopped.

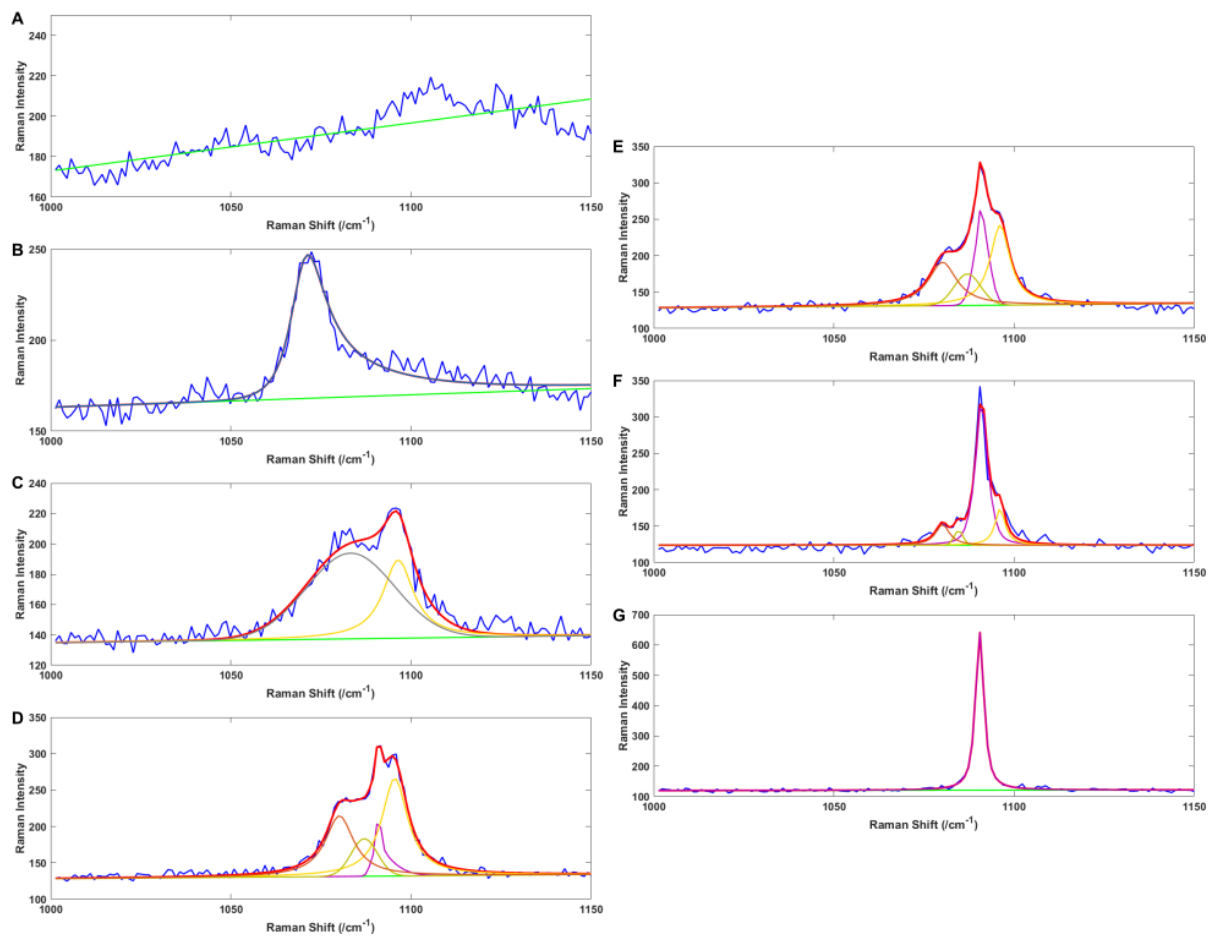


Figure 8.5 G at 7280 s demonstrates the full conversion of vaterite into calcite.

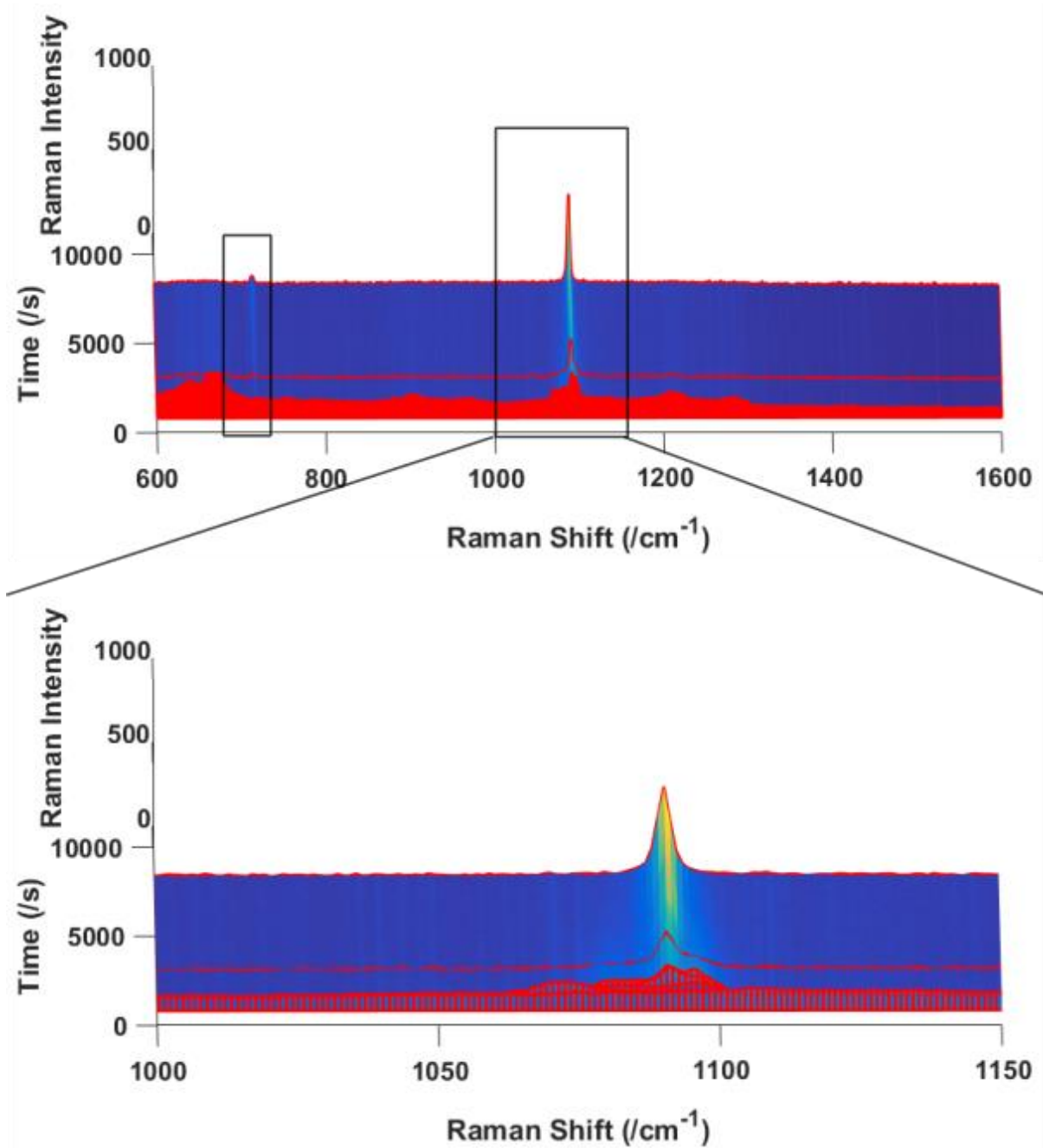


Figure 8.4 Maps of spectra of a chemical reaction demonstrating the formation of calcite from amorphous carbonate via the formation of vaterite. The reaction shows that initially a mixture of vaterite and calcite, which later equilibrates to pure calcite.

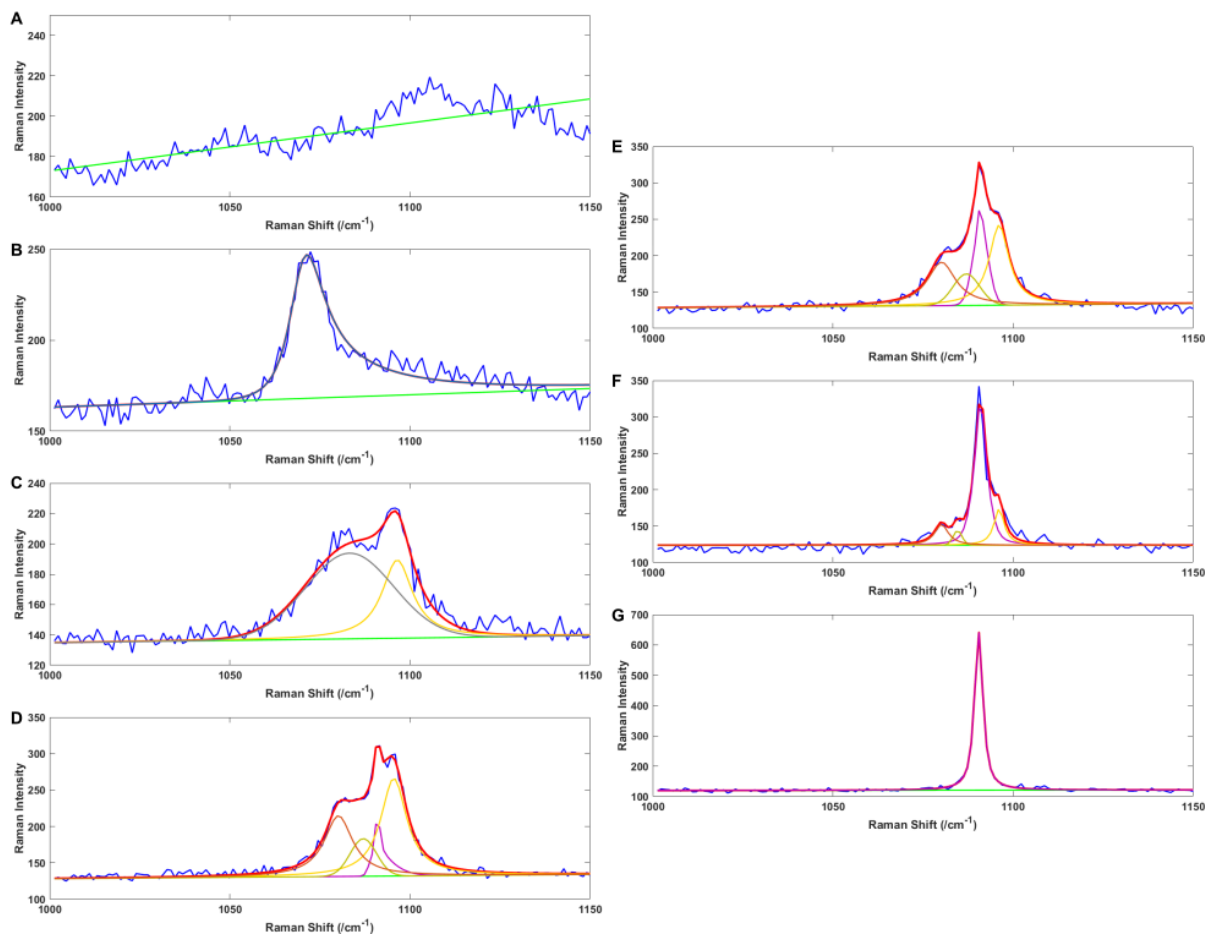


Figure 8.5 Spectroscopic decomposition of the highlighted individual spectra from **Figure 8.4**. The spectra **A-G** are arranged consecutively from the earliest to the the latest recorded in the experiment. In the decomposition blue is the experimental data, red is the total theoretical profile green is the background dark blue is the CO_3^{2-} peak; grey – ACC; purple – calcite; and vaterite as yellow, gold and orange peaks. **A** at 10 s; **B** at 90 s; **C** at 280 s; **D** at 300 s; **E** and **F** at 310 s and 2000 s; **G** at 7280 s.

8.2.2.3. Stability of vaterite

Another reaction pathway in agreement with the literature is the stability of vaterite. As it can be seen in both Figure 8.6 and highlighted in Figure 8.7, it is possible to produce stable vaterite as a stable polymorph, confirming that it can be a stable polymorph, rather than solely a chemical intermediate. The reaction in more: Figure 8.7 A at 10 s recording demonstrates the a lack of a C-O stretch identifying the initial droplet composition as a CaCl₂ droplet. Figure 8.7 B spectrum was recorded after the addition of Na₂CO₃ solution to the initial droplet at 410 s. Figure 8.7 C demonstrates that at 1010 s the chemical reaction has not yet started, as there is no major change in the position of the C-O peak. Figure 8.7D recorded at 1030 s demonstrates the chemical reaction occurring, however it is impossible to discern the formed polymorph hence labelled as ACC and some of the CO₃²⁻ ions have not been consumed during the reaction. Figure 8.7 E at 1050 s shows that a chemical reaction is occurring as there is no discernable presence of CO₃²⁻ ions. Figure 8.7 F at 1250 s demonstrates the fully formed vaterite. Figure 8.7 G at 11570 s demonstrates the stability of the formed vaterite.

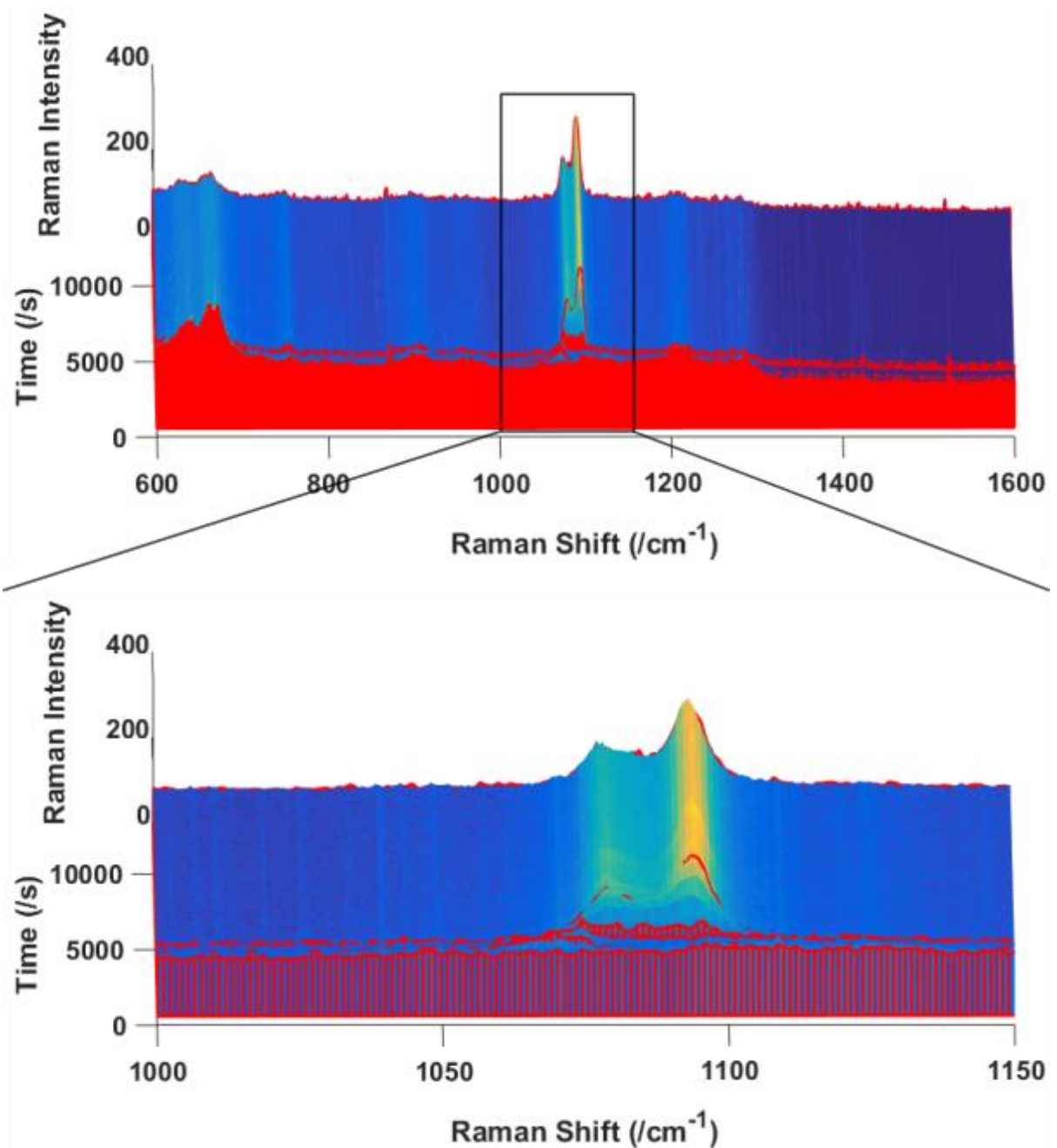


Figure 8.6 Maps of spectra of a chemical reaction demonstrating the formation of vaterite, demonstrating that vaterite can be both a precursor to other CaCO_3 polymorphs and stable on its own see **Figure 8.4**, **Figure 8.5**, **Figure 8.8** and **Figure 8.9**. A detailed decomposition of the individual spectra highlighted in red can be seen in **Figure 8.7**

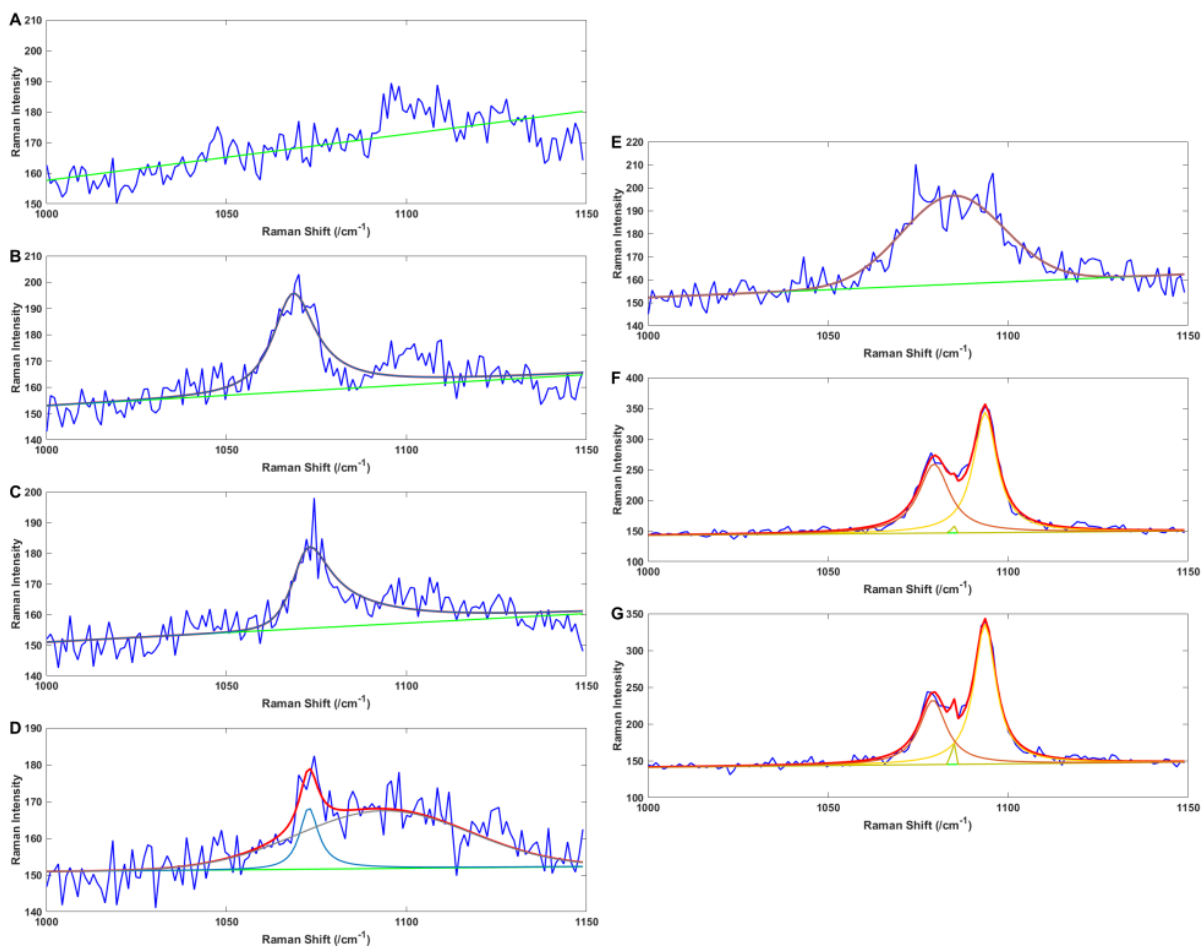


Figure 8.7 Spectroscopic decomposition of the highlighted individual spectra from **Figure 8.6**. The spectra **A-G** are arranged concecursively from the earliest to the the latest recorded in the experiment. In the decomposition blue is the experimental data, red is the total theoretical profile green is the background drk blue is the CO_3^{2-} peak; grey – ACC, and vaterite as yellow, gold and orange peaks. **A** at 10 s; **B** at 410 s. **C** at 1010 s; **D** at 1030 s; **E** at 1050 s; **F** at 1250 s; **G** at 11570 s.

8.2.2.4. Addition of excess Na₂CO₃ solution and formation of ikaite

Ikaite can be formed through the same reaction as vaterite and calcite. Figure demonstrates the formation of ikaite in the presence of excess Na₂CO₃ solution as that of pure vaterite. Initially vaterite and ikaite are formed simultaneously, however after the rapid formation of CaCO₃ polymorphs, vaterite is then slowly converted in to ikaite. (See *Figure 8.8* and *Figure 8.9*)

This can be seen in detail in Figure 8.9. and Figure 8.9. A at 10 s recording demonstrates the a lack of a C-O stretch identifying the initial droplet composition as a CaCl₂ droplet. In Figure 8.9 B spectrum was recorded after the addition of Na₂CO₃ solution to the initial droplet at 30 s, which immediately forms ACC. In Figure 8.9 C demonstrates that at 50 s shows the end of addition of the Na₂CO₃ solution. In Figure 8.9 D recorded at 350 s demonstrates the chemical reaction occurring, forming both vaterite and ikaite. In Figure 8.9 E and F at 2000 s and 5500 s respectively show the progression of the conversion of vaterite in to ikaite. In Figure 8.9 G at 10400 s demonstrates the stability of the formed ikaite.

This can be contrasted with addition of Na₂CO₃ to calcite seen in Figure 8.10 and Figure 8.11. The map of spectra (see Figure 8.10) can be divided in to two parts. Firstly, the formation of calcite via the formation of vaterite same as in Figure 8.4 and Figure 8.5, and the second part after the addition of excess Na₂CO₃. The excess of Na₂CO₃ reacts with remaining CaCl₂ in the solution producing additional calcite, as part of a seeded nucleation (seeded by the calcite produced earlier). The rest of the Na₂CO₃ remains in the solution without reacting with the calcite, which demonstrates that unlike vaterite, calcite will not be transformed into other polymorphs in the presence of additional Na₂CO₃, which can be seen in detail in Figure 8.11. Figure 8.11 A spectrum recorded at 10 s recording demonstrates the presence of a C-O stretch identifying the initial droplet composition as a Na₂CO₃ droplet. Figure 8.11 B spectrum was recorded after the addition of CaCl₂ solution to the initial droplet at 80 s. Figure 8.11 C demonstrates the formation of CaCO₃ polymorphs, primarily calcite at 100 s. Figure 8.11 D recorded at 150 s demonstrates the presence of calcite and vaterite. E at 1000 s shows slow conversion of all CaCO₃ into calcite. Figure 8.11 F and G are spectra recorded at 2500 s and 4660 s respectively, demonstrate the stability of calcite in the presence of the excess of Na₂CO₃.

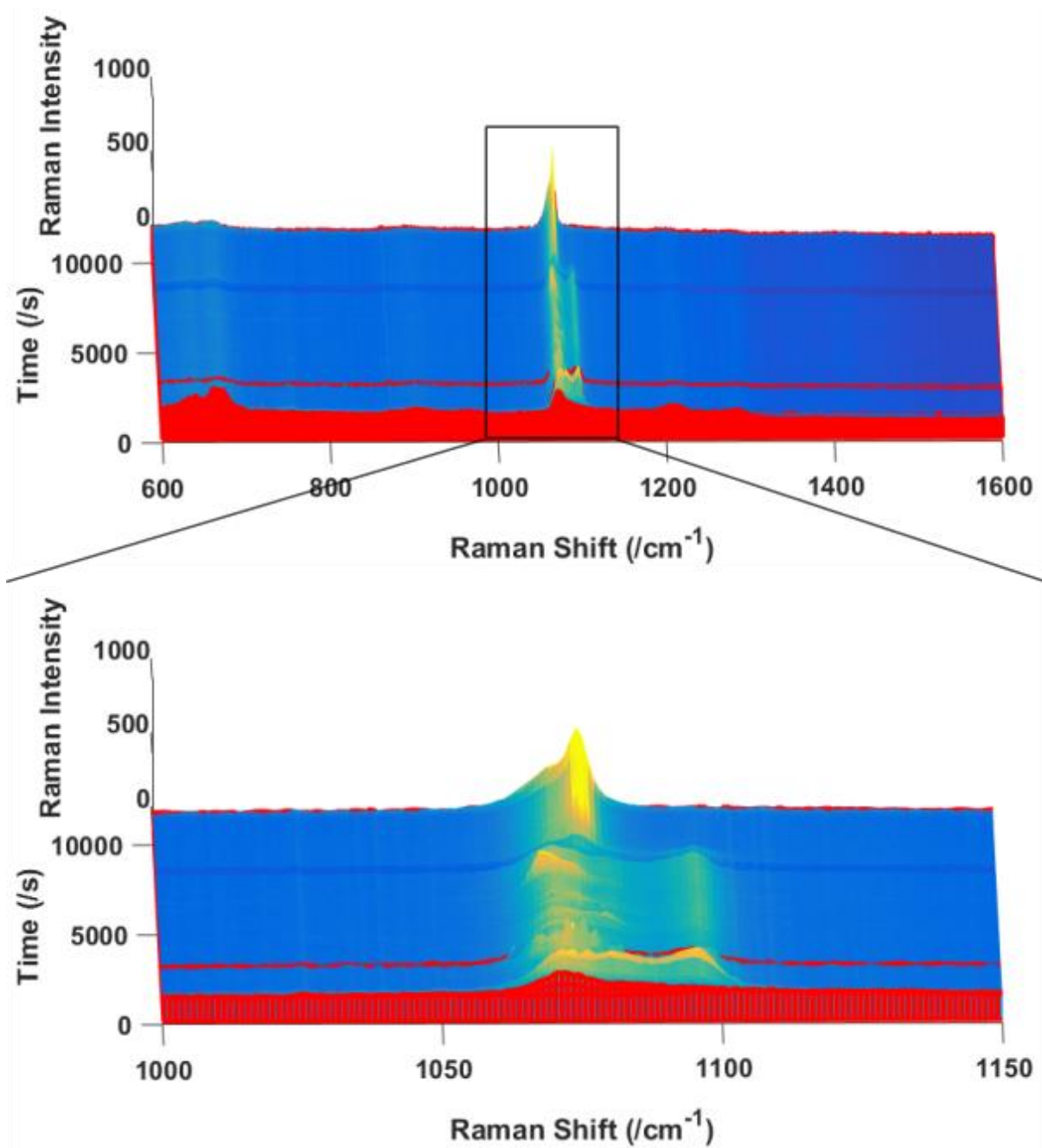


Figure 8.8 Maps of spectra of a chemical reaction demonstrating the formation of ikaite via vaterite in the presence of Na_2CO_3 . The red marks highlight the individual spectra decomposed in Figure 8.9.

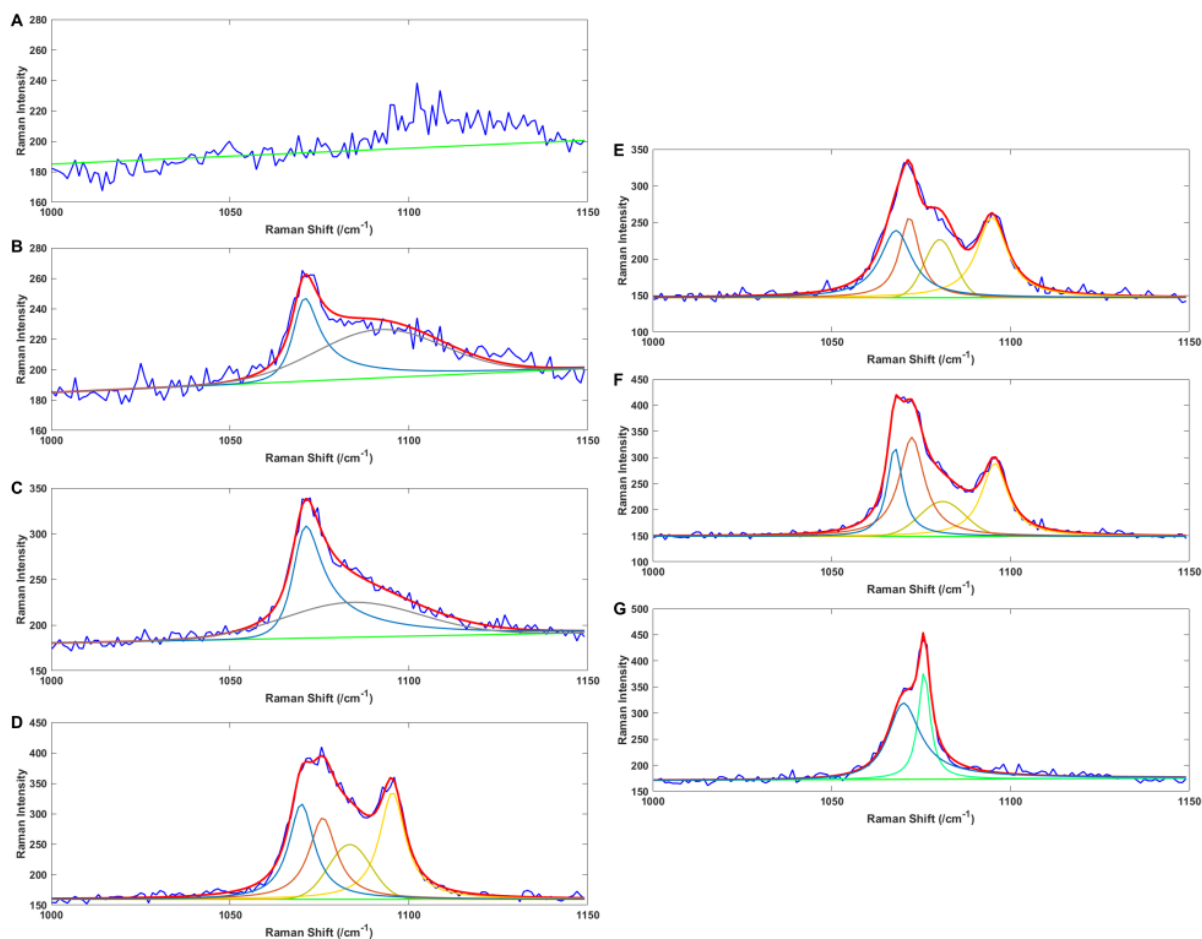


Figure 8.9 Spectroscopic decomposition of the highlighted individual spectra from **Figure 8.8**. The spectra **A-G** are arranged consecutively from the earliest to the the latest recorded in the experiment. In the decomposition blue is the experimental data, red is the total theoretical profile green is the background drk blue is the CO_3^{2-} peak; grey – AC; aqua – ikaite, and vaterite as yellow, gold and orange peaks. **A** at 10 s; **B** at 30 s; **C** at 50 s; **D** at 350 s; **E** at 2000 s; **F** at 5500 s; **G** at 10400 s.

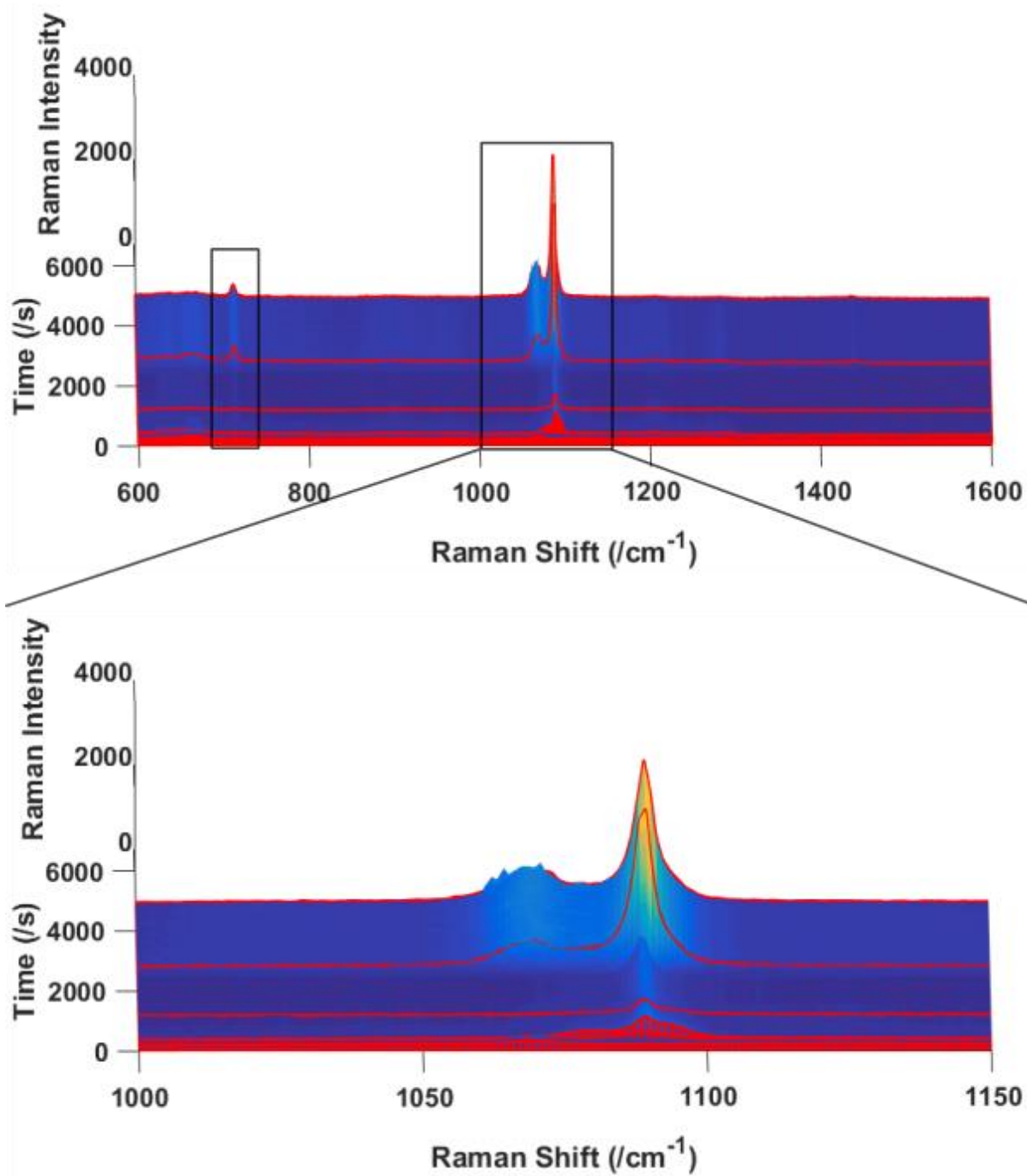


Figure 8.10 Maps of spectra of a chemical reaction demonstrating the formation of calcite via vaterite, and addition an excess of Na_2CO_3 to calcite. The map of spectra can be divided in to two parts.

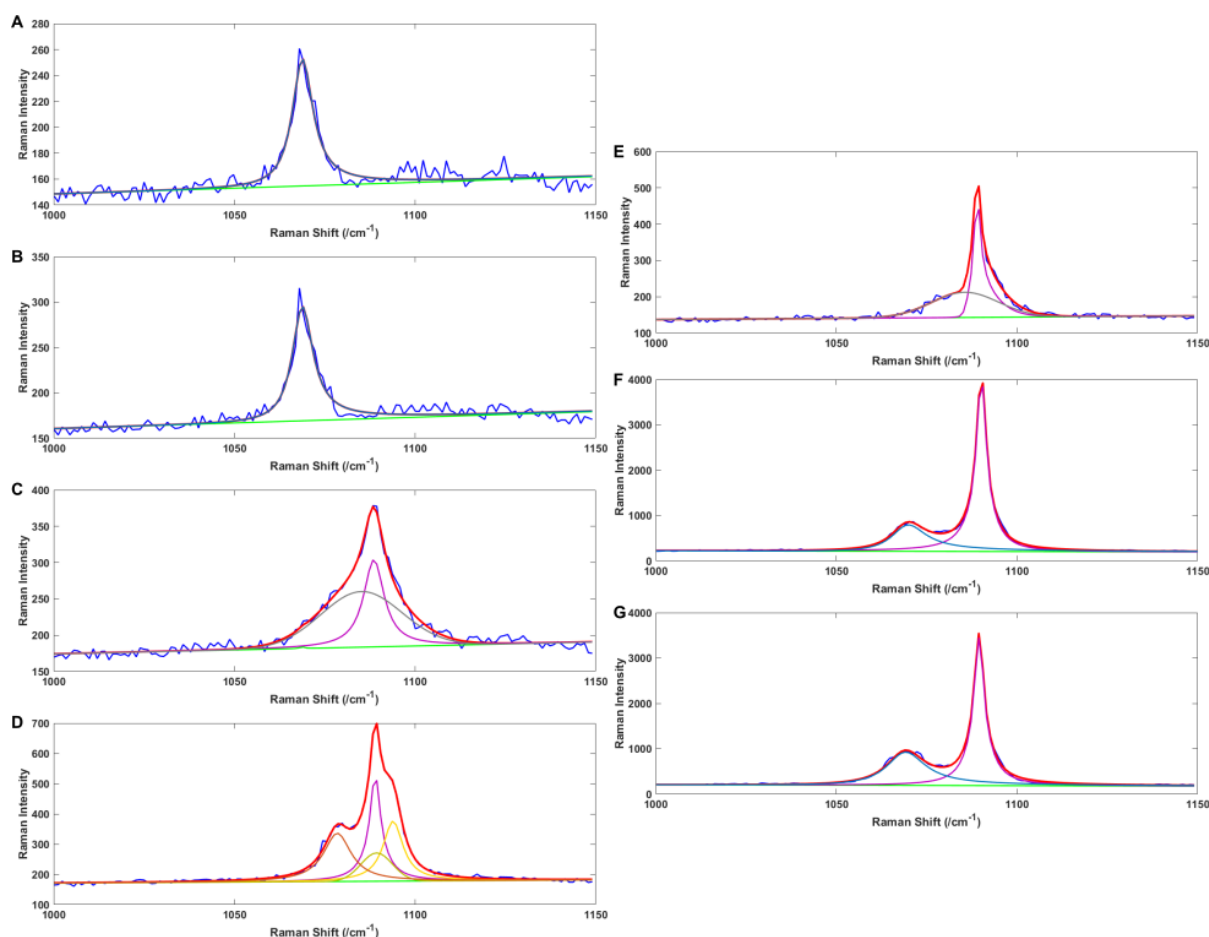


Figure 8.11 Spectroscopic decomposition of the highlighted individual spectra from **Figure 8.10**. The spectra **A-G** are arranged concecutively from the earliest to the the latest recorded in the experiment. In the decomposition blue is the experimental data, red is the total theoretical profile green is the background drk blue is the CO_3^{2-} peak; grey – ACC; purple – calcite; and vaterite as yellow, gold and orange peaks. **A** at 10 s; **B** at 80 s; **C** at 100 s; **D** at 150 s; **E** at 1000 s; **F** and **G** are spectra recorded at 2500 s and 4660 s respectively.

8.2.3. pH of solutions

As identified in the first section of this chapter pH and the presence of ions can have a significant influence on the chemical reaction. As the pH of the solution in the aerosol droplet could not be directly measured, it was measured in bulk solutions (See **Table 8.1**, **Table 8.2** and **Table 8.3**).

	CaCl ₂ g L ⁻¹	CaCl ₂ M	pH
High Concentration	109.90	0.99	6.28
Medium Concentration	82.43	0.74	6.08
Low Concentration	54.45	0.50	6.00

Table 8.1 Concentrations and pH values of CaCl₂ solutions used for the pH experiments with the molar mass of CaCl₂ 110.98 g mol⁻¹. pH of pure water was 7.46. pH probe was also calibrated with a standard pH buffer at pH 7.

	Na ₂ CO ₃ g L ⁻¹	Na ₂ CO ₃ M	pH
High Concentration	106.10	1.00	10.49
Medium Concentration	79.58	0.75	10.55
Low Concentration	53.05	0.50	10.62

Table 8.2 Concentrations and pH values of Na₂CO₃ solutions used for the pH experiments with the molar mass of Na₂CO₃ 105.99 g mol⁻¹. pH of pure water was 7.46. pH of pure water was 7.46. pH probe was also calibrated with a standard pH buffer at pH 7.

[Na ₂ CO ₃]/[CaCl ₂]	pH values			
	High Concentrations	Medium Concentrations	Low Concentrations	Average
2.02	10.24	10.08	10.07	10.13
1.01	9.75	9.65	9.56	9.65
0.51	6.80	6.60	6.49	6.63

Table 8.3 A table of solution mixtures and their pH values after the reaction. The concentrations indicate that within the range of concentrations of the solutions tested, the concentrations do not significantly affect the pH.

8.3. Discussion

8.3.1. Direct formation of calcite

One interesting, and somewhat counter intuitive observation can be made across all of the samples forming CaCO_3 is the time delay between the coalescence of the droplets with CaCl_2 and Na_2CO_3 , and the formation of CaCO_3 . This is particularly evident in reactions producing vaterite, as in those reactions it is possible to observe the C-O peak at the same wavelength as in an aqueous Na_2CO_3 solution persisting for ~ 100 s, whereas the reaction in bulk solutions happens instantaneously (< 1 s). This raises the question of the mechanism of coalescence between two aerosol droplets.

There are two potential approaches for explaining this phenomenon the nucleation approach and the mixing approach. The nucleation approach would be to look at the nucleation theory, and specifically at the formation of the stable nuclei. The main idea behind it is that clusters that are smaller than the critical nucleus size will preferentially dissolve rather than grow forming a crystal. This would mean that for a certain period of time CaCO_3 clusters do not reach the critical nucleus size, however due to the low solubility of CaCO_3 , regardless of the polymorph this theory seems less likely.

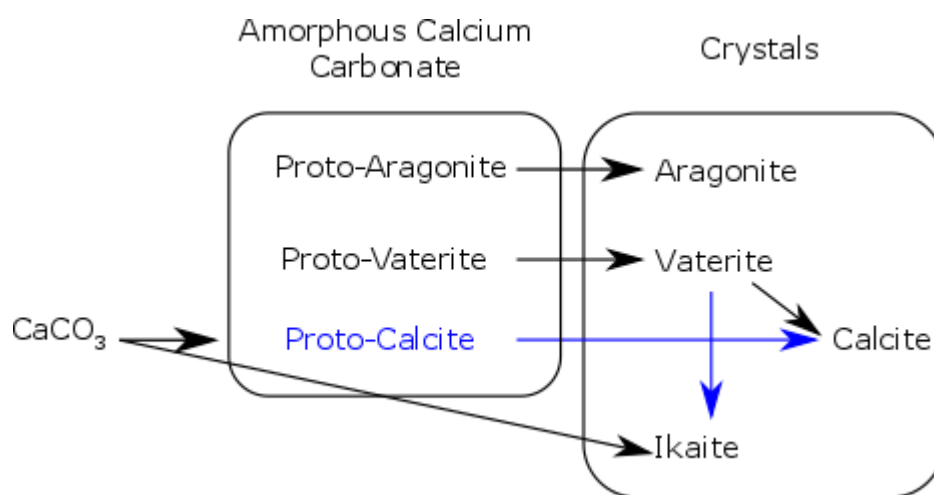


Figure 8.12 A Schematic of all possible routes of forming CaCO_3 polymorphs. Highlighted in blue are the novel pathways discussed in this thesis that have not been experimentally reported in inorganic systems.

The mixing approach relies on the idea that mixing of the two solutions does not happen immediately. This would mean that the droplets form a core-shell structure,

without mixing, thus flowing in a laminar flow, rather than a turbulent flow, as the turbulent flow would mix the solutions.

The chemical reaction pathways observed in the course of the research done during this PhD is summarised in Figure 8.13.

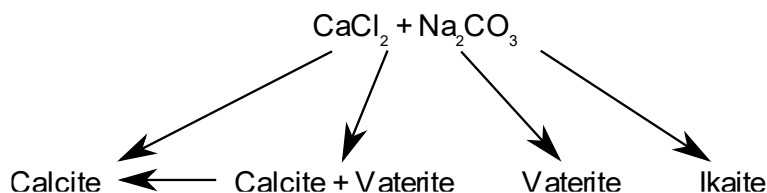


Figure 8.13 A Schematic of the chemical reactions observed in the experiments done for this thesis.

8.3.2. Direct formation of calcite from the ACC

Contradicting some of the experimental work previously done is the direct formation of calcite from the ACC, as evidenced by the spectroscopic data.^[216] Noticeably the formation this reaction occurs in two phases: the formation of kinetic calcite, and then the thermodynamic equilibration.

The kinetic formation phase is the formation of calcite directly from the ACC. The calcite formed in this stage is likely to have a high degree of distortion in the crystalline lattice, which is due to the rapid formation of the crystals. This can be seen in the experimental spectra as the C-O peak of the newly formed calcite is broader than that of the calcite that has been left to equilibrate. This also shows that the crystalline structure of the newly formed calcite has a lot of defects, which contribute to widening the distribution of states, thus producing widening the peak in the Raman spectrum. It is important to note that the peak is widened asymmetrically towards lower wavenumbers, indicating a preference of some defects over others. The asymmetrical shape of the peak in the Raman spectrum being wider at the lower Raman shifts, which is slightly closer to the C-O peak of CO_3^{2-} ion in an aqueous solution, indicates that the defects are likely to resemble the “free” CO_3^{2-} ions. However, it is important to keep in mind that these defects are very small, and the mineral formed is calcite.

The second phase is the thermodynamic equilibration, which happens after the kinetic formation phase. During this phase the defects discussed above equilibrate to a more “perfect” crystalline structure, which is the thermodynamic equilibrium of

CaCO₃. This can be considered a direct consequence of the entropy of the system (S). Similarly, to the Clausius caloric entropy formulation, the energy of the system will tend towards uniform distribution. This process can be observed during the chemical reactions forming calcite by comparing the width of the v1 C-O calcite peak in the Raman spectra as time progresses. The same process can be noticed by comparing the width of the v1 C-O Raman peak between natural and synthetic calcite.

8.3.3. The classic route formation of calcite via vaterite

The “classical” and the most observed pathway of formation of calcite. Similarly, to the direct formation of calcite, this reaction pathway can also be split up into two steps: formation of the kinetic polymorph – vaterite, and the thermodynamic equilibration – transformation of the formed vaterite into calcite. This step indicates the meta-stability of the vaterite polymorph, indicating that there is a barrier preventing direct formation of calcite.

From the point of view of the Raman spectroscopy of the v1 vibrational mode of the C-O bond in carbonates, vaterite has a broad triple peak with the strongest peak being at a larger Raman shift than that of the calcite. The other two peaks that combine to produce the characteristic triple peak, characteristic of vaterite are at a smaller shift, in between the position of the calcite peak and the pure CO₃²⁻ solution. Following the logic outlined for the crystalline lattice defects in the direct formation of calcite, the positions of the two peaks would suggest that the structure of vaterite has 3 v1 vibrational mode C-O bond environments, one that requires more energy to change the polarization of the bond than in the structure of calcite, and the other two less. The broadness of the peaks also suggests that these environments are formed with a variety of defects, indicating that there is a wider distribution of meta-stable sub-states. Thus, there will be more defects in the crystalline structure of vaterite than in calcite and that the energy required for a change in polarizability in the two peaks at a lower Raman shift will be closer to that of solvated CO₃²⁻ ion than that in calcite. Basing on the fact that calcite is the thermodynamically stable polymorph, vaterite has one strained environment and two relatively relaxed environments stabilized by the environment.

From the point of view of the energy distribution the landscape is likely to have local minimum corresponding to the vaterite and a global energy minimum corresponding

to calcite. The fact that vaterite is converted into calcite indicates that the energy barrier of the transformation is relatively low, allowing the transformation to occur. (see **Figure 8.4**, **Figure 8.5** and **Figure 8.14**)

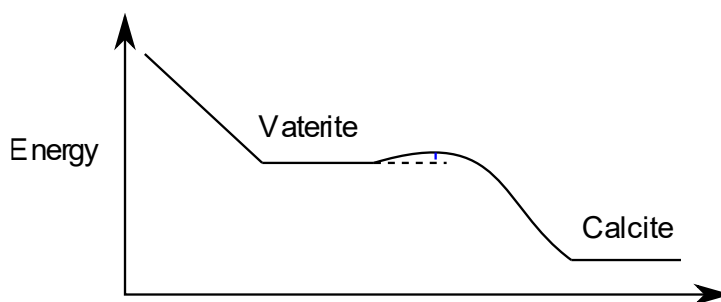


Figure 8.14 The potential energy landscape of the chemical reaction that produces vaterite that is later converted into calcite.

The decomposition of the map of spectra in Figure 8.4 and Figure 8.5 using the model described in table 8.14 demonstrates the decrease in the width of the calcite peak. The decomposition also demonstrates that some calcite is formed initially, and that vaterite is later consumed to form additional calcite. In principle, this decomposition exemplifies the use of Raman spectroscopy and mathematical analysis in analysing chemical reactions. A more refined version of the decomposition along with the necessary adjustments for the influence of pH on chemical reaction could be used to study the kinetics of complex chemical reactions in fine detail (with the use of the total peak area, peak width and asymmetry).

8.3.4. Stable vaterite

It is possible to stabilize vaterite by increasing the amount of Na_2CO_3 aerosol added to the reaction, from the amount needed to form vaterite which later transforms into calcite. As seen in **Figure 8.6**, **Figure 8.7** before the formation of vaterite the peak corresponding to CO_3^{2-} ion is more pronounced than when vaterite is converted into calcite, which is indicative of a higher ratio of Na_2CO_3 to CaCl_2 in solution. This in turn can be linked to a higher pH of the resulting mixture and is known to produce vaterite.

Considering the proposed energy landscape for the reaction with a conversion of vaterite into calcite, the stability of vaterite can be considered from the point of view

of the energy barrier required to transform vaterite into calcite. (see **Figure 8.6**, **Figure 8.7** and **Figure 8.15**)

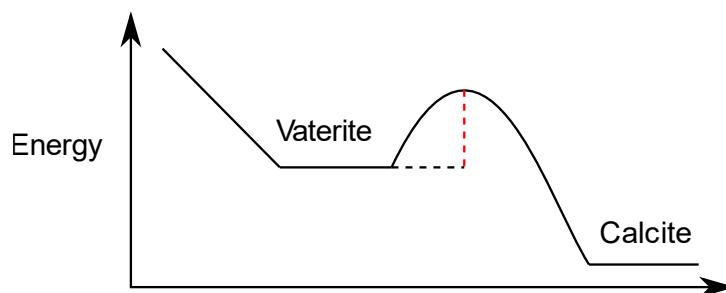


Figure 8.15 The potential energy landscape of the chemical reaction that produces stable vaterite. The energy barrier in this scenario is too high for the CaCO_3 to transform from vaterite into calcite, therefore stabilizing vaterite.

8.3.5. Forming ikaite

Ikaite, is the polymorph that has been shown to form at higher pH than vaterite at the same temperature and without the presence of any other ions.^[62] Therefore, it is not unreasonable to assume that the formed polymorph is ikaite. This can also be corroborated by the relative position of the CO_3^{2-} ion peak produced in the experiments. In these experiments ikaite was produced via coalescing small volume of CaCl_2 aerosol with a large Na_2CO_3 droplet, which could be seen as a small shift (a few cm^{-1}) of the ν_1 C-O bond vibration. (see **Figure 8.8** and **Figure 8.9**) Another way of forming ikaite is by adding an excess of Na_2CO_3 to a droplet containing vaterite. (see **Figure 8.17**) It is however impossible to form ikaite from calcite by adding additional Na_2CO_3 , which would suggest that the energy barrier for this process is prohibitively high. (see **Figure 8.10**) Thus, making the energy landscape look as shown in **Figure 8.16**.

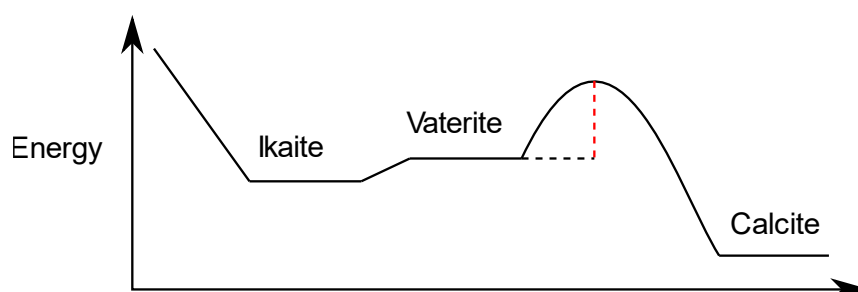


Figure 8.16 The energy landscape of the formation of ikaite. This process can be seen under highly basic conditions close to the pH of the Na_2CO_3 aqueous solution. In this case the energy barrier for the transformation of vaterite into calcite remains

high enough to prevent the formation of calcite, however under those conditions ikaite becomes more stable than vaterite, forcing vaterite to transform into ikaite. This can be evidenced by the transformation of vaterite into ikaite by addition of excess Na_2CO_3 effectively raising the pH of the droplet. It can also be noted that by adding additional Na_2CO_3 solution into a droplet containing calcite there is no reaction occurring, demonstrating that calcite is the thermodynamically stable polymorph and that the meta-stability of vaterite is crucial to this process.



Figure 8.17 A Schematic of the chemical reaction of forming ikaite from vaterite by adding additional Na_2CO_3 into the droplet containing vaterite.

8.3.6. pH of solutions

When considering the topic of pH, it is important to look at how the acid-base equilibrium as well as acids and bases are defined.

The simplest modern model used was the Arrhenius model, produced by S.A. Arrhenius in 1887. [224] This model accounts only for compounds producing H^+ and OH^- ions, with compounds producing H^+ ions being an acid and OH^- produced by bases. An improvement on this theory was introduced in 1923 by Bronsted and Lowry, known as Bronsted – Lowry acid-base theory. [224] The key difference of this theory from the Arrhenius is in the model of the acid considers the acid after it has produced H^+ as a conjugate base, i.e. a deprotonated acid is a conjugate base. A theory that builds upon these two theories is the M.I. Usanovich theory proposed in 1939. [224] In this theory the duality of a compound is taken into account, defining an acid as something that either donates H^+ or accepts OH^- ions. Similarly, bases are defined as donating OH^- or accepting H^+ ions. [224]

Also, in 1923 G.N. Lewis produced a completely new way of defining acids and bases. [224] In the Lewis acid-base theory is based on the donation and accepting electrons, where acids accept electrons and bases donate electrons. In contrast with both Arrhenius and Bronsted – Lowry acid-base theories, in the Lewis theory the proton itself is treated as an acid, rather than an elementary particle. [224]

In the carbonate system interrogated in this research it is important to consider both ways of defining acids and bases as the carbonate ion can both react as a Lewis base by forming calcium carbonate, as well as the potential to form HCO_3^- (bicarbonate ion), which is a base both by Lewis and Usanovich theory.^[224]

pH is an important property of aqueous solutions. When considering the pH of pure water is ~7 at standard conditions. The addition of a solute to water will alter the pH of the solution from that of pure water. The solute itself will have a specific pH to which the solution will equilibrate to. Notably, the pH of the solution will depend on the solute and the concentration of solute, however the equilibrium pH can be reached at lower solute concentrations than the saturation concentration. This is due to the fact pH is related to the concentration of H^+ ($[\text{H}^+]$) ions on a logarithmic (base 10) scale, following equation 8.1.

$$pH = -\log_{10}([\text{H}^+]) \quad \text{Equation 8.1}$$

When considering aerosols, it is important to note that the solute concentration of the nebulised solution is likely to be lower than the solute concentration in an optically trapped aerosol droplet, i.e. as the solution is nebulised the solute concentration increases. However as mentioned earlier an increase in the amount of solute in an aqueous solution containing one solute will not lead to a change in pH, hence the pH could be considered the same.

In the literature it is possible to note that the measurement of the pH in aerosol droplets is typically done by assuming that the pH of a droplet would be the same as that of a solution calculate the pH based on the concentration of the solute.

Alternatively, there have been attempts to measure the pH directly in the droplet. One of the downfalls of the direct droplet measurement articles is that they do not seem to account for any other components in the system. For example, a method of determining the pH by tracking the relative concentrations of protonated and deprotonated ions using Raman spectroscopy has been demonstrated.^[225] One of the examples they use to demonstrate their method is the conversion of the bicarbonate ion to the carbonate ion. In that publication they demonstrate that it is possible to detect both ions in an aerosol droplet and quantify them relative to one-another, which can be used to measure the pH. In the data reported there is a distinct drop in pH from that of the bulk solution to that measured in the aerosol droplet, with no explanation provided.^[225]

This discrepancy was likely a result of the solution having a third component in it HCl at low concentration, which was stated in the supporting material, as necessary to lower the pH of the solution to have a quantifiable measure of the bicarbonate ions.^[225] While the presence of the bicarbonate ion is indeed crucial in this experiment, neither the main publication, nor the supporting information seem to account for the change in the concentration of HCl, neither due to the preconcentration of the sample, nor due to the evaporation of volatile components of the aerosol mixture, namely water and HCl.^[225] It can be pointed out that HCl will be less volatile than water^[175] and thus will be concentrated as the water evaporates in the droplets produced in the mentioned paper.^[225] This implies that the concentrations of both NaHCO_3 and HCl dissolved in the solution will increase. Another issue lies in the fact that the pH and concentration are not linearly dependent, thus for example a 2-fold increase in concentration of in a low concentrated component will potentially have a larger effect on the pH, than that of a high concentrated component, even if it is simply due to the values of pH being on a logarithmic (base 10) scale, therefore explaining the discrepancy of the pH values measured in bulk solution and aerosol droplet.^[226]

Similarly, most publications reporting on pH measurement of pH in aerosols tend to neglect accounting for the phase partition an evaporation of volatile components such as HCl and ammonia (NH_3),^[175] which are used to introduce changes in pH of the solution. A publication showing a difference in pH in aerosol droplets compared to bulk aqueous solutions containing mixtures of $(\text{NH}_4)_2\text{SO}_4$ and H_2SO_4 . The experiments show that the pH of aerosol is lower than that of the bulk solutions, with smaller aerosol droplets having a more pronounced effect on the pH. This effect is likely caused by the phase partitioning between NH_4^+ and NH_3 with NH_3 evaporating from the droplet, due to an increase in the surface area to volume ratio in smaller particles and the increase in the partial pressure of the volatile components. A similar conclusion was reached by the authors.^[227]

Other methods of determining of aerosol pH are the ion balance, molar ratio, thermodynamic models and phase partitioning methods. While the ion balance and molar ratio methods are considered relatively unreliable the thermodynamic models such as E-AIM and AIOMFAC-web^[171,172] and phase partition methods are considered more reliable.^[228,229] Regardless, all of these methods were initially

created and validated based on experimental data produced in bulk solutions or are extensions of the Debye–Hückel theory (also designed for bulk solutions). (see chapter 7.3.5) Therefore, it can be assumed that, when taking into account the volatility of components of the aerosol along with the aerosol droplet's curvature, at RH values above the supersaturation point, the ions in solutions will behave in the same way as in bulk solutions.

These aspects of measuring pH in aerosols it does make sense to use the pH of the bulk solutions as an approximation for the pH changes caused by a chemical reaction in an aerosol droplet when the solvent is the only volatile substance in the chemical reaction. The data presented in **Table 8.1** and **Error! Reference source not found.** the chemical reactions demonstrates that the reactions produced using aqueous solutions of Na_2CO_3 and CaCl_2 at 0.5 M, 0.75 M and 1 M concentrations produce reaction mixtures of approximately same pH. This would mean that even at 0.5 M concentrations of the reagents, the products of the reaction reach the equilibrium pH, therefore any increase in their concentrations would have no significant effect on the resulting solution. Thus, the pH measurement obtained in bulk could be used as a potential pH range indicators for the reaction occurring in the optically trapped aerosol droplets.

Considering the pH of the solutions, a trend can be noticed, which shows that the higher the ratio of Na_2CO_3 to CaCl_2 the higher the pH, which is also evident from the pH of the individual solutions. It can also be noticed that the concentrations of both Na_2CO_3 and CaCl_2 in aqueous solutions measured, do not significantly affect the pH of the solutions. This data however demonstrates that by changing the relative amounts of reagents added to the solution influence the pH of the solutions which indicates the different conditions of forming the different polymorphs in the optically tweezed aerosol droplets during the experiments. It would also suggest that at high pH values ikaite is formed, at slightly lower pH vaterite is stable, and at pH values close to that of the CaCl_2 Calcite is formed directly from the ACC indicating the presence of proto-calcite phase of the ACC. The combination of this data with the experimental spectra produce consistent results with regards to the formation of vaterite and ikaite with the literature values presented earlier in this chapter.

Taking in to account the literature on the formation of ikaite, vaterite and calcite, it is possible to notice a pattern that the pH values around the equilibrium pH of a Na_2CO_3

solution the thermodynamic equilibrium is shifted toward the formation of ikaite polymorph. At a somewhat lower pH vaterite becomes stable with a range of stability as both a kinetically stable intermediate, i.e. as a precursor, to the formation of ikaite at the higher end of the range, or calcite at the lower end of the range. Additionally, it has been demonstrated experimentally that vaterite itself can be thermodynamically stable at a certain pH range. Finally, in the course of the research done for this thesis it has been demonstrated that at a pH range approaching pH 9.5 vaterite ceases being stable enough to be a kinetic intermediate in the reaction, allowing the reaction to proceed directly to the formation of the thermodynamically stable calcite.

Once considered together with the relative amounts of CaCl_2 and Na_2CO_3 aerosols added it is possible to see that at a relatively low amount of Na_2CO_3 coalesced with a CaCl_2 droplet the calcite polymorph is produced, and the environment corresponds to a low pH of ~ 6.6 . Similar amounts of CaCl_2 and Na_2CO_3 in the droplet result in producing vaterite, with the environment's pH at ~ 9.65 , which is roughly consistent with the pH of formation of vaterite in the literature.^[62] And lastly the droplets with high amounts of Na_2CO_3 and low amounts of CaCl_2 , are likely producing ikaite, with the droplet's pH at ~ 10.13 , which is higher than the pH of formation of vaterite, with the trend being consistent with the literature values.^[62] (see Table 7.3) This correlation suggests that the pH of the environment is likely a major factor in the formation of the various polymorphs of CaCO_3 . This could also be a part of the explanation of the transformation of the polymorphs into one another, as the pH of the solution does favour the initially formed polymorph, for example vaterite, the pH is low enough for it to slowly transform into calcite, but if the pH would be lower the transformation of vaterite into calcite would be faster. This process would be dependent on the pH as a stabilising factor, thus at pH values closer to the range of pH where vaterite is stable, the rate of the transformation of vaterite into calcite will be slower.

This could be one of the reasons why the rate equation of this process is yet to be determined, as neither the standard rate equations (kinetic stability) nor the equilibrium reaction constants (thermodynamic stability) take effects such as pH into account. The experimental data clearly demonstrates that the stability of the polymorphs is dependent on pH, meaning that both the kinetics and the thermodynamics of the reaction are pH dependent.

The equilibrium constant of a chemical reaction is defined as:

$$K = e^{-\Delta_r G / RT}, \quad \text{Equation 8.2}$$

Where $\Delta_r G$ is the standard Gibbs energy of the reaction, R is the gas constant and T – temperature in K.^[15]

The equations supporting the equation defining the equilibrium constant are^[230]:

$$\Delta_r G = \sum_B \nu_B \mu_B, \quad \text{Equation 8.3}$$

Where ν_B is the stoichiometric number of component B (positive for products, negative for reactants) and μ_B is the chemical potential of component B of the mixture (also known as molar Gibbs energy). In this representation of a chemical reaction there are only 2 components (A and B), thus for a total standard Gibbs energy of the reaction.^[230]

$$\mu_B = \frac{\delta G}{\delta n_B} \quad \text{Equation 8.4}$$

Where G is the Gibbs free energy of the system and n_B is the amount of component B in the system. One of the standard equations that describes the Gibbs free energy is:^[230]

$$G = H - TS, \quad \text{Equation 8.5}$$

Where H is the enthalpy, S is the entropy.

$$H = U + pV, \quad \text{Equation 8.6}$$

Where U is the internal energy of the system, p – pressure, V – volume. Entropy is a property of a system that was initially defined by R. Clausius as “*transformational content*”.^[231–234] In general, it is considered as a measure of the disorder in the system, as well as the number of the possible states that the system can be in as seen in the Boltzmann relationship (see equation 7.8).^[230]

$$S = \frac{\Delta_{rev} Q}{T} \quad \text{Equation 8.7}$$

$$S = k_B \ln \Gamma \quad \text{Equation 8.8}$$

Here $\Delta_{rev} Q$ is the reversible change in heat of the system (i.e. with no irreversible changes occurring in the system), k_B is the Boltzmann constant, and Γ is the number of possible states that the system can be in.^[230,233,234]

$$U = \delta Q + \delta W \quad \text{Equation 8.9}$$

Alternatively expressed as:

$$\Delta U = Q + W, \quad \text{Equation 8.10}$$

Where Q is the heat brought in to the system, and W is the work performed on the system.^[230]

As it can be seen in equations 7.3 and 7.10 none of these parameters represent changes reflective of the changes in pH of the system. ^[230]

In the case of the commonly used chemical kinetics equations the general expression for the rate equation for an unspecified order is:

$$-\frac{\delta[A]}{\delta t} = k[A]^n, \quad \text{Equation 8.11}$$

Where $[A]$ – is the concentration of the rate limiting reactant, t – time, and k – the rate constant. Similarly, to the case of the thermodynamic equilibrium constant equations the rate constant has no terms that can account for a change in or any effects of pH.^[230]

From the position of transition state theory the same case can be made. The Gibbs energy of activation (also known as standard free energy of activation) describes the standard energy barrier, which needs to be overcome in order for the reaction to proceed. The general equations for the Gibbs energy of activation are:^[230]

$$\Delta G^\ddagger = \Delta H^\ddagger - T\Delta S^\ddagger \quad \text{Equation 8.12}$$

And

$$\Delta G^\ddagger = RT \left[\ln \left(\frac{k_B}{h} \right) - \ln \left(\frac{k}{T} \right) \right] \quad \text{Equation 8.13}$$

Where ΔG^\ddagger is the Gibbs energy of activation, ΔH^\ddagger is the enthalpy of the transition state, ΔS^\ddagger is the entropy of the transition state, h is the Plank constant, and k is the rate constant. The equation 7.12 expresses the ΔG^\ddagger in terms of the thermodynamic equilibrium and as demonstrated earlier in the case of the equilibrium constant, therefore similarly contains no terms that would account for the influence of pH on the Gibbs energy of activation.^[230] Equation 7.13 is an alternative way of expressing the Gibbs energy of activation, which expresses it through constants R , T , k_B and h ,

and the rate constant, none of which can potentially account for the effect of pH on the reaction.

8.4. The conjecture on the electromagnetic approach to ions in solution

The multitude of factors influencing the formation and transformation of calcium carbonates, demonstrate the complexity of the reaction mechanism of a seemingly simple chemical reaction. The lack of a clear mechanism of reaction that underlies all factors affecting the chemical reaction suggests that the answer to this question at the time is non-trivial. Thus, to solve this problem an approach that looks at the fundamental aspects of the factors influencing formation and transformation of CaCO_3 , i.e. “What does this [factor that influences the chemical reaction] fundamentally change?”

8.4.1. Electromagnetic model of nucleation

Looking at the formation of CaCO_3 in inorganic systems, one trend can be noticed: the introduction of ions changes the number of ions in the aqueous system, the change in pH also changes the relative concentrations of OH^- and H^+ ions, and the temperature affect the K_w parameter of water, which is in itself is the increase of the concentrations of OH^- and H^+ ions relative to the number of H_2O molecules.^[226] All of these factors, each in their own way influence the local environment surrounding the Ca^{2+} and CO_3^{2-} ions constituting all CaCO_3 polymorphs.

A similar process that could be drawn upon is the Derjaguin-Landau-Verwey-Overbeek (DLVO) theory, which is used to analyse the interaction between (typically metallic) nanoparticles with changing electrokinetic potential (the zeta potential) of the nanoparticles.^[226,235] The zeta-potential is known to be affected by the ions surrounding the nanoparticle, which can be noticed by the dependency of the zeta potential of nanoparticles on the pH of the surrounding solution.^[235,236] This mechanism seems similar to the ion/dipole induced dipole moment in molecules, thus in a way ions can be considered as charged particles.

Returning to the properties of the nanoparticles, the zeta potential of the nanoparticles can be used as an indicator of aggregation of the nanoparticles in solution which can be interpreted as a point at which the repulsion and attraction forces between the nanoparticles are in equilibrium. The repulsion force can also be

viewed as the particle's affinity to water, hence reinterpreting the zeta potential as the balance of affinity of the nanoparticles towards each other and water molecules.^[237]

When considering the zeta potential of a nanoparticle it is often modelled with the use of the electrical double layer models, which is commonly modelled using the Stern model. The Stern model was initially developed for modelling electrodes, which can be used to approximate sufficiently large nanoparticles with the electrode's potential equalling the surface potential of the nanoparticle. In this models the electrode, and by extension the nanoparticles, are coated with two layers of molecules the tightly bound Stern layer and the loosely bound, diffuse layer.^[237,238]

This can also be used to draw a parallel between nanoparticles and ions, in a sense that the multi-layer model could be applied could be applied to ions. The application of the electric double layer model to ions can be justified by the existence of the Eigen (H_9O_4^+), Zundel (H_5O_2^+), H_7O_3^+ and $\text{H}_{11}\text{O}_5^+$ cation models of the H^+ ion and $[\text{H}(\text{H}_2\text{O})_n]^+$ clusters ,including magic number clusters, where the magic number in this representation is $n=21$ (also represented as $[\text{H}_3\text{O}(\text{H}_2\text{O})_{20}]^+$)^[126,239–243] and other studies^[244]. Such model would indicate that the water molecules directly interacting with the ion will be affected more significantly by the core ion than the water molecules further away from the ion.

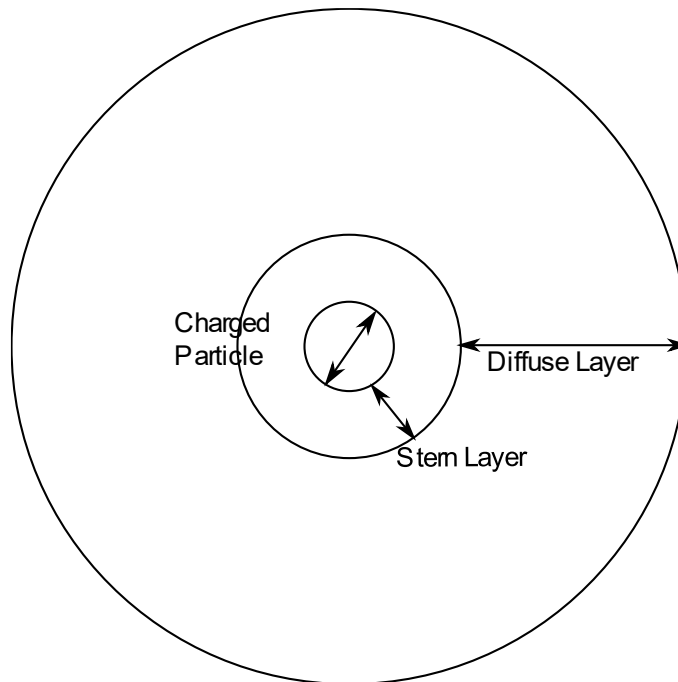


Figure 8.18 A schematic of the Stern double layer model. The inner most circle is the charged particle, the second circle denotes the Stern layer, and the outermost circle denotes the diffuse layer.

Another property dependent on the zeta potential also known as the electrokinetic potential, and indeed the overall charge of a charged particle in general, is the electrophoretic mobility of a particle, i.e. the movement of the particle in an electric field. The charged particles are attracted to the electrodes of the opposite polarity. The same can be said for ions as evident from the principles governing electrophoretic separation techniques.^[126]

On the other hand, polar molecules (molecular dipoles), having a net charge of 0, will reorient themselves in a similar fashion to the flow of ions, positively charged pole of the molecule will orient itself towards the anode (negatively charged electrode) and *vice versa*. Fundamentally, both the cathode and anode are charged surfaces, thus the effects caused by the electric current passing through the electrodes to some degree will apply to charged particles in general. A good example of this are the intermolecular forces, such as dipole-dipole, ion-dipole and ion-induced dipole interactions, caused by the interaction of charged surfaces with each other and inductively charged surfaces. The case of ion-induced dipole is extremely interesting as it demonstrates that a charged particles are capable of inducing charge separation

by interacting with particles. It must be noted that here particles mainly refer to molecules and ions, however due to the similarities of properties outlined earlier, it is likely that such interactions are not strictly limited to ions and molecules.^[126]

As charges are caused by excess or deficiency of electrons in the overall molecular or atomic structure (ions) or locally within the molecular structure (dipoles), the intermolecular interactions can also be understood as weak attractive and repulsive interactions between the protons and electrons in both interacting structures which do not form a chemical bond.^[126,245] The repulsive interactions are between the subatomic particles of the same polarity in both particles such as electron-electron and proton-proton repulsion. In contrast to the repulsive interactions the attractive interactions are between the subatomic particles of opposite polarities, i.e. the electron-proton interaction. To simplify the concept only the interactions between subatomic particles in different systems will be considered, which although less accurate would be enough to highlight the ideas presented in this conjecture. In **Figure 8.19** helium like schematics were chosen to demonstrate the forces acting in the overall system, and the same principle applies to all other atoms and ions except for the H^+ ion, which lacks electrons, thus having no electron-electron repulsion with the interacting atom.

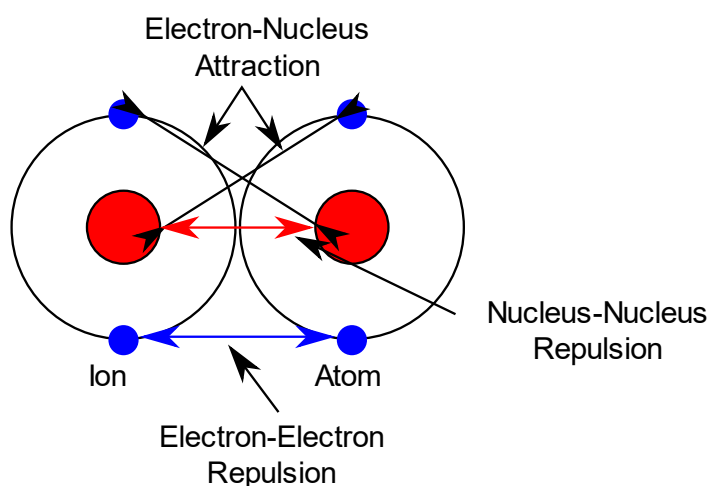


Figure 8.19 A schematic demonstrating the basic repulsion and attraction forces happening in two atoms close to one another.

With this in mind, the Stern layer model could be applied to ion clusters as follows: the shell of water molecules in direct contact with the core ion will be tightly bound and structurally oriented with the pole of opposite polarity facing the ion. This interaction would have 2 major consequences. The first consequence would be the

distortion of the water molecule due to one pole being attracted towards the ion whereas the other pole would be pushed further away from it due to having opposite and same charges respectively. This could be corroborated by the study done on the hydrated crystals of CaCl_2 discussed in Chapter 6.1.4. In this example the profile of the O-H band at $\sim 3500\text{ cm}^{-1}$ is dependent on the stoichiometry of the crystal. Another example of this would be the distortion of the same O-H band at $\sim 3500\text{ cm}^{-1}$ dependant on the concentration of Na_2CO_3 in solution.

The second consequence would be that the core ion would be able to interact with water molecules further away from the centre in what would be the diffuse layer in the Stern layer model. This effect could be potentially exemplified by the influence of the PO_4^{3-} and Mg^{2+} ions affecting the formation of the CaCO_3 polymorphs. It is also evident in the way the pH ions influence the formation of CaCO_3 polymers discussed earlier in this chapter. Assuming that the equation 7.14 holds true, the electromagnetic fields produced by the “Stern” layer of water molecules would not be as strong as the one produced by the core ion, allowing the core ion to react to the molecules and ions in the diffuse layer.

In **Figure 8.20** a positively charged particle is surrounded by the negatively charged pole of the water molecule and the positive poles of the H_2O molecules protrude away from the charged particle. This creates the appearance of a larger “particle” with the same surface polarity as the charged particle, however with different electromagnetic properties, due to being part of a dipole molecule and having a different electronegativity to the charged particle.

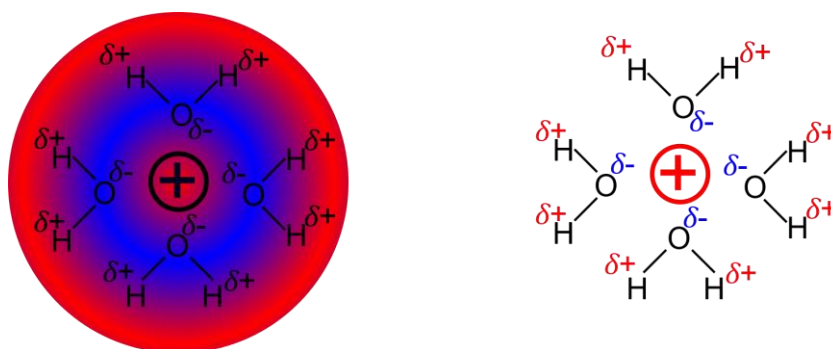


Figure 8.20 A schematic of a charged particle the respective orientation of water molecules in the stern layer (right). The left image shows the polarity of the fields surrounding the charged particle.

$$|z_{ion}| > |\partial| \quad \text{Equation 8.14}$$

Where z_{ion} is the charge of an ion, and ∂ is the partial charge in a dipole molecule. This is also supported by the fact that in a dipole molecule the chemical bonds are not broken to for the poles.

The effect of the ion (which has a magnetic field) and the Stern layer consisting of dipole molecules on the diffuse layer, will follow the superposition principle of electrodynamics, which states that solutions to Maxwell's equations can be combined linearly to find new solutions.^[246]

Another part of the Stern electric double layer model is the diffuse layer, which consists of loosely bound molecules that are interacting with the charged particle. The presence of the diffuse layer signifies that the Stern layer does not fully isolate the surroundings from the attraction and repulsion forces produced by the ion or charged particle.

This means that ions in general and specifically H^+ and OH^- will interact with the ion shielded by the Stern layer. Coming back to the DLVO model, it is reliant on the mean field approximation, which approximates the electromagnetic fields created by the H^+ and OH^- ions as being uniform throughout the solution, i.e. the aqueous solution consisting of H_2O molecules and H^+ and OH^- ions, will have on average a uniform effect on all particles in the system. This can be substantiated by the mobility of the H^+ and OH^- ions, potentially explained by the Grotthuss mechanism (see Figure 8.21).

The mechanism acts by the free proton attaching itself to a water molecule temporarily forming a hydronium ion, which could be considered a transition state. Then a proton detaches from the water molecule, returning to the free proton state. It is important to point out that the detached proton is not necessarily the same proton as the one that previously attached to the water molecule. This mechanism then proceeds to continue as a chain reaction, which allows the proton to "travel" while the atoms remain relatively stationary, thus allowing for the process to happen rapidly. A similar mechanism can also be used for the "movement" of the OH^- ion, except this time a proton from a water molecule will bind to the OH^- ion, breaking the bond with the water molecule it was previously bound with. The speed of the mechanism allows

the mean field theory to be valid approximation of the movement of the ions in the Arrhenius theory of pH.

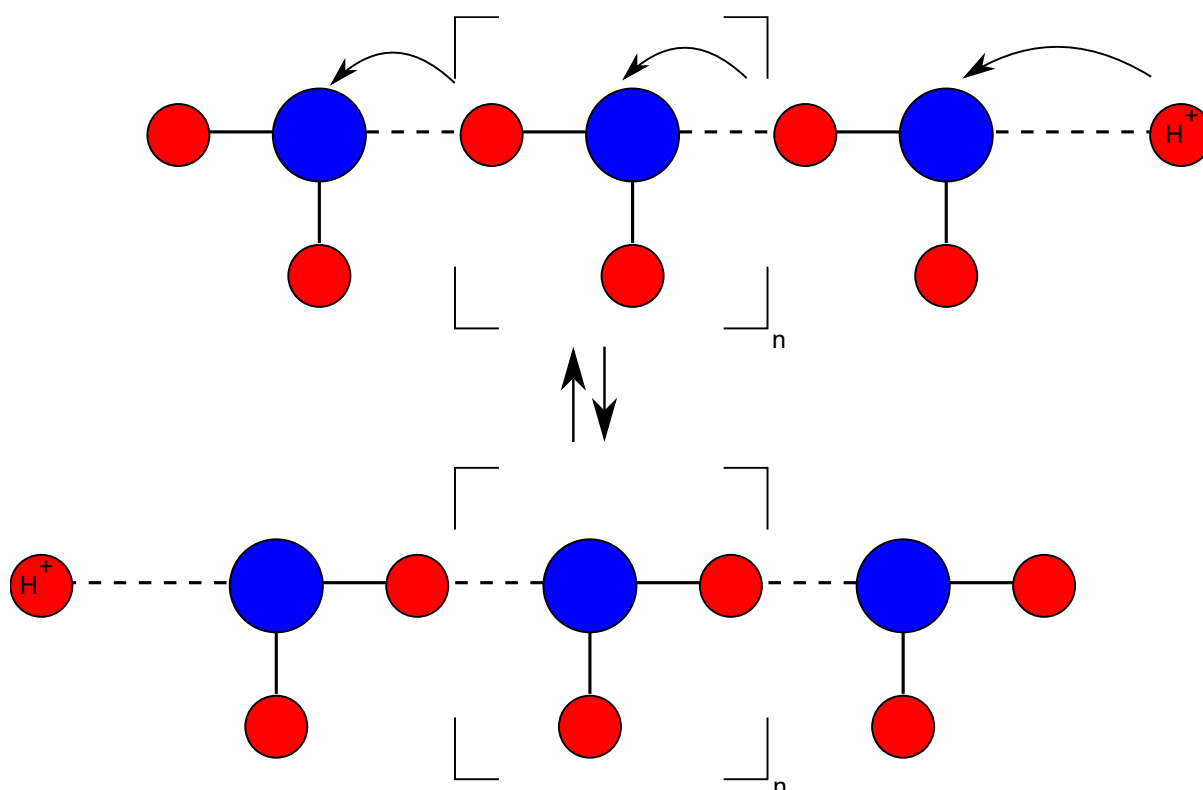


Figure 8.21 A schematic representation of the Grotthuss movement mechanism of a free proton (labelled as H^+) assuming the free proton structure rather than the hydronium ion.

This implies that the total effect of an ion, and by extension an ion cluster, on a system in question will be a product of all electromagnetic fields in the vicinity. Therefore, anything within the Diffuse layer will interact with both the ion and the molecules in the Stern layer, potentially altering the effect of the ion. The increased solubility of the $CaCO_3$ polymorphs with increasing pH of formation (i.e. Ikaite is more soluble than vaterite, which is more soluble than calcite) could potentially indicate this.

8.4.2. Presence of H^+ and OH^- ions within the ion hydration cluster

Considering the interaction of the core ions with the H^+ and OH^- it is important to note that there is no evidence of the principle of electromagnetic attraction/repulsion (same charged particles repel, opposite charges attract) not applying to ions and other charged particles. Thus, it is important to consider the effect the ions of solute have on the pH ions (H^+ and OH^-). The screened structure is more insulated from

influencing the bulk solution, effectively reducing the interaction distance between the screened ion and any other ion it can react with.

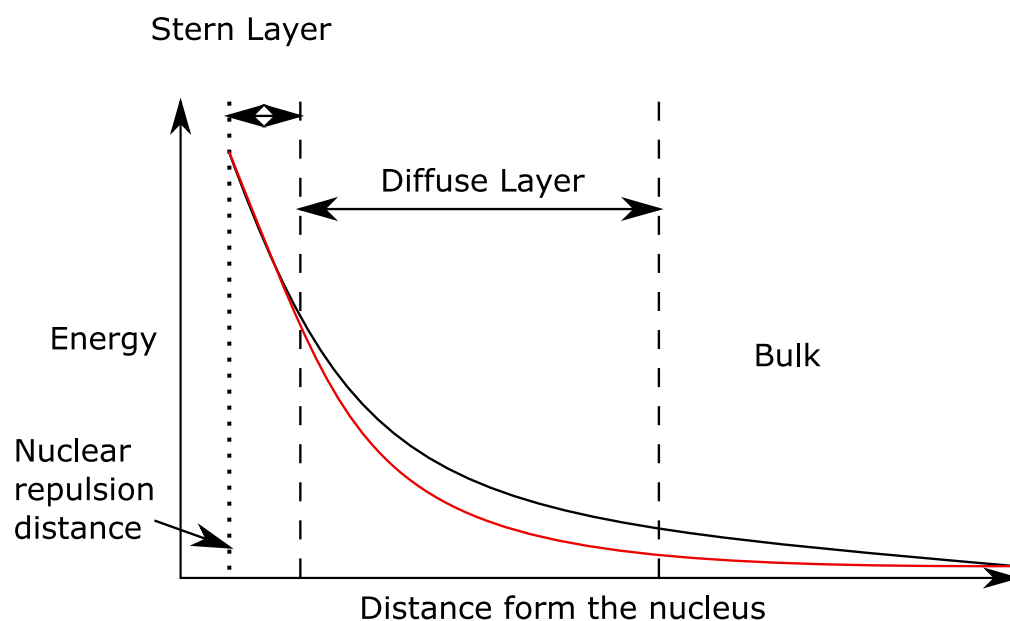


Figure 8.22 A schematic of the strength of the electromagnetic field produced by and ion surrounded only by water (black line) and affected by H^+ or OH^- ions (red line).

As established earlier the ion cluster is a structured environment based around the properties of the core ion, which results in a distortion of the electromagnetic field that is naturally present in pure water. This does also imply that the core ion will produce a positively or negatively charged local environment in its surroundings, primarily the Stern and the diffuse layers of the Stern electrical double layer model. Therefore, depending on the ion at the core of the ion cluster, protons and hydroxide ions will either gain or lose stability while existing in the ion cluster. As a pH ion enters the space affected by the electromagnetic field produced by a solute ion it will be either attracted if the ions have opposing polarities and repulsed from the area if the ions have the same polarity (see **Figure 8.23**).

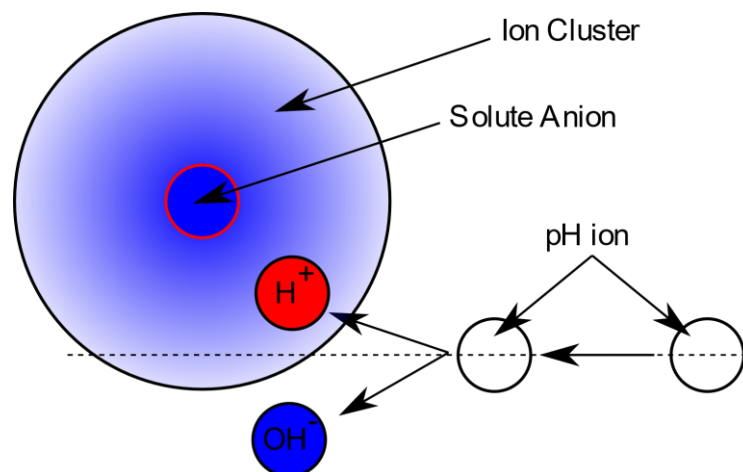


Figure 8.23 A 2D schematic of the mechanism of attraction/repulsion of a pH ion (H^+ or OH^-) by a solute ion, which in this case is an anion. The straight dashed line is the idealised movement trajectory of the pH ion unaltered by the presence of a solute ion. The black circle around the solute ion is the border of the area of influence of the electromagnetic field produced by the solute ion.

For example, a proton will be attracted by interacting with an anionic ion cluster, and repulsed while interaction with a cationic ion cluster, relatively to the water outside of the clusters. This could also be interpreted in the context of a dynamic system as speeding up or slowing down the Grotthuss mechanism, forcing the ion to spend more or less time in the proximity of the ion cluster. This would result in the solute ions affecting the interaction time of the pH ion within the ion cluster and its local environment. A distinction needs to be made that this would not affect the pH value, as the total concentration of protons and hydroxide ions remains the same and the only thing that is altered is the interaction time. This would produce an effect similar to what is known in electronics as pulse-duration modulation (also known as pulse-width modulation)^[247], where the duration of a pulse, which in the case of ions will be the time either a H^+ or an OH^- ion will be present in the environment, will affect the perceived amplitude over a discrete time interval, i.e. if a proton exists in a local environment for half the time due to the presence of a cation it will have half of the effect than a proton existing for the entire time period.

Such a mechanism would explain the influence of the presence of phosphate ions on the formation of the $CaCO_3$ polymorphs, as PO_4^{3-} ions have been shown to lower the pH of formation of ikaite. A similar mechanism exists in organic super bases,

specifically proton sponges, which absorb protons from their environment due to sterically positioned lone electron pairs. In the case of ions such an effect would be much less pronounced, as the ions discussed simply retain ions for a fraction of time rather than fully absorbing ions as proton sponges do.

This would also mean that that the pH ions will also affect the bonding properties of the solute ions explaining the dependency of the CaCO₃ polymorphs on the pH of the reaction, as well as their stability. This would also be corroborated by the dependency of the zeta potential of nanoparticles on the pH of the solution. While the nanoparticles themselves do not have a formal charge, the charge is induced by the pH ions in the solution, which signifies the effect of the pH ions on the nanoparticle at the core of the Stern double layer model.

8.4.3. Solubility and phase separation of non-polar compounds

The described model does also explain the solubility of a non-polar compound in polar solvent, as well as separation of two non-polar compounds in an applied electromagnetic field. Both phenomena rely on the same basic principle of dipole moment induction either by an ion, a permanent dipole or by an electromagnetic field directly. Fundamentally the induced dipole moment will be a property of a covalent bond between two different atoms, caused by the electronegativity mismatch between the atoms. The same statement can also be said for the permanent dipole moment, however in the case of the permanent dipole the electronegativity mismatch between the atoms is large enough to produce a constant charge separation, whereas in the case of an induced dipole, an external electromagnetic field (produced by either ion, permanent dipole or an electromagnetic field) is necessary of the charge separation to occur.

It is likely insolubility of non-polar compounds is caused by the degree of charge separation within the molecule, which could be induced by the molecules environment. The induction of will alter the energy of the chemical bonds of the molecule, from its lowest energy state (for example molecule in a box, i.e. nothing interacting with that molecule). This leads to a scenario where the molecule will be closer to it's lowest energy state surrounded by molecules with a similar degree of charge separation, rather than dissimilar, aggregating into clusters of lowest energy state environment. This logic could be used to explain the phase separation between polar and non-polar liquids, and the mechanisms of dipole moment induction.

The other side of this same effect is that the presence of induced dipole moments will allow non-polar molecules have a small degree of solubility. Thus, if the molecule is too far away to interact with any molecules other than the molecules of the solvent, the molecule will remain dissolved. The distance over which it would be able to interact would be dependent on degree of the induced charge separation. This can be supported by the classical homogeneous nucleation theory, even if two non-polar molecules would find each other and interact that would not be enough to create a separate phase, as the induction of the of the dipole would separate the molecules. Therefore, in this context it is possible to define a threshold for what could be considered a separate phase as the same radius at which it passes the nucleation energy barrier, i.e. the radius of the molecular cluster at which spontaneous dissolution becomes unlikely, which also corresponds to the definition of a nucleation nucleus.

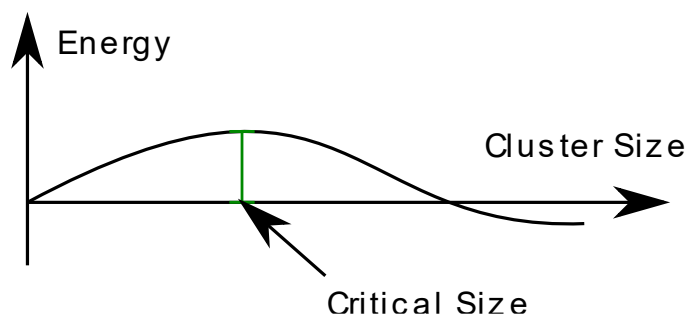


Figure 8.24 A schematic of the critical size of a critical nucleation cluster size (shown in green). If the cluster's size is less than the critical size the cluster will dissolve to lose energy, whereas if its size is larger than the critical size it will prefer to increase in size to lose energy.

Such definition of the phase separation has 2 major consequences: that for any compound there will always be a concentration at which it will dissolve in a solvent, for example water. This is readily corroborated by the fact that the compounds classified as insoluble will still be soluble, which enables the mechanism of Ostwald ripening. When looking at what concentration is it is possible to notice that on one hand it expresses the number of solute molecules per unit volume, and on the other hand it can be conceptualised as a distance between non-polar molecules that will prevent them from interacting. This also allows interpreting solubility of molecules and ions as a dynamic equilibrium between dissolution and precipitation.

This mechanism however is not restricted to non-polar compounds, rather applying to any mixtures that are not completely miscible (i.e. from a homogeneous solution in any proportion). Thus, by interpreting solubility this way it is possible to state that in a thermodynamically equilibrated solution interacting molecules or ions will be distant enough from each other not to produce a meaningful chemical reaction, for example nucleate.

The second consequence is that the entire solution is the same phase. By using this and the definition of the refractive index: "*The ratio of the speed of light in vacuum to that in a given medium.*"^[15] it is possible to say that the existence of different refractive indexes in an equilibrated solution is impossible. However, separation of a solution of two non-polar compounds into two compounds was experimentally demonstrated Walton and Wynne, where they separated decane and nitrobenzene from one another using optical tweezers.^[248]

As mentioned in Chapter 2, dielectric particles significantly smaller than the wavelength (Rayleigh particles) will be trapped as point dipoles. What fundamentally distinguishes between a dielectric and insulators, is the ability of the dielectric to be polarised in an electric field, creating charge separation within the molecule, which is the definition of an induced dipole. Decane is a non-polar solvent, and the magnetic field induced by the laser creates charge separation in both decane and nitrobenzene, however to a much larger extent in nitrobenzene, due to the presence of the nitro group in its structure. The induced dipole moment will create an attractive dipole-dipole interaction between nitrobenzene molecules, similarly to hydrogen bonding mechanism in water. This would explain the increase in the concentration of nitrobenzene in the optical tweezers and the depletion zone around it. A logical conclusion would be that the shape of the laser-induced nitrobenzene enriched area will reflect the beam intensity profile of the laser. Thus, it would lead to conclusion that the effect is spatially constrained by the effective radius of the electromagnetic field.^[248]

The approach that Walton and Wynne took to explain their results was using the refractive indexes of nitrobenzene and decane.^[248] As mentioned earlier the fundamental concept of two different refractive indexes in a homogeneous solution is contradicting the concept of a homogeneous solution. Thus, while being a perfect explanation if the two compounds would have existed as a micro-emulsion. On a

molecular it seems to be more appropriate to utilise the polarizabilities of each of the compounds which are related to the refractive index through the Lorentz–Lorenz relationship.^[249–252]

This demonstrates the fact that electromagnetic fields produced by either radiation, ions or molecular dipoles can have a significant influence on molecules ions and molecules. This effect however would be spatially restricted to the area of effect of the electromagnetic field, and anything outside of that area will remain unchanged.

8.4.4. Opposite polarities of ions in solution, proximity interactions and the dissolution-precipitation equilibrium

When considering the solubility of ionic compounds such as CaCl_2 , Na_2CO_3 NaCl and CaCO_3 , it is important to identify that fundamentally their aqueous solutions will have 2 cluster systems simultaneously present in the solution: cationic and anionic systems. This is also true for pure H_2O solutions due to the autoionization of water, which produces both H^+ and OH^- ions, however due to the Grotthuss mechanism of transportation (see Figure 8.21) it would not serve as a good example, even though as demonstrated previously cationic clusters will still form.

Therefore, when considering solutions, it is important to consider the interactions of the ions and their hydration clusters between the cationic and anionic systems. On their own the cation and the anion will produce a force attracting each other, forming the dry crystals with their specific stoichiometry. An example of this would be NaCl crystals, which forms a nice, simple cubic lattice, where all Na^+ ions are surrounded by Cl^- ions and *vice versa*, having a 1:1 stoichiometry. CaCl_2 for example will have a 1:2 cation to anion stoichiometry forming a crystal with a different structure than that of NaCl .

When considering an aqueous solution of NaCl it will consist of hydrated Na^+ and Cl^- ion clusters. As Na^+ and Cl^- are charged they will orientate a Stern layer of water molecules in accordance with the charge of the core ion. The diffuse layer will also orient itself accordingly, with a decreasing influence of the core ion on the water molecules. The dependence of the influence of the core ion on its local environment on the distance to the ion can again be thought of as supporting the interpretation of the solute concentration as the distance between cations and anions at which they do not interact well enough to precipitate. As also mentioned previously,

electromagnetic fields can have a significant impact on ions and molecules, therefore it should be considered that they affect the distance of the interaction between ions in solution.

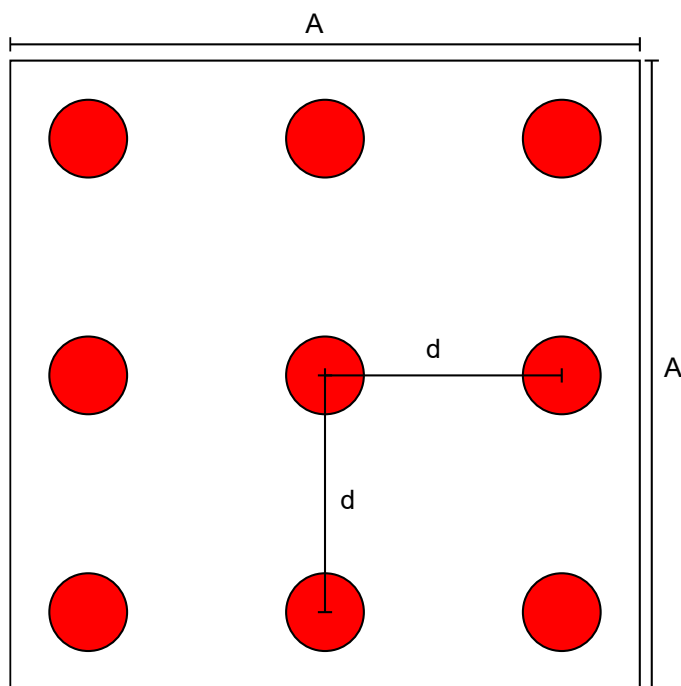


Figure 8.25 A 2D schematic demonstrating the concept of converting a concentration to distance between two closest ions. In this case a number of ions (red dots) per unit of space (2D – Area, 3D – Volume), or viewed as a distance between the neighbouring ions or particles, assuming equal distribution.

8.4.5. Comparison with the Debye–Hückel theory

It would be impossible to omit the similarities of the ideas presented in this conjecture. Both view ions as charged particles that attract counterions from the solvent, typically water, which do not chemically react with the core ion. The solvent counterions are also represented using mean field theory, i.e. not as discrete particles but as a spread-out field. Both theories also consider the area affected by the core ion either as part the ionic atmosphere or as part of an electric double layer model (specifically Stern electric double layer model). Both theories also consider the attraction and repulsion forces produced by the ion as dependent on the distance away from the core ion, in the Debye–Hückel theory Coulomb's inverse square law is utilised to quantify these interactions. Both models also consider the non-randomness of the solvent ion distribution within the area affected by the core ion.^[253]

What makes this conjecture distinct from the Debye–Hückel theory are that in this conjecture water is not treated as a uniform medium and that water is reoriented in the presence of the core ion.^[253] Next point that makes this conjecture distinct is that the core ion is influenced by the presence of solvent ions within the core ions solvation cluster, and distinctly from the AIOMFAC model considers the entire cluster rather than the equivalent of the stern layer^[171,172]. Another unique point of this theory is that the presence of a solute ion will affect the pH ions, altering their effect on a local scale as a time averaged effect. Fundamentally this conjecture was designed as a potential explanation to the effect of the pH and ions that do not participate in the chemical reaction on the chemical reactants. Specifically, the reactions observed in the literature and experimental data discussed earlier in this chapter.

Considering the entirety of the reaction it is crucial to point out that the formation of CaCO₃ polymorphs is not only pH dependent, but temperature dependent as well, as seen in the literature with the formation of aragonite.^[59,62] Therefore, it must be stated that in this conjecture does not account for temperature. It is plausible that the rise in temperature would increase the influence of the pH ions by increasing the total number of ions produced by autoionization of water molecules. Additionally, the increase in temperature would increase the total energy of the system, allowing vaterite to transform via a pathway that requires a higher activation energy than the formation of calcite.

8.4.6. Influence of additional ions on the localised distribution of H⁺ and OH⁻ ions, and by proxy the local electric field

Similarly, to the Ca²⁺ and CO₃²⁻ ions, other ions such as Mg²⁺ and PO₄²⁻ ions will produce their own electromagnetic field which will deplete the surrounding solution of OH⁻ and H⁺ ions respectively. This effect will also be influenced by the types of ions (anion/cation, atomic/molecular, etc.) and their structure. The net effect of depletion of the solution of the H⁺ and OH⁻ ions will remain, thus even though the pH of the solution would remain the same, the mean field approximation would not account for the local influence of the additional ions, which would result in different conditions experienced by the reacting ions, thus altering their chemistry, resulting in different polymorphs.

The simplest example of this would be a potential explanation of the influence of pH and phosphate ions on the different polymorphs produced by the reaction. As the

PO_4^{2-} ion is negatively charged and therefore will preferentially attract H^+ ions from the aqueous solution. As the pH is dependent on the relative concentrations of the H^+ and OH^- in the aqueous solution, the preferential attraction of the H^+ ions from the solution will locally increase the relative concentration of the OH^- ions, thus producing an effect similar to an increase in pH, within the local vicinity of the PO_4^{2-} ions. This effect could be evidenced by the formation of ikaite at lower pH in the presence of phosphate ions than in the absence of PO_4^{2-} ions.

Such an approach, which looks at ions and dielectric molecules not as individual chemical, but as polar particles influencing and influenced by the external fields produced by other charged particles and fields. This implies that the chemical reaction and physical transformation mechanisms between molecules will be influenced by their electromagnetic environments, as it is possible to see in the case of formation of CaCO_3 polymorphs. An important point to address is the transformation of polymorphs of CaCO_3 between each other, which can also be explained using this electromagnetic interaction framework.

A well-known transformation is the gradual transformation of vaterite into calcite in an aqueous environment, which was observed experimentally and is noted in the literature earlier in this chapter. The electromagnetic approach would suggest that during the formation process of the reaction vaterite is kinetically stable, due to the electromagnetic environment produced by the pH of the solution. Meaning that the electromagnetic environment will create an energy barrier for the transformation of vaterite into calcite, and as the electromagnetic can be influenced by the pH and ions locally altering the pH can be high enough to prevent the transformation from happening, thus kinetically governing it. In a case of the energy barrier being small enough for the process to occur the probability of the ions passing the energy barrier will govern the kinetics of the transformation.

Taking into account that the Ca^{2+} and CO_3^{2-} ions in vaterite crystals will exist surrounded by other Ca^{2+} and CO_3^{2-} ions, means that the ion pairs on the surface of the crystal will transition due to the electromagnetic environment of the solution, whilst simultaneously being stabilised by the crystal. This would make the formation of a core-shell particles of different polymorphs unfavourable, as reported by Ogino et al.^[59] However, this also suggests that if the crystal is small enough there could be

a certain set of conditions allowing a chain transformation to proceed, so that the entire crystal is transformed simultaneously.

8.4.7. Literature and rationale

There is an abundance of literature considering electromagnetic interactions between atoms, molecules and in molecular systems. The vast amount of literature available cannot be fully studied and addressed to full extent, hence the ideas outlined in this part of the chapter can only be considered a conjecture. However, it is possible to briefly address some of the underlying principles of the studies found in the literature outlining the key differences between the approach used in the literature and this conjecture.

The overall approach of using electromagnetic interactions for modelling chemical systems can be justified by the fact that the electromagnetic force is one of the fundamental forces in physics is responsible for all interatomic atomic interactions such as chemical bonding, dispersion forces, Van der Waals interactions, etc. The other forces of the standard model are the strong and weak nuclear forces, both of which are responsible for the interactions on a sub-atomic level, and gravity.^[254]

Among the key proposals of this conjecture is the lack of use of the Debye–Hückel theory and the mean-field approximation, which are the basis of calculations of electromagnetic forces.^[255,256] While it is not impossible to use the approaches existing in the literature to model systems in a similar way to what is proposed in this conjecture, one would need to modify them similarly to the AIOMFAC model, however likely to a larger extent.

8.4.7.1. Affected aspects of biological systems

Ions can affect many aspects of biological systems. One of the most significant aspects of which are the co-factors, which are necessary for the activity of some enzymes, with examples including hydrogenases and DNA polymerases.^[257,258] One of the general areas that would also be affected by pH activity of the enzymes.^[259] The disorders associated with pH being outside of the normal range are acidosis and alkalosis.

8.4.7.2. Ion transfer through the membrane

Ion transport through the membrane can be achieved via both active and passive transport typically classified as channels (passive) and pumps (active).^[260] Both of these can be selectively opened or closed by binding of molecules, or changes in the membrane such as a change in voltage, and in the case of the H⁺ ion channel pH.^[261–263]

8.4.7.3. Electrostatic modelling of proteins

Currently electrostatic models of molecules and all-atom molecular simulations are used primarily for analysing intermolecular interactions, with one of the major applications in modelling passive molecular transport through cellular outer membranes (OM). One of such classes of molecules are known as porins which forms pores on the outer membrane of bacteria, and are suspected to be the primary route of small molecule transport across the OM. One of the primary ways of studying of these proteins is by using electrostatic all-atom molecular simulation determining free energy flow of across, correlating to the molecular flux across the pyrene. This is especially important for a group of bacteria known as ESKAPE bacteria as they are primarily known to be hospital bacteria and are resistant to antibiotics. This makes the ESKAPE pathogens critical and of high importance for development of new antibiotics by the WHO and CDC (UK).^[264–267]

One of the drawbacks of these studies is that accurate and varied matrix composition is rarely used, hence are unlikely to accurately account for the influence of the solvents or the ions within the solvent. These models can however account for the molecules neighboring the porin such as the membrane molecules and can be varied, as it can be seen in symmetric (both sides of the modelled membrane are modelled from the same compound) and asymmetric (different compounds on each side of the membrane, which more closely resemble the bacterial OM).^[268]

The consideration given to these factors can also be given to other molecules within the other systems of cells. Another example of a pH sensitive molecule is the transcriptase molecular complex, which transcribes the DNA sequence on to the tRNA (transfer RNA). The changes in pH of the is complex have been associated with a large variety of diseases including cancer. Within the cell such a change in pH

can be caused by overproduction of citrate used within the Krebs cycle (a part of cellular breathing).^[269]

Electrostatic modelling of organics and proteins consider the same aspects of the of electrostatics and are deficient in overlooking the same aspects of molecular interaction such as the matrix composition. These factors may incline researchers to overlook such factors in studying the behaviour of these molecules. On a more technical side of the same conversation the outlined considerations can be applied to engineering, with one of the examples being the lifetime of liquid cooling systems, which can be significantly affected by pH. Other similar aspects could be in the systematised diffusion of solid catalysts into the product on a sub-ultratrace levels, known as component exhaustion. The outlined conjecture suggests a way of systematising the dissolution of compounds that are considered insoluble, such as the solubility of calcium carbonate at 0.135 mg L^{-1} considered insoluble.

8.4.8. Implications

Such an approach to chemical reactions and physical transformations has multiple implications for the analysis of the reaction mechanisms, crystallization of compounds potentially allowing a more detailed and systematic approach to their study, “shedding new light on an old problem”.

8.4.8.1. Reaction mechanisms

The outlined electromagnetic approach to chemical reactions could potentially allow for the possibility of finer control of chemical reactions, using pH, additional ions and electromagnetic fields, than is currently available. The other side of this approach is that it looks at the fundamental interactions between atoms, molecules and ions, which could be used to gain insight into complex chemical reactions, one of which is the full mechanism of formation of CaCO_3 and account for the different morphologies. Another example of a complex reaction is the reaction producing MgCO_3 compounds, which can have multiple hydration states, forming multiple different minerals. This approach could be used to study the influence of not only ions, but also more complex processes such as the influence of proteins on the formation of minerals and the stabilization of the proto-states in the ACC in skeletal structures.^[76,214,223]

8.4.8.2. Aerosol super saturation

When considering the outlined conjecture can be noted that it suggests a degree of binding of solvent dipole molecules to a solute ion. This interaction also shows that there is likely a degree of order in the arrangement of the water molecules, both of which will influence the binding of the molecules to one-another, thus influencing the vapour pressure of water above the surface of a liquid consisting of ionic clusters. This effect would be dependent on the concentration of the solute in the solution, as outlined earlier concentration can be interpreted as distance between different core ions, thus demonstrating the influence of the ion clusters on the vapour pressure of the solvent. The ions and water molecules are not to scale relative to one another. It is however worth noting that the distance between the interacting particles will affect the strength of the interaction. (See **Figure 8.26**)

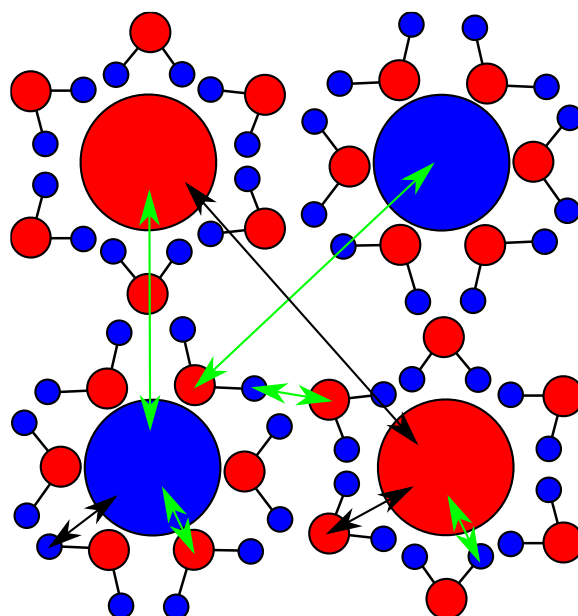


Figure 8.26 A schematic showing the equilibrium of forces acting on both ions and water molecules in their Stokes layer (the tightly bound layer of coordinated water molecules interacting with an ion in an immediate vicinity). The green arrows represent the attractive interactions, whereas the black arrows represent repulsive interactions. In this schematic the particles with the charge or partial charge of the same polarity are of the same colour regardless of the amplitude, with the black lines representing covalent chemical bonds in the water molecules.

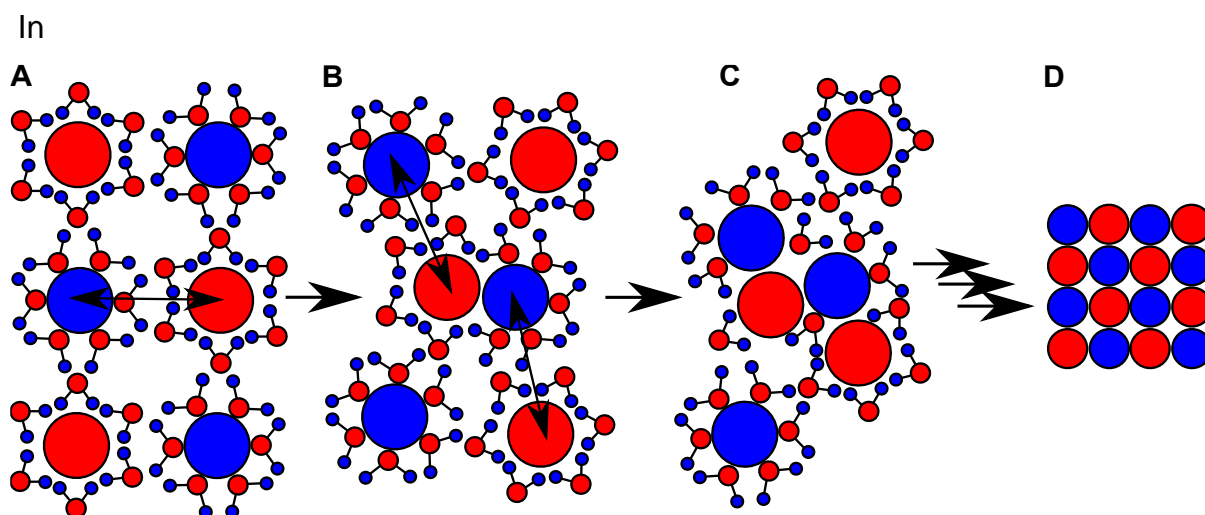


Figure 8.27, the particles with the charge or partial charge of the same polarity are of the same colour, with the black lines representing covalent chemical bonds in the water molecules. The ions and water molecules are not to scale relative to one another. Part **A** depicts the super-saturation equilibrium, with the black double arrow representing a collapse of this equilibrium of forces. Part **B** represents the reacted ion pair and that the disturbance of the equilibrium in **A** causes other ions to react with the newly formed ion pair, thus perpetuating a chain reaction. Part **C** shows the immediate consequence of the reaction in **B**. Part **D** demonstrates the finished result of the chain reaction – a formed crystal.

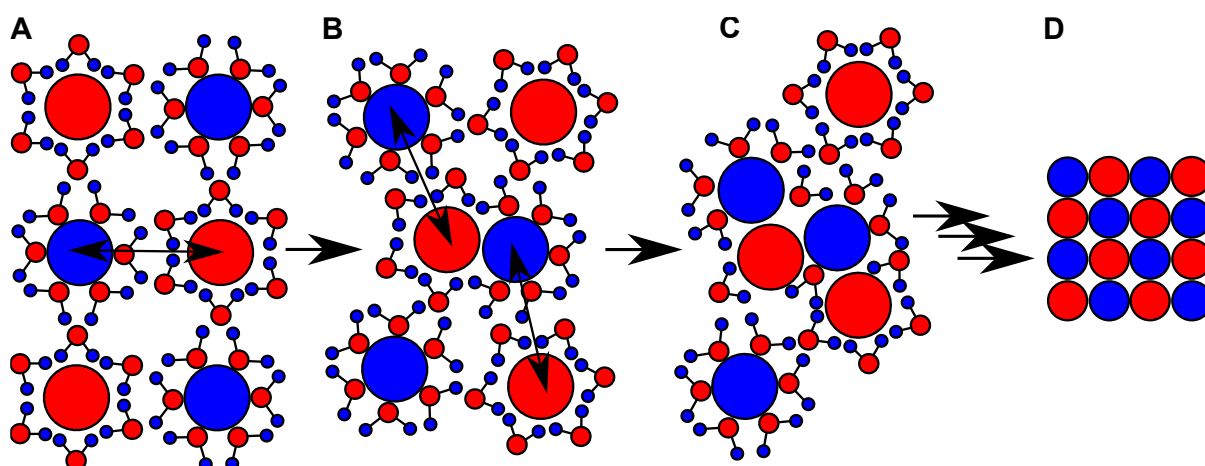


Figure 8.27 A schematic of the mechanism of the collapse of the electrostatic equilibrium between the ions and water molecules under super-saturation conditions. The black double-headed arrows represent an attractive interaction, whereas the single-headed black arrows represent the progression between the different states of the systems (from **A** to **C**).

Another point this approach to ions in an aqueous solution, would also be a step towards explaining the mechanism allowing super-saturated states to occur. As water molecules close to core ion are more tightly bound to the ionic cluster structure additional energy is required to remove them, for example by evaporation. With the number of water molecules decreasing to the number of molecules in the Stern layer, which is extremely tightly bound to the core ion the energy required to strip them from the structure also rises. However aqueous solutions will always have counterions within them, thus at low water content there will be some interactions between the ions of different polarities. Both of the ions will still have the Stern layer of water molecules surrounding the core ions, and the same molecule will interact with both ions, the interaction with the ion to which Stern layer it belongs will be significantly stronger than to the other ion. Thus, the structure depicted in figure N will interact with the counterion and its Stern layer of water molecules, preventing the ions from interacting and forming a solid. This mechanism would allow the solute to retain water molecules until there was something that could disturb the equilibrium between the ions surrounded only by the Stern layer of water molecules, remaining in equilibrium with each other, under conditions of purely homogeneous nucleation. However, if this equilibrium would be destroyed providing a bound ion pair or a surface with which other ions could interact, a chain reaction would ensue, producing rapid crystallization, with the amount of water that could be attracted not being enough to dissolve the crystal.

This approach is extremely similar to the experimentally proven concept of ion association mechanism. Distinctly from the ion association model, this conjecture relies on molecular rotation of water molecules bound to the ions as well as any charges, polarization and polarizabilities, rather than the dielectric properties and donicity (also known as donor number, a measure of basicity in the Lewis acid-base model).^[224]

8.4.8.3. Classical chemical kinetics and thermodynamics

While it is possible to account for the influence of pH on kinetics and thermodynamics of a chemical reaction by introducing an experimentally derived factor into the final equilibrium constant, activation energy and rate equations, it would likely be more accurate to work out the exact factors that would be influenced by changes in the pH. Fundamentally as pH would have an influence on the enthalpy of the chemical

system as the pH, and in the purest form the K_w , would influence the internal energy of the system. From the other point of view pH in the case of additional ion such as PO_4^{3-} will affect the pH on a local scale thus altering the number of possible states a local environments, changing the entropy of the system.

It is not inconceivable that an approach based on the electrostatic and electrodynamic interactions could produce a system alternative to the currently used classical kinetic and thermodynamic models. If that would be the case, such a model would require software to be practically usable and would likely in practical applications outperform the relative simplicity and accuracy of the classical models only select applications (i.e. more likely than not it would not be universally better). The likely necessity of decision support tools also needs to be approached with caution, as careless use in order to accelerate the speed of publication based on a lack of adequate knowledge of the working principles could lead to critical miscalculation or misuse, thus spreading misinformation.

8.4.8.4. Crystallization of highly soluble compounds and proteins

As examined using the example of nitrobenzene in decane mixtures and nanoparticles, local electromagnetic fields can alter the crystallization, aggregation, and other interactions between molecules and particles. This provides a different view on the classic theory of nucleation, adding the complexity of external electromagnetic fields, ionic and dipole screening, and the localised electromagnetic effects of additional ions, which as stated earlier in this chapter, can be used in the analysis of complex chemical reactions. Another side of this, is the use of these principles to force nucleation, as done with nitrobenzene.^[248]

An immediate application of this theory could be in protein structure determination, which relies heavily on the use of x-ray crystallography. As the name suggests crystallography requires the material to be crystallized, which could provide a challenge. The application of this electromagnetic theory of nucleation could be used to optimize the crystallization conditions allowing increased control over the crystal formation, potentially reducing the time needed to produce the crystals, and the amount of experiments and reagents necessary to find the crystallization conditions. Such an approach would also increase the certainty of whether the protein is likely to crystallize or not, which would allow such decisions to be made quicker, thus avoiding some of the unnecessary delays.^[270–274]

This approach to nucleation also highlights a drawback of structure elucidation using crystallographic methods: the influence of the local environment. This would mean that the structures of molecules could be different in solid state such as a crystal, and liquid state in a solution, as the environment in a crystalline lattice or an amorphous compound would be different than those in as liquid state or a solution. This is likely to have implications to protein structure identification, as the structures are identified in their crystalline forms and in cells primarily exist surrounded by a liquid medium, almost constantly interacting with other proteins, which would alter the local environment of the molecule, thus potentially changing the structure of the protein. This theory could also be used to account for such interactions.^[270–274]

In terms of modelling the chemical reactions it would be possible to view the reaction with its conditions as a function, of the reaction conditions, such as temperature, pH, ions, etc., and properties such as the rate of the reaction, the stability of the formed polymorph, the equilibrium constant, etc., as independent and dependent variables, allowing to view the chemical reactions as N-dimensional function spaces, similarly to the principles of mathematical optimization discussed earlier in this work (see chapter 3.2).

This would allow viewing the reaction parameters in terms of the topological analysis of the function space of all of the parameters influencing the reaction, allowing precise calculation of the optimal conditions for the reaction, which would be useful for a better understanding of chemical reactions, and bring a huge toolkit of mathematical methods into chemistry.

It also allows viewing the changes in the reaction produced by a parameter as a differential of the total chemical reaction equations with respect to the parameter. For example, the rate constant of reaction is dependent on the temperature as seen in the Arrhenius reaction^[126]:

$$k = A \exp\left(\frac{-E_a}{RT}\right), \quad \text{Equation 8.15}$$

Where k is the rate constant, A is the pre-exponential factor (constant by definition, specific to the reaction), E_a is the activation energy (energy of the energy barrier of the reaction), R - gas constant, and T is the temperature. When considering this reaction only with respect to the change in T , with all other variables being held constant, the rate constant becomes proportional to the temperature.

This approach is also likely to bring benefits to researchers in synthetic chemistry by providing a route to maximize yields and in biological sciences as a framework for complex biochemical processes and for accounting for the influence of the conditions on the protein structure and function.

The same framework could also benefit industry as it can be used for optimizing the chemical reactions with a cost-to-benefit analysis, by relating the reaction conditions to the respective cost elements.

8.4.8.5. Some self-criticism

This conjecture is by no means complete or comprehensive, and therefore multiple factors need to be included in order to formulate a full theory. One of the major points necessary to address is the huge amount of literature on solvent effects, which may render some of the aspects discussed in this section obsolete. However, the lack of variables addressing the influences of pH and ions chemical kinetics and thermodynamic equations signifies potential benefits of doing so.

These factors include a comprehensive estimation of the effects of temperature, shape of the ion, any specific aspects of multipoles both as a core of a cluster and as a solvent molecule, molecular vibrations, particle motion, viscosity of the liquid, the rotational reorientation time and the frequency of the applied external fields, all of which will contribute to attractive and repulsive interactions between molecules and ions. Another important parameter is mass, as it can be signified by the influence of mass on the polarizability tensor and electric susceptibility, evidenced by the different Raman shifts of the broad peaks: H₂O and D₂O in the Raman spectrum. From a purely physics perspective it would be beneficial to look at the influence of the Casimir and Casimir-Polder forces and include a more in-depth account of the van der Waals forces as outlined in the literature^[61,275–281].

8.5. Conclusions

In this chapter the literature regarding the chemical reactions forming the different polymorphs of calcium carbonate ranging from the computational aspects, the influence of temperature, pH and other ions, and some of the relevant work on biogenic calcium carbonate was reviewed to establish a background and provide a clear distinction between the literature and the original work and arguments presented in this thesis.

The original work presented in this chapter demonstrates the different pathways that a reaction between aqueous solutions of CaCl₂ and Na₂CO₃ can take depending on the ratios of the reagents used. Namely, the reaction can form hexahydrocalcite (more commonly known as ikaite) both directly and from an anhydrous polymorph – vaterite. Vaterite can also be stable in an aqueous solution as well as to me a kinetic intermediate in the formation of calcite. In this chapter I also provide experimental evidence of the direct formation of the calcite polymorph from the amorphous calcium

carbonate. The same data also demonstrates that fundamentally the reaction does not end with the formation of a specific polymorph, but the polymorph itself continues to equilibrate to a more regular crystalline structure.

The work presented in this chapter also supports the theory of formation of short-range crystalline orders, which serve as precursors to the polymorphs formed from the amorphous polymorphs, named for example proto-vaterite, when it is a precursor for the vaterite crystal. This is supported by experimental data in both inorganic and biogenic systems, however in this work the direct formation of calcite is presented, thus supporting the existence of proto-calcite in inorganic systems, as it has been found in biological systems. This implies that there could be more to the amorphous morphologies of compounds than simply lacking a crystalline order, and that the term amorphous could be an umbrella term describing multiple possibly temporarily formed precursor morphologies.

In this chapter the pH of the chemical reactions as well as the measurement of pH in aerosols are also discussed. One of the fundamental concepts regarding pH outlined in this chapter is that while concentration of solute in a solution affects the pH of an aqueous solution the dependency is not linear, and the equilibrium pH of the solution can be reached at lower concentrations than the saturation point of the solution. This point is used to argue that while it was impossible to measure the pH in the aerosol droplet during the reaction it is however possible to use the pH of the solutions mixed in bulk and measured using a standard pH electrode as an estimate for the pH of the reaction. This is used as a basis for stating that the formation of calcium carbonates is pH dependent in both its kinetics and thermodynamics, which is a potential reason why neither the rate of formation of calcium carbonate nor an accurate range of conditions at which vaterite is stable have been determined.

Finally, in this chapter several conjectures with supporting arguments are provided in an attempt to provide a potential way of explaining some of the observed phenomena discussed in this chapter.

This detailed understanding of the processes involved in crystal formation, particularly the formation and transformation of ACC could lead to important advances in the ability of controlling overall formation of crystals. This will likely lead to two types of possible benefits. The first type is the improved ability to form crystals, which would allow producing crystals of new materials, such as some proteins that

are hard to crystallize^[270–274,282], and potentially optimization of yields in precipitation and crystal forming reactions. The second benefit type is preventing the formation of crystals, which can lead improvements in cryopreservation of cells, and potential development of cryopreservation technologies capable of storing tissues and organs, as formation of ice crystals inside cells damages their structure, killing the cells.^[283–285]

Chapter 9 What we see ... we measure

In this chapter the potential use of imaging and image analysis techniques as a potential way of analysing aerosols and chemical reactions in aerosol droplets will be explored, specifically the use of Brownian motion. The aim of this chapter is to provide a rough background on Brownian motion and some the factors affecting the quality of an image produced by the system, as well as mentioning other techniques that utilize aerosol imaging in an optical tweezer. Some preliminary data will also be shown as examples of the data obtained and analysed using the custom-built software, also described in this chapter.

9.1. Aerosols from yet another perspective

Yet another way of looking at aerosol droplet is by using optical imaging techniques, which is an extremely important tool in optical trapping. One of the most immediate and obvious uses is to image the trapped droplet. This allows first of all seeing if the droplet is actually trapped in the optical tweezers. Second, the visualization of the droplet allows monitoring of coalescence events happening, which is important in both growing the droplet, so that it would be large enough to produce an O-H band at $\sim 3500\text{ cm}^{-1}$, and for roughly estimating the amount of the second reagent added to the droplet, which is important in during chemical reactions. However, brightfield imaging is not a reliable method of accurately sizing microscopic aerosol droplets, because of the difference between the optical and geometrical crosssections of the

droplet. Lastly, video images can also be used to determine some of the characteristics of the trapped aerosol droplet. These characteristics can include, however is not limited to the morphology of the droplet, a presence of insoluble inclusions and determination of size of the droplet by using the Brownian motion of the droplet in the trap.

The presence of inclusions is another crucial part of imaging the droplet which allows noticing when the Na_2CO_3 has reacted with the CaCl_2 within the droplet producing the insoluble CaCO_3 . This reaction however comes at the cost of the whispering gallery modes, as the morphology of the particle is disrupted by the precipitate. Therefore, a potential way of measuring the droplet in order to derive characteristics of the droplet using the ZSR based model described in chapter 5.

9.1.1. Some physics

Some of the physics of a particle trapped in an optical tweezers are that any movement of the particle will be met with a restoration force produced by the gradient force (see chapter 2). This however allows approximating the movement of the particle in the trap by a harmonic oscillator model used in classical mechanics. Thus, a model of an object on a spring connected to a surface can be used to illustrate the concept:

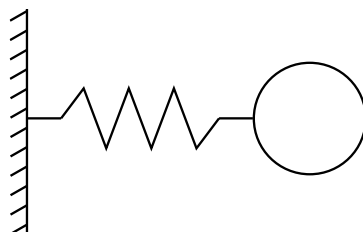


Figure 9.1 A schematic of an object on a spring connected to a surface, which represents a basic harmonic oscillator.

In this object on a spring model the restoring force produced by the spring in equation 9.1, where F is the restoring force, k is the spring constant and x is the displacement from the equilibrium position.^[286]

$$F = -kx \quad \text{Equation 9.1}$$

As previously mentioned, in case of an optically tweezed particle the restoring force (F) is the gradient force produced by the optical tweezers, and the equilibrium

position is the position where the net gradient force is 0. Assuming that, the beam has a circular beam waist, the restoring force will act equally in every direction, hence only the modulus of the displacement has any bearing on the force.^[287]

9.1.2. Dampening

When dealing with experimental systems, it is important to account for the environmental conditions that the droplet is in. These conditions can include the dampening of the system, the relative size of the particle compared to the mass of the molecules in its environment, viscosity of the environment. These effects can be due to the Brownian motion (motion of the droplet caused by gas molecules colliding with it) itself and to the factors that affect the dampening of the harmonic oscillator. In optical traps the forces that counteract the dampening of a harmonic oscillator, such as the interaction of the droplet moving in the proximity of a liquid surface. This interaction is accounted for by the Faxen's correction, which is a correction to the Stoke's drag forces, due to the proximity of the droplet to a surface.^[287] In order to simplify the calculation this correction was omitted from the initial calculations.

9.1.3. Brownian motion

In physics, Brownian motion is the random motion of a particle due to the collisions of the molecules of the environment with the particle. Brownian motion is named after Robert Brown who reported it in 1827, however it was not until Einstein's paper in 1905^[288,289] that the phenomenon was explained theoretically, with other derivations provided by M. Smoluchowski in 1906^[290] (later proven by P. Langevin to contain an error, which when corrected produces the same derivation as Einstein), and derived differently by P. Langevin in 1908^[291] (the end result agrees with Einstein's calculations). In 1908^[292] both Einstein's and Langevin's were both experimentally validated in a series of papers by Jean Perrin.^[293,294]

Currently the concept of Brownian motion has applications outside of physics, particularly in mathematics and economics where it is used to describe and model trends.^[295]

9.1.4. General basics

As mentioned, Brownian motion is dependent on the collisions of the molecules in the environment with the particle, thus the amount of displacement of the particle by the molecules will be proportional to the size of the particle, the size of the molecule and the velocity of the molecule. This means that the amount of displacement will be inversely proportional to the size of the particle, i.e. the larger the particle will be less displaced after an average collision (see Figure 9.2). It was noted by Uhlenbeck and Ornstein that the mean displacement of the particle follows a Gaussian probability distribution, i.e. some of the collisions will displace the particle more and some less, thus it is important to look at the average displacement over a period of time, rather than the displacement caused by individual collisions.^[287,296,297]

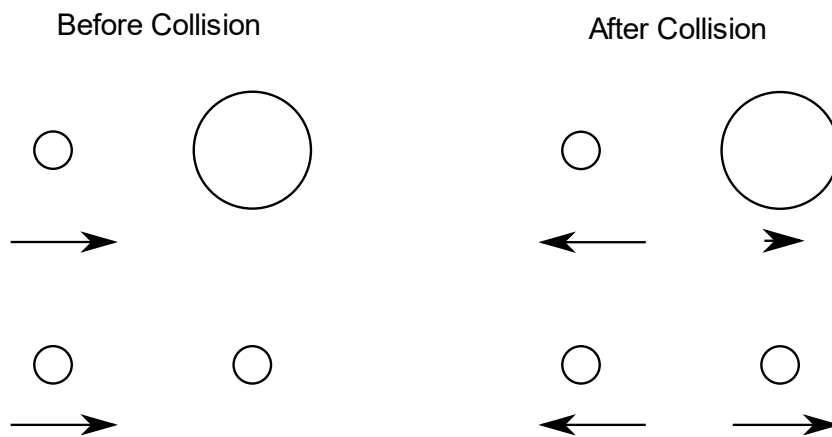


Figure 9.2 A schematic of the Brownian motion as a result of particle collisions. As a particle collides with a larger particle the momentum imparted on to the larger particle is less than that if the particles were of the same size or the particle initially at rest would be smaller.

9.1.5. Spring stiffness

As the droplet is optically tweezed an important factor is the strength of the gradient force acting on the droplet. In Figure 9.1 this is represented by the spring, which is represented by k in equation 9.1. In this case spring stiffness refers to the amplitude of the forces keeping the droplet in the optical trap, which is primarily the gradient force.

When considering a droplet trapped in a single beam optical tweezers it must be noted that the gradient force of the optical trap must be proportional to the size of the

droplet, in order to maintain it in the trap. This means that determining the gradient force of the optical trap is essential to the determination of the droplet size.

One of the ways to approximately determine the gradient force of the optical trap is by measuring the Brownian motion of droplets of a known sizes, determined for example using WGMs. This way it will be possible to relate the motion of the droplet in the trap with the expected motion in the absence of the “spring”, determining the correlation between the droplet size and the “spring”. By also factoring in the power of the laser and the efficiency of the optical trap, it would be possible to correlate the “spring” stiffness to the laser power.

This would produce the calibration necessary to measure the size of the droplet by it’s Brownian motion. This calibration would also be transferable to different optical tweezers systems, so long as appropriate corrections are made, for example corrections for the laser wavelength.

Seinfeld and Pandis describe the Brownian motion^[1] as:

$$\langle r^2 \rangle = \frac{1}{3} \langle x^2 \rangle = \frac{1}{3} \times \frac{2k_B T C_c}{3\pi\mu D_p} t = \frac{2k_B T C_c}{9\pi\mu D_p} t \quad \text{Equation 9.2}$$

Where r - total displacement, x – displacement along x axis, k_B – Boltzmann’s constant, T – temperature, C_c – slip correction, μ – viscosity of the medium, D_p – Particle diameter, t – time. As this describes the motion of a free-floating particle, and the analysed particle is in an optical tweezer it would be important to introduce an empirical correction factor A , therefore transforming N into:

$$\langle r^2 \rangle = \frac{2k_B T C_c}{9\pi\mu D_p} t A \quad \text{Equation 9.3}$$

In this case the empirical correction factor would be used to correct for all effects acting on the particle that are not related to the Brownian motion of a free-floating aerosol particle, such as the effects of the optical trap itself on the aerosol droplet, such as the gradient force, or any effects related to the proximity of surface, such as the Faxen’s correction. A purely experimental approach, such as using the WGMs of the aerosol droplet to calibrate the corrections necessary to size the aerosol particle using Brownian motion, would allow a way to avoid additional errors caused by the well-known phenomenon of the difference between the light extinction and geometrical cross-sections of optically trapped aerosol droplets.^[27]

9.2. Image analysis basics

Image analysis is a method of analysis which as the name suggests, relies a video image (aka a picture) or consecutive images (a video) in order to gain insight in to physical phenomena. There are multiple areas of research benefitting from the image analysis such as facial recognition, motion tracking and phase function analysis. All three of the areas are focus on distinct features of the image.

Facial recognition or more broadly pattern recognition, is an area of image analysis that is designed to identify similar patterns in an image. This is especially useful in cases where automatically counting the number of objects fitting a pattern such as automatic cell viability counters^[298] and as mentioned earlier in facial recognition.^[299]

Motion tracking is another powerful tool in image analysis. This requires identifying the same object in a series of consecutive images and determining the position the object in these images. Combined with pattern recognition it becomes an even more powerful tool, as this allows identifying and tracking the motion of an object. Such a combination would be an extremely powerful tool when combined with microscopy as this would allow to track the motion of a particle and observe its evolution over time.

9.2.1. Optical transfer function

An important characteristic of all imaging systems is how well they transmit the image, or how much will the image be distorted by the imaging system. This is known as the optical transfer function (OTF) which is commonly divided into the phase transfer function (PTF) and the modulation transfer function (MTF). The PTF accounts for the distortion of phases of the images, which is of less concern for imaging, as most imaging systems do not discriminate between the phases of the illumination. The MFT is concerned with the resolution of fine details of images and is crucial for the quality images. An example of this is how easy it is to see a series of thick black and white lines in comparison to a series of narrow lines, as exemplified in figure 9.4.^[184]

The principle of the MTF has been used in paintings as part of the post-impressionism style with a famous example of “A Sunday Afternoon on the Island of La Grande Jatte” by Georges-Pierre Seurat (see Figure 9.3), where dots are used to create the painting. The painting itself is designed to be viewed from a distance,

making the individual dots blur together creating the image. This utilizes the optical properties of the human eye, and its limitations to construct the desired image.^[300]

As an optical system, the human eye is analogous to imaging systems using digital cameras, as both will have limited precision both in terms of detection and their ability to accurately resolve images. This can be additionally evidenced by the use of optical lenses to counteract refractive errors, such as myopia, astigmatism, etc.^[301]



Figure 9.3 “A Sunday Afternoon on the Island of La Grande Jatte” by Georges-Pierre Seurat 1884-1886. This is a famous example of the post-impressionism style in painting, which uses small dots blurring together at a distance to create an image, without using any long strokes, or uniformly coloured surfaces. The physical characteristics human eye that are responsible for the MTF are utilised in order to achieve this effect. (Image copyright CC0 public domain)

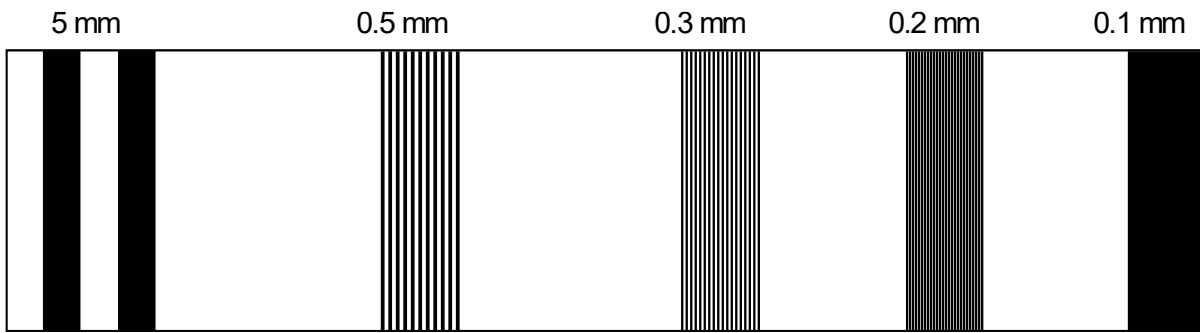


Figure 9.4 A Schematic of different spatial frequencies of the modulation transfer function. The lines are made of black and white lines of the same width within each set, with sets of lines of 5mm, 0.5 mm, 0.3 mm, 0.2 mm and 0.1 mm per line. As the lines become thinner and closer to another line of the same colour, it becomes more and more difficult to optically resolve individual lines, as they blur together.

Some of the qualities that influence the MTF of optical systems are the quality of the optical components and the number of pixels of the camera. The quality of the optical components determines the quality of the image itself, whereas the number and size of the pixels determine the capability of the camera to accurately record the image. In both cases the edges of the different features of the image are affected, and the finer details blur together as the different rays carrying the image are slightly distorted by the optical system, and the rays corresponding to the edges in an image are intermixed, reducing the clarity of fine edges, which is especially important for resolving the fine details of the image.

9.3. Motion tracking software

The Brownian motion software relies on the imaging of the droplet in the tweezers. The image is then converted into a grayscale image and then converted into a binary image by converting the grayscale values above a threshold to 1 and below to 0. This creates an image which could be analysed with the NI LabVIEW Vision package, which finds the centre of mass of the binary image of the droplet. This allows recording the x and y positions of the droplet in the images. As consecutive images are analysed the position of the droplet can be tracked, which can be analysed to track the changes in the position of the droplet, thus calculating the equilibrium position and using the Pythagoras theorem to find the displacement of the droplet. The time averaged displacement is then used to calculate the size of the particle based on the Brownian motion equations outlined earlier in this chapter.

The downsides of using video imaging of the droplet to size the droplet using Brownian motion are the quality of the image itself and the intensity of the back lighting of the droplet. The intensity of the lighting is dependent on the fluctuations in the voltage supplied to the LED, which due to the nature of electrical circuits will always have some amount of fluctuation. The background lighting issue can be dealt with digitally, by correcting the brightness, gamma and contrast parameters of the image. This produces a more uniform sequence of images and reducing the variation of the size of the droplet on the binary images, thus providing more consistent measurement of the position of the droplet.

A much harder issue to deal with is the quality of the image is harder to deal with, as it relies on the physical characteristics of the imaging system. This becomes a significant issue, when precipitation or crystallization occurs. One of the examples of this is during the reaction producing CaCO_3 , as due to nebulization some amount of both solutions deposit on the sides of the trapping cell, which includes the replaceable bottom coverslip. Thus, the reaction happens not only in the droplet itself but also on the coverslip, depositing a thin layer of CaCO_3 on it. The layer of CaCO_3 will then distort the image of the droplet, blurring it, drastically reducing the quality of the image, altering the OTF of the system. This has a major consequence on the ability of the software to size the droplet, as the blurred image does not have a well-defined contour of the droplet, necessary for the motion tracking software to function properly.

9.3.1. Comparison of principles of motion tracking with WGMs

Comparing the WGMs with Brownian motion tracking approaches for sizing aerosol droplets, it is important to firstly distinguish the two methods as they rely on completely different physical phenomena. This can be advantageous, as both approaches could be used complementary, providing a toolkit capable of overcoming the drawbacks of one another. An example of this would be during the formation of CaCO_3 the precipitate inclusion can disrupt the WGMs, however if it is still possible to use video imaging the droplet can still be sized. This is important in the analysis of chemical reactions in aerosol droplets, specifically when a precipitate is formed. (see Figure 9.10) On the other hand, the WGMs can be used to accurately determine the size of the droplet and therefore used to test and calibrate the Brownian motion

software, as it depends on the microcavity enhanced frequencies rather than imaging.

A possible benefit of combining the two approaches is that by looking both WGMs and Brownian motion it would be possible to size inclusions and core-shell aerosol droplets, where the inclusions or the core of the aerosol droplet does not allow sizing it using WGMs (i.e. with a radius of less than 1 μm). This would require distinguishing the inclusion from the rest of the droplet, and that the inclusion does not disturb the morphology too severely, as that would destroy the WGMs. A similar effect could be achieved purely using the video imaging, however the combination of WGMs and image analysis provides internal calibration for the image analysis.

9.3.2. Image analysis

Image analysis of optically tweezed aerosol droplets can be used to provide many insights into the droplet's physical properties. Apart from Brownian motion it is possible to interrogate the phase functions produced by optically trapped droplets, which can be compared with Mie theory calculations in order to size the droplet. Another option that can be accessed via image analysis is the analysis of the diffraction patterns produced by the optically trapped particle. This approach has been shown to be capable of sizing both spherical and rough particles.^[302,303]

As mentioned previously this work focuses on the Brownian motion of the droplet and the necessary image analysis. Note the pre-programmed and inbuilt algorithms refer to the ready-to-use functions in NI LabView.

The image analysis is designed to happen in several stages. The first stage is the image correction, which alter the Brightness, gamma and contrast (BCG) of the image, increasing the contrast between light and dark areas of the image, as well as improving the sharpness of the borders between light and dark parts of the image. The second stage is the conversion of the image from colour to grayscale, which converts the originally coloured image in to a black and white image (see Figure 9.5). the third stage of is the conversion of the grayscale image to a binary image, which has only black and white pixels, whereas the grayscale image has a gradient from black to white.

The image processing steps are used to enable the use of the pre-programmed blob detection algorithm, which detects white areas on the binary image and is used in

this case to detect the position of centre of these white areas on the X and Y axes of the image, as well as quantify the size of the white area. The BCG image correction step plays a crucial role in this blob detection as at least partially corrects for the lighting intensity of the LED used for imaging, and increases the intensity of the centre of the droplet, both of which heavily contribute to the ability of the blob detection algorithm to consistently find the middle of the droplet across each frame of the analysed video. The usefulness of the blob detection algorithm is two-fold, as it allows tracking the positions of the particles of the image and helps with filtering out any particles that do not correspond to the droplet. These particles are potentially caused by some of the aerosol particles settling on the cover slips of the trapping cell and any dust on the optics, etc.

Once the data is filtered off (see Figure 9.6 and figure 9.7) it can then be used to find the average position of the droplet, as an average of all of the positions of the droplet over time. after that is accounted for the resulting positions will correspond to the displacement of the droplet along X and Y axes converted from pixels to the corresponding distance, using a graticule and an inbuilt line profile analysis algorithm (see Figure 9.8). Assuming that the droplet moves linearly, the Pythagorean theorem can be used to calculate the distance of displacement (see Figure 9.9), that can be used to size the droplet once the necessary corrections to this values are applied.

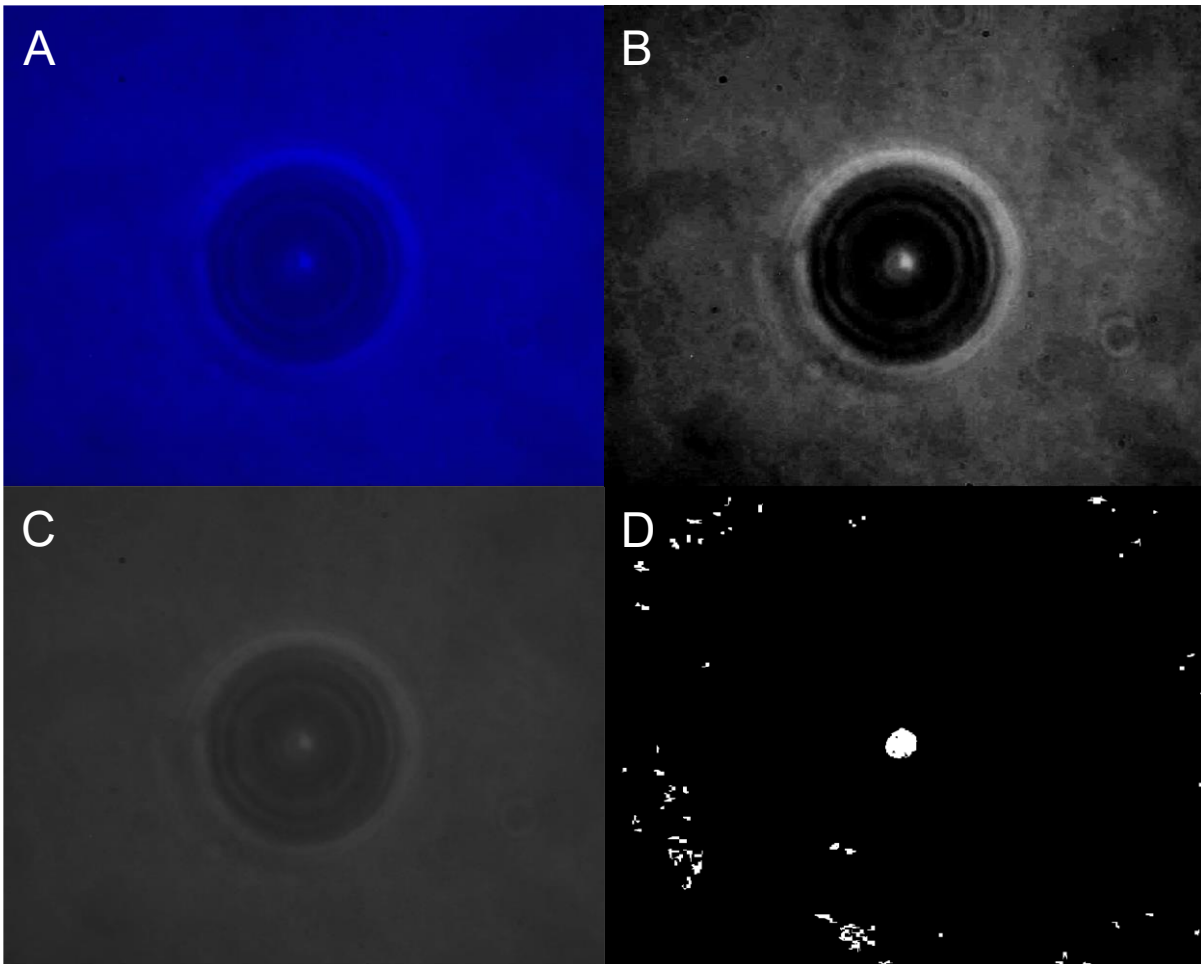


Figure 9.5 Processed images of a video of a droplet in an optical tweezer. A – a frame of the video without any correction. B – a frame converted to grayscale and corrected by adjusting brightness, contrast and gamma (BCG correction) of the image in order to produce a clear large particle on a binary image (D). C – an example frame of an error in the BCG correction of a video frame, which are most likely caused by the fluctuations in the intensity of the lighting. D – a binary image constructed using the BCG corrected grayscale image (B), produced by setting a brightness threshold on the grayscale image, converting the image to a series of black and white pixels. The binary image is later used in the blob detection algorithm (pre-programmed in the LabView environment), calculating the centre of mass of the blob, which allows tracking the position of the particle (white blob on the binary image) at a sub-pixel level, and is a way of correcting for the OTF of the imaging system.

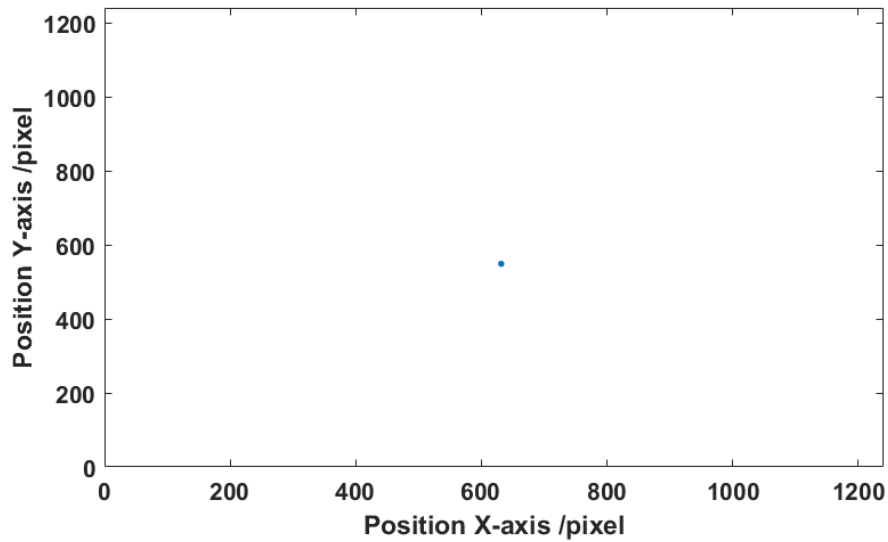


Figure 9.6 A plot of the position of the droplet on a full image. In this image the movement of the droplet is not noticeable at this scale (corresponding to the resolution of the original video).

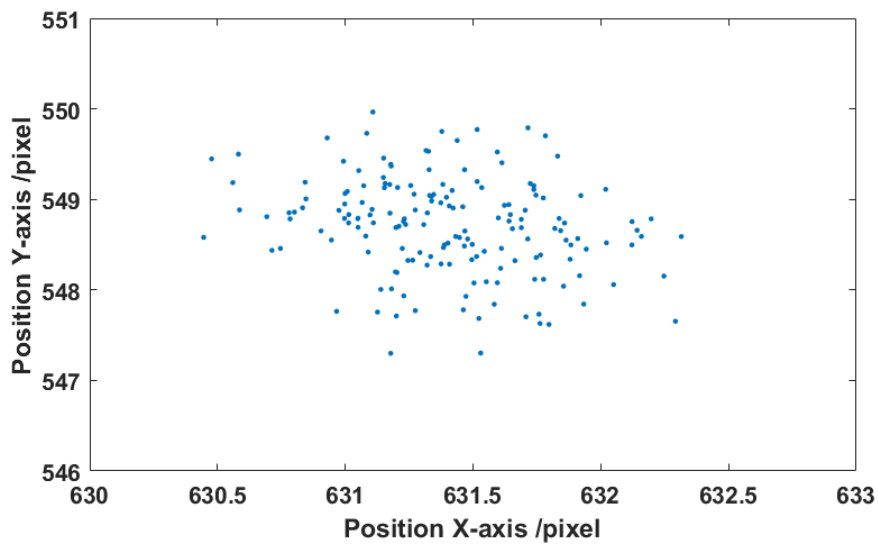


Figure 9.7 A zoomed in version of the Figure 9.6. This demonstrates the amount of movement detectable on the video image.

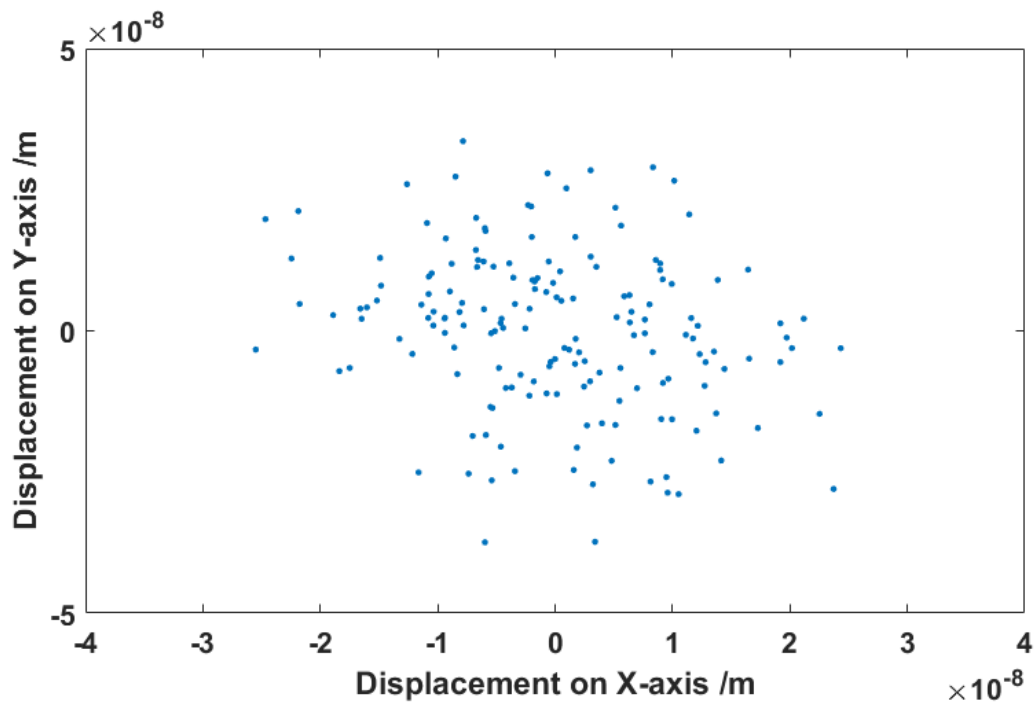


Figure 9.8 The relative position of the droplet based on the average position of the droplet (the average position of the droplet across all frames is taken as 0,0 position).

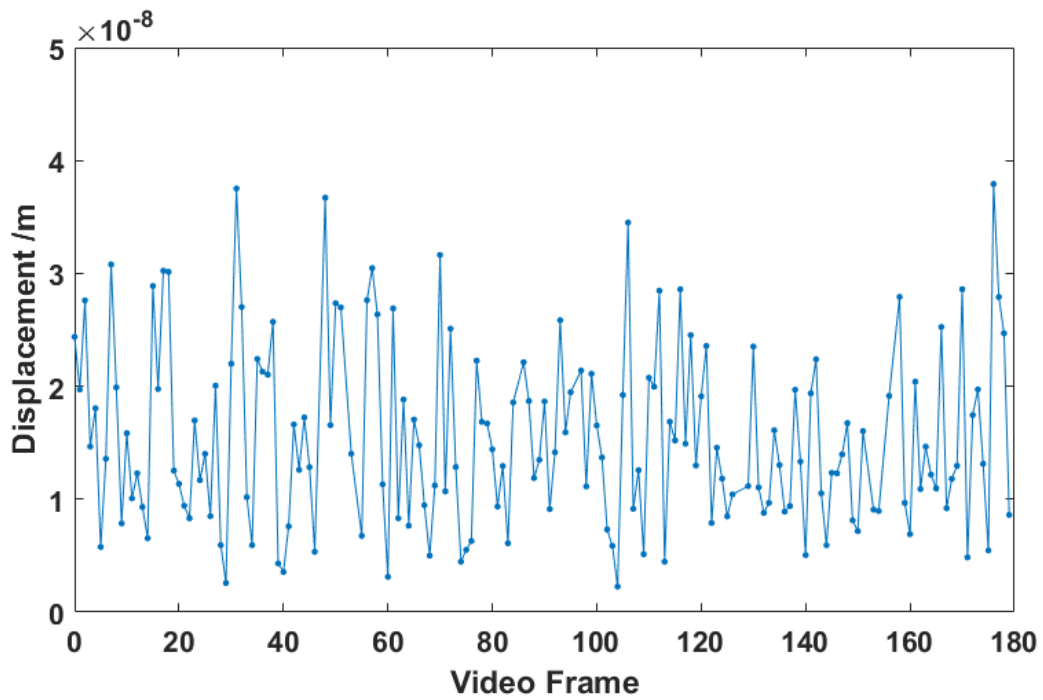


Figure 9.9 The distance of the displacement from the average position in Figure 9.8, calculated using the Pythagorean theorem.

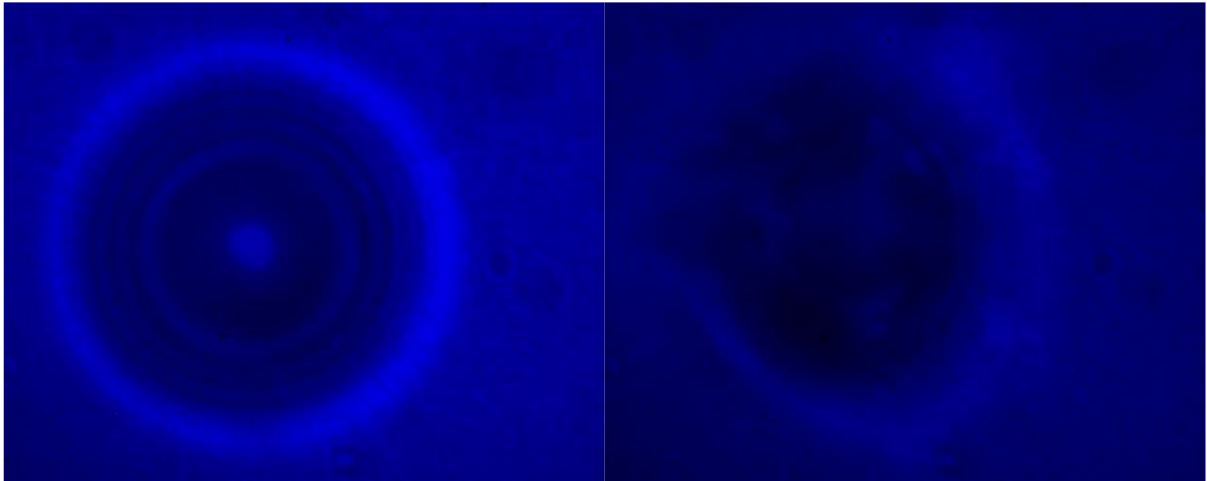


Figure 9.10 Examples of images of an aerosol droplet before the reaction (left) and after the formation of CaCO_3 (right). This demonstrates that additional computational image refinement is necessary to visually distinguish the droplet from its background.

9.3.3. Current issues

The issue of this analysis of aerosol droplets using the motion tracking software described in this chapter are: the lack of calibration, reliability of the image correction in the motion tracking software, and the measurements of the Brownian motion of the aerosol droplet along the Z axis.

The reliability of the image correction can be solved by designing an algorithm that would correct the image in a way that would produce similar histograms of the grayscale image, which simply quantify the number of the pixels of a certain brightness. The crucial parameters of that histogram would be the total width of the histogram, as even with correction no pixels reach the maximal brightness values (with the values being between the 0 and 255, an 8-bit value), and distribution of the pixels on the histogram. Maintaining the distribution of pixels would also be important, as it is possible to increase the brightness of the image, however on its own the brightness would not achieve the image enhancement effect necessary in order for the blob detection algorithm to consistently detect the centre of the droplet and for it to be the largest particle detected by the algorithm on a binary image.

The motion of the droplet along the Z axis could be measured by detecting the concentric ringed structure of the aerosol droplet. This concentric diffraction pattern is extremely similar to an airy disc, likely resulting from the Phase Function (PF)^[304,305] predicted by Mie scattering theory, which in itself can be used as a way of sizing the

aerosol droplet. (see Figure 9.11) On the other hand, by increasing and decreasing the laser power it is possible to purposefully move the droplet along the Z axis, as that would change the gradient and scattering forces acting on the droplet, it is also possible to observe that the distance of the first concentric ring of the PF also moves relative to the centre of the droplet, which could be potentially used to determine the motion of the particle along the Z axis. This is likely caused by the different parts of the droplet coming in and out of focus, as the imaging system has no moving components.

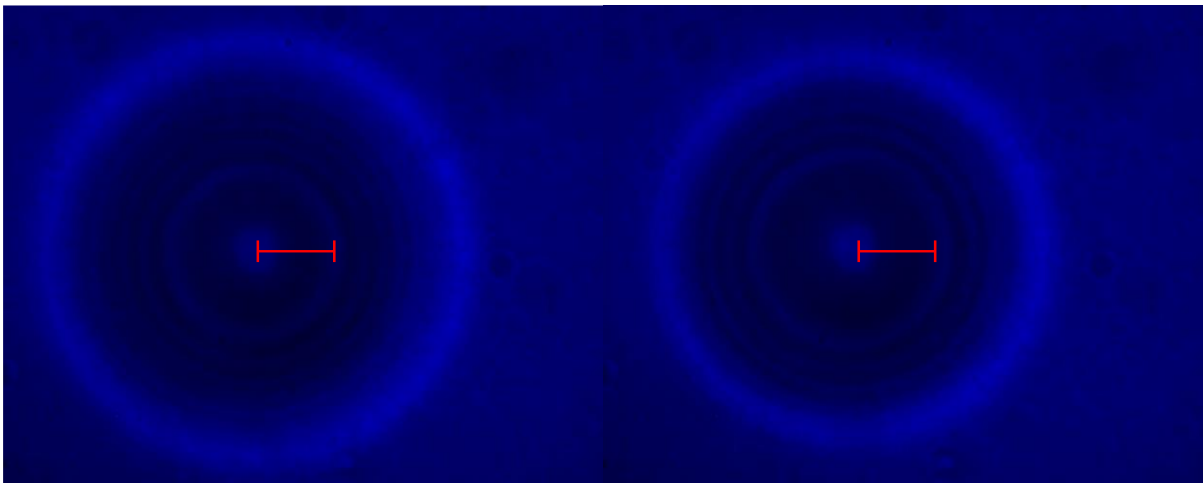


Figure 9.11 Images of the same aerosol droplet at different laser power. The images are taken from a video file 2 seconds apart. The red bars are of the same length and are used to highlight the different distances between the centre of the droplet and the first ring that likely corresponds to the PF.

9.4. Conclusion

Image analysis of optically trapped aerosols is a powerful tool for analysing the physical properties of the trapped particles. This approach is capable of utilising multiple ways of sizing such as the interrogation of the phase transfer function, Brownian motion and the analysis of the diffraction pattern. The diffraction pattern analysis is also a potential tool for analysing the contents of the droplet.

At present the software is capable of tracking a clearly visible particle, when there is no need to enhance the image to correct for any precipitate forming on the coverslip, however it is not yet capable of fully sizing a droplet based on its Brownian motion. In order to be able to size the software also needs to be calibrated, comparing the calculated results to the sizing data obtained using the WGMs. The calibration will

allow fully sizing the droplets, that are not obscured by precipitates forming on the trapping chamber's coverslips, thus useful for sizing the droplet without the need for a Raman spectrograph. This could potentially bring down the cost of the instrument necessary to build hygroscopic growth curves.

In order to solve the issue of precipitates forming on the coverslip of the trapping chamber, a high degree of image enhancement would be necessary to consistently find the droplet's centre. Due to the relatively large number of frames necessary to obtain a reliable measurement of the Brownian motion of the droplet, it would be impractical to rely on a researcher to manually analyse each frame. Therefore, a narrow AI would be necessary to enhance the image, ensuring consistent detection of the droplet's centre. This will most likely be based on a looping system controlling the BCG correction, specifically the histogram of the grayscale values, and the binary threshold (grayscale to binary conversion) values. In this case the loop will act as a quality assurance mechanism, ensuring that the Brownian motion of the droplet is measured consistently.

Both of these methods suffer from the same issue of the unpredictable change of the droplet's optical properties and the MTF caused by the formation of CaCO_3 inside the droplet and on the sides of the trapping cell. In this case the use of Brownian motion approach is more beneficial as it is likely possible enhance the image to the point where a part of the droplet (ideally the centre) could be consistently imaged on a binary image, therefore allowing to track it. The same image enhancement procedure could also be beneficial to the diffraction pattern analysis of the aerosol droplet. However, the diffraction pattern analysis may require further image enhancement, beyond what is necessary for the Brownian motion analysis, making the Brownian motion analysis a better practical solution.

Chapter 10 Summary, Conclusions and Future Prospects

In this thesis a seemingly simple chemical reaction between CaCl_2 and Na_2CO_3 was examined to various extents from the points of view of hygroscopic growth, Raman spectroscopy and video imaging. Each of requiring different software approaches and demonstrating that even the simplest reactions such as an ion exchange reaction can pose many challenges, and that the study of these reactions can shed light on more complex phenomena. However, in order to achieve this one must not only look at the reaction but also carefully examine the tools utilised, and when necessary create new ones in order to gain a more complete understanding of the studied phenomenon and the mechanisms responsible for its deterministic outcome.

10.1. Summary

In this thesis the hygroscopic parameter models: the Kreidenweis model and κ -Kohler model are compared as well as the process of finding optimized hygroscopicity parameters using a system of equations and the Generalized Reduced Gradient algorithm built into the MS Excel Solver add-on. (see Chapter 5 for the details on the software, assumptions made, and its validation based on data artificially produced using E-AIM, Chapter 4 for the details on the aerosol hygroscopic response and models used and Chapter 6 on its application to real data). The overall software provides a potentially useful tool for deriving hygroscopic parameters based only on the hygroscopic response of several droplets assuming the validity of the

hygroscopic model. The same software also provides the capability of assessing the necessity of any changes to the hygroscopic models to account for the formation of hydrated crystal states. The same software also demonstrates that the RH range over which the experimental data was obtained can have an impact on the optimized hygroscopicity parameters, potentially explaining the difference in the values between different research groups. The same software is demonstrated to be usable with data obtained by both DVS and AOT methods.

All of this demonstrates the various aspects of determining the hygroscopic response of a single solute aerosol droplet, however the main focus of this thesis is the exploration of the formation of insoluble CaCO_3 by reacting CaCl_2 with Na_2CO_3 in an aerosol droplet. As stated in this thesis this reaction produces soluble NaCl as a by-product. In chapter 6 it is proposed that the reaction could be quantified by the use of the ZSR assumption, treating the insoluble CaCO_3 as a single component, and calculating the amount of CaCO_3 produced as the difference in the hygroscopic response between the initial CaCl_2 droplet and the resulting $\text{CaCl}_2 + \text{NaCl} + \text{CaCO}_3$ droplet, assuming that 100% of Na_2CO_3 is consumed in the reaction. This concept also provides a way of quantifying the hygroscopic response of solution with solute-solute interaction, by treating the formed solute-solute complex as a single hygroscopic component in a mixture with other single components such as one of the interacting solutes and any reaction by-products, if there are any.

Another way of viewing the formation CaCO_3 is by using the Raman scattering of the droplet. In the Raman spectra of the chemical reaction it is possible to notice that several polymorphs of CaCO_3 namely calcite vaterite and ikaite can be produced by reacting CaCl_2 and Na_2CO_3 . It is possible to differentiate between these polymorphs and an aqueous solution of Na_2CO_3 based on the Raman shift of the ν_1 vibrational mode peak position. It is also possible to rule out the formation of another anhydrous polymer of CaCO_3 - aragonite, by the position of the ν_4 vibrational mode peak, which also suggests that the temperature of the aerosol droplet was not sufficient to produce aragonite. By adding various amounts of Na_2CO_3 to CaCl_2 droplets it was possible to produce different polymorphs, based on the relative amounts of components in the resulting droplet. By measuring the pH of the solutions of CaCl_2 and Na_2CO_3 it was possible to establish the approximate boundaries of the reaction in terms of pH, and the formation of the different polymorphs based on the relative

amounts of CaCl_2 and Na_2CO_3 in the reacting droplet would be consistent with the literature on the influence of the pH on the formation of vaterite and ikaite. This established that pH is a determining factor in the formation of ikaite and vaterite, as well as the factor determining the kinetics of the transformation between the discussed polymorphs. In these experiments the direct formation of calcite was observed for the first time in inorganic systems^[216,306], at very low amounts of Na_2CO_3 relative to the amounts of CaCl_2 present in the droplets, which corresponds to the pH ranges much lower than this reaction is typically studied at^[307]. A decomposition of the maps of spectra recorded pre-, during and post- reaction can be used to study the presence of multiple polymorphs in a mixture, providing a powerful tool for studying the transformation of one polymorph in to the other, when it will be possible to account for the influence of pH on the kinetics and thermodynamics of chemical reaction.

The decomposition analysis also provides additional insight into the structure of the calcite crystals formed. From the literature it is possible to determine that calcite has a highly ordered structure, which can be related to the width of the v1 peak of calcite. In the process of the decomposition of the map of spectra in the reactions where only calcite is formed it is possible to notice the decrease in the width of the peak as time progresses suggesting that calcite initially forms with a more disordered structure, and later slowly equilibrates into a more ordered crystal structure.

In this thesis a conjecture viewing interactions based on the electromagnetic fields produced by the components of the system, namely: solute ions/molecules, pH ions and water molecules. This conjecture also provides a novel view of concentration, as the distance between solute ions/molecules, the electromagnetic fields produced by them, and interacting with its surroundings, with saturation being the shortest distance between the solute ions/molecules in solution at which stable nucleation does not occur. The approach used in this conjecture would provide an explanation to the effects of additional ions on crystal formation, supersaturation in aerosols, and a potential way of reformulating the equations in chemical kinetics and thermodynamics to account for pH effects, a potentially easier way of accounting for temperature effects, as well as including a way of modifying them in order to account for other effects, such as external electromagnetic fields and quantum mechanical effects, such as Casimir forces.

A drawback of the studied chemical reaction is that the inclusion of CaCO_3 disturbs the internal morphology of the aerosol droplet, destroying the WGMs that are normally used for sizing aerosol droplets in AOT. To circumvent this issue an approach based on imaging the droplet and calculating the size of the droplet based on its Brownian motion was attempted. This however was complicated by the formation of a thin layer of CaCO_3 on the coverslip of the trapping chamber, altering the resulting image of the droplet. An incomplete program was built in NI LabView that with proper calibration should be capable of handling the necessary image processing and computational aspects necessary to size the aerosol droplets despite any inclusions or image distortion caused by CaCO_3 forming on the coverslip.

10.2. Conclusions

The aims of this work, stated in chapter 1 are:

- Investigate and compare single optically tweezed aerosol droplet and dynamic vapour sorption (DVS) methods of investigating the hygroscopic properties of chemical compounds.
- Produce and analyse a phase transition ion exchange chemical reaction between CaCl_2 and Na_2CO_3 forming CaCO_3 polymorphs in an optically tweezed aerosol droplet using Raman spectroscopy and video imaging.

Comparing the AOT and DVS both techniques are capable of measuring the hygroscopic response of compounds, as demonstrated in chapter 7. The difference between the two techniques arises with the fact that DVS is not capable of accessing the supersaturated states that can be accessed by AOT. This is a consequence of the DVS having direct contact with the sample, whereas AOT uses a tightly focussed laser to maintain. However, this also provides the DVS with a benefit, as it allows easier access to low RH conditions and allows confirming that substances form hydrated crystals after efflorescence, as it can be seen in the example of CaCl_2 . In the case of AOT it is hard to maintain the droplet/formed crystal trapped as it effloresces, rapidly changing its refractive index, thus its interaction with the balance of the gradient and scattering forces acting on it. To an extent the same thing happens with a droplet as a precipitate forms as it can be seen in the formation of CaCO_3 .

A novel way of determining the hygroscopic parameters of an aerosol based on extracting the parameters themselves and the dry size of the droplet as latent variables of mathematical models of hygroscopic growth: the Kreidenweis and κ -Kohler models^[121,122]. This provides additional benefits as it is capable of deriving the hygroscopic parameters from the size of the droplet and the corresponding RH, without the need for additional calculation or explicit necessity for a theoretical model. This allows exploring the hygroscopic properties of compounds that are not yet computationally predicted by theoretical models. Additionally, it provides a benefit of LARA being more sensitive to the changes in size rather than RI, relying solely on the size measurement, while the RI measurements can be used to find errors in the LARA processed data. Finally, it eliminates the human error of the need to pick a specific measurement, assuming its accuracy, and determining the dry size of the droplet based on that one measurement, by being dependent on all of the measurements simultaneously, thus in a sense independent of the individual measurements. This also ensures that random error do not have a significant impact on determining the hygroscopicity parameters. This way of determining the hygroscopic parameters also demonstrates that the range of RH values over which the data is gathered can also influence the values of the determined hygroscopic parameters, thus influencing their accuracy.

The chemical reaction between Na_2CO_3 and CaCl_2 was examined from multiple perspectives: hygroscopic change, spectroscopic tracking and video imaging.

In this thesis a model for tracking the completeness of a chemical reaction based on the ZSR assumption is proposed. This model is based on the fact that CaCO_3 is insoluble in water, hence this newly formed solute-solute complex should be treated as a single hygroscopic entity. This model would be capable of determining the amounts of reagents transformed by the deviation of the hygroscopic properties of the post-reaction droplet compared to the initial droplet. The principle underlying this model could also be used to describe the behaviour of any solute-solute complexes, not just CaCO_3 , thus it is likely that it will prove useful in studying other solute-solute interactions in the hygroscopic growth of aerosols.

The tracking of the chemical reaction via the changing chemical signature of the CO_3^{2-} ion in different environments, in water as dissolved Na_2CO_3 , and polymorphs of CaCO_3 : calcite, vaterite and ikaite. In this thesis 2 programmes are used to fit the

experimental spectra with various line profiles, demonstrating their capability to analyse data, allowing a more detailed tracking of the chemical reaction and identification of trends in chemical reactions. In the investigation of the formation of CaCO_3 polymorphs the reaction had demonstrated several reaction pathways by forming ikaite, vaterite transforming into ikaite, stable vaterite, vaterite transforming into calcite, and a novel pathway in inorganic systems direct formation of calcite. By decomposing the maps of spectra, it is also possible to observe the formation of substructures in the amorphous CaCO_3 , which correspond to the polymorphs that will form from the ACC. In the decomposition the direct formation of calcite it is also possible to notice a decrease in the width of the calcite peak over the entire time that the reaction was monitored, suggesting that in the initial formation of calcite there are small defects in the crystalline structure, which with time equilibrate to form a more uniform crystal. This demonstrates that the process of crystal formation is complex consisting from multiple steps, explaining the differences in peak widths of freshly formed calcite and naturally formed mineral calcite.

The chemical reaction was also observed using video imaging and analysed with motion tracking software, as a way of circumventing the difficulties with sizing the optically trapped aerosol droplet using the WGMs. While the motion tracking and Brownian motion analysis software is at this stage is not fully capable of accomplishing the task it is intended for, it demonstrates the utility of software in uncovering the effects that can be missed by a human observer. Additionally, the description of the possible pathways of overcoming the issues with the current state of the software, provides a good starting point and direction for future development.

In the analysis of the literature and experimental data it was noted that pH plays a major role in determining the polymorph of calcite formed as the result of the reaction. From the analysis of the literature on chemical kinetics and thermodynamics it was determined that neither are fully capable of accounting for the effects of the pH. Thus, a conjecture that could serve as a basis for reformulating the chemical kinetics and thermodynamics was proposed. In this conjecture a new way of treating ions in an aqueous solution was proposed based on the charge of the ion and its interactions with the surrounding dipole molecules of water and passing pH (H^+ and OH^-) ions. The conjecture also describes a way of viewing concentration of solute in the solution as well as: ways of the pH ions interacting with other ions, affecting their

reactivity, and proposing that the mean field approximation used in measuring pH could be violated locally by solute ions, which would explain some of the findings in the literature on the influence of ions and pH of the formation of CaCO₃ polymers. This conjecture provides an open-ended framework for redesigning chemical kinetics and thermodynamic equations, at the same time providing additional insight into chemical reactivity and crystal formation. The principles outlined in this conjecture can also be applied to study the solubility of compounds, providing a concept that could be used to explain the mostly negligible solubility of non-polar compounds in polar compounds and *vice versa*, along with a framework for accounting for other conditions such as external electromagnetic fields on solubility of compounds.

10.3. Future prospects

The ability to track a chemical reactions using various means can shed new light on them, as well as discover and study new reaction mechanisms.^[216,306,307] As it can be seen throughout this thesis there are multitudes of ways of extending the work described, with applications to a vast array of complex problems in areas of physical chemistry, aerosol research, biology, biochemistry and beyond. Some of these ways will be discussed below.

10.3.1. *Molecular fine structure determination using Raman spectroscopy*

As it had been eluded to in chapter 7, Raman spectroscopy, although complicated, is a powerful tool that can be used for determining molecular structures. Therefore, one of the primary extensions of this work would be to produce a reliable system of relating the local environments, determining the fine structure directly from the Raman spectra. As Raman spectroscopy can be done on gaseous, liquid or solid samples it would provide a route to studying the changes in ions related to changes in the local environment in fine detail. This would potentially provide insight into the influence of pH and other solute ions, as well as thermal effects and the influence of external electromagnetic fields on the formation of CaCO₃ polymorphs, mutually complementing the theoretical work suggested in the conjecture in chapter 8.4.

As also demonstrated in chapter 8 Raman spectroscopy can also be used to monitor chemical reactions, which coupled with its structural capabilities could be used to identify the kinetics of chemical processes involving transition states. Another area of

application of this technique could be protein research, as it could be used on samples without the need to crystallise the proteins, and as Raman spectroscopy had been proven to detect single molecules^[308], potentially allowing the molecules to be analysed in vivo. Coupled with an understanding of the influence of local environments on the chemical structure as suggested in the conjecture, would also allow compensating for any sample pre-treatment necessary for the Raman analysis, effectively reconstructing the protein as it would be in its natural state.

10.3.2. *Extending the conjecture on the electromagnetic approach to ions in solution*

It should come as no surprise that extending the conjecture outlined in chapter 8.3 is one of the future prospects of this thesis. The framework presented as is lacks full calculations, which would be capable of calculating the energies required for various processes to happen, for example calculating the kinetics and thermodynamics of formation of CaCO₃, along with the influence of pH and external electromagnetic fields on the reaction. It stands to reason that due to its openness to various effects on the levels of both quantum and classical mechanics, a standard of calculations needs to be implemented, as well as procedure for the modification of the equations, so that newly discovered effects can be accounted for, and their significance to the chemical process properly qualified and quantified.

10.3.3. *Additional verification of the ZSR model*

As it is demonstrated in this thesis the ZSR based model needs further testing, by using it to calculate various types of solute-solute interaction, such as other reactions or dimerization. It is likely that with insoluble solutes some correction that would account for the fact that not all of the molecules in the insoluble solute particles will be in contact, thus the amount of moisture that they will attract will likely depend on the surface area of the precipitated crystal.

10.3.4. *Aerosol droplets as microreactors*

As demonstrated in this thesis optically tweezed aerosol droplets can be used to produce chemical reactions. With the sizes of the droplets being only several μm in radius, the amount of reagents consumed in the reaction is very small and coupled with the capabilities of Raman systems, and the decomposition of Raman spectra also demonstrated in this thesis, it stands to reason that chemical reactions can be

studied using aerosols as microreactors. This would allow the reactions to be performed with incredibly small amounts of reagents consumed, allowing to lower the cost of the experiments, with continuous monitoring using Raman spectroscopy. The continuous monitoring of the reaction using Raman spectroscopy could be used to uncover new steps in the chemical reaction, such as the formation of pre nucleation clusters in the ACC and the slow equilibration of small defects in the crystalline structure as observed with the formation of calcite. The spectroscopic decomposition could also be used to monitor characteristic peaks, qualifying and potentially quantifying the kinetics of the chemical reactions, as well as providing insight on the reaction mechanism.

10.3.5. Aerosols as tunable optical cavities

It has been demonstrated that the size of the aerosol droplets can be manipulated by changing the relative humidity. This will also alter the position of the WGMs on the Raman spectrum. As the differences between microcavity amplified Raman signal and stimulated Raman spectroscopy were stated in chapter 2, by tuning the size of the aerosol droplet it would be possible to coincide it with the spontaneous Raman signal produced by the chemical signature of the aerosol droplet. This would allow the droplet to be used as a tunable optical microcavity, improving the sensitivity of the instrument to specific parts of the chemical signature. This method of amplification could be used to amplify specific low intensity vibrational modes, potentially allowing the analysis of some of the minor components in a chemical reaction, as well as a more detailed study of the Raman signature of a new compound obtained by using aerosol droplets as micro reactors.

10.3.6. AOT automation

As mentioned in chapter 9, the video imaging of the droplet can provide useful information about the droplet. One of the examples of such information is the potential to determine the position of the droplet along the Z axis, based on the size of the droplet and laser power used. The ability to measure this ratio along with digital control of the MFCs and the laser would enable automatic control of the AOT. This would enable automatic control over the laser power based on the position of the droplet, and RH control, allowing the software to make any necessary corrections following pre-programmed RH changes. Such a setup would require a researcher to only setup the experiment, i.e. trap the droplet, grow the droplet if necessary, and

start the software, with leaving the researcher to focus on other tasks, or perform multiple experiments if multiple suitable AOT setups where available.

10.4. Final remarks

The multiple perspectives on chemical reactions in optically tweezed aerosol droplets provided in this thesis demonstrates the complexity of what seems to be a simple ion exchange reaction. The same combination perspectives also provide a more complete view of the chemical reaction, allowing to notice novel reaction pathways, and providing new insight on fundamental questions, and allowing the re-evaluation of current knowledge. Building upon the work presented in this thesis will provide even greater insight into the physical chemistry of interactions, benefitting many areas of research, including aerosol science and physical chemistry in general.

Chapter 11 Bibliography

1. John H. Seinfeld SNP. Atmospheric Chemistry and Physics [Internet]. John Wiley & Sons Inc.; 2016.
2. Chan CK, Yao X. Air pollution in mega cities in China. *Atmos Environ.* 2008;42:1–42.
3. Capelle V, Chédin A, Pondrom M, Crevoisier C, Armante R, Crepeau L, et al. Infrared dust aerosol optical depth retrieved daily from IASI and comparison with AERONET over the period 2007–2016. *Remote Sens Environ.* Elsevier; 2018;206:15–32.
4. Kun L, Hirose K, Katsumi B, Albin M, Prendergast K, Mendoza M. The impact of Fukushima on global health: Lessons learned from man-made and natural disasters. *Health Technol (Berl).* 2014;4:177–203.
5. Kawamura H, Kobayashi T, Furuno A, Usui N, Kamachi M. Numerical simulation on the long-term variation of radioactive cesium concentration in the North Pacific due to the Fukushima disaster. *J Environ Radioact.* Elsevier Ltd; 2014;136:64–75.
6. Edenhofer, O., R. Pichs-Madruga, Y. Sokona, E. Farahani, S. Kadner K, Seyboth, A. Adler, I. Baum, S. Brunner, P. Eickemeier, B. Kriemann, J. Savolainen, S. Schlömer, C. von Stechow TZ and JC, (eds.) M. IPCC, 2014: Climate Change 2014: Mitigation of Climate Change. Contribution of Working Group III to the Fifth Assessment Report of the Intergovernmental Panel on Climate Change. 2014.
7. Wang H, Zhao L. A joint prevention and control mechanism for air pollution in the Beijing-Tianjin-Hebei region in china based on long-term and massive data mining of pollutant concentration. *Atmos Environ.* Elsevier; 2018;174:25–42.
8. Dong G. Ambient Air Pollution and Health Impact in China [Internet]. Dong G, editor. Springer Nature Singapore Pte Ltd.; 2017.
9. Davis BL, Jixiang G. Airborne particulate study in five cities of China. *Atmos Environ.* 2000;34:2703–11.
10. Goudie AS. Dust storms: Recent developments. *J Environ Manage.* Elsevier Ltd; 2009;90:89–94.
11. Bory AJM, Biscaye PE, Svensson A, Grousset FE. Seasonal variability in the

- origin of recent atmospheric mineral dust at NorthGRIP, Greenland. *Earth Planet Sci Lett.* 2002;196:123–34.
12. Prospero JM, Lamb PJ. African droughts and dust transport to the Caribbean: climate change implications. *Science* (80-). 2003;302:1024–7.
 13. Prospero JM, Bonatti E, Schubert C, Carlson TN. DUST IN THE CARIBBEAN ATMOSPHERE TRACED TO AN AFRICAN DUST STORM. *Earth Planet Sci Lett.* 1970;9:287–93.
 14. Voltz FE. Spectral Skylight and Solar Radiance Measurements in the Caribbean: Maritime Aerosols and Sahara Dust. *J Atmos Sci.* 1970;27:1041–7.
 15. International Union of Pure and Applied Chemistry. IUPAC Compendium of Chemical Terminology, Gold Book. IUPAC Compend Chem Terminol. Research Triangle Park, NC: IUPAC; 2014.
 16. Zender CS. Mineral Dust Entrainment and Deposition (DEAD) model: Description and 1990s dust climatology. *J Geophys Res.* 2003;108:4416.
 17. Kandler K, Benker N, Bundke U, Cuevas E, Ebert M, Knippertz P, et al. Chemical composition and complex refractive index of Saharan Mineral Dust at Izaña, Tenerife (Spain) derived by electron microscopy. *Atmos Environ.* 2007;41:8058–74.
 18. Stewart ID, Oke TR. Local climate zones for urban temperature studies. *Bull Am Meteorol Soc.* 2012;93:1879–900.
 19. Kotharkar R, Bagade A. Local Climate Zone classification for Indian cities: A case study of Nagpur. *Urban Clim.* Elsevier B.V.; 2018;24:369–92.
 20. George K, Ziska LH, Bunce JA, Quebedeaux B. Elevated atmospheric CO₂ concentration and temperature across an urban-rural transect. *Atmos Environ.* 2007;41:7654–65.
 21. Takemura T, Nakajima T, Dubovik O, Holben BN, Kinne S. Single-scattering albedo and radiative forcing of various aerosol species with a global three-dimensional model. *J Clim.* 2002;15:333–52.
 22. Hadley OL, Kirchstetter TW. Black-carbon reduction of snow albedo. *Nat Clim Chang.* Nature Publishing Group; 2012;2:437–40.
 23. Warren SG. Impurities in snow: effects on albedo and snowmelt. *Ann Glaciol.* 1984;5:177–9.
 24. Krinner G, Boucher O, Balkanski Y. Ice-free glacial northern Asia due to dust deposition on snow. *Clim Dyn.* 2006;27:613–25.
 25. Telloli C, Chicca M, Pepi S, Vaccaro C. Saharan dust particles in snow samples of Alps and Apennines during an exceptional event of transboundary air pollution. *Environ Monit Assess. Environmental Monitoring and Assessment;* 2018;190.
 26. Zhang Y, Kang S, Sprenger M, Cong Z, Gao T, Li C. Black carbon and mineral dust in snow cover on the Third Pole. *Cryosph.* 2018;12:413–31.
 27. Reid JP, Meresman H, Mitchem L, Symes R. Spectroscopic studies of the size and composition of single aerosol droplets. *Int. Rev. Phys. Chem.* 2007.
 28. Tang MJ, Whitehead J, Davidson NM, Pope FD, Alfara MR, McFiggans G, et al. Cloud condensation nucleation activities of calcium carbonate and its atmospheric ageing products. *Phys Chem Chem Phys. Royal Society of Chemistry;* 2015;17:32194–203.
 29. Beggs CB, Shepherd SJ, Kerr KG. Potential for airborne transmission of infection in the waiting areas of healthcare premises: Stochastic analysis using a Monte Carlo model. *BMC Infect Dis.* 2010;10:1–8.
 30. Norman PS, Winkenwerder WL. Suppression of hay fever symptoms with intranasal dexamethasone aerosol. *J Allergy.* 1965;36:284–92.
 31. Strachan DP. Hay fever, hygiene, and household size. *BMJ Br Med J.* 1989;299:1259–60.

32. Blake K, Madabushi R, Derendorf H, Lima J. Population pharmacodynamic model of bronchodilator response to inhaled albuterol in children and adults with asthma. *Chest. The American College of Chest Physicians*; 2008;134:981–9.
33. Shah NJ, Vinod Kumar S, Gurusamy U, Annan Sudarsan AK, Shewade DG. Effect of ADRB2 (adrenergic receptor β 2) gene polymorphisms on the occurrence of asthma and on the response to nebulized salbutamol in South Indian patients with bronchial asthma. *J. Asthma*. 2015. p. 755–62.
34. Dhuper S, Chandra A, Ahmed A, Bista S, Moghekar A, Verma R, et al. Efficacy and cost comparisons of bronchodilator administration between metered dose inhalers with disposable spacers and nebulizers for acute asthma treatment. *J Emerg Med. Elsevier Inc.*; 2011;40:247–55.
35. Barnes PJ. Inhaled corticosteroids. *Pharmaceuticals*. 2010;3:514–40.
36. Baur X, Barbinova L. Occupational airborne exposure, specific sensitization and the atopic status: Evidence of a complex interrelationship. *J Occup Med Toxicol*. 2013;8:1–12.
37. Bell ML, Davis DL, Fletcher T. A retrospective assessment of mortality from the London smog episode of 1952: The role of influenza and pollution. *Urban Ecol An Int Perspect Interact Between Humans Nat*. 2008;6:263–8.
38. Nikander K, Sanders M. The early evolution of nebulizers. *Medicamundi*. 2010;54:47–53.
39. Stein SW, Thiel CG. The History of Therapeutic Aerosols: A Chronological Review. *J Aerosol Med Pulm Drug Deliv*. 2017;30:20–41.
40. Merida MT. Puerto Cabello and the Bubonic Plague epidemic (1903-1908). *Vesalius*. 1999;5:94–9.
41. Haynes S. Tobacco smoke enemas. *B C Med J*. 2008;12:24–53.
42. Lawrence G. Tools of the Trade Tobacco smoke enemas. *Lancet*. 2002;359:1442.
43. Hunt EH, Space DR. The Airplane Cabin Environment: Issues Pertaining to Flight Attendant Comfort. 1995;1–12.
44. Han Z, Sze To GN, Fu SC, Chao CY-H, Weng W, Huang Q. Effect of human movement on airborne disease transmission in an airplane cabin: study using numerical modeling and quantitative risk analysis. *BMC Infect Dis*. 2014;14:434.
45. Thornley CN, Emslie NA, Sprott TW, Greening GE, Rapana JP. Recurring norovirus transmission on an airplane. *Clin Infect Dis*. 2011;53:515–20.
46. Finkelstein Y, Bournissen FG, Hutson JR, Shannon M. Polymorphism of the ADRB2 gene and response to inhaled beta- agonists in children with asthma: A meta-analysis. *J Asthma*. 2009;46:900–5.
47. Mandelberg A, Priel IE, Chen E, Noviski N. Nebulized wet aerosol treatment in emergency department - Is it essential? Comparison with large spacer device for metered-dose inhaler. *Chest. The American College of Chest Physicians*; 1997;112:1501–5.
48. Kilpatrick GS, Oldham PD. Calcium chloride and adrenaline as bronchial dilators compared by sequential analysis. *Br Med J*. 1954;2:1388–91.
49. McClure R, Yanagisawa D, Stec D, Abdollahian D, Koktysh D, Xhillari D, et al. Inhalable Curcumin: Offering the Potential for Translation to Imaging and Treatment of Alzheimer's Disease. *J Alzheimer's Dis*. 2015;44:283–295.
50. McClure R, Ong H, Janve V, Barton S, Zhu M, Li B, et al. Aerosol Delivery of Curcumin Reduced Amyloid- β Deposition and Improved Cognitive Performance in a Transgenic Model of Alzheimer's Disease. *J. Alzheimer's Dis*. 2017. p. 797–811.
51. Wermeling DP. A response to the opioid overdose epidemic: Naloxone nasal spray. *Drug Deliv Transl Res*. 2013;3:63–74.

52. Davis DL, Bell ML, Fletcher T. A look back at the London smog of 1952 and the half century since. *Environ Health Perspect.* 2002;110:734–5.
53. Hunt A, Abraham JL, Judson B, Berry CL. Toxicologic and epidemiologic clues from the characterization of the 1952 London smog fine particulate matter in archival autopsy lung tissues. *Environ Health Perspect.* 2003;111:1209–14.
54. Al Omari MMH, Rashid IS, Qinna NA, Jaber AM, Badwan AA. Calcium Carbonate. *Profiles Drug Subst Excipients, Relat Methodol Vol 41.* 2016. p. 31–132.
55. Neal C, Jarvie HP, Williams RJ, Neal M, Wickham H, Hill L. Phosphorus-calcium carbonate saturation relationships in a lowland chalk river impacted by sewage inputs and phosphorus remediation: An assessment of phosphorus self-cleansing mechanisms in natural waters. *Sci Total Environ.* 2002;282–283:295–310.
56. Johnston J. The several forms of calcium carbonate. *Am. J. Sci.* 1916. p. 473–512.
57. Rodriguez-Blanco JD, Shaw S, Benning LG. The kinetics and mechanisms of amorphous calcium carbonate (ACC) crystallization to calcite, via vaterite. *Nanoscale.* 2011;3:265–71.
58. Nagamune R, Choi J. Parameter Reduction of Nonlinear Least-Squares Estimates via the Singular Value Decomposition [Internet]. *IFAC Proc. Vol. IFAC;* 2008.
59. Ogino T, Suzuki T, Sawada K. The formation and transformation mechanism of calcium carbonate in water. *Geochim Cosmochim Acta.* 1987;51:2757–67.
60. Mikkelsen A, Andersen AB, Engelsen SB, Hansen HCB, Larsen O, Skibsted LH. Presence and dehydration of ikaite, calcium carbonate hexahydrate, in frozen shrimp shell. *J Agric Food Chem.* 1999;47:911–7.
61. Costa SN, Freire VN, Caetano EWS, Maia FF, Barboza CA, Fulco UL, et al. DFT Calculations with van der Waals Interactions of Hydrated Calcium Carbonate Crystals $\text{CaCO}_3 \cdot (\text{H}_2\text{O}, 6\text{H}_2\text{O})$: Structural, Electronic, Optical, and Vibrational Properties. *J Phys Chem A.* 2016;120:5752–65.
62. Hu Y Bin, Wolthers M, Wolf-Gladrow DA, Nehrke G. Effect of pH and phosphate on calcium carbonate polymorphs precipitated at near-freezing temperature. *Cryst Growth Des.* 2015;15:1596–601.
63. Michel FM, MacDonald J, Feng J, Phillips BL, Ehm L, Tarabrella C, et al. Structural characteristics of synthetic amorphous calcium carbonate. *Chem Mater.* 2008;20:4720–8.
64. Ito T, Matsubara S. Vaterite after Ikaite in carbonate sediment. *J Mineral Petrol Econ Geol.* 1999;94:176–82.
65. Coleyshaw EE, Crump G, Griffith WP. Vibrational spectra of the hydrated carbonate minerals ikaite, monohydrocalcite, lansfordite and nesquehonite. *Spectrochim Acta Part A Mol Biomol Spectrosc.* 2003;59:2231–9.
66. Omelon CR, Pollard WH, Marion GM. Seasonal formation of ikaite ($\text{CaCO}_3 \cdot 6\text{H}_2\text{O}$) in saline spring discharge at Expedition Fiord, Canadian high arctic: Assessing conditional constraints for natural crystal growth. *Geochim Cosmochim Acta.* 2001;65:1429–37.
67. Council TC, Bennett PC. Geochemistry of ikaite formation at Mono Lake, California: implications for the origin of tufa mounds. *Geology.* 1993;21:971–4.
68. TATENO N, KYONO A. Structural change induced by dehydration in ikaite ($\text{CaCO}_3 \cdot 6\text{H}_2\text{O}$). *J Mineral Petrol Sci.* 2014;109:157–68.
69. Hesse KF, Suess E. Refinement of the structure of Ikaite, $\text{CaCO}_3 \cdot 6\text{H}_2\text{O}$. *Zeitschrift fur Krist - New Cryst Struct.* 1983;163:227–31.
70. Bischoff JL, Fitzpatrick JA, Rosenbauer RJ. The Solubility and Stabilization of Ikaite ($\text{CaCO}_3 \cdot 6\text{H}_2\text{O}$) from 0° to 25°C: Environmental and Paleoclimatic

- Implications for Thinolite Tufa. *J Geol.* 1993;101:21–33.
71. Suess E, Balzer W, Hesse KF, Müller PJ, Ungerer CA, Wefer G. Calcium carbonate hexahydrate from organic-rich sediments of the antarctic shelf: Precursors of glendonites. *Science* (80-). 1982;216:1128–31.
72. Bots P, Benning LG, Rodriguez-Blanco J-D, Roncal-Herrero T, Shaw S. Mechanistic Insights into the Crystallization of Amorphous Calcium Carbonate (ACC). *Cryst Growth Des.* 2012;12:3806–14.
73. Cartwright JHE, Checa AG, Gale JD, Gebauer D, Sainz-Díaz CI. Calcium carbonate polyamorphism and its role in biomineralization: How many amorphous calcium carbonates are there? *Angew Chemie - Int Ed.* 2012;51:11960–70.
74. Farhadi-Khouzani M, Chevrier DM, Zhang P, Hedin N, Gebauer D. Water as the Key to Proto-Aragonite Amorphous CaCO₃. *Angew Chemie - Int Ed.* 2016;55:8117–20.
75. Politi Y, Batchelor DR, Zaslansky P, Chmelka BF, Weaver JC, Sagi I, et al. Role of Magnesium Ion in the Stabilization of Biogenic Amorphous Calcium Carbonate: A Structure–Function Investigation. *Chem Mater.* 2010;22:161–6.
76. Raz S, Hamilton PC, Wilt FH, Weiner S, Addadi L. The transient phase of amorphous calcium carbonate in sea urchin larval spicules: The involvement of proteins and magnesium ions in its formation and stabilization. *Adv Funct Mater.* 2003;13:480–6.
77. Aizenberg J, Lambert G, Weiner S, Addadi L. Factors involved in the formation of amorphous and crystalline calcium carbonate: A study of an ascidian skeleton. *J Am Chem Soc.* 2002;124:32–9.
78. Ito T. Factors controlling the transformation of natural ikaite from Shiwakka, Japan. *Geochem J.* 1998;32:267–73.
79. Hu Y Bin, Wolf-Gladrow DA, Dieckmann GS, Völker C, Nehrke G. A laboratory study of ikaite (CaCO₃·6H₂O) precipitation as a function of pH, salinity, temperature and phosphate concentration. *Mar Chem. The Authors;* 2014;162:10–8.
80. Matsumoto M, Fukunaga T, Onoe K. Polymorph control of calcium carbonate by reactive crystallization using microbubble technique. *Chem Eng Res Des. Institution of Chemical Engineers;* 2010;88:1624–30.
81. Kitamura M, Konno H, Yasui A, Masuoka H. Controlling factors and mechanism of reactive crystallization of calcium carbonate polymorphs from calcium hydroxide suspensions. *J Cryst Growth.* 2002;236:323–32.
82. Rodriguez-Blanco JDD, Shaw S, Bots P, Roncal-Herrero T, Benning LGG. The role of pH and Mg on the stability and crystallization of amorphous calcium carbonate. *J Alloys Compd. Elsevier B.V.;* 2012;536:S477–9.
83. Carteret C, Dandeu A, Moussaoui S, Muhr H, Humbert B, Plasari E. Polymorphism Studied by Lattice Phonon Raman Spectroscopy and Statistical Mixture Analysis Method. Application to Calcium Carbonate Polymorphs during Batch Crystallization. *Cryst Growth Des.* 2009;9:807–12.
84. Levi-Kalisman Y, Raz S, Weiner S, Addadi L, Sagi I. Structural Differences Between Biogenic Amorphous Calcium Carbonate Phases Using X-ray Absorption Spectroscopy. *Adv Funct Mater.* 2002;12:43.
85. Opdyke BN, Walker JCG. Return of the coral reef hypothesis: Basin to shelf partitioning of CaCO₃ and its effect on atmospheric CO₂. *Geology.* 1992;20:733.
86. Gladfelter E. Skeletal Development in *Acropora cervicornis*: I. Patterns of Calcium Carbonate Accretion in the Axial Corallite. *Coral Reefs.* 1982;45–51.
87. Stubler AD, Peterson BJ. Ocean acidification accelerates net calcium carbonate loss in a coral rubble community. *Coral Reefs. Springer Berlin Heidelberg;* 2016;35:795–803.

88. Bruneval F, Donadio D, Parrinello M. Molecular dynamics study of the solvation of calcium carbonate in water. *J Phys Chem B*. 2007;111:12219–27.
89. Greenfield EM, Wilson DC, Crenshaw MA. Ionotropic nucleation of calcium carbonate by molluscan matrix. *Integr Comp Biol*. 1984;24:925–32.
90. Falini G, Albeck S, Weiner S, Addadi L. Control of aragonite or calcite polymorphism by mollusk shell macromolecules. *Science (80-)*. 1996;271:67–9.
91. Weiss IM, Tuross N, Addadi L, Weiner S. Mollusc larval shell formation: Amorphous calcium carbonate is a precursor phase for aragonite. *J Exp Zool*. 2002;293:478–91.
92. Feng QL, Pu G, Pei Y, Cui FZ, Li HD, Kim TN. Polymorph and morphology of calcium carbonate crystals induced by proteins extracted from mollusk shell. *J Cryst Growth*. 2000;216:459–65.
93. Hasse B, Gmbh I. Calcium carbonate modifications in the mineralized shell of the freshwater snail *Biomphalaria glabrata* Calcium Carbonate Modifications in the Mineralized Shell of the Freshwater. *Chem A Eur J*. 2015;6:3679–85.
94. Feely R a. Impact of Anthropogenic CO₂ on the CaCO₃ System in the Oceans. *Science (80-)*. 2004;305:362–6.
95. Mucci A, Canuel R, Zhong S. The solubility of calcite and aragonite in sulfate-free seawater and the seeded growth kinetics and composition of the precipitates at 25°C. *Chem Geol*. 1989;74:309–20.
96. Frear GL, Johnston J. THE SOLUBILITY OF CALCIUM CARBONATE (CALCITE) IN CERTAIN AQUEOUS SOLUTIONS AT 25° 1. *J Am Chem Soc*. 1929;51:2082–93.
97. Segnit ER, Holland HD, Biscardi CJ. The solubility of calcite in aqueous solutions-I The solubility of calcite in water between 75° and 200° at CO₂ pressures up to 60 atm. *Geochim Cosmochim Acta*. 1962;26:1301–31.
98. Coto B, Martos C, Peña JL, Rodríguez R, Pastor G. Effects in the solubility of CaCO₃: Experimental study and model description. *Fluid Phase Equilib*. 2012;324:1–7.
99. Donnet M, Bowen P, Lemaître J. A thermodynamic solution model for calcium carbonate: Towards an understanding of multi-equilibria precipitation pathways. *J Colloid Interface Sci*. 2009;340:218–24.
100. Euzen A, Gaill F, Lacroix D, Cury P. *The Ocean Revealed*. 2017.
101. Garbalińska H, Bochenek M, Malorny W, von Werder J. Comparative analysis of the dynamic vapor sorption (DVS) technique and the traditional method for sorption isotherms determination — Exemplified at autoclaved aerated concrete samples of four density classes. *Cem Concr Res*. 2017;91:97–105.
102. Gorsky MP, Maksimyak PP, Maksimyak AP. Interference Investigation of Concrete Structure and Dynamics During Hydration. *Fringe*. 2009;3–6.
103. Wiktor V, Jonkers HM. Quantification of crack-healing in novel bacteria-based self-healing concrete. *Cem Concr Compos*. Elsevier Ltd; 2011;33:763–70.
104. Eiben AE, Smith JE. *Introduction to Evolutionary Computing [Internet]*. Second. Berlin, Heidelberg: Springer Berlin Heidelberg; 2015.
105. Blanchard P, Brüning E. *Mathematical Methods in Physics [Internet]*. Cham: Springer International Publishing; 2015.
106. Beiglböck W. From Gravity to Thermal Gauge Theories: The AdS/CFT Correspondence [Internet]. Papantonopoulos E, editor. Berlin, Heidelberg: Springer Berlin Heidelberg; 2011.
107. Natsuume M. *AdS/CFT Duality User Guide [Internet]*. Tokyo: Springer Japan; 2015.
108. Marquardt DW. An Algorithm for Least-Squares Estimation of Nonlinear Parameters [Internet]. *J. Soc. Ind. Appl. Math*. 1963. p. 431–41.

109. Lange K. Optimization (Springer Texts in Statistics) [Internet]. 2013.
110. WENYU S, YUAN Y-X. Optimization Theory and Methods [Internet]. Boston: Springer, Boston, MA; 2006.
111. Marquardt DW. An Algorithm for Least-Squares Estimation of Nonlinear Parameters Author (s): Source : Journal of the Society for Industrial and Applied Mathematics , Vol . 11 , No . 2 Published by : Society fDonald W . Marquardt Industrial and Applied Mathematics S. J Soc Ind Appl Math. 1963;11:431–41.
112. Levenberg K. A method for the solution of certain non-linear problems in least squares. Q Appl Math. 1944;2:164–8.
113. Wu SF. The Helmholtz equation least squares theory for reconstructing and predicting acoustic radiation [Internet]. 2015.
114. Lasdon LS, Fox RL, Ratner MW. Nonlinear optimization using the generalized reduced gradient method. Rev FRANÇAISE D'AUTOMATIQUE, INFORMATIQUE, Rech OPÉRATIONNELLE Rech OPÉRATIONNELLE. 1974;73–103.
115. Lourakis MIA. A Brief Description of the Levenberg-Marquardt Algorithm Implemented by levmar. Found Res Technol. 2005;3:2.
116. Lampton M. Damping-undamping strategies for the Levenberg-Marquardt nonlinear least-squares method. Comput Phys. 1997;11:110–5.
117. Kumar A, Jones DD, Hanna MA, Soediono B, Bartocci AC. Design of Modern Heuristics [Internet]. J. Chem. Inf. Model. 2009.
118. Hoffmann R, Minkin VI, Carpenter BK. Ockham' s Razor. Int J Philos Chem. 1997;3:3–28.
119. Tirozzi B, Puca S, Pittalis S, Bruschi A, Morucci S, Ferraro E, et al. Neural Networks and Sea Time Series [Internet]. Boston, MA: Birkhäuser Boston; 2006.
120. Christensen O, Christensen KL. Approximation Theory [Internet]. Boston, MA: Birkhäuser Boston; 2005.
121. Petters MD, Kreidenweis SM. A single parameter representation of hygroscopic growth and cloud condensation nucleus activity. Atmos Chem Phys. 2013;13:1081–91.
122. Kreidenweis SM, Koehler K, DeMott PJ, Prenni AJ, Carrico C, Ervens B. Water activity and activation diameters from hygroscopicity data - Part I: Theory and application to inorganic salts. Atmos Chem Phys. 2005;5:1357–70.
123. Fisher LR, Gamble RA, Middlehurst J. The Kelvin equation and the capillary condensation of water. Nature. 1981;290:575–6.
124. Buff FP. Curved Fluid Interfaces. I. The Generalized Gibbs-Kelvin Equation. J Chem Phys. 1956;25:146–53.
125. Skinner LM, Sambles JR. The Kelvin equation—a review. J Aerosol Sci. 1972;3:199–210.
126. Atkins P, De Paula J. Physical Chemistry [Internet]. New York. 2006.
127. Virtanen A, Joutsensaari J, Koop T, Kannosto J, Yli-Pirilä P, Leskinen J, et al. An amorphous solid state of biogenic secondary organic aerosol particles. Nature. 2010;467:824–7.
128. Rickards AMJ, Song YC, Miles REH, Preston TC, Reid JP. Variabilities and uncertainties in characterising water transport kinetics in glassy and ultraviscous aerosol. Phys Chem Chem Phys. Royal Society of Chemistry; 2015;17:10059–73.
129. Bones DL, Reid JP, Lienhard DM, Krieger UK. Comparing the mechanism of water condensation and evaporation in glassy aerosol. Proc Natl Acad Sci. 2012;109:11613–8.
130. Giordano D, Potuzak M, Romano C, Dingwell DB, Nowak M. Viscosity and glass transition temperature of hydrous melts in the system $\text{CaAl}_2\text{Si}_2\text{O}_8$ – $\text{CaMgSi}_2\text{O}_6$. Chem Geol. Elsevier B.V.; 2008;256:203–15.

131. Innocenzi P. The Sol to Gel Transition [Internet]. 2016.
132. Melorose J, Perroy R, Careas S. Polymer Macro- and Micro-Gel Beads. Statew. Agric. L. Use Baseline 2015. 2015.
133. Ross-Murphy SB. Rheological characterization of polymer gels and networks. *Polym Gels Networks*. 1994;2:229–37.
134. Addadi L, Joester D, Nudelman F, Weiner S. Mollusk shell formation: A source of new concepts for understanding biomineralization processes. *Chem - A Eur J*. 2006;12:980–7.
135. Tadros T. Encyclopedia of Colloid and Interface Science [Internet]. Tadros T, editor. Berlin, Heidelberg: Springer Berlin Heidelberg; 2013.
136. Soediono B. Sol-Gel Methods for Materials Processing. *J. Chem. Inf. Model*. 1989.
137. Guglielmi M, Kickelbick G, Martucci A. Sol-Gel Nanocomposites. *Sol-Gel Nanocomposites*. 2014.
138. Mishra KA. Sol-gel Based Nanoceramic Materials: Preparation, Properties and Applications. 2016.
139. Muller R, Gérard E, Dugand P, Rempp P, Gnanou Y. Rheological Characterization of the Gel Point: A New Interpretation. *Macromolecules*. 1991;24:1321–6.
140. Kavanagh GM, Ross-Murphy SB. Rheological characterisation of polymer gels. *Prog Polym Sci*. 1998;23:533–62.
141. Martin JE, Adolf D, Wilcoxon JP. Viscoelasticity near the sol-gel transition. *Phys Rev A*. 1989;39:1325–32.
142. Adolf D, Martin JE. Viscoelasticity of crosslinked gels. *J Acoust Soc Am*. 1992;91:2378–2378.
143. Lam L, Wong Y., Poon C. Degree of hydration and gel/space ratio of high-volume fly ash/cement systems. *Cem Concr Res*. 2000;30:747–56.
144. Henkel M, Sanctuary R, Pleimling M. Ageing and the Glass Transition [Internet]. 2007.
145. Vannoni M, Sordini A, Molesini G. Relaxation time and viscosity of fused silica glass at room temperature. *Eur Phys J E*. 2011;34:92.
146. Napolitano A, Hawkins EG. Viscosity of a standard soda-lime-silica glass. *J Res Natl Bur Stand Sect A Phys Chem*. 1964;68A:439.
147. Cohen MH, Grest GS. Liquid-glass transition, a free-volume approach. *Phys Rev B*. 1979;20:1077–98.
148. Hill AJ, Tant MR. The Structure and Properties of Glassy Polymers. 1999;1–20.
149. Behrens SH, Grier DG. The charge of glass and silica surfaces. *J Chem Phys*. 2001;115:6716–21.
150. Tarjus G. Glass transitions may be similar in two and three dimensions, after all. *Proc Natl Acad Sci*. 2017;114:2440–2.
151. Rainone C. Metastable glassy states under external perturbations : monitoring the effects of compression and shear-strain [Internet]. 2017.
152. Besselink R, Rodriguez-Blanco JD, Stawski TM, Benning LG, Tobler DJ. How short-lived ikaite affects calcite crystallization. *Cryst Growth Des*. 2017;17:6224–30.
153. Rickaby REM, Shaw S, Bennitt G, Kennedy H, Zabel M, Lennie A. Potential of ikaite to record the evolution of oceanic $\delta^{18}\text{O}$. *Geology*. 2006. p. 497–500.
154. Huggett JM, Schultz BP, Shearman DJ, Smith AJ. The petrology of ikaite pseudomorphs and their diagenesis. *Proc Geol Assoc. The Geologists' Association*; 2005;116:207–20.
155. Young PM, Chiou H, Tee T, Traini D, Chan HK, Thielmann F, et al. The use of organic vapor sorption to determine low levels of amorphous content in processed

- pharmaceutical powders. *Drug Dev Ind Pharm.* 2007;33:91–7.
156. Bronlund J, Paterson T. Moisture sorption isotherms for crystalline, amorphous and predominantly crystalline lactose powders. *Int Dairy J.* 2004;14:247–54.
157. 2. Equation of interphase sorption equilibria. *Interface Sci Technol Vol 13.* 2007. p. 41–87.
158. Harley SJ, Glascoe EA, Maxwell RS. Thermodynamic Study on Dynamic Water Vapor Sorption in Sylgard-184. *J Phys Chem B.* 2012;116:14183–90.
159. Hogan SE, Buckton G. The Application of Near Infrared Spectroscopy and Dynamic Vapor Sorption to Quantify Low Amorphous Contents of Crystalline Lactose. *Pharm Res.* 2001;18:112–6.
160. Murti Vemuri N, Chrzan Z, Cavatur R. Use of isothermal microcalorimetry in pharmaceutical preformulation studies part II. Amorphous phase quantification in a predominantly crystalline phase. *J Therm Anal Calorim.* 2004;78:55–62.
161. Park SJ, Seo MK. Solid-Gas Interaction. *Interface Sci. Technol.* 2011.
162. Brunauer S, Emmett PH, Teller E. Adsorption of Gases in Multimolecular Layers. *J Am Chem Soc.* 1938;60:309–19.
163. Gelb LD, Gubbins KE. Characterization of Porous Glasses: Simulation Models, Adsorption Isotherms, and the Brunauer–Emmett–Teller Analysis Method [Internet]. *Langmuir.* 1998. p. 2097–111.
164. Mackin L, Zanon R, Park JM, Foster K, Opalenik H, Demonte M. Quantification of low levels (<10%) of amorphous content in micronised active batches using dynamic vapour sorption and isothermal microcalorimetry. *Int J Pharm.* 2002;231:227–36.
165. Knox KJ. *Light-Induced Processes in Optically-Tweezed Aerosol Droplets.* Springer-Verlag; 2011.
166. Sullivan RC, Moore MJK, Petters MD, Kreidenweis SM, Roberts GC, Prather KA. Effect of chemical mixing state on the hygroscopicity and cloud nucleation properties of calcium mineral dust particles. *Atmos Chem Phys.* 2009;9:3303–16.
167. Zdanovskii AB. *Fundamental Aspects of Variation of Properties of Mixed Solutions: Works of Salt Laboratory.* Tr Solyanoi Lab Vses Inst Galurgii Akad Nauk SSSR. 1936;6.
168. Stokes RH, Robinson RA. Interactions in Nonelectrolyte Solutions. I. Solute-Solvent Equilibria. *J Phys Chem.* 1965;8:2126–31.
169. Randles CA, Russell LM. Hygroscopic and optical properties of organic sea salt aerosol and consequences for climate forcing. *Geophys Res Lett.* 2004;31:4–7.
170. AIOMFAC-web [Internet].
171. Zuend A, Marcolli C, Booth AM, Lienhard DM, Soonsin V, Krieger UK, et al. and Physics New and extended parameterization of the thermodynamic model AIOMFAC : calculation of activity coefficients for organic-inorganic mixtures containing carboxyl , hydroxyl , carbonyl , ether , ester , alkenyl , alkyl , and aromatic functional gr. 2011;9155–206.
172. Zuend A, Marcolli C, Luo BP, Peter T. and Physics A thermodynamic model of mixed organic-inorganic aerosols to predict activity coefficients. 2008;4559–93.
173. Clegg SL, Brimblecombe P, Wexler AS, Wexler AS. Thermodynamic Model of the System H – NH – Na – SO – NO – Cl – H O at 298 . 15 K. 1998;
174. Friese E, Ebel A. Temperature Dependent Thermodynamic Model of the System H + - NH 4 + - Na + - SO 4 2 - - NO 3 - - Cl - - H 2 O. 2010.
175. Lide DR, Haynes WMM, Baysinger G, Berger LI, Roth DL, Zwillinger D, et al. *CRC Handbook of Chemistry and Physics.* 2010;
176. Brewster ME, Loftsson T. Cyclodextrins as pharmaceutical solubilizers. 2007;59:645–66.

177. Del Valle EMM. Cyclodextrins and their uses : a review. *Process Biochem.* 2004;39:1033–46.
178. Uriarte LM, Dubessy J, Boulet P, Baonza VG, Bihannic I, Robert P. Reference Raman spectra of synthesized $\text{CaCl}_2 \cdot n \text{H}_2\text{O}$ solids ($n = 0, 2, 4, 6$). *J Raman Spectrosc.* 2015;46:822–8.
179. Chemspider β -Cyclodextrin [Internet]. [cited 2019 May 7].
180. Rocke DM, Lorenzato S. A Two-Component Model for Measurement Error in Analytical Chemistry. *Technometrics.* 1995;37:176–84.
181. Bezerra MA, Santelli RE, Oliveira EP, Villar LS, Escalreira LA. Response surface methodology (RSM) as a tool for optimization in analytical chemistry. *Talanta.* 2008;76:965–77.
182. Ferraro JR, Nakamoto K, Brown CW. *Introductory Raman Spectroscopy.* Elsevier. 2003.
183. Socrates G. *Infrared and Raman Characteristic Group Frequencies: Tables and Charts.* 3rd ed. JOHN WILEY & SONS, LTD; 2001;
184. Träger F, editor. *Springer Handbook of Lasers and Optics* [Internet]. New York, NY: Springer New York; 2007.
185. Uriarte LM, Dubessy J, Boulet P, Baonza VG, Bihannic I, Robert P. Reference Raman spectra of synthesized $\text{CaCl}_2 \cdot n\text{H}_2\text{O}$ solids ($n=0, 2, 4, 6$). *J Raman Spectrosc.* 2015;46:822–8.
186. Dresselhaus MS, Jorio A, Hofmann M, Dresselhaus G, Saito R. Perspectives on carbon nanotubes and graphene Raman spectroscopy. *Nano Lett.* 2010;10:751–8.
187. Anthony JW, Bideaux RA, Bladh KW, Nichols MC, editors. *Vaterite.* *Handb Mineral.* Chantilly: Mineralogical Society of America; 2005.
188. Anthony JW, Bideaux RA, Bladh KW, Nichols MC, editors. *Aragonite.* *Handb Mineral.* Chantilly: Mineralogical Society of America; 2005.
189. Anthony JW, Bideaux RA, Bladh KW, Nichols MC, editors. *Ikaite.* *Handb Mineral.* Chantilly: Mineralogical Society of America; 2005.
190. Anthony JW, Bideaux RA, Bladh KW, Nichols MC, editors. *Monohydrocalcite.* *Handb Mineral.* Chantilly: Mineralogical Society of America; 2005.
191. Zolotoyabko E, Caspi EN, Fieramosca JS, Von Dreele RB, Marin F, Mor G, et al. Differences between bond lengths in biogenic and geological calcite. *Cryst Growth Des.* 2010;10:1207–14.
192. Wehrmeister U, Soldati AL, Jacob DE, Häger T, Hofmeister W. Raman spectroscopy of synthetic, geological and biological vaterite: a Raman spectroscopic study. *J Raman Spectrosc.* 2009;41:n/a-n/a.
193. Meekes H, Rasing T, Wyder P, Janner A, Janssen T. Raman and infrared spectra of the incommensurate crystal Na_2CO_3 . *Phys Rev B.* 1986;34:4240–54.
194. Buzgar N, Apopei AI. The Raman study of certain carbonates. *Analele Stiint ale Univ "Al I Cuza" Iasi Geol.* 2009;113:97–112.
195. Zubkova N V., Pushcharovsky DY, Ivaldi G, Ferraris G, Pekov I V., Chukanov N V. Crystal structure of natrite, $\gamma\text{-Na}_2\text{CO}_3$. *Neues Jahrb für Mineral - Monatshefte.* 2002;2002:85–96.
196. Dusek M, Chapuis G, Meyer M, Petricek V. Sodium carbonate revisited. *Acta Crystallogr Sect B Struct Sci.* 2003;59:337–52.
197. Brooker MH, Bates JB. Raman and Infrared Spectral Studies of Anhydrous Li_2CO_3 and Na_2CO_3 . *J Chem Phys.* 1971;54:4788–96.
198. Stephens CJ, Ladden SF, Meldrum FC, Christenson HK. Amorphous Calcium Carbonate is Stabilized in Confinement. *Adv Funct Mater.* 2010;20:2108–15.
199. Wang D, Hamm LM, Bodnar RJ, Dove PM. Raman spectroscopic characterization of the magnesium content in amorphous calcium carbonates. *J*

- Raman Spectrosc. 2012;43:543–8.
200. Morse JW, Arvidson RS, Lüttge A. Calcium carbonate formation and dissolution. *Chem Rev.* 2007;107:342–81.
201. Meldrum FC. Calcium carbonate in biomineralisation and biomimetic chemistry. *Int Mater Rev.* 2003;48:187–224.
202. John W. Anthony, Bideaux RA, Kenneth W. Bladh, Nichols MC, editors. *Calcite. Handb Mineral. Mineral Data Publishing; 2005.*
203. Chan QHS, Zolensky ME, Bodnar RJ, Farley C, Cheung JCH. A Raman Study of Carbonates and Organic Contents in Five CM Chondrites [Internet]. 2016.
204. Sánchez-Pastor N, Gigler AM, Cruz JA, Park SH, Jordan G, Fernández-Díaz L. Growth of calcium carbonate in the presence of Cr(VI). *Cryst Growth Des.* 2011;11:3081–9.
205. Hu Y-B, Wolthers M, Wolf-Gladrow DA, Nehrke G. Effect of pH and Phosphate on Calcium Carbonate Polymorphs Precipitated at near-Freezing Temperature. *Cryst Growth Des.* 2015;15:1596–601.
206. Arita Y, Mazilu M, Dholakia K. Laser-induced rotation and cooling of a trapped microgyroscope in vacuum. *Nat Commun. Nature Publishing Group; 2013;4:1–7.*
207. Arita Y, McKinley AW, Mazilu M, Rubinsztein-Dunlop H, Dholakia K. Picoliter Rheology of Gaseous Media Using a Rotating Optically Trapped Birefringent Microparticle. *Anal Chem.* 2011;83:8855–8.
208. Gaudie RW, Sharma SK, Volk E. Micro-Raman spectral study of vaterite and aragonite otoliths of the coho salmon, *Oncorhynchus kisutch*. *Comp Biochem Physiol - A Physiol.* 1997;118:753–7.
209. Lu Z, Rickaby REM, Kennedy H, Kennedy P, Pancost RD, Shaw S, et al. An ikaite record of late Holocene climate at the Antarctic Peninsula. *Earth Planet Sci Lett. Elsevier B.V.; 2012;325–326:108–15.*
210. Di Marco VB, Bombi GG. Mathematical functions for the representation of chromatographic peaks. *J Chromatogr A.* 2001;931:1–30.
211. Zaghoul MR. On the calculation of the Voigt line profile: A single proper integral with a damped sine integrand. *Mon Not R Astron Soc.* 2007;375:1–6.
212. de Leeuw NH, Parker SC. Surface Structure and Morphology of Calcium Carbonate Polymorphs Calcite, Aragonite, and Vaterite: An Atomistic Approach. *J Phys Chem B.* 1998;102:2914–22.
213. Stancik AL, Brauns EB. A simple asymmetric lineshape for fitting infrared absorption spectra. *Vib Spectrosc.* 2008;47:66–9.
214. Addadi L, Raz S, Weiner S. Taking advantage of disorder: Amorphous calcium carbonate and its roles in biomineralization. *Adv Mater.* 2003;15:959–70.
215. Gebauer D, Völkel A, Cölfen H. Stable prenucleation calcium carbonate clusters. *Science (80-).* 2008;322:1819–22.
216. Nielsen MH, Aloni S, De Yoreo JJ. In situ TEM imaging of CaCO₃ nucleation reveals coexistence of direct and indirect pathways. *Science (80-).* 2014;345:1158–62.
217. Singer JW, Yazaydin AÖ, Kirkpatrick RJ, Bowers GM. Structure and transformation of amorphous calcium carbonate: A solid-state ⁴³Ca NMR and computational molecular dynamics investigation. *Chem Mater.* 2012;24:1828–36.
218. Effenberger H, Zemmann J, Mereiter K. Crystal structure refinements of magnesite, calcite, rhodochrosite, siderite, smithonite, and dolomite, with discussion of some aspects of the stereochemistry of calcite type carbonates. *Zeitschrift für Krist - New Cryst Struct.* 1981;156:233–43.
219. Wang Q. A computational study of calcium carbonate. PhD thesis. 2011;
220. Wang J, Becker U. Structure and carbonate orientation of vaterite (CaCO₃). *Am*

Mineral. 2009;94:380–6.

221. Plummer LN, Busenberg E. The solubilities of calcite, aragonite and vaterite in CO₂-H₂O solutions between 0 and 90°C, and an evaluation of the aqueous model for the system CaCO₃-CO₂-H₂O. *Geochim Cosmochim Acta*. 1982;46:1011–40.
222. Bischoff JL, Fitzpatrick JA, Rosenbauer RJ. The Solubility and Stabilization of Ikaite ((CaCO₃·6H₂O)) from 0° to 25°C: Environmental and Paleoclimatic Implications for Thinalite Tufa. *J Geol*. 1993;101:21–33.
223. Weiner S, Levi-Kalisman Y, Raz S, Addadi L. Biologically Formed Amorphous Calcium Carbonate. *Connect Tissue Res*. 2003;44:214–8.
224. Hall NF. Systems of acids and bases. *J Chem Educ*. 2009;17:124.
225. Craig RL, Nandy L, Axson JL, Dutcher CS, Ault AP. Spectroscopic Determination of Aerosol pH from Acid-Base Equilibria in Inorganic, Organic, and Mixed Systems. *J Phys Chem A*. 2017;121:5690–9.
226. Clayden J, Greeves N, Warren S. *Organic Chemistry*. Second. 2012.
227. Craig RL, Peterson PK, Nandy L, Lei Z, Hossain MA, Camarena S, et al. Direct Determination of Aerosol pH: Size-Resolved Measurements of Submicrometer and Supermicrometer Aqueous Particles. *Anal Chem*. American Chemical Society; 2018;90:11232–9.
228. Freedman MA, Ott EJE, Marak KE. Role of pH in Aerosol Processes and Measurement Challenges. *J Phys Chem A*. American Chemical Society; 2019;123:1275–84.
229. Hennigan CJ, Izumi J, Sullivan AP, Weber RJ, Nenes A. A critical evaluation of proxy methods used to estimate the acidity of atmospheric particles. *Atmos Chem Phys*. 2015;15:2775–90.
230. IUPAC. Quantities, Units and Symbols in Physical Chemistry [Internet]. Cohen ER, Cvitas T, Frey JG, Holström B, Kuchitsu K, Marquardt R, et al., editors. IUPAC Green B. Cambridge: Royal Society of Chemistry; 2007.
231. Clausius R. The Mechanical Theory of Heat with its applications to the steam-engine and to the physical properties of bodies. 1867.
232. Brown OLI. The Clausius-Clapeyron equation. *J Chem Educ*. 1951;28:428.
233. Camacho FF, Lugo NU, Martínez HC. The concept of entropy, from its origins to teachers. *Rev Mex Física*. 2015;61:69–80.
234. Goldstein S, Lebowitz JL. On the (Boltzmann) entropy of non-equilibrium systems. *Phys D Nonlinear Phenom*. 2004;193:53–66.
235. McNeil SE. Challenges for Nanoparticle Characterization. 2011. p. 9–15.
236. Jiang J, Oberdörster G, Biswas P. Characterization of size, surface charge, and agglomeration state of nanoparticle dispersions for toxicological studies. *J Nanoparticle Res*. 2009;11:77–89.
237. Delgado A V., González-Caballero F, Hunter RJ, Koopal LK, Lyklema J. Measurement and Interpretation of Electrokinetic Phenomena (IUPAC Technical Report). *Pure Appl Chem*. 2005;77:1753–805.
238. Chakraborty S. Encyclopedia of Microfluidics and Nanofluidics [Internet]. Li D, editor. *Encycl. Microfluid. Nanofluidics*. Boston, MA: Springer US; 2013.
239. Hulthe G, Stenhagen G, Wennerström O, Ottosson CH. Water clusters studied by electrospray mass spectrometry. *J Chromatogr A*. 1997;777:155–65.
240. Iyengar SS, Petersen MK, Day TJF, Burnham CJ, Teige VE, Voth GA. The properties of ion-water clusters. I. the protonated 21-water cluster. *J Chem Phys*. 2005;123:1–9.
241. Stoyanov ES, Stoyanova I V, Reed C a. The Structure of the Hydrogen Ion in Water. *JACS Commun*. 2010;132:1484–5.
242. Reed CA. Myths about the Proton. The Nature of H + in Condensed Media. *Acc*

- Chem Res. 2013;46:2567–75.
243. Ryding MJ, Izsák R, Merlot P, Reine S, Helgaker T, Uggerud E. Geometry of the magic number $H + (H_2O)_n$ 21 water cluster by proxy. *Phys Chem Chem Phys*. 2015;17:5466–73.
244. Duignan TT, Parsons DF, Ninham BW. A Continuum Solvent Model of the Multipolar Dispersion Solvation Energy. *J Phys Chem B*. 2013;117:9412–20.
245. Koprnikov IG. Nonadiabatic induced dipole moment by high intensity femtosecond optical pulses. *Appl Phys B Lasers Opt*. 2004;78:821–4.
246. Armin Wachter, Hoeber H. *Compendium of Theoretical Physics* [Internet]. New York: Springer-Verlag; 2006.
247. Assef AA, Maia JM, Schneider FK, Button VLSN, Costa ET. A reconfigurable arbitrary waveform generator using PWM modulation for ultrasound research. *Biomed Eng Online*. 2013;12:1–13.
248. Walton F, Wynne K. Control over phase separation and nucleation using a laser-tweezing potential. *Nat Chem*. Springer US; 2018;10:506–10.
249. Iwadate Y, Kawamura K, Igarashi K, Mochinaga J. Effective ionic radii of nitrite and thiocyanate estimated in terms of the Boettcher equation and the Lorentz-Lorenz equation. *J Phys Chem*. 1982;86:5205–8.
250. Lorentz HA. Ueber die Beziehung zwischen der Fortpflanzungsgeschwindigkeit des Lichtes und der Körperdichte. *Ann der Phys und Chemie*. 1880;245:641–65.
251. Krishnaswamy RK, Janzen J. Exploiting refractometry to estimate the density of polyethylene: The Lorentz–Lorenz approach re-visited. *Polym Test*. 2005;24:762–5.
252. Francesconi R, Ottani S. Correlation of density and refraction index for liquid binary mixtures containing polyglycols. Use of the group contributions in the Lorentz–Lorenz, Gladstone–Dale and Vogel equations to evaluate the density of mixtures. *J Mol Liq*. 2007;133:125–33.
253. Wright MR. *An Introduction to Aqueous Electrolyte Solutions*. 2007.
254. Lancaster JL. *Introduction to Classical Field Theory A tour of the fundamental interactions* [Internet]. IOP Publishing; 2018.
255. Warwicker J. PK a predictions with a coupled finite difference Poisson-Boltzmann and Debye–Hückel method. *Proteins Struct Funct Bioinforma*. 2011;79:3374–80.
256. Lu BZ, Zhou YC, Holst MJ, McCammon JA. Recent progress in numerical methods for the Poisson-Boltzmann equation in biophysical applications. *Commun Comput Phys*. 2008;3:973–1009.
257. Ralec C, Henry E, Lemor M, Killelea T, Henneke G. Calcium-driven DNA synthesis by a high-fidelity DNA Polymerase. *Nucleic Acids Res*. 2017;45:12425–40.
258. Stripp ST, Lindenstrauss U, Granich C, Sawers RG, Soboh B. The influence of oxygen on [NiFe]-hydrogenase cofactor biosynthesis and how ligation of carbon monoxide precedes cyanation. *PLoS One*. 2014;9.
259. Bearne SL. Illustrating the effect of pH on enzyme activity using Gibbs energy profiles. *J Chem Educ*. 2014;91:84–90.
260. Gadsby DC. Ion channels versus ion pumps: the principal difference, in principle. *Nat Rev Mol Cell Biol*. 2009;10:344–52.
261. Cherny V V., Markin VS, Decoursey TE. The Voltage-activated hydrogen ion conductance in rat alveolar epithelial cells is determined by the pH gradient. *J Gen Physiol*. 1995;105:861–96.
262. Ramsey IS, Mokrab Y, Carvacho I, Sands ZA, Sansom MSP, Clapham DE. An aqueous H^+ permeation pathway in the voltage-gated proton channel Hv1. *Nat Struct Mol Biol*. 2010;17:869–75.
263. Purves D, Augustine GJ, Fitzpatrick D, Hall WC, LaMantia A-S, McNamara JO,

- et al. *NEUROSCIENCE: Third Edition*. 3rd. Sinauer Associates, Inc.; 2004.
264. Mulani MS, Kamble EE, Kumkar SN, Tawre MS, Pardesi KR. Emerging strategies to combat ESKAPE pathogens in the era of antimicrobial resistance: A review. *Front Microbiol*. 2019;10.
265. Tommasi R, Brown DG, Walkup GK, Manchester JI, Miller AA. ESKAPEing the labyrinth of antibacterial discovery. *Nat Rev Drug Discov*. 2015;14:529–42.
266. U.S. Department of Health and Human Services C. Antibiotic resistance threats in the United States, 2019 [Internet]. Centers Dis. Control Prev. Atlanta, Georgia; 2019 Nov.
267. World Health Organization. World health organization releases global priority list of antibiotic-resistant bacteria to guide research, discovery, and development of new antibiotics. 2017.
268. Vergalli J, Bodrenko I V., Masi M, Moynié L, Acosta-Gutiérrez S, Naismith JH, et al. Porins and small-molecule translocation across the outer membrane of Gram-negative bacteria. *Nat Rev Microbiol*. Springer US; 2020;18:164–76.
269. Voet D, Voet J. *Biochemistry*, 4th Edition. 4th ed. John Wiley & Sons, Inc; 2010.
270. McPherson A, Gavira JA. Introduction to protein crystallization. *Acta Crystallogr Sect FStructural Biol Commun*. International Union of Crystallography; 2014;70:2–20.
271. Uversky VN. Intrinsically Disordered Proteins and Their “Mysterious” (Meta)Physics. *Front Phys*. 2019;7:8–23.
272. Na JH, Lee WK, Yu YG. How do we study the dynamic structure of unstructured proteins: A case study on nopp140 as an example of a large, intrinsically disordered protein. *Int J Mol Sci*. 2018;19.
273. Dunker AK, Lawson JD, Brown CJ, Williams RM, Romero P, Oh JS, et al. Intrinsically disordered protein. *J Mol Graph Model*. 2001;19:26–59.
274. Carpenter EP, Beis K, Cameron AD, Iwata S. Overcoming the challenges of membrane protein crystallography. *Curr Opin Struct Biol*. Elsevier Ltd; 2008;18:581–6.
275. Buhmann SY. *Dispersion Forces I* [Internet]. Berlin, Heidelberg: Springer Berlin Heidelberg; 2012.
276. Musher JI. Calculation of London—van der Waals Energies. *J Chem Phys*. 1963;39:2409–17.
277. Parsegian VA, Ninham BW. Temperature-Dependent van der Waals Forces. *Biophys J*. Elsevier; 1970;10:664–74.
278. Salam A. Non-Relativistic QED Theory of the van der Waals Dispersion Interaction [Internet]. Cham: Springer International Publishing; 2016.
279. Sernelius BE. *Fundamentals of van der Waals and Casimir Interactions* [Internet]. Cham: Springer International Publishing; 2018.
280. Cherepanov VN, Kalugina YN, Buldakov MA. Interaction-induced Electric Properties of van der Waals Complexes [Internet]. Cham: Springer International Publishing; 2017.
281. Muñoz J, Dimitrijević MS, Yubero C, Calzada MD. Using the van der Waals broadening of spectral atomic lines to measure the gas temperature of an argon-helium microwave plasma at atmospheric pressure. *Spectrochim Acta - Part B At Spectrosc*. 2009;64:167–72.
282. Lacapère JJ, Pebay-Peyroula E, Neumann JM, Etchebest C. Determining membrane protein structures: still a challenge! *Trends Biochem Sci*. 2007;32:259–70.
283. Stolzing A, Naaldijk Y, Fedorova V, Sethe S. Hydroxyethylstarch in cryopreservation - Mechanisms, benefits and problems. *Transfus Apher Sci*. Elsevier Ltd; 2012;46:137–47.
284. Eagle MJ, Rooney P, Kearney J. Effect of “non-controlled” freezing on

- cryopreserved skin viability. *Cell Tissue Bank*. 2010. p. 131–2.
285. Deller RC, Vatish M, Mitchell DA, Gibson MI. Synthetic polymers enable non-vitreous cellular cryopreservation by reducing ice crystal growth during thawing. *Nat Commun*. Nature Publishing Group; 2014;5:1–7.
286. Jearl Walker, Halliday D, Resnick R. *Fundamentals of Physics*. 10th ed. Wiley. John Wiley & Sons, Inc; 2014.
287. Burnham DR, McGloin D. Radius measurements of optically trapped aerosols through Brownian motion. *New J Phys*. 2009;11:063022.
288. Einstein A. Über die von der molekularkinetischen Theorie der Wärme geforderte Bewegung von in ruhenden Flüssigkeiten suspendierten Teilchen. *Ann der Phys*. 1905;8:549–560.
289. Furth R, Cowper A. Investigations on the theory of the Brownian movement by Albert Einstein. Ed Transl Artic *Ann der Phys*. 1956;
290. Smoluchowski M. Zur kinetischen Theorie der Brownschen Molekularbewegung und der Suspensionen. *Ann Phys*. 1906;14:756–780.
291. Lemons DS, Gythiel A. Paul Langevin's 1908 paper "On the Theory of Brownian Motion" ["Sur la théorie du mouvement brownien," *C. R. Acad. Sci. (Paris)* **146**, 530–533 (1908)]. *Am J Phys*. 1997;65:1079–81.
292. Perrin MJ. *Brownian Movement and Molecular Reality* (translated by F. Soddy). Taylor & Francis Ltd.; 1910.
293. Bui AAM, Stilgoe AB, Lenton ICD, Gibson LJ, Kashchuk A V., Zhang S, et al. Theory and practice of simulation of optical tweezers. *J Quant Spectrosc Radiat Transf*. Elsevier Ltd; 2017;195:66–75.
294. Haw MD. Colloidal suspensions, brownian motion, molecular reality: A short history. *J Phys Condens Matter*. 2002;14:7769–79.
295. Löffler A, Kruschwitz L. *The Brownian Motion* [Internet]. Cham: Springer International Publishing; 2019.
296. Uhlenbeck GE, Ornstein LS. On the theory of the Brownian motion. *Phys Rev*. 1930;36:823–41.
297. Wang MC, Uhlenbeck GE. On The Theory of the Brownian Motion II. *Rev Mod Phys*. 1945;17:323–42.
298. Cadena-Herrera D, Esparza-De Lara JE, Ramírez-Ibañez ND, López-Morales CA, Pérez NO, Flores-Ortiz LF, et al. Validation of three viable-cell counting methods: Manual, semi-automated, and automated. *Biotechnol Reports*. Elsevier B.V.; 2015;7:9–16.
299. SunitaDevi N, Hemachandran K. Automatic Face Recognition System using Pattern Recognition Techniques: A Survey. *Int J Comput Appl*. 2013;83:10–3.
300. Seurat G. "A Sunday on La Grande Jatte" [Internet]. 1884.
301. Sakimoto T, Rosenblatt MI, Azar DT. Laser eye surgery for refractive errors. *Lancet*. 2006;367:1432–47.
302. Kaye PH. Spatial light-scattering analysis as a means of characterizing and classifying non-spherical particles. *Meas Sci Technol*. 1998;9:141–9.
303. Ulanowski Z, Hirst E, Kaye PH, Greenaway R. Retrieving the size of particles with rough and complex surfaces from two-dimensional scattering patterns. *J Quant Spectrosc Radiat Transf*. Elsevier; 2012;113:2457–64.
304. Miles REH, Carruthers AE, Reid JP. Novel optical techniques for measurements of light extinction, scattering and absorption by single aerosol particles. *Laser Photonics Rev*. 2011;5:534–52.
305. Meresman H, Wills JB, Summers M, McGloin D, Reid JP. Manipulation and characterisation of accumulation and coarse mode aerosol particles using a Bessel beam trap. *Phys Chem Chem Phys*. 2009;11:11333.

306. Carruthers AE, Horrocks BR, Rosario GL, Miloserdov A, Day CPF. Probing chemical transformation in picolitre volume aerosol droplets. In: Dholakia K, Spalding GC, editors. *Opt Trapp Opt Micromanipulation XIV*. SPIE; 2017. p. 79.
307. Gebauer D, Völkel A, Cölfen H. Stable Prenucleation Calcium Carbonate Clusters. *Science (80-)*. 2008;322:1819–22.
308. Nie S. Probing Single Molecules and Single Nanoparticles by Surface-Enhanced Raman Scattering. *Science (80-)*. 1997;275:1102–6.